University of Latvia

LATVIJAS
UNIVERSITĀTE

INGA BRICE

WHISPERING GALLERY MODE SILICA MICROSPHERE RESONATOR APPLICATIONS FOR BIOSENSING AND OPTICAL FREQUENCY COMBS

DOCTORAL THESIS

Submitted for the degree of Doctor of physics
Subfield of laser physics and spectroscopy

Riga, 2021

The doctoral thesis was carried out in Faculty of Physics, Mathematics and Optometry, Faculty of Physics University of Latvia and Institute of Atomic Physics and Spectroscopy of the University of Latvia from 2013 to 2021.

The thesis contains five chapters, reference list and three appendices.

Form of the thesis: dissertation in physics, laser physics and spectroscopy.

Supervisor : Dr. phys. Janis Alnis, leading researcher at IAPS, University of Latvia

Reviewers:

1. Dr. phys. Artūrs Bundulis, leading researcher, Institute of Solid State Physics, University of Latvia, Latvia;
2. Dr. phys. Gita Rēvalde, leading researcher, Institute of Atomic Physics and Spectroscopy, University of Latvia, professor, Riga Technical University, Latvia;
3. PhD. Jose Alfredo Alvarez Chavez, Assistant Professor, Faculty of Science and Technology, University of Twente, Netherlands.

The thesis is available at the Library of the University of Latvia, Kalpaka blvd. 4.

Whispering gallery mode silica microsphere resonator applications for biosensing and optical frequency combs

ABSTRACT

Whispering gallery modes resonators (WGMRs) have attracted interest due to their optical properties and variety of potential applications. By choosing an appropriate material with very low absorption, and fabricating a very smooth surface, WGMRs can reach ultra-high quality (Q) factors. Whispering gallery mode (WGM) resonances in the resonators are a function of their geometry and refractive index which makes them interesting for sensor applications while the high Q makes them suitable for nonlinear interaction and optical frequency comb generation. The frequency combs cover a broad spectral interval that allows the substitution of an expensive laser arrays for telecommunication data transmission systems.

Any perturbation to the optical path of the light circulating inside the WGMR results in the shift of the WGM resonances. To enhance optical properties or detect molecules or biomolecules, the surface of WGMR has to be functionalized with a nanomaterial layer. Sensing molecule adhesion to the surface is a good step towards biosensor development without forgetting the selectivity.

In this thesis, fabricated in house silica microsphere WGMRs with Q factors 10^6 - 10^8 and diameter of 500 - 700 μm were used to coat the surface with multiple different functionalizing layers. A glucose sensor model was developed and tested. Gold (Au) nanoparticles (NPs) were used to enhance the sensitivity together with glucose oxidase (GOx) to ensure selectivity. Several zinc oxide (ZnO) structures were tested to increase surface area for protein binding which were selective for antigen/antibody reactions of developed toxin sensor for Bovine leukemia virus. For the toxin sensor model, the quality of ZnO layer was important to reduce Q factor losses. ZnO nanolayer had an optimal thickness of 10 - 20 nm. Further testing of toxin sensor has to be done to validate the drawn conclusions about the observed sensor response.

Different WGMR geometries and materials have been used to generate frequency combs (WCombs) with low-power pumping. For microspheres, the resonator radius can be modified to change the free spectral range (FSR) and distance between the generated WComb lines. For application in data transmission, the FSR of 200 GHz or less, matching the ITU-T spectral grid, is desirable.

In this thesis, fabricated in house silica microsphere WGMRs with Q factors 10^7 and diameter of 120 - 300 μm were used to generate WComb. Pumping lasers in the C-band telecommunication diapason (1530 - 1565 nm) were used for WComb excitation. The WComb spectra were observed for both Kerr (1500 - 1600 nm) and Raman combs

(1400 - 1500 nm and 1600 -1700 nm). Long-term stability was investigated. The stability was mainly affected by temperature.

PUBLICITY

PUBLICATIONS INCORPORATED IN THE THESIS:

All publications by the author that are related with the whispering gallery mode resonator applications are listed here. Main ideas and figures shown in the thesis have appeared in the following publications:

[P1] I. Brice, K. Grundsteins, A. Atvars, J. Alnis, and R. Viter. "Whispering gallery mode resonators coated with Au nanoparticles." In: *Nanoengineering: Fabrication, Properties, Optics, Thin Films, and Devices XVI*. Ed. by A.J. Attias and B. Panchapakesan. Proceedings of SPIE, 2019, p. 65. DOI: 10.1117/12.2528677
Author contribution 80%.

[P2] I. Brice, K. Grundsteins, A. Atvars, J. Alnis, R. Viter, and A. Ramanavicius. "Whispering gallery mode resonator and glucose oxidase based glucose biosensor." In: *Sensors and Actuators B: Chemical* 318 (2020), p. 128004. DOI: 10.1016/j.snb.2020.128004
Author contribution 70%.

[P3] I. Brice, R. Viter, K. Draguns, K. Grundsteins, A. Atvars, J. Alnis, E. Coy, and I. Iatsunskyi. "Whispering gallery mode resonators covered by a ZnO nanolayer." In: *Optik* 219 (2020), p. 165296. DOI: 10.1016/j.ijleo.2020.165296
Author contribution 60%.

[P4] I. Brice, K. Grundsteins, A. Sedulis, T. Salgals, S. Spolitis, V. Bobrovs, and J. Alnis. "Frequency comb generation in whispering gallery mode silica microsphere resonators." In: *Laser Resonators, Microresonators, and Beam Control XXIII*. Ed. by A.M. Armani, A.V. Kudryashov, A.H. Paxton, V.S. Ilchenko, and J.V. Sheldakova. Vol. 11672. Proceedings of SPIE, 2021, p. 1167213. DOI: 10.1117/12.2577148
Author contribution 70%.

Full text of publications P1-P4 can be found in the Appx. A.
Some ideas and figures shown in the thesis have appeared also in the following publications:

[P5] J. Alnis, I. Brice, A. Pirktina, A. Ubele, K. Grundsteins, A. Atvars, and R. Viter. "Development of optical WGM resonators for

biosensors." In: *Biophotonics—Riga 2017*. Ed. by J. Spigulis. Vol. 10592. Proceedings of SPIE, 2017, p. 19. DOI: 10.1117/12.2297551

[P6] J. Braunfelds, R. Murnieks, T. Salgals, I. Brice, T. Sharashidze, I. Lyashuk, A. Ostrovskis, S. Spolitis, J. Alnis, J. Porins, and V.S Bobrovs. "Frequency comb generation in WGM microsphere based generators for telecommunication applications." In: *Quantum Electronics* 50 (2020), pp. 1043–1049. DOI: 10.1070/QEL17409

[P7] T. Salgals, J. Alnis, R. Murnieks, I. Brice, J. Porins, A.V. Andrianov, E.A. Anashkina, S. Spolitis, and V. Bobrovs. "Demonstration of a fiber optical communication system employing a silica microsphere-based OFC source." In: *Optics Express* 29 (2021), p. 10903. DOI: 10.1364/OE.419546

[P8] K. Draguns, I. Brice, A. Atvars, and J. Alnis. "Computer modelling of WGM microresonators with a zinc oxide nanolayer using COMSOL multiphysics software." In: *Laser Resonators, Microresonators, and Beam Control XXIII*. Ed. by A.M. Armani, A.V. Kudryashov, A.H. Paxton, V.S. Ilchenko, and J.V. Sheldakova. Vol. 11672. Proceedings of SPIE, 2021, p. 1167216. DOI: 10.1117/12.2578210

Other publications, whose ideas do not appear directly in the thesis, but are related to the topic of WGMRs:

[P9] R. Berkis, J. Alnis, A. Atvars, I. Brice, K. Draguns, and K. Grundsteins. "Quality Factor Measurements for PMMA WGM Microsphere Resonators Using Fixed Wavelength Laser and Temperature Changes." In: *2019 IEEE 9th International Conference Nanomaterials: Applications & Properties (NAP)*. IEEE, 2019, 01P05–1–01P05–4. DOI: 10.1109/NAP47236.2019.219072

[P10] R. Berkis, J. Alnis, I. Brice, A. Atvars, K. Draguns, K. Grundšteins, and P.K. Reinis. "Mode family analysis for PMMA WGM micro resonators using spot intensity changes." In: *Laser Resonators, Microresonators, and Beam Control XXIII*. Ed. by A.M. Armani, A.V. Kudryashov, A.H. Paxton, V.S. Ilchenko, and J.V. Sheldakova. Vol. 11672. Proceedings of SPIE, 2021, p. 1167217. DOI: 10.1117/12.2577025

[P11] P.K. Reinis, L. Milgrave, K. Draguns, I. Brice, J. Alnis, and A. Atvars. "High-Sensitivity Whispering Gallery Mode Humidity Sensor Based on Glycerol Microdroplet Volumetric Expansion." In: *Sensors* 21 (2021), p. 1746. DOI: 10.3390/s21051746

[P12] E.A. Anashkina, V. Bobrovs, T. Salgals, I. Brice, J. Alnis, and A.V. Andrianov. "Kerr Optical Frequency Combs With Multi-FSR Mode

Spacing in Silica Microspheres." In: *IEEE Photonics Technology Letters* 33 (2021), pp. 453–456. DOI: 10.1109/LPT.2021.3068373

CONFERENCES:

[C1] 1st International Conference "Biophotonics - Riga 2013", Riga, Latvia (August 29-31, 2013), poster presentation "Towards Skin Fluorescence Diagnostics Using Femtosecond Frequency Comb Laser" I. Brice, I. Ferulova, J. Spigulis, J. Alnis

[C2] 1st International Conference "Nocturnal Atmosphere, Remote Sensing and Laser Ranging: NOCTURNAL - Riga 2014" Riga, Latvia (October 17, 2014), poster presentation "GNSS More Than a Tool for Navigation" , I. Brice, J. Alnis

[C3] 11th International Young Scientist conference "Developments in Optics and Communications" Riga, Latvia (April 8-10, 2015), poster presentation "GNSS – More Than A Simple Tool For Navigation", Inga Brice, Janis Alnis, p. 26 (2015)

[C4] Fifth International School and Conference on Photonics "Photonica 2015" Belgrade, Serbia, (August 24-28, 2015), poster presentation "Measurements of Rb hyperfine splitting with a femtosecond optical frequency comb", I. Brice, J. Alnis, J. Rutkis, p. 98 (2015)

[C5] 12th International Young Scientist conference "Developments in Optics and Communications Riga", Latvia (March 21.-23, 2016), poster presentation "Measurements of Rb 5S-5P Transition with a femtosecond optical frequency comb", Inga Brice, Janis Alnis, Jazeps Rutkis, p. 11 (2016)

[C6] 60th International Conference for Students of Physics and Natural Sciences "Open readings 2017" Vilnius, Lithuania (March 14-17, 2017), poster presentation "TOWARDS WGM RESONATOR STABILISED ON Rb 5S-5P TRANSITION LINES" Inga Brice, Antons Pribitoks, Janis Alnis, p. 212 (2017)

[C7] 2nd International Conference "Biophotocis Riga 2017" Riga, Latvia (August 27-29, 2017), poster presentation "Development of Optical WGM Resonators for Biosensors", I. Brice, A. Pirktina, A. Ubele, K. Grundsteins, A. Atvars, R. Viter, J. Alnis, p. 34 (2017)

[C8] International conference "Nanomaterials for biosensors and biomedical applications" Jurmala, Latvia (July 2-4, 2019), poster pre-

sentation "WGMR coated with Au NPs to enhance the sensitivity" I. Brice , K. Grundsteins, A. Atvars, R. Viter, J. Alnis, p. 62 (2019)

[C9] 10th Optoelectronics and Photonics Winter School:NLP2019-Nonlinear Photonics, Trento-Andalo, Italy (January 20-26, 2019), poster presentation "Temperature scanning the WGMR resonances in air and water" I. Brice, D. Damberga, K. Grundsteins, U. Berzins, A. Atvars, R. Viter, J. Alnis

[C10] "SPIE Optics + Photonics 2019" San Diego, USA (August 11-15 2019), poster presentation "Whispering gallery mode resonators coated with Au nanoparticles", I. Brice, K. Grundsteins, A. Atvars, J. Alnis, R. Viter, Proceedings of SPIE: Nanoengineering: Fabrication, Properties, Optics, Thin Films, and Devices XVI. Vol. 110892019 p. 110891T (2019)

[C11] Third edition of Photonics Online Meet-up "POM2021" USA - online event (January 11-14, 2021), poster presentation "Optical frequency comb generated inside silica microsphere for WDM Data Transmission System" Inga Brice, Karlis Grundsteins, Toms Salgals, Janis Alnis, p. 132 (2021)

[C12] "SPIE Photonics West 2021" San Francisko, USA - online event (March 6-11, 2021), poster presentation "Frequency comb generation in whispering gallery mode silica microsphere resonators" Inga Brice, Karlis Grundsteins, Arvids Sedulis, Toms Salgals, Sandis Spolitis, Vjaceslavs Bobrovs, Janis Alnis, Proceedings of SPIE: Laser Resonators, Microresonators, and Beam Control XXIII. Vol. 11672, p. 1167213 (2021)

[C13] International Conference "Quantum Optics and Photonics 2021" Riga, Latvia - online event (April 22-23, 2021), poster presentation "Whispering gallery mode silica microsphere resonator applications for biosensing and communications" Inga Brice, Toms Salgals, Vjaceslavs Bobrovs, Roman Viter, Janis Alnis, p. 35 (2021)

CONTENTS

LIST OF FIGURES

LIST OF TABLES

ACRONYMS

ALD Atomic Layer Deposition

BLV Bovine Leukemia Virus

BSA Bovine Serum Albumin

CW Continious Wave

ECDL External Cavity Diode Laser

EDFA Erbium-Doped Fiber Amplifier

FFT Fast Fourier Transform

FSR Free Spectral Range

FWHM Full Width at Half Maximum

FWM Four Wave Mixing

GOx Glucose Oxidase

LoD Limit of Detection

LSPR Localized Surface Plasmon Resonance

NP NanoParticle

NR NanoRod

OBPF Optical BandPass Filter

OFC Optical Frequency Comb

OSA Optical Spectrum Analyzer

PBS Phosphate Buffered Saline

PS Power Splitter

PC Polarization Controller

PD Photo Detector

RIU Refractive Index Unit

Q factor Optical Quality factor

VAO Optical Variable Attenuator

WDM Wavelength Division Multiplexing

WGM Whispering Gallery Mode

WGMR Whispering Gallery Mode Resonator

WComb Optical Frequency Comb Generated Inside WGMR

ZDW Zero Dispersion Wavelength

Part I

DISSERTATION

1 INTRODUCTION

1.1 MOTIVATION

Optical resonators, devices that confine and store light, are made up of mirrors, for example, Fabry–Perot resonator consisting of two flat mirrors, or dielectric material, for example, transparent dielectric sphere. They are used for a variety of applications: laser resonators, etalon, filters, enhancement of power, etc. Bulk optical resonators are large when compared with the wavelength of the light confined inside, therefore, miniaturized optical resonators play an important role in modern optics.

In recent years whispering gallery modes resonators (WGMRs) have attracted increasing attention and a growing number of papers about them have been published [13–18]. WGMRs have attracted interest due to their many potential applications. By confining the light beam inside a circular symmetry structure whispering gallery modes (WGMs) can be sustained inside with small reflection losses. By choosing an appropriate material with very low absorption, and fabricating a very smooth surface, WGMRs can reach ultra-high quality (Q) factors. Ultra-high Q allows light circulating inside to have a lengthy ring down allowing it to interact with the surrounding environment multiple times enhancing the light-matter interaction. High Q factors allow high energy densities to circulate inside and have very narrow resonances (< 100 KHz at 1550 nm [15]). This makes WGMRs suited as [19]: laser cavities, resonant filters, sensitive sensors, generation of nonlinear effects at relatively low powers.

1.1.1 *WGMR Biosensors*

WGMR sensor operation principles are based on a shift of WGM resonance due to external influence (temperature, pressure, humidity, etc.). WGM resonances in the WGMRs are a function of their geometry and refractive index. WGMRs have been used for sensor applications such as temperature sensors [20–22], pressure sensors [22–24], force sensors [22], humidity sensors [25] etc. The key is finding suitable fabrication material and WGMR geometry for different applications. To enhance optical properties or detect molecules, including biomolecules, the surface of WGMR has to be functionalized with a nanomaterial layer. It is important to form a homogeneous and thin coating in the range 10 - 100 nm to provide effective light coupling [14, 24, 26] as adding any type of nanoparticles (NPs) through depo-

sition on the surface will lead to the degradation of the Q factor. The Q factor decreases because of the absorption losses in the coating and scattering losses from the surface roughness increase.

WGMR can be combined with localized surface plasmon resonance (LSPR) nanostructures. LSPR enhances the sensitivity of WGMR sensors as the evanescent field around the resonator is extended with large tails around the metal NPs [27].

ZnO is well known material for different optoelectronic applications, such as sensors, biosensors, and optical coatings [28]. ZnO microstructures have been used as WGMRs for laser and sensor applications [29] due to the biocompatibility and functionality of the surface.

Sensing molecule adhesion to the surface is a good step towards biosensor development but not enough to call it a biosensor. One of the requirements for WGMR biosensors, which is often forgotten, is selectivity - the ability to distinguish the desired biomolecules from other molecules. Many enzymes, for example, glucose oxidase (GOx) which oxidizes glucose, or genes/antigens have selective properties and have to be tailored for each biomolecule [24, 26].

Microspheres are the simplest 3D WGMR. Silica microspheres can be easily fabricated by melting a tip of an optical fiber. Microsphere WGMR can support many WGMs with equatorial, radial, and polar dependencies which have very low optical losses, resulting in high Q factor [30]. It is easy to coat microspheres to functionalize the surface and enhance the optical properties or add new properties.

In this thesis, fabricated silica microsphere WGMRs surface was coated with multiple different functionalizing layers. Au NPs were used to enhance the sensitivity together with GOx to ensure selectivity. Several ZnO structures were tested to increase surface area for protein binding which were selective for antigen/antibody reactions. The modified WGMR surface was characterized by excitation of WGM resonances and determination of the Q factor. The sensor response was tested in a liquid drop by observing the resonance shift.

1.1.2 *WGMR generated Optical frequency Comb*

An optical frequency comb - spectrum composed of many equidistantly spaced narrow modes at known optical frequencies like an optical ruler [31] - can be generated using third-order $\chi^{(3)}$ Kerr-nonlinearity. It is induced by four-wave mixing (FWM), and generates the equidistant optical side-bands in the WGM microresonators [32–34]. WGMRs are suitable for nonlinear interactions due to their ultrahigh Q factors, the efficiency of FWM, and low-power pumping required, for example, 10 mW or 10 dBm, [35, 36]. Different WGMR geometries and materials have been used to generate the WCombs. Optical frequency combs have many applications in optical clocks, spectroscopy, and communications [36–40]. WCombs when compared to regular optical

frequency comb tradeoff stability for power consumption, cost, and size.

The frequency combs cover a broad spectral interval that, with a proper line spacing, allows the substitution of an expensive laser array solution for wavelength-division multiplexing (WDM) data transmission system [41, 42].

Microsphere WGMRs can be manufactured more easily and quickly with somewhat reproducible parameters by melting the end of an optical fiber. The Q factor for microspheres is high $10^7 - 10^9$.

In this thesis, fabricated silica microsphere WGMRs were used to generate an optical frequency come inside WGMR (WComb). WComb excitation spectra were observed by pumping with 32 laser wavelengths C-band channels. Generated WComb long-term stability without any active stabilization elements was observed. Generated WCombs were further examined for the suitability for wavelength division multiplexing (WDM) data transmission systems [7].

1.2 STRUCTURE OF THE THESIS

The thesis "Whispering gallery mode silica microsphere resonator applications for biosensing and optical frequency combs" is composed of five chapters and three appendices.

Chapter 1 is introductory and describes the motivation behind the research. The aim and objectives and author contributions are listed here.

Chapter 2 examines the theory of WGMRs. The chapter consists of three parts. Part 1 focuses on main laser components in general and investigates more in-depth laser resonator. Part 2 describes WGM resonances, WGMRs geometry, and main characterization parameters. Part 3 addresses the issue of coupling the light inside the WGMR.

Chapter 3 concentrates on WGMR biosensor application and is subdivided into seven parts. Part 1 provides theoretical information about sensors and WGMR sensing mechanisms. Parts 2 and 3 illustrate the WGMR silica microsphere fabrication process and WGMR surface functionalization respectively. Parts 4 and 5 look at constructed setups and workflow for WGMR characterization in air and sensor testing in liquid drop. Parts 6 and 7 describe the obtained results for different coated resonator characterization with tested glucose and toxin sensor responses.

Chapter 4 focuses on WGMR application for WComb generation and is subdivided into three parts. Parts 1 and 2 describe the theory about optical frequency combs and focuses on explaining the WCombs generation. Part 2 illustrates the constructed setups with prism and tapered fiber coupling for WComb generation in silica microspheres. Part 3 looks at the generated WComb and their long-term stability results.

Conclusions are drawn in Chapter 5. The main aim of the thesis has been reached. Four thesis statements were formulated.

Appendix A includes 4 main publications which are incorporated in the thesis.

Appendix B focuses on atom spectroscopy. Part 1 describes the spectral linewidth important for understanding Doppler free saturation spectroscopy. Part 2 focuses on atomic structure and explains the energy splitting of Rb atoms.

Appendix C illustrates the examples of more complicated calculations from Chapter 4. Part 1 looks closer at material dispersion. Part 2 shows power build up calculation example.

1.2.1 *Aim*

To develop whispering gallery mode microsphere resonators as potential biosensors by coating the surface with several functionalizing layers to build a glucose and a toxin sensor, and to evaluate the potential of bare microsphere resonators as optical frequency comb source for data transmission application.

1.2.2 *Objectives*

1. To develop WGMR biosensor models and choose surface WGMR functionalization layers for glucose and toxin sensors.
2. To coat microsphere WGMR with ZnO nanostructures and Au nanoparticles and investigate the influence of each layer on the Q factor.
3. To add a selective layer on WGMR to fabricate glucose and toxin biosensors.
4. To examine the influence of Au NPs and GOx layers for glucose sensor.
5. To investigate the influence of temperature and glucose drop evaporation on WGMR resonances.
6. To determine the relationship between the ZnO nanostructures and ZnO layer thickness for the Q factor.
7. To examine the influence of ZnO and protein layers for toxin sensor.
8. To generate a WComb inside a silica microsphere WGMR with a line spacing aligned with ITU-T grid for WDM.
9. To calculate the power buildup inside the silica microspheres.
10. To check the long term stability of the generated WComb.

1.3 AUTHOR CONTRIBUTION

The research was conducted at the Laboratory of Quantum optics of the Institute of Atomic Physics and Spectroscopy in 2013 - 2021. The results presented in this thesis were achieved by teamwork. In this section, author contributions are listed and other contributors are credited.

LITERATURE REVIEW Literature and publications about lasers, applications of WGMRs, and WCombs was analyzed by the author.

WGMR FABRICATION The fabrication of WGMRs was done by Karlis Grundsteins and Arvids Sedulis. The author contributed by recording and updating various fabrication process details and protocols. WGMR degradation was investigated by the author. 166 and 170 μm microspheres for WComb were fabricated by the E. Anaskina and A. Andrianov group from the Institute of Applied Physics of the Russian Academy of Sciences, Nizhny Novgorod. Chemicals for WGMR surface functionalization and testing were prepared by Roman Viter. Coating protocols were developed together with Roman Viter. Author coated WGMRs with Au NPs and GOx for glucose sensor testing. ZnO ALD layers were coated by Igor Iatsunskyi from NanoBioMedical Centre of Adam Mickiewicz University with Roman Viter. ZnO drop coating method was developed together with Karlis Grundsteins under Roman Viter's guidance. BLV and BSA proteins were coated on the WGMRs by the author.

TESTING BIOSENSORS Experimental setups were constructed and modified together with Janis Alnis. The calibration method using Rb and interferometric fringes was implemented by the author. Both bare and coated WGMR characterization experiments and WGMR sensor testings were done by the author. Obtained data processing and analysis were done by the author. The results were interpenetrated with help from Roman Viter and Arunas Ramanavicius. ZnO surface simulations were done by Kristians Draguns. First drafts of the publications [P1] and [P2] were prepared by the author, and first draft of [P3] was prepared together with Roman Viter.

GENERATING WCOMB WComb testing was performed together with Janis Alnis and Toms Salgals. Simulations were done by Kristians Draguns. Data processing and analysis of WComb spectra, power buildup calculations, and stability assessment were done by the author. The results were interpreted with help from Janis Alnis. First drafts of the publications [P4] was prepared by the author.

The research results of the dissertation have been used for the implementation of scientific research projects:

- ERDF No. 1.1.1.1/16/A/259 “Development of novel WGM microresonators for optical frequency standards and biosensors, and their characterization with a femtosecond optical frequency comb”;
- ERDF No. 1.1.1.1/18/A/155 "Development of Optical Frequency Comb Generator Based on a Whispering Gallery Mode Microresonator and its Applications in Telecommunications";
- LZP No. lzp-2018/1-0510 "Optical whispering gallery mode microresonator sensors".

2 WHISPERING GALLERY MODE RESONATORS

2.1 THE MAIN COMPONENTS OF THE LASER

A laser is a device that both generates and amplifies a coherent light beam [43]. To create a laser one needs the following components:

- a laser gain medium;
- a pumping process;
- optical feedback elements.

2.1.1 *Gain Medium*

A laser gain medium or a laser active medium is a substance that can amplify the power of the light beam passing through. The increase in power is necessary to compensate for the power loss which occurs in the laser resonator.

Different materials can be used as a laser gain medium. The most common materials are [44]:

- semiconductors, for example, GaAs, AlGaAs or InGaAs;
- crystals and glasses doped with active ions, for example, Nd:YAG, Ti:sapphire, Yb:glass, ruby;
- ceramics doped with various rare-earth ions;
- liquids that "dye" lasers with their broad fluorescence spectra, for example, rhodamine, fluorescein, coumarin, stilbene;
- gases and gas mixtures, for example, He-Ne, Ar, CO_2.

2.1.2 *Pumping Process*

Population inversion is the redistribution of atoms in the energy levels by pumping energy into the system so more atoms are in high energy states than in lower ones.

The laser loses energy by emitting it in the form of either a continuous light beam or light pulses. To obtain amplification, the laser medium must receive energy from the outside, for example by electric current, other light sources, etc. The received energy is turned into light and amplified in the laser medium. This process is called pumping. The pumping process replenishes the energy lost and maintains the necessary population inversion, which in turn ensures the operation of the laser. The population inversion is required to maintain stimulated emissions.

2.1.2.1 *Stimulated emission*

The concept of stimulated emission, which is essential for lasers, was first mentioned in Einstein's 1915-1916 publication "Strahlungs Emission und Absorption nach der Quantentheorie" (Radiation Emission and Absorption in Quantum Theory). It is an important publication where Einstein showed a very simple and elegant proof of the quantum nature of light, as well as significant results in light absorption and emission in atoms and molecules [45]. Einstein assumed that molecules could interact with radiation in three different processes.

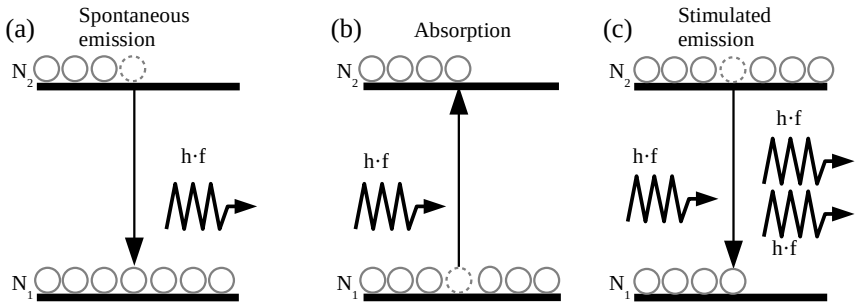

Figure 2.1: Three processes of molecules interacting with radiation: when population in the energy levels $N_1 > N_2$ a photon can be (a) emitted in spontaneous emission or (b) absorbed; (c) when $N_2 > N_1$ stimulated emission happens and the first photon stimulates the emission of the second photon in the same direction.

SPONTANEOUS EMISSION The first process is spontaneous emission. This occurs when the molecule is in the excited state and relaxes by spontaneously emitting a photon and the electron moves to a lower energy level [45] (see Fig. 2.1 a). The frequency f of the photon corresponds to the energy difference between the levels. The formula for describing this relationship is:

$$E = h \cdot f, \tag{2.1}$$

where E is the energy, h is the Planck's constant and f is the frequency.

ABSORPTION The second process can be considered as the opposite of the first process - absorption. When a molecule interacts with a photon, its energy can be absorbed if the energy of the photon corresponds to the energy difference between two energy levels in the molecule [45] (see Fig. 2.1 b). The molecule is excited as the electron moves to a higher energy level.

STIMULATED EMISSION The third process was presented by Einstein. It is known as stimulated emission. If the molecule is in the

excited energy state and interacts with a photon whose energy corresponds to the energy difference between the two states, then it can relax to a lower energy level. As a result, a photon is emitted, the energy of which corresponds to the first photon. The first photon is not affected by this interaction and only "stimulates" the molecule to relax and the second emitted photon also moves in the same direction and has the same momentum [45] (see Fig. 2.1 c).

2.1.2.2 *Population Inversion*

Population inversion is an important precondition for obtaining stimulated emissions. Electrons usually inhabit the lowest available energy level. Thus population in the lower energy level N_1 is larger than the population N_2 in higher energy level. Electrons can be excited at a higher energy level by absorption, but that alone is not enough because the spontaneous emissions of these electrons return to the lowest energy level. Population inversion cannot be obtained with only two energy levels, because the probabilities of absorption and spontaneous emission are equal and $N_1 = N_2$. At least three energy levels are required to achieve population inversion.

2.1.3 *Optical Feedback Elements*

By using a laser medium and a pumping process, it is possible to increase the light intensity. So the laser amplifier was already created using only the first two components (see Fig. 2.2 a). Optical feedback elements allow the laser beam to bounce back and forth through the laser medium multiple times creating a laser oscillator. If a single mirror with a reflection coefficient of 100% is added to the system, two systems are obtained and the light is amplified twice [46] because its image is formed in the mirror (see Fig. 2.2 ab). When a system is

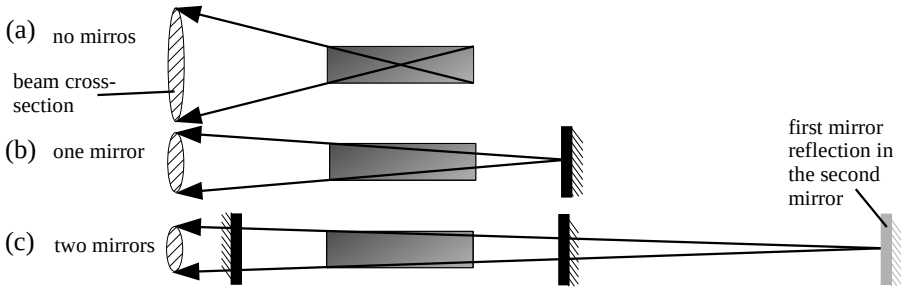

Figure 2.2: Optical feedback elements redirect some portion of the light back into the laser medium: (a) without optical feedback the output beam is diverging, (b) with one mirror the divergence is smaller and (c) with two mirrors the beam is the narrower with the smallest divergence governed by diffraction.

made up of two mirrors, an infinite number of images are obtained in the mirrors and the light is amplified many many times (see Fig. 2.2 c). For the light to escape from the system, the second mirror has to have a lower reflection coefficient, for example, 99.9%. Some of the light will pass outside the laser system and can be used. The laser beam, which is often reflected from mirrors, is narrower and less diverging, so laser systems prefer designs with at least two optical feedback elements.

2.1.4 *Laser Resonator*

Laser amplifiers with feedback elements can be divided into two groups [46]: mirror array amplifiers and laser resonators. In both cases, the light beam travels through the laser medium multiple times.

MIRROR ARRAY In a mirror array, when the beam is reflected, it continues the trajectory in a slightly different place in the medium. It is similar to the Fabry-Perot interferometer and extends the optical path through the laser medium (see Fig. 2.3 a).

RESONATOR The laser resonator or regenerative amplifier is designed so that the beam travels through the same region of the laser medium using the same trajectory (see Fig. 2.3 b). The simplest laser resonator can be created with two mirrors. At least one mirror has to have a reflection coefficient of just under 100%. Both mirrors have to be mounted parallel to each other at a distance L. This type of resonator is known as the Fabri-Perot resonator. If concave mirrors are chosen instead of a flat mirror, the system can become significantly more stable.

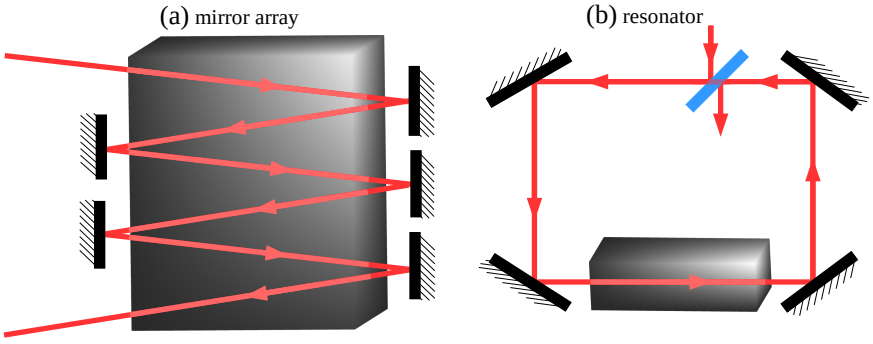

Figure 2.3: The types of laser amplifiers with feedback elements: (a) mirror array amplifier where light beam trajectory through the laser medium each time is different and (b) laser resonators where light beam trajectory through the laser medium is the same.

LONGITIUDIAL MODES Light of any wavelength can propagate in a laser resonator, but only a certain set of wavelengths will be amplified in the resonator. These wavelengths are called modes or eigenmodes [46]. For a resonator to maintain and amplify the modes, the solutions of the Helmholtz equation (Eq. 2.2) must be satisfied. The following boundary conditions are also essential - the vector E must be equal to zero at the resonator boundary (Eq. 2.3). If the boundary condition is not met, destructive interference occurs and the mode is erased.

Helmholtz equation:

$$\nabla^2 E(x) + k^2 E(x) = 0 \tag{2.2}$$

and the boundary conditions:

$$E(0) = 0 \text{ and } E(L) = 0. \tag{2.3}$$

The corresponding solution to the Helmholtz equation with the boundary conditions:

$$E(x) = A\sin(kx), \tag{2.4}$$

where A is the amplitude and k is the wave number:

$$k = \frac{2\pi f}{c}, \tag{2.5}$$

if a condition applies that:

$$kL = N\pi. \tag{2.6}$$

By transforming equation 2.6, the relation can be obtained:

$$2L = N\lambda = N\frac{c}{f}, \tag{2.7}$$

indicating that the length L of the resonator corresponds to a whole number N of half-waves. If the resonator is 15 cm long, then the resonance frequencies repetition rate f_{rep} is 1 GHz. These modes are called longitudinal modes of the laser resonator. The actual laser output modes are limited to the longitudinal modes which fall within the gain curve of the laser medium (see Fig. 2.4).

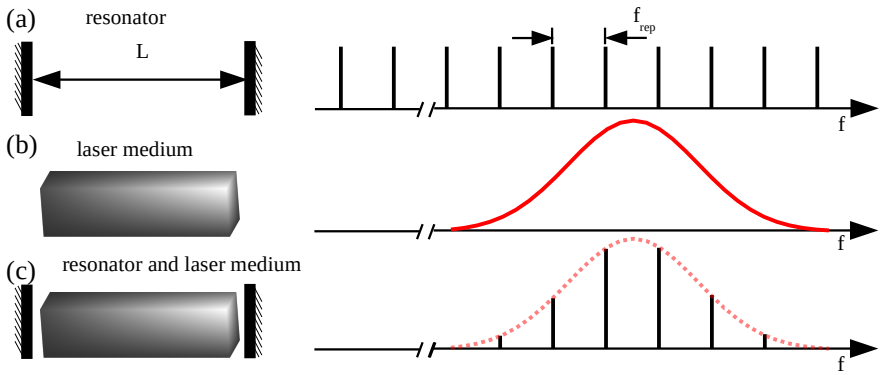

Figure 2.4: Laser output longitudinal modes: (a) length of resonator determines the spacing of the longitudinal modes, (b) laser medium gain curve determines which modes are amplified and (c) the actual laser output modes.

TRANSVERSE MODES In real life, the resonator has not only length L but also height a and width b. By looking at the cross-sectional area of the outgoing beam, it is possible to observe different distributions of light intensity. This intensity distribution in the resonator cross-section is called the transverse modes or TEM. Transverse modes are caused by the properties of a light wave. Diffraction occurs in the beam spread.

Transverse modes can be described by two parameters. The notation TEMmn is used, where m and n are the horizontal and vertical mode numbers. In the case of cylindrical symmetry, the notation TEMpl may also be used, where p and l are the corresponding radial and angular mode numbers. The notation TEMplq is also used, where q describes the longitudinal mode. Higher-order modes are difficult to focus on at one point, so the TEMoo, which forms a Gaussian distribution, is preferred.

2.2 WGM RESONATORS

Whispering-gallery modes (WGM) are waves that can travel around a concave surface. The light waves inside the resonator cavity are almost perfectly guided round by repeated optical total internal reflection. The trajectory of modes can be imagined like a polygon bound by the surface (see Fig. 2.5 a). Additionally, in the case of a 3D model the mode is tracing a zig-zag path around the optical equatorial plane (see Fig. 2.5 b).

If the radius of the resonator is significantly larger than the wavelength ($R >> \lambda$) then for constructive interference to occur after making a whole round-trip around the resonator because of total internal reflection the optical path length has to equal a whole number of wavelengths in the medium. The resonance condition, therefore, is

$$l \approx \frac{2\pi R n}{\lambda}, \tag{2.8}$$

where n is the index of refraction, R is the radius, λ is the wavelength and l is an integer linked to the angular momentum of a circulating photon in a spherical microresonator.

2.2.1 *WGM Mode Numbers*

Any whispering gallery mode resonator WGMR can support multiple WGMs of differing order - a discrete set of eigenmodes and eigenfrequencies. This spatial structure and the resonance frequencies can be characterized by a unique set of numbers – mode numbers $\boldsymbol{q}$, $\boldsymbol{l}$ and $\boldsymbol{m}$ (the letters used to describe mode numbers differ in different articles) which respectively represents **radial** component, **azimuthal** component and **polar** component [47] (see Fig. 2.5 c). The resonant frequency depends only on q and l.

RADIAL MODE NUMBER Radial mode number q shows the number of field maxima along the radial direction inside of the sphere [16]. Lower numbers of q are better confined.

AZIMUTHAL MODE NUMBER The azimuthal component l roughly shows the number of wavelengths that can fit into the optical length of the equator [16] (see the integer from Eq. 2.8). For small values of l, the mode fills almost the entire volume of the sphere while for large values of l the mode is near the surface of the sphere (see Fig. 2.6).

POLAR MODE NUMBER The polar component m determines whether the circulation around the equator is clockwise or counter-clockwise as well as its wavenumber (number of waves that exist over a specified distance) in this direction [16], so the WGM can be described as reflecting m times off of the edge of the cavity due to total internal

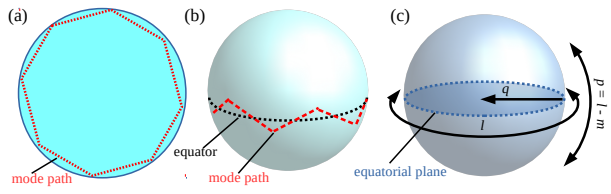

Figure 2.5: WGM trajectory imagined: (a) like a polygon bound by the resonator surface (2D model); (b) the mode zig-zagging around the equator (3D model); different possible modes (c) radial modes determined by radial mode number q, azimuthal modes - mode number l and polar modes - mode number m (angular mode number $p = l - m$ can also be used).

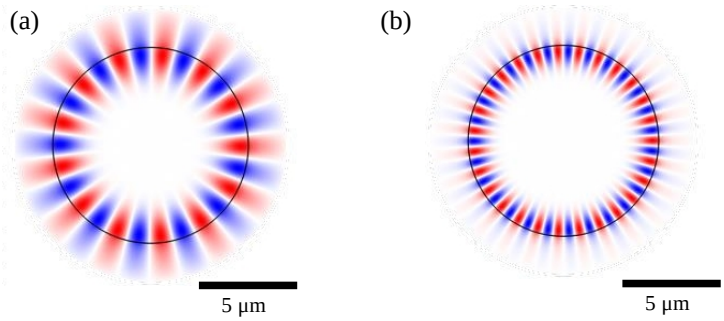

Figure 2.6: The eigenmode profile comparison for 10 μm sphere: (a) l = 13 when coupling inside 2.9 μm radiation and (b) l = 26 when coupling inside 1.5 μm radiation.

reflection, before circling the cavity one full time and returning to the starting point with the same phase. m can take $2l + 1$ values from -l to l.

ANGULAR MODE NUMBER The number of the maxima for the field polar component, which is perpendicular to the equatorial plane and comprised between the two poles, is equal to l - $m + 1$. Therefore, an additional parameter - angular mode number $\boldsymbol{p = l - m}$ - can be used to describe the modes in the polar direction [47]. If there is only one maximum in the polar direction, then $l = m$, and the mode is called the fundamental mode. The inclination of the fundamental mode to the equatorial plane θ is the smallest and strives to 0. Moreover, the region of the sphere closer to the evanescent spot on the coupling prism surface or tapered fiber may not coincide with the position of the fundamental mode and then the coupling for higher-order modes is more efficient.

2.2.2 *WGM Spectra*

The resonant wavelength of a microsphere is fixed by azimuthal mode number l and radial mode number q. An arbitrary polar mode number m has the same resonant wavelengths but propagates along different circular planes with different inclinations to the equatorial plane [14] (see Fig. 2.7). Also, larger microresonators have a denser spectrum.

The intensity distributions for various radial mode numbers q and angular mode numbers $p = l$ - m (see Fig. 2.7 a) using slice from Fig. 2.7 b, that is obtained by cutting the equatorial plane of a sphere, is shown in the Fig. 2.7 c. The radial and polar field distribution intensity can be seen in Fig. 2.8. For radial modes, the simulations show also evanescent part of the modes which can be used both to cou-

ple light inside the resonator (see Section 2.3) and interact with the surrounding medium.

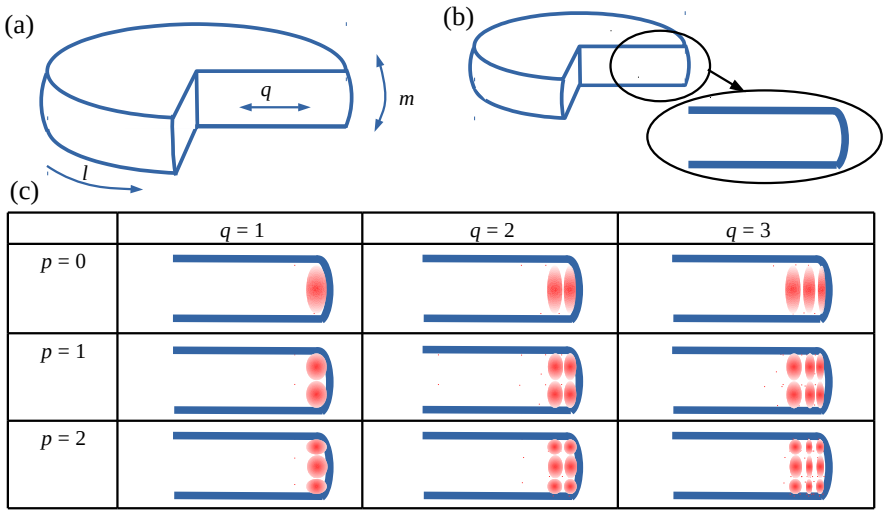

Figure 2.7: Understanding different WGMs: (a) radial mode number q, azimuthal mode number l and polar mode number m directions; (b) the region for plane sliced from a microsphere WGM resonator and (c) the intensity distributions for various modes in the slice.

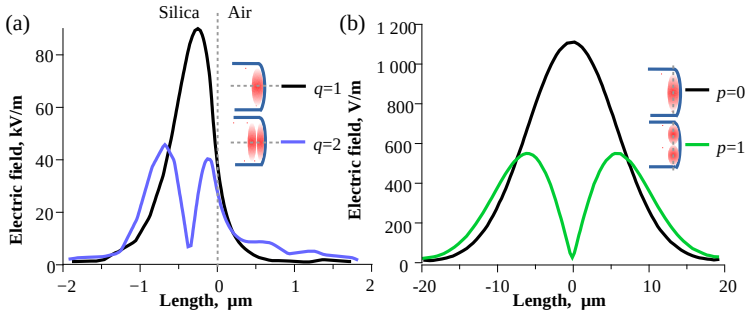

Figure 2.8: The electric field intensity for (a) radial and (b) polar modes of a spherical resonator.

A further distinction between WGMs can be made based on their polarization [26]. Two distinct polarizations can be supported in the resonator: transverse electric (TE) and transverse magnetic (TM) polarized modes.

2.2.3 *WGM Geometry*

There exist many resonators with different geometry that can support WGMs because the basic geometric requirement to achieve WGM resonances is circular symmetry. Besides microspheres it is possible to use hemispheres, microrings, microdiscs, microtoroids, optical

fibers, microcapillaries [17] as WGM resonators (see Fig. 2.9). More complex structures like microbottles, microbubbles, sausage-like resonators [48], spiral resonators, etc. can also support WGMs. Crystalline CaF_2 WGM resonators currently have the highest Q factor of 10^{11} [23], while amorphous silica resonators have Q factor 10^{10} for microspheres and 10^9 for planar structures like wedged microdiscs [23], as well as Q factors of 10^7 in silicon nitride waveguide on-chip resonators [23].

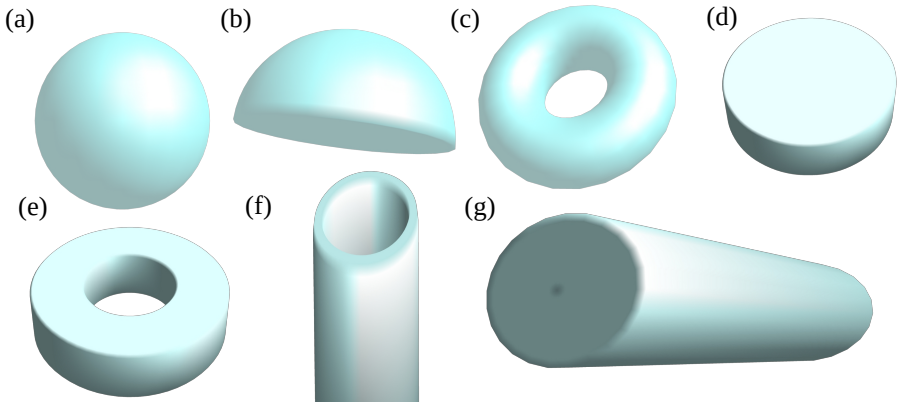

Figure 2.9: Different geometries that support WGM resonances: (a) microsphere, (b) hemisphere, (c) toroid, (d) microdisc, (e) microring, (f) microcapillary, (g) optical fiber.

Microsphere, microdisc, microbottle, and microbubble structures are formed individually. They can be melted or polished using fibers and capillaries of suitable materials and form very smooth and axisymmetric structures. On-chip microfabricated structures like microring, microdisc, and microtoroid can be mass-produced using suitable materials.

Asymmetric resonant cavities (ARC), for example, elliptical resonators [49] or other deformations that break the rotation symmetry [50], have also been proposed. ARCs may have several advantages liken easier coupling of the light and a directional emission as well as less dense transmission spectra.

2.2.3.1 *Microsphere Resonators*

The simplest 3D WGM resonator is a sphere (see Fig. 2.9 a). These microsphere resonators are easy to fabricate. The principle is based on melting the tip of an optical waveguide fiber and allowing the surface tension of liquid glass to do all the work to reform the material into a sphere. The only disadvantage is the requirement of glass in form of a rod or fiber and the fabrication of only one microsphere at a time. The sphere has low surface roughness, helping the sensor achieve ultrahigh Q factors in the range of 10^6 to 10^9 [51]. Also, the 3D geometry of a microsphere resonator allows various light coupling methods. One

can use tapered fiber coupling, prism coupling, prism-fiber coupler. Despite the geometrical advantages and the simplicity of the fabrication of microsphere resonators, the formation of microspheres has low reproducibility. Typically microsphere resonators have only one controllable parameter - the sphere radius.

2.2.3.2 *Microdisc Resonators*

Microcylinders and microdiscs - cylinders with small height - can also support whispering gallery modes (see Fig. 2.9 d) because light similarly circulates around the cylinder to light circling around the equator of the sphere. There is, however, one essential difference. While the polar curvature of the sphere surface confines and focuses light in the polar direction and as a result can support very complicated modes with equatorial, radial, as well as polar field dependencies, in a disc resonator a light beam can escape through the top or bottom and thus leave the resonator. This adds mode instability due to the lack of focusing in the polar direction. Furthermore, it is harder to manufacture disks with comparably low surface roughness, because the resonators are produced by mechanical polishing. As a result, the magnitude of optical Q in the current device is primarily limited by the sidewall roughness of the microdisc. The typical Q factor for resonators fabricated using lithography methods is 10^4. Optical fiber can be carved using a CO_2 laser to achieve Q factors $10^5 - 10^8$ [16, 52]. Polished crystalline microdiscs theoretically can have Q factors $10^9 - 10^{12}$ [53] which is higher than microspheres. The mum and mm-sized disks are more easily integrable than microspheres in an integrated optical network or on a chip and their fabrication is easier, except for hand polishing, faster and more controllable. This makes them very useful for practical applications. They can be characterized using the radius of the resonator and side curvature radius for carved or polished microdiscs or the radius, thickness, and disc angle for lithographed microdiscs [54].

2.2.3.3 *Microring Resonators*

Variants of microdisc resonators are microring resonators - disk resonators with a circular hole in the middle (see Fig. 2.9 e). Since whispering gallery modes are already highly localized at the cavity-air interface they have much higher mode volume. This resonator also has the advantage of the ease of fabrication and the resonator and coupling waveguide can also be fabricated on the same substrate. The resulting Q factor of ring resonators the same as with microdisc resonators is comparably low $10^4 - 10^7$ [51] because same as with microdiscs the surface roughness of the device is often generated during the fabrication process.

2.2.3.4 *Microtoroid Resonators*

A microtoroid resonator is made in the shape of a solid toroid along the inside of which light can circulate by continuously bouncing off the toroid-air interface by total internal reflection (see Fig. 2.9 c). It combines the advantages of microsphere and microdisc resonators. Same as the microdisc resonators the device is fabricated on a chip while addressing the signal loss due to the absence of serious surface roughness. Leaks from evanescent scattering to the substrate are prevented by raising the microtoroid structure above the substrate with a pillar. They are comparable to microsphere resonators due to the role of surface tension in their fabrication giving them a very smooth surface. As a result, a high Q factor can be observed, with values up to 10^8 [51]. However, the microtoroid has difficulty coupling light since the resonators are perched atop a pillar. The main issue is the difficulty of coupling alignment. They can be characterized using the radius of the resonator and side curvature radius.

2.2.3.5 *Other Resonators*

MICROBOTTLE AND MICROBUBBLE RESONATORS A microbottle resonator is a deformation of a cylinder usually made from an optical fiber and has a bulge in the middle, where the radius increases smoothly up to a maximum and then decreases (see Fig. 2.10 a). In the microbottle resonator, the propagation is limited in the axial direction of the deformed cylinder, with the Q factor of 10^7 [23]. A hollow microbottle resonator - also called microbubble resonator if the hollow spherical section is larger radial size than the cylindrical ones of the overall device (see Fig. 2.10 a and b) [55] - is made from a capillary and has a hollow "bubble" in the middle. The physical structure of hollow microbottle and microbubble resonator is similar to respectively a microbottle and a microsphere, therefore, the distribution of the WGMs is similar in the azimuthal and polar directions. However, in the radial direction, this changes if the wall is thin or the hollow microbottle or microbubble is filled with fluid. Unlike solid structures this "bubble" has two surfaces and offers the advantage of coupling the light through the outer surface whereas using liquid samples for interaction with the optical resonance through the inner surface, thus avoiding unwanted interactions between the probing light and fluid. The extent to which the WGM interacts with the fluid depends on the wall thickness and the mode order - higher-order radial modes overlap more with the fluid inside the hallow. Microbubble resonators are more sensitive due to thinner walls by extending the WGM evanescent field because it starts to lose its capability to confine the WGMs within itself. Additionally, chemical etching may be used to further reduce wall thickness.

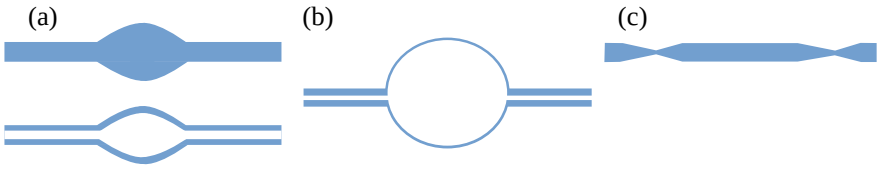

Figure 2.10: Three types of micro resonators fabricated from a fiber or a capillary: (a) microbottle resonator; (b) microbubble resonator; (c) sausage-like resonator.

Most microbottle resonators are fabricated using optical fiber as the material source. The fabrication process involves thermal softening of the fiber by heating it to 1665°C using a flame, CO_2 laser, or a ceramic microheater and pulling it to decrease the diameter. The same step is repeated at another location. Also, reverse mechanical motion of softening and compressing produces a microbottle resonator. An alternative way to obtain bottle-like confinement is by creating a localized change in the refractive index of a dielectric cylinder, generally induced by the photo-refractive effect [23]. The fabrication of the hollow microbottles and microbubbles is similar to that of solid microbottles, except that instead of a solid cylinder a capillary is used. The process is done carefully, to avoid collapsing the hollow interior. For microbubbles, the hollow core of the capillary has to be internally pressurized.

A sausage-like resonator is similar to a microbottle resonator (see Fig. 2.10 c). It is made by adding two tapers on a fiber (softening and pulling) and between them, there is still a length of smooth fiber region [48]. The shape of the resonator resembles a sausage hence the name - sausage-like microresonator. Varying the length of the fiber between the tapers change the features of the transmission spectra[48].

SPIRAL RESONATORS An unique attribute of a spiral shaped microresonator is the it lacks the rotational symmetry. The radius of the spiral shape varies with the azimuthal angle:

$$r(\phi) = r_0(1 - \frac{\epsilon\phi}{2\pi}) \tag{2.9}$$

where r_0 is the radius r when angle $\phi = 0$ and ϵ is a deformation parameter (see Fig. 2.11 a). This enables non-evanescent coupling. Also, the modal distributions are asymmetric and, therefore, different from other WGM microresonators. As a result, the notch can be used as a drop-off or add-on filter and easily connected to waveguides. For best results, a ring-like spiral structure is achieved by removing the central part of the spiral cavity [56]. Such a structure suppresses the high radial order modes.

A continuous single loop path can be achieved with four spirals (see Fig. 2.11 b) that can be considered a spiral microresonator. Fur-

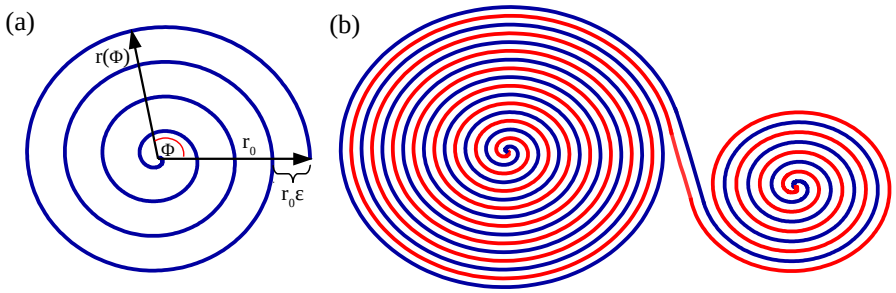

Figure 2.11: Spiral microresonators: (a) geometry of the spiral described by formula 2.9; (b) a spiral resonator consisting of four spirals to create a continuous path for light.

thermore, this structure still preserves modes and a high Q factor and by increasing the path length the light is much less sensitive to thermodynamic noise. Using these spiral waveguides devices that are smaller than $5.4cm^2$ has been demonstrated to have over 1 m length with Q factors of 10^8 [50]. Beyond the thermo-refractive noise immunity, the device also provides enhanced immunity to photo-thermal noise due to the large mode volume, which greatly reduces the circulating intensity at a given coupled optical power [50].

2.2.4 *Materials for Fabrication*

SILICA Different silica properties are listed in Table 2.1. Optical fiber is a convenient source of silica for WGMR fabrication. Different diameter sizes and grades are commercially available. Telecommunication optical fibers are a good choice for melting the fiber tip with flame or CO_2 lasers. A microsphere forms as the silica melts and reforms. To form microbottle resonators optical fiber can be pushed or pulled by the fiber ends as the middle is softened by heat. Capillaries can be used instead to fabricate hollow microbottle or microbubble resonators. Microdisc resonators can be carved from optical fiber with CO_2 laser.

CRYSTALLINE DIFLUORIDES Crystals CaF_2, MgF_2, BaF_2 can be polished to fabricate microdisc resonators. They can have a higher Q factor than silica microspheres. Also, crystal resonators do not draw water from ambient air. Same as silica microresonators made from optical fiber, polished crystal microdiscs have to be handcrafted.

SILICON On-chip silicon technology compatible materials (Si, SiO_2, Si_3N_4, etc.) can be fabricated on-chip using lithography techniques. These resonators can have microdisc, microring, microtoroid, etc. geometry. They typically have lower Q factors (except microtoroid resonators) but can be mass-produced on chips. For microdisc, micror-

Table 2.1: Advantageous and disadvantageous silica properties for WGMR fabrication.

advantages	disadvantages
low material absorption in visible and telecommunication region Q limit 10^{11} [57]	absorbs water from air Q limit $< 10^{9}$ [57]
low expansion factor $\beta = 0.55 \cdot 10^{-6}$ (1/K)	refractive index dependence on temperature [58] $\alpha = 12.8 \cdot 10^{-6}$ (1/K) for 780 nm, $\alpha = 8.52 \cdot 10^{-6}$ (1/K) for 1550 nm
chemically stable	Van der Waals forces between silica WGMR and glass prism or tapered fiber

ing resonators an integrated waveguide is an option. Vast support of other on-chip silicon technology elements is available for integration and fabrication on the same chip.

2.2.5 *Parameters for Characterization*

Resonator parameters are quantities that quantify different aspects of the said resonators.

2.2.5.1 *Quality Factor*

One of the most important parameters as well as most often used to describe the microresonators is the quality factor Q because it determines the interaction length with optical resonators. Q factor is a dimensionless quantity that describes the ability to store energy inside a microcavity and is the inverse quantity to the fraction of light lost during each cycle around the cavity (Eq. 2.10). It can be mathematically described as the product of the photon lifetime τ inside the cavity for a given resonant frequency f (Eq. 2.11) or the ratio of the resonant frequency to the spectral linewidth Δf_{FWHM} of the resonance [24] (Eq. 2.12):

$$Q = 2\pi f \frac{\text{Stored energy}}{\text{Power loss}} \tag{2.10}$$

$$Q = 2\pi f \tau = 2\pi \frac{L}{\lambda} \tag{2.11}$$

$$Q = \frac{f}{\Delta f_{FWHM}}. \tag{2.12}$$

L is the length of the path that the photon travels in the resonator. The Q factor is commonly measured using either cavity ringdown or linewidth calibration techniques.

Several losses from many processes limit the maximum value of the optical Q factor in materials. The Beer-Lambert law for light absorption is $I(x) = I_0 e^{(-\alpha_t x)}$, where α_t is a total optical loss coefficient and describes the decay of intensity when nonlinear optical processes are not present, and x is the path length. To measure the higher Q factors, lower pump power levels must be used to avoid additional nonlinear processes and losses. The contributions from several linear loss mechanisms are added. Energy losses happen due to:

- scattering losses (rough surface);
- surface absorption losses;
- intrinsic material absorption;
- coupling losses;
- radiative loss.

Therefore, loss coefficient consists of surface scattering, material losses, influence of the coupler, and the radiative loss [53]:

$$\alpha_t = \alpha_{ss} + \alpha_{mat} + \alpha_{coupling} + \alpha_{rad}. \tag{2.13}$$

SURFACE SCATTERING LOSSES Surface scattering is induced by the imperfections of the surface. Surface roughness can be the result of imperfect polishing for crystalline resonators or capillary waves for melted glass resonators. Also, the surface might be "dirty" because tiny particles, for example, dust is almost always present on the surface. Since we have tried to functionalize the microsphere resonators by coating them with nanostructures, these loss mechanisms may be an important limiter for the Q factor.

MATERIAL ABSORPTION LOSSES Material losses are caused by the fundamental absorption in the material, atomic impurities, and three types of bulk scattering: Raman, Brillouin, and Rayleigh. Each material if there are no impurities and defects present has an unique window of transparency. In ideal crystals, these scattering mechanisms are also present. Only Raman scattering plays a significant role in crystalline cavities.

COUPLER LOSSES The coupling strength can change the Q factor of the resonator. It can be adjusted, for example, by changing the distance between the resonator and the coupling element - coupling prism or tapered fiber. Over-coupled resonators have poor Q. Over-coupling usually happens when the resonator is too close or touches the coupling element. Optimal-coupling or critical-coupling happens when the distance is optimal. Under-coupling - when the resonator is further away. The coupler losses can be made small by performing measurements in a strongly under-coupled regime. Both critical and under-coupling provide a larger dynamic range for changes in the distance between the resonator and coupling element [59].

RADIATIVE LOSSES Due to the curved boundary between two media total internal reflection inside the WGMR always results in a transmitted wave on the lower refractive index side. As a result, the light inside a whispering gallery resonator cannot be perfectly trapped and loss of energy happens. The radiative loss also called bending loss is only significant in small microresonators and happens due to imperfect total internal reflection from the curved surface. The existence of WGMs in optical cavities relies on total internal reflection at the cavity surface. Therefore, larger refractive index contrasts between the cavity and the host help to minimize radiative losses, and the WGMs are stronger confined. Thus the obtainable Q factors improve.

INTRINSIC AND EXTRINSIC QUALITY FACTOR Q factor can be split in two fractions - intrinsic Q_{intr} and extrinsic Q_{extr}. Q_{intr} is limited by losses defined by the resonator cavity: material losses from absorption, surface scattering losses from surface roughness including any contaminate on the resonator surface and radiation losses from the curved surface. Q_{extr} is limited by the coupling losses and can be affected by changing the coupling conditions - position and distance against the coupling element. Total Q factor:

$$\frac{1}{Q} = \frac{1}{Q_{intr}} + \frac{1}{Q_{extr}}. \tag{2.14}$$

Coupling parameter K can be defined as a ratio between the intrinsic and extrinsic Q factor [60]:

$$K = \frac{Q_{intr}}{Q_{extr}} \tag{2.15}$$

and for $K < 1$ indicate an under-coupled regime, for $K > 1$ an over-coupled regime and $K = 1$ critically coupled regime when coupling conditions are optimal.

The transmission at the resonance frequency can be expressed as [60]:

$$T = \left(\frac{1-K}{1+K}\right)^2. \tag{2.16}$$

The deepest WGM resonance dips in the transmission spectrum can be observed for optimal coupling conditions when $K = 1$.

In many applications large Q factor is essential. If resonators have Q factors from about 10^3 to 10^6 then they are high Q factors while Q factors above 10^7 are considered ultra-high [16].

Let us compare the distance 1.55 µm light travels inside 1 mm microsphere resonators with Q factor 10^4, 10^6 and 10^8 respectively. First, the photon lifetime circling inside the resonator can be found using Eq. 2.11 as 0.05 ns, 5 ns and 500 ns, the traveled distance 0.01 m in 2.4 round trips, 1 m in m in 240 round trips, and 100 m in 24000 round trips respectively allowing the light photon to interact with the surrounding environment each round trip.

Harnessing high Q values may enable microspheres to find potential for unprecedented performance in applications for ultra-narrow linewidths, long energy decay times, large energy densities, or fine sensing of environmental changes [61].

2.2.5.2 *Other parameters*

FREE SPECTRAL RANGE Free spectral range is the distance between the resonant peaks of the fundamental WGM resonance. It is the inverse of the round-trip time.

$$\Delta f_{FSR} = \frac{c}{2\pi R n} = \frac{1}{\tau_{rep}}, \tag{2.17}$$

where R is the radius of the resonator and n is the refractive index and τ_{rep} is the round-trip time.

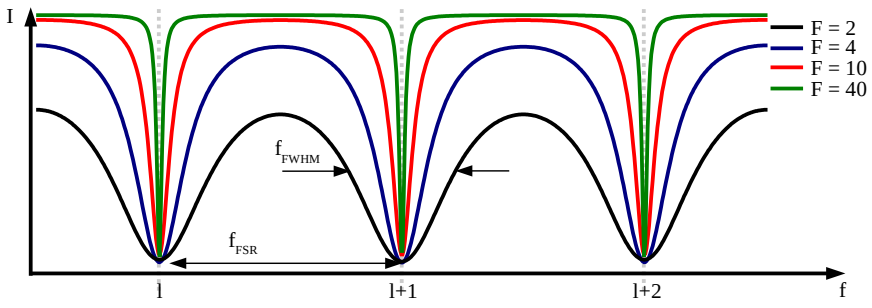

Figure 2.12: A high-finesse shows sharper transmission dips and higher maxima when compared to a low-finesse.

FINESSE Finesse is a parameter that describes the performance of a resonator and is also important. It is defined as the ratio of the free spectral range and the FWHM linewidth and tells the distance between the resonant peaks in terms of the number of FWHM linewidths that go in between two consecutive resonant peaks (see Eq. 2.18 and Fig. 2.12).

$$F = \frac{\Delta f_{FSR}}{\Delta f_{FWHM}} \tag{2.18}$$

MODE VOLUME The ratio of the total energy stored inside the resonator in that mode and the maximum energy density of that mode.

PUMP THRESHOLD The pump threshold tells the minimum pump power needed for lasing. It is proportional to the mode volume V. High Q factors and very low mode volumes directly translate into ultra-low lasing thresholds.

2.3 COUPLING LIGHT INSIDE WGM RESONATORS

If one examines the field intensity by the boundary of the resonators in Fig. 2.8, then a small "tail" of the field is present outside the media. This evanescent field tail at the resonator boundary explains the possibility to excite the WGMs by employing suitable coupling systems as well as sensitivity to the surrounding environment. The intensity of said tail decreases exponentially if the distance to the resonator surface increases. Using free space coupling is possible to excite WGM resonances but it is not efficient. The coupling efficiency is less than $\left(\frac{\lambda}{a}\right)^2$ [19], where a is the beam cross-section radius (compatible with sphere radius R) and λ is the wavelength of the light coupled inside.

2.3.1 *Total Internal Reflection*

When light travels from one medium to another with a lesser refraction index, the exit angle is always larger than the incident angle. If the incident angle is small the ray will be split - part of it will reflect off the boundary and the rest will bend as it passes through. Critical incident angle α_c corresponds with exit angle 90°. Therefore the Snell's law for the critical angle is:

$$n_1 \sin\alpha_c = n_2 \sin 90° \tag{2.19}$$

where $n_1 > n_2$. This law can't be used for incident angles larger than the critical because the sine function is limited and can't be greater than 1. So what happens to a ray, which cannot satisfy Snell's law at all. For incident angles greater than the critical angle the refracted ray

disappears and no light passes through, instead, it will be reflected from the media interface. This is known as total internal reflection. The light will get through the interface and enter the medium with a lower refractive index. This occurring effect is in nanoscale and is known as an evanescent wave. Geometrical optics description has severe limitations - it cannot explain the presence of the evanescent wave or how it can be used to couple light into the resonator. A complete description can be provided by the electromagnetic theory.

Frustrated total internal reflection, was first observed by Newton in his experiments on Newton's rings.

FRUSTRATED INTERNAL REFLECTION The total internal reflection using a simple prism and a lens with a large radius was first studied and detail by Isaac Newton. Newton observed three main cases of light refraction/reflection as shown in Fig. 2.13 a, b and c. He was the first person reported to attempt using evanescent waves in optics. The experiments consisted of placing a prism against a lens and observing the light transfer trough. Even in areas where the lens was not in contact with the prism but the distance was small enough the light was transmitted and could be detected [62] (see Fig. 2.13 d). Although he managed to observe the evanescent field outside the prism, Newton didn't have a good explanation for the frustrated internal reflection effect. The effect can be interpreted as a kind of optical tunneling using the evanescent field. As a result, more and more light can be coupled in or out when the prism is put closer and closer to a second prism [63]. Commercial devices known as cube beam splitters use frustrated internal reflection.

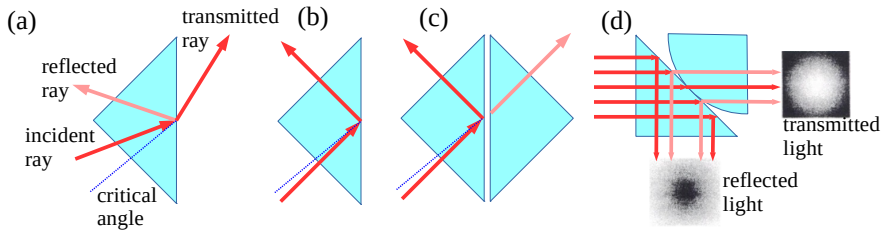

Figure 2.13: Light reflection and refraction in a prism: (a) normal reflection when light gets both reflected and transmitted; (b) the total internal reflection when light gets reflected; (c) frustrated total internal reflection when a second prism is brought really close to the first one and light starts to transmit again; (d) scheme of Newton's experiment where an illuminated area was larger than observed point of contact [62].

The evanescent field clings closely to the surface (see Fig. 2.14 a). The field strength amplitude decreases exponentially and reaches zero after a distance of approximately the wavelength of the light used (see Fig. 2.14 b). The penetration depth of the evanescent field into the optically less dense media depends on various factors - incidence angle, media indices, and wavelength. When WGMR is placed

at a distance below the penetration depth of the evanescent field tunnels through the "forbidden" area between the resonator and the coupling element just like a particle that tunnels a potential tunnel barrier. Time-dependent Helmholtz equation (for evanescent field tunneling) is similar to time-dependent Schrodinger equation (for electron tunneling) and it is suitable for propagation, tunneling, transmission, penetration calculations [64]. Alternatively, Heisenberg uncertainty principle and the wave–particle duality can be used to show there are no solutions for the position and the momentum of a particle at the same time with a probability of exactly zero. The photon will appear on the other side due to the non-zero probability.

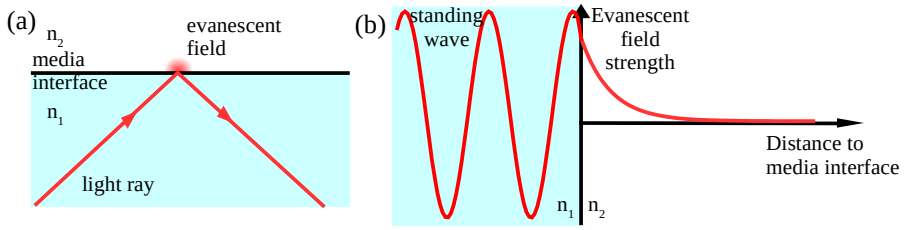

Figure 2.14: Schematic of a total reflection with its evanescent field: (a) light enters into the medium with a low refractive index n_2 and (b) the field strength amplitude decreases exponentially further from the media interface.

2.3.2 *Prism Coupler*

The oldest method and a common technique to couple light into the resonator is prism coupling. Similarly as explained in subsection 2.3.1 in case of frustrated internal reflection, by using a prism and a convex surface - WGM resonator - of similar density material some transmission of light will occur leaving a partial internal reflection. So a prism coupler that uses the evanescent field can be used to couple light into a WGM resonator.

A laser beam undergoes total internal reflection inside a dielectric prism and creates an evanescent field. The actual surface of the resonator at the coupling region is not flat. This has to be taken into consideration since the air gap is now variable between the laser beam on the prism interface and the resonator. The evanescent field overlaps with the evanescent field of a WGM resonator and as a result, the laser beam is coupled inside the resonator (see Fig. 2.15 a).

The prism coupler is efficient and tunable. Experimental studies have shown that prism coupling has approximately 80% efficiency [51, 65]. The system is quite robust. However, it is a bulky component, and achieving optimal alignment is quite challenging, in addition, requiring collimation optics. As a result, it is more desirable for applications that call for sturdiness. Also, it is hard to control which

whispering gallery modes get excited when coupling light using a prism.

A variation on the prism coupler is a hybrid prism-fiber coupler, where the tip of a single-mode fiber is angle polished (see Fig. 2.15 b). It makes use of the efficiency of the bulk prism, with the versatility of optical fibers. The prism-fiber coupling has 60% efficiency [51].

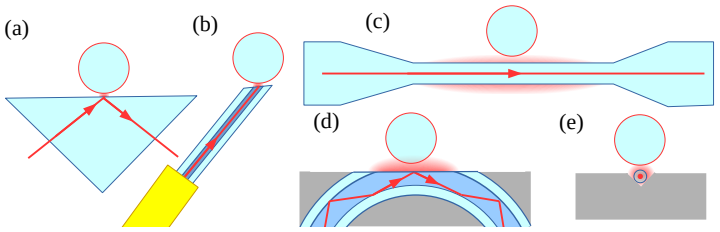

Figure 2.15: Exciting WGM using (a) a prism coupler; (b) a hybrid prism-fiber coupler; (c) a tapered fiber; (d) an integrated half block coupler [66]; (e) tapered fiber fixed inside a v-grove.

2.3.3 *Tapered Fiber Coupler*

The best known way to couple light with whispering gallery mode resonators is by using tapered optical fiber. Tapered coupling with 98% coupling efficiency has been demonstrated [51].

The tapered fiber is a single-mode optical fiber that is stretched and therefore significantly thinned in the middle (see Fig. 2.15 c). Light traveling inside the optical fiber has an evanescent field. Just like the evanescent field outside the prism after the total internal reflection, it decays exponentially, and thus, before tapering, most of the optical power is concentrated on the inside of the fiber. A tapered optical fiber, on the other hand, has a diameter significantly smaller therefore the thinness of the fiber would force light to focus to a diameter close to or less than its wavelength. The evanescent field of the light can stretch out so far, that most of the optical power of the guided beam is actually outside the fiber. When this evanescent field is brought to overlap with the evanescent field of the resonator highly efficient resonator-waveguide coupling can occur.

The tapered fiber coupler is efficient and is an easy to align coupling system. The process of fabrication is rather delicate as the fiber is pulled with a waist less than 10 µm in diameter suspended in the air. These thin fibers are very brittle and require careful handling [67]. To deal with the brittleness one can try to make integrated tapered fibers.

One way to make an integrated fiber coupler is by using single-mode fibers glued into a curved narrow groove in a substrate block and polished down until the block surface is near the fiber core (see Fig. 2.15 d). These polished half-block couplers offer a more robust

coupling platform but yield low efficiencies because of the energy in the sphere couples to the cladding radiation modes of the half-block. Another way is to try preserving the ultra-thin characteristics of tapered fiber by aligning and fixing it inside a v-groove carved into a substrate block (see Fig. 2.15 e). Achieving an efficient coupling is rather important. It requires careful positioning and alignment. However, the resulting system is more compact and robust than the fiber taper.

2.3.4 *Under-coupling, Over-coupling and Critical coupling*

The Q factor is formed by intrinsic and extrinsic losses (see Eq. 2.14). Q_{extr} can be adjusted by changing the gap between the coupling prism or tapered fiber and the resonator, thus changing the overlap between the evanescent fields of the resonator and coupling element.

If the resonator is too far from the surface of the prism, where the evanescent wave is located, then the field is too faint to efficiently couple the light into the resonator. Then $Q_{extr} > Q_{intr}$, coupling parameter $K < 1$ (see Eq. 2.15) and it is known as the under-coupling. It can also be easily observed experimentally (see Fig. 3.17 a in Chapter 3).

However, if the resonator is too close to the surface, the intensity also drops. This phenomenon happens when $Q_{extr} < Q_{intr}$ and is known as over-coupling. It happens if the prism surface of the fiber taper directly touches the resonator or there is a fairly small gap between them. Additionally, one has to take the van der Waals force pulling the resonator to the surface into consideration.

Critical coupling is the point where a certain gap is achieved between coupler and microresonator so that $Q_{extr} = Q_{intr}$ and the entire coupled power is lost inside the resonator. This distance is considered the optimal distance.

3

WHISPERING GALLERY MODE RESONATOR BIOSENSORS

3.1 WGM RESONATOR SENSORS

A sensors is a fancy word for a tool designed to acquire quantitative information about our surroundings. Sensor detects and responds to some type of input - heat, light, pressure, moisture, etc. The output signal is either converted to human - readable display or transmitted electronically for further processing by other electronic equipment.

Optical microsensors are systems that utilize light. They are fast, flexible and relatively cheap, as well as have supporting optical technology such as photodiodes, optical fibers, and light sources. Optical sensors that are based on microcavities supporting whispering gallery modes have attracted a significant level of interest recently because of an extreme level of sensitivity, compactness, fast response, real-time measurements and cost-effective integration with fibre optics.

3.1.1 *Important Parameters of Optical Sensors*

Ideally a sensor aims to obtain the maximum amount of information from the smallest amount of sample. Miniaturized optical resonators are very sensitive sensors. Sensitivity, however, is only one of many important qualities of optical resonator sensors. Others are limit of detection (LoD), resolution, dynamic range, selectivity, stability, repeatability and response time.

SENSITIVITY Sensitivity conveys how much the output changes when the input being measured changes. The units are usually given as $\frac{nm}{RIU}$ (wavelength shift over refractive index unit) and $\frac{W}{(m^2 \cdot RIU)}$. WGM sensors derive their extraordinary sensitivity from their high quality factor and have potential to detect even a single molecule.

LOD LoD is the lowest analyte concentration likely to be reliably distinguished from the "blank" sample containing no analyte and at which detection is viable. It is limited by noise source, efficiency of the optical detector in the optical system, and the amount of light that can be detected. The lowest surface density of molecules that can be detected by the resonator depends on the resonance line width $\delta\lambda$, which in turn depends on the quality factor Q. Optical system noise can come from:

- thermal noise;
- microsphere vibrations;
- dark current of the detector;
- loss due to material defects.

RESOLUTION Resolution is the smallest detectable incremental change of input parameter that can be detected in the output signal. A close term to resolution is accuracy - how well the sensor measures the environment and how good the data is when compared with a recognized standard. Resolution and accuracy are related, however, not the same thing. Resolution can be much higher than accuracy and is usually limited by the digital output or an offset. For example, a temperature sensor may have a resolution of 0.0001 K, but only be accurate to 0.001 K.

DYNAMIC RANGE The range of the sensor is the maximum and minimum values of applied parameter that can be measured. The dynamic range is the total range of the sensor from minimum to maximum.

SELECTIVITY Selectivity portrays the ability of the sensor to distinguish between the desired analyte and other biomolecules in the environment. It can be achieved by surface modification of the resonator called functionalization - chemical modification of the surface. Functionalization controls the selectivity and can enhance the sensitivity of the sensor.

STABILITY Stability of a sensor shows how long the same output when measuring a constant input over a period of time can be achieved. The change in output that occurs in time is called drift.

REPEATABILITY Repeatability shows the capability of a sensor to give same output for repeated measurements of the same input.

RESPONSE TIME Response time describes how fast the output changes when the input is changed in a step quantity.

3.1.2 *Sensing Mechanisms*

WGM sensors also referred to as optical cavity sensors, or resonance evanescent wave sensors operate by monitoring the changes in the spectral properties like resonance wavelength (frequency) shift $\Delta\lambda$ (Δf) or linewidth broadening $\Delta\gamma$ caused by changes in the system.

WAVELENGTH SHIFT $\Delta\lambda$ When light is confined in a dielectric microstructure and interferes with itself, only specific optical frequencies can be supported and reside within the cavity without suffering large losses. Therefore, if the microcavity geometry (size see Fig. 3.1) or material properties (refractive index) change, for example, by deforming or heating the cavity, a change in resonance parameters or supported optical frequencies follows and it can be detected. As a result any small change in the refractive index or in the radius must be balanced by a small change in the resonant wavelength:

$$\frac{\Delta\lambda}{\lambda} = \frac{\Delta R}{R} + \frac{\Delta n_h}{n_h} F + \frac{\Delta n_r}{n_r}(1 - F), \tag{3.1}$$

where λ is the resonant wavelength, R is the radius of the resonator, n_h is the is the refractive index of the host medium, n_r is the refractive index of the resonator and F is a sensitivity function related to the phase acquired upon reflection at the resonator surface [26]. Greater sensitivity is found in smaller resonators and for lower refractive index contrast. This happens because the evanescent tail extends further into the host medium.

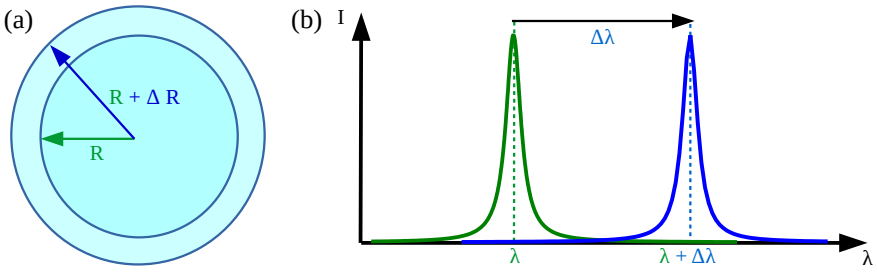

Figure 3.1: WGM resonance shift caused by the change of the resonator radius: (a) the increase of the radius ΔR causes the (b) increase of the resonance wavelength $\Delta\lambda$.

Resonators with ultra high Q factors have ultra-narrow linewidth resonances which makes the resolution very high. However, it is not the ultimate limit of the detectable shift of the resonance. The accuracy drops due to thermal fluctuation noise and significantly affects the detection limit [26].

LINE BROADENING $\Delta\gamma$ When WGM resonator interacts with a particle can also introduce additional absorption and scattering losses. The losses reduce the quality factor Q. As a result, these changes broaden the linewidth of the resonance since the linewidth is directly linked with the Q factor. Line broadening should not be confused with a drop of intensity because both involve the decrease of the peak intensity as seen in Fig. 3.2 b but only in case of line broadening the width of the mode changes as seen in Fig. 3.2 a.

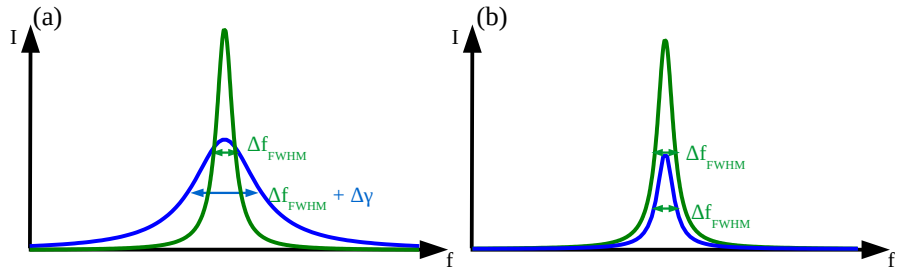

Figure 3.2: WGM resonance line broadening and intensity: comparison of (a) the line broadening and (b) the change of mode intensity.

.

This method is a self-referenced detection mechanism, isolating the fluctuation of environment temperature or system instability. Also, it does not require narrow linewidth. Mode broadening has a lower detection limit than mode shift because mode shift is limited by the thermal noise [26].

3.1.3 *Specific Applications of WGM Sensors*

The WGMR aim for real-world applications and have been proposed for sensing applications, for example, measurements of temperature, pressure, force, humidity, gas detection, biosensing etc., for more than a decade. In this section various sensing applications are reviewed.

TEMPERATURE SENSING WGM temperature sensor is an optical temperature sensor for measuring 10^{-4}K temperature changes. The key components of the temperature sensor are of course the WGM resonators and a coupling component. The WGMs in all silica glass resonators experience a red shift with increasing temperature due to the positive thermo-optical coefficient and the positive thermal expansion coefficient of the glass.

One way to sense temperature is the resonance wavelength shift due to the temperature change. The temperature sensitivity of wavelength shift per unit temperature change for the microspheres can be determined by linear fitting of the experimental data. A slight difference in the sensitivities among different size WGM resonators can observed and smaller resonators have larger sensitivity due to larger wavelength shift [20]. Such WGMR temperature sensors are researched [20, 21].

PRESSURE SENSING WGM pressure sensors are very sensitive to pressure changes in the liquid or gas medium surrounding the resonator which causes both deformations of the surface or changes of the resonator size and the index of refraction. These changes induce possible WGM resonance spectrum changes:

1. spectral shift;
2. resonance depth changes;
3. resonance width changes.

Silica-based WGM pressure sensor would not be a good candidate due to big pressure differences needed to observe the resonance shift. At the same time atmospheric pressure changes are unlikely to interfere with resonances in silica microspheres used to sense other parameters such as temperature.

Better candidate for pressure sensing is hollow PMMA-based pressure sensor with larger $\Delta\lambda$ shifts with relatively moderate pressure change [68]. Another candidate is droplets instead of solid particles to enhance the pressure sensitivity [69].

WGM BIOSENSORS In biomedicine and biotechnology, sensors which detect analytes thanks to a biological component, such as cells, protein, nucleic acid or biopolymers, are called biosensors. It is easy to use the word biosensor incorrectly. The requirements for a biosensor are selectivity, sensitivity, and stability. Therefore, a device, which can definitely be interesting for potential use in biosensing applications but does not fulfill all the the requirements, for example, specificity and selectivity for a given molecule, is not a biosensor.

WGM sensors can be biosensors. Proteins can adhere to any glass surface, increasing the unwanted non-selective effects. The way to bestow the selectivity for the WGM resonator can be achieved by a process of introducing a binding material to the surface of the resonator and it is called surface functionalization. The coating layer has to be very thin - from 10 to 100 nm [14] -, which is below the evanescent penetration depth, and homogeneous in order to preserve the high quality factor of the resonator.

The surface of a biosensor can be functionalized in ways. A covalent binding provides the best stability and durability. The most common methods are based on the silanization. Molecules bind to the glass or silicon surface through covalent binding of the silane groups.

Besides selectivity high signal-to-noise-ratio, short response time, low LoD, integration capabilities and high sensitivity at low cost in real samples are important.

3.2 MICROSPHERE WGM RESONATOR FABRICATION

Silica microsphere resonators can be fabricated using optical fiber as a source material. The microsphere geometry has only one parameter - resonator radius which can be controlled in the fabrication process. Material absorption losses for silica are very low and limit the Q in order of 10^{11} [57]. Water absorption by the silica surface, on the other hand, limits Q to below 10^9 at 1550 nm [57]. Radiation losses play a

significant role only for very small WGMRs. Overall, the intrinsic Q factor of silica spheres is limited to $10^8 - 10^9$ due to water absorption. Additional losses may arise from surface scattering and material contaminants. Our fabricated silica microspheres have the Q of $10^6 - 10^8$.

The disadvantage of microsphere fabrication is the need to handcraft the microsphere resonators on the tip of the fiber one by one. Each resonator will be unique, as it is almost impossible to fabricate two identical spheres. The process can be optimized to increase the success rate which allows the fabrication of multiple WGM resonators with a high Q factor in succession.

3.2.1 *Fabrication Process*

A single-mode commercial telecommunication optical fiber was chosen to fabricate the microsphere resonators. To achieve the best results, specific optical fiber preparation steps before the melting were performed to clean the surface to minimize the amount of dust on the surface. An appropriate heating source - a hydrogen flame torch - was to be chosen to avoid any unwanted fumes adhering to the surface of the sphere. The surface tension of liquid glass does all the work to reform the material into a sphere. After fabrication, the resonator has to be protected from dust and stored properly to slow down the degradation of the Q factor.

3.2.1.1 *Materials*

The Corning SMF28 Optical Telecommunication Fiber made up of 16 threads of single-mode fibers with a diameter of 125 µm, Thorlabs SMF28 single-mode optical jacketed with 900 µm, 125 µm fiber thread and 8.2 µm core, Light Guide Optics International Ltd. optical fiber with 125 µm fiber thread and 10 µm core were used to fabricate the microsphere resonators. The fabrication results were spheres with a diameter of 300 - 700 µm. To fabricate spheres below 300 µm the fiber first had to be tapered.

3.2.1.2 *Preparation Before Melting*

The fiber was cut into 7 cm long strips. First, the jacket needed to be striped to access the fiber thread. Second, the fiber coating had to be removed (see Fig. 3.3 a).

CORNING SMF28 FIBER For Corning SMF28 fiber the jacket can be easily stripped and 16 individual threads located inside. To remove the plastic coating fiber stripper can be used or, alternatively, the fiber can be soaked in an acetone bath for 5 - 10 minutes inside a shallow dish. The coating swelled and could be easily separated from the

cladding. An aluminum foil was used to cover the dish and prevent the acetone from evaporating.

THORLABS SMF28 The Thorlabs SMF28 fiber had a single thread inside the jacket. Removing the coating was tougher. It had to be soaked in pure acetone for several hours to easily remove both the jacket and coating using the fiber stripper. The soaking was done in a small glass jar with a lid to minimize the evaporation of the acetone.

LIGHT GUIDE OPTICS INTERNATIONAL LTD. FIBER The Light Guide Optics International Ltd. optical fiber with a 125 µm diameter was used to fabricate microspheres for WComb generation. It was harder to strip the coating from this fiber as the soaking in acetone was not effective. The coating was burned using a flame.

Next, the fiber end was cut using a fiber cleaver (FC-6S) to achieve a perfect 90° angle to make sure that no residue could adhere to the tip of the fiber or at least reduce the chances of unwanted residual adhesion.

Following steps were performed while wearing gloves to protect the fiber from grease and other dirt. After soaking the fiber thread in acetone it is wiped with special cleaning tissues, which does not leave any lint or fibers behind on the surface, soaked in ethanol. This removed grease, dust, residuals from the coating, etc. Second, the fiber was dipped in a glass beaker with ethanol and cleaned in an ultrasonic cleaner (Skymen JP-008) for 3 minutes. The stripped and cleaned telecom fiber should be exposed to air for the least amount of time before used for fabrication.

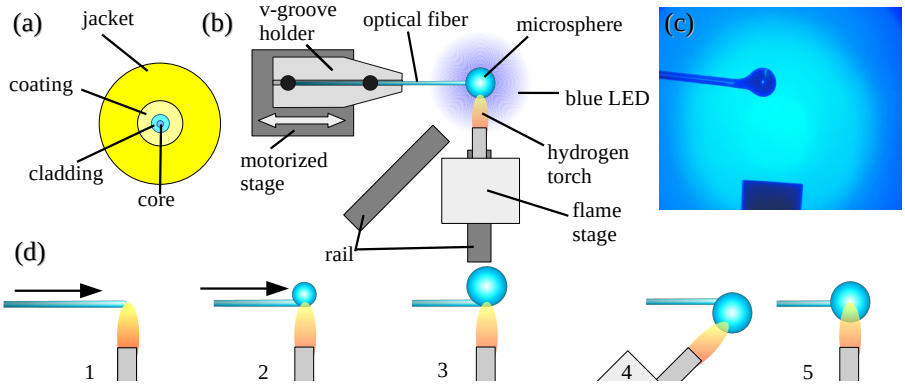

Figure 3.3: Fabrication of silica microsphere resonators: (a) the structure of the fiber; (b) fabrication station setup scheme; (c) fabricated microsphere; (d) straightening the bent stem.

3.2.1.3 *Melting*

A hydrogen flame torch was chosen as a heating source because the combustion of hydrogen and oxygen produces only heat and water without any soot, toxic or unwanted fumes that could reside on the surface of the microresonator. Also, no hydrogen storage is necessary as the gas is only produced on-demand using water and electricity. The torch was attached to a stage which was controlled manually on a rail. The flame stage was also used for positioning the sphere and centering it with the microsphere. The scheme of the fabrication station can be seen in Fig. 3.3 b.

To handle the prepared fiber thread a holder with a v-groove was used. The v-groove was attached to a motorized stage for moving fiber and a microscope, which was built on a slide stage to easily observe the whole length of the fiber. A blue LED light was used for contrast to better see the transparent fiber and the growing sphere (see Fig. 3.3 c). The pulling stage was controlled by a DC motor with a constant supply voltage of 12 volts and was easily controllable in both directions by a control unit with directional switches. The motor drove the translation stage that pushed the fiber into the flame, and the delivered length was controlled by the number of motor steps or revolutions. Due to the surface tension, the melting part of the fiber starts to form a spherical shaped tip gradually (see Fig. 3.3 d steps 1-3). Within about 10 seconds a small sphere was formed. The working principle was based on the preservation of material volume – the volume of the portion of the fiber pushed into the flame tended to be close to the volume of the microsphere. For a 125 µm fiber smallest spheres were about 300 µm. The size of the resonator could be controlled by varying the speed with which the fiber was moved towards the flame. By slowly moving the fiber the resulting resonator was small and round, the fiber core and cladding melted together (see Fig. 3.4 a). If the speed was increased, the resonators could be made bigger, they were more elliptical in shape. For bigger resonators fabricated from Thorlabs fiber, the core spiraled inside the sphere made out of the cladding not fully melting together (see Fig. 3.4 b). To obtain a large sphere the flame temperature had to be taken into account because if the temperature was too high, then the fiber evaporated and the sphere did not get bigger. Therefore, a smaller flame was needed to fabricate larger spheres. To provide more roundness to the sphere, a longer time for melting was needed, which also meant that the sphere was going to be smaller, limiting the diameter below 1 mm for 125 µm fiber.

The remaining fiber thread stem was left attached to the sphere for the convenience of handling it. However, the stem of the fiber got bent away from the flame due to the force of the flowing hydrogen. The stem needed to be straightened (see Fig. 3.3 d steps 3-5). The torch stage was attached at 45° angle and by slowly rotating the mi-

crosphere using the stem it was straightened. After straightening the stem it was advised to melt the surface of the sphere to some more in the flame to undo any unwanted deformations to the roundness. It was done carefully to avoid bending the stem repeatedly due to the hydrogen flow.

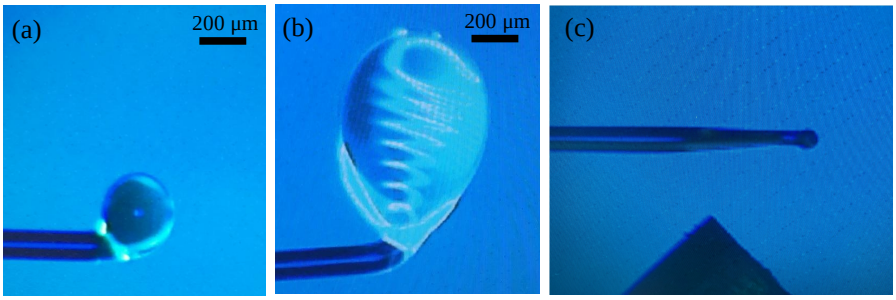

Figure 3.4: The size and internal structure of microsphere WGMR depended on the speed the fiber was melted: (a) slowly moved towards the flame and (b) moved fast towards the flame the core spiraled;(c) to make smaller resonators the fiber was tapered first.

The automation of fabrication helped to reproduce high Q resonators with better odds.

3.2.2 *Degradation of Microsphere Resonators*

If WGMRs are not stored properly the Q factor decays relatively quickly. The degradation of the Q factor of the resonators was investigated by leaving it in ambient air. If resonators got dirty due to dust the Q factor of the resonator dropped over the 21 days (see Fig. 3.5 a curve 2 and b). It was possible to clean the degraded resonator using acetone or methanol, however, the effect of reviving the dirty resonator was limited. Leaving the resonator in a more protected environment - a box where the air is filtered inside from dust - resulted in slower degradation (see Fig. 3.5 a curve 3). For another resonator, an individual container with a lid was used to store it. This was done to minimize the chance of contaminating other resonators each time the container lid was opened to access the resonator. The chosen type of container had a stem in the middle of the lid which was used to tape the microsphere stem. The concern for storing the resonator was the atmospheric moisture. The silica absorbed the moisture and as a result increased the absorption lowering the Q factor in time (see Fig. 3.5 a curve 1). The WGM resonators could be revived by heating and evaporating the excess moisture but also this effect was limited.

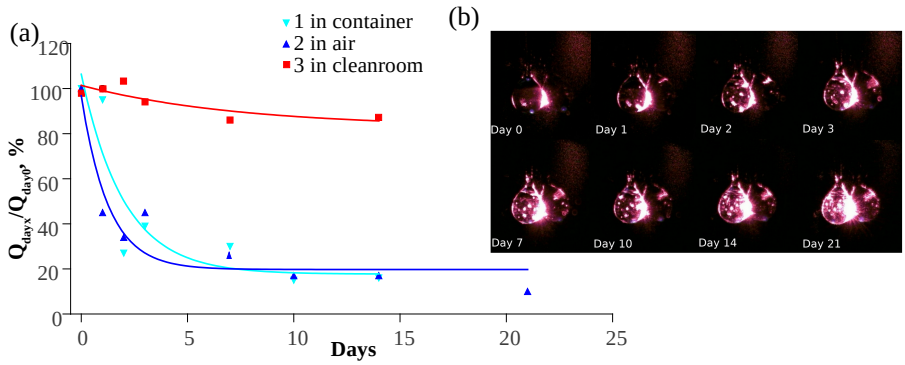

Figure 3.5: The degradation of the Q factor: (a) resonator left in a protected environment degraded slower than resonator left in ambient air, however, resonator inside a container can degrade due to moisture as in the ambient air; (b) resonator degradation due to the dust settling on the surface over time.

3.3 COATING MICROSPHERE WGMRS

WGMRs are candidates for all kinds of sensor applications. The requirements for a biosensor are selectivity, sensitivity, stability. The selectivity for the WGM microspheres can be achieved by surface functionalization - the introduction of a binding material to the surface. The coating layer has to be very thin, below the evanescent penetration depth, 10 to 100 nm [14]. The coating may have a higher index of refraction, for example, ZnO, or a lower index of refraction, for example, gold, than the WGM microsphere. The function of the coating also changes accordingly. For higher index coatings the propagating WGMs are almost entirely inside the coating unless it is very thin. This ensures the stability of the whispering gallery mode. A coating with the lower index makes the microsphere more sensitive to the surrounding environment.

The silica microsphere fabrication method is fast and cheap. It is possible to make many microsphere WGMRs for testing various coatings for surface functionalization by coupling the light inside and exciting WGM resonances, calculating the Q factor, investigating the triggers of WGM resonance frequency shift. Control measurements are also a vital part of biosensor testing.

3.3.1 *Gold Nanoparticles*

The WGM resonators can be combined with localized surface plasmon (LSP) nanostructures to enhance the sensitivity of WGM sensors. The WGM resonance can be made more accessible to the analyte by extending the evanescent field with large tails out of the metal particles. In metals, plasmon resonances occur from the presence of free

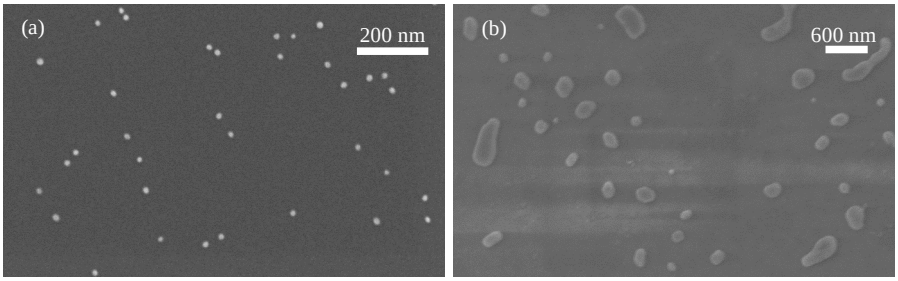

Figure 3.6: SEM images of Au nanoparticles (a) on Si substrate, (b) on WGMR.

electrons. Free electrons can interact with electromagnetic radiation. When electrons are confined into a very small volume, they can oscillate in phase with the incident electric field, thus generating a localized surface plasmon resonance [27]. The success of Au nanoparticles plasmon resonances is because of the high chemical and physical stability and biocompatibility of gold nanostructures and the ability to amplify the electromagnetic field at a nanometric distance from the metal surface.

A colloidal suspension containing the Au NPs, which were 10-13 nm in diameter (see Fig. 3.6 a) was used for coating. Nanostructures of the particles determine the sensitivity of resonators. Larger diameters have lower sensitivity. WGM resonator was coated with Au nanoparticles by dip coating for 20 seconds to obtain WGMR/Au-NPs.

The structure of Au coating is studied using SEM images. Agglomeration of the Au nanoparticles occurred when deposited on WGM surface (see Fig. 3.6 b). The nanoparticles cling to some places instead of forming an uniform layer.

3.3.2 *Glucose Oxidase*

Shortly before sensor testing, microsphere resonators were coated with glucose oxidase (GOx) - an enzyme that oxidizes glucose and is often used in the design of various types of glucose sensors. The resonator was dipped into the solution of 10 mg/mL of GOx to make WGMR/GOx or WGMR/Au-NPs/GOx if the resonator was coated with Au nanoparticles first.

3.3.3 *ZnO*

ZnO is well known material for different optoelectronic applications, such as sensors, biosensors, and optical coatings [28]. ZnO microstructures have been used as WGMRs for laser and sensor applications [29] due to the biocompatibility and functionality of the surface.

3.3.3.1 *ZnO Nanorods*

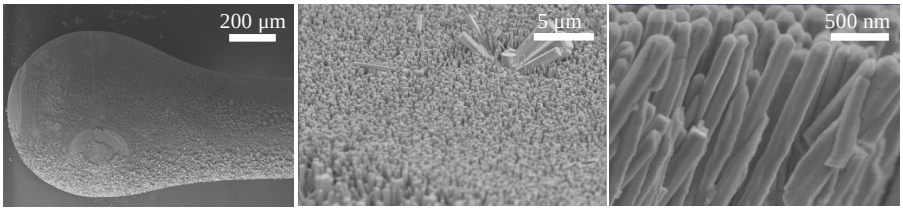

Figure 3.7: SEM images of ZnO nanorods grown on WGM microsphere resonator.

ZnO nanorods (NRs) as a potential material were chosen as low cost and simply produced nanomaterial with a high surface to volume aspect ratio. ZnO nanorods were grown on both a flat surface and WGMRs using hydrothermal syntheses of ZnO. Initial ZnO seed layer was prepared on optical fiber by drop-casting 20 µL of zinc acetate methanol solution (1 mg/mL), followed by annealing at 350°C for 1 hour. Hydrothermal growth of ZnO-NRs was performed. The samples were washed and then dried at room temperature. The ZnO structure characterization was performed using SEM. ZnO nanorods formed a dense "forest-like" structure on the surface (see Fig. 3.7). Growing the structures on a curved surface also provided some challenges. The defects at the cap region of the WGMR should not interfere with the WGM resonances excited in the central part of the resonator.

3.3.4 *ZnO Nanolayer*

Atomic layer deposition (ALD) was chosen as the coating method because it is possible to control the structure and optical properties of the nanolayer. ZnO thickness is an important parameter. It influences crystallization, grain size, band-gap, and defect concentration so we believe that there has to be an optimal thickness for coating microsphere resonators.

The coating process of ZnO was as followed. WGMRs were cleaned by oxygen plasma for 30 minutes using the Reactive Ion Etching (RIE) machine (Microsystems). After plasma cleaning the WGMRs were placed in the ALD reactor (Picosun). The ZnO thin films were deposited onto the resonators using Diethylzinc and deionized water as ALD precursors. Nitrogen (N_2) flow was used as a carrier and the purging gas. Zn precursor and water were evaporated at 200°C. ZnO thin films were grown at temperature 200°C. The growth rate was typically 2 Å/cycle for ZnO grown on a plane surface. The growth per cycle has been controlled by measuring the film thickness on Si-

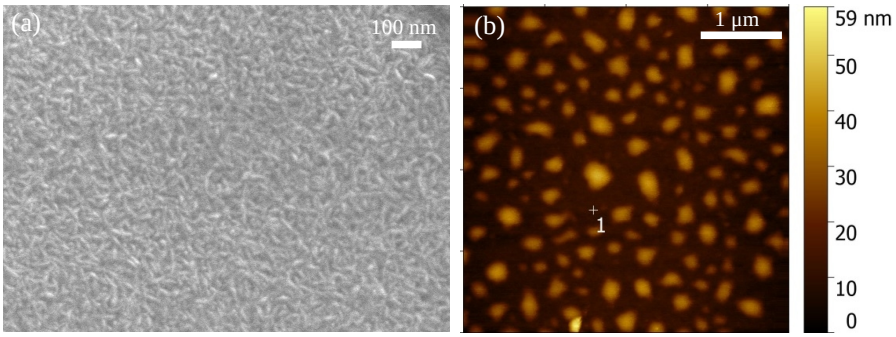

Figure 3.8: ALD coated ZnO nanolayer structure: 50 nm thick ZnO layer (a) SEM image and (b) AFM image show the nanoscrystals about 50 nm in length.

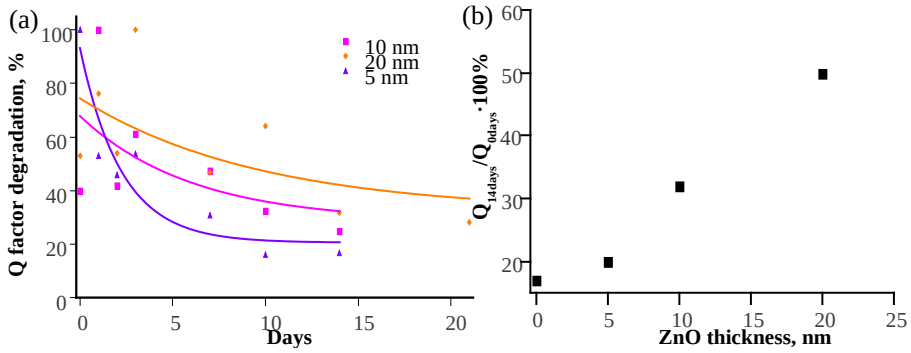

Figure 3.9: Degradation of WGMRs coated with ZnO:(a) Q factor degraded in time the same as bare WGMRs, however, the degradation rate appeared to be slower for thicker ZnO layer; (b) Q factor degradation rate dependence on ZnO thickness at the end of the second week after coating.

wafer reference substrates placed in the reactor. The thickness of ZnO coatings varies from 5 to 100 nm.

The structural properties of ZnO coated WGMRs were studied using SEM (JEOL, JSM-7001F) and AFM (Icon Bruker). The initial WGMR has an almost smooth and mirror-like surface. After ALD, SEM images indicate that the ZnO layer conformally coats the WGMR. The rough surface can be seen (see Fig. 3.8 a and b) with the polycrystalline structure of produced ZnO layer consisting of elongated crystallites with an average size of about 20-30 nm in length.

Q factor degradation of ZnO coated WGMRs was investigated (see Fig. 3.9 a). ZnO coating on WGMR could provide a protective coating against Q factor degradation. Thickness dependence of the Q-factor degradation of ZnO-WGMR structures is shown in Fig. 3.9 b. Degradation of 5 nm ZnO layer showed a drop of Q factor below 20% which was similar to bare WGMR. Degradation of 10 nm ZnO layer showed a drop of Q factor up to 30% at the end of the second week and 20

nm Zn layer - 50%. The degradation percentage decreased with an increase of the thickness.

3.3.5 *ZnO Nanocrystals*

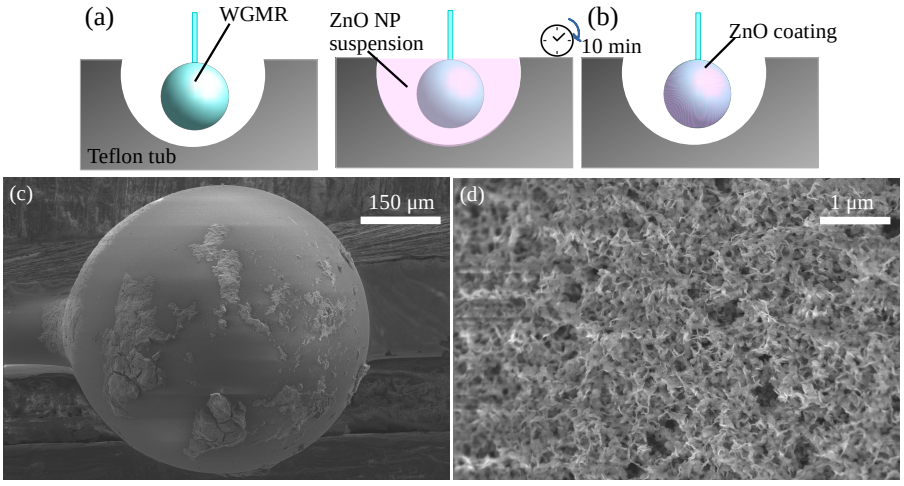

Figure 3.10: Drop coated ZnO structures on WGM resonator:(a) small Teflon tub was used to contain suspension with ZnO; (b) as the solvent evaporated ZnO was coated on the WGMR; (c) and (d) SEM images of ZnO nanocrystal structure.

The WGMRs coated with ZnO using the ALD method were very good. The whole surface was covered and the thickness could be controlled. However, special equipment is necessary to use ALD and it is time-consuming. A cheaper and faster method was necessary to make many samples for bio-testing. The most important property for the newer method was the high enough Q factor to observe WGM resonances. A drop method was tried.

A solution containing zinc acetate methanol (1mg/mL) for deposition of ZnO nanoparticles was prepared. WGMR resonator was positioned above a little Teflon tub and a 20 µL solution dropped using a pipette (see Fig. 3.10 a). In about 10 minutes the solvent evaporated leaving ZnO particles on the surface of the WGMR (see Fig. 3.10). The SEM images of drop coated ZnO on the WGMRs are shown in Fig. 3.10 and 3.10. The ZnO coats only some parts of the WGMR surface. WGMR/ZnO structure was obtained.

ZNO AND AU STRUCTURES As the Au NPs agglomerated when dip-coated on the WGMR surface, Au was coated on the ZnO coated WGMRs. The WGMR/ZnO structure was placed inside a transparent container with liquid Au nanoparticle suspension. The resonator was irradiated with UV lamp for 2h (see Fig. 3.11 a). When the ZnO was coated on the surface, due to a chemical reaction Au coated the ZnO

covered structures. SEM images of WGMR/ZnO before and WGMR/ZnO/Au after comparison confirm that Au attachment to the ZnO surface (see Fig. 3.11 b and c) as the ZnO structure was finer before Au.

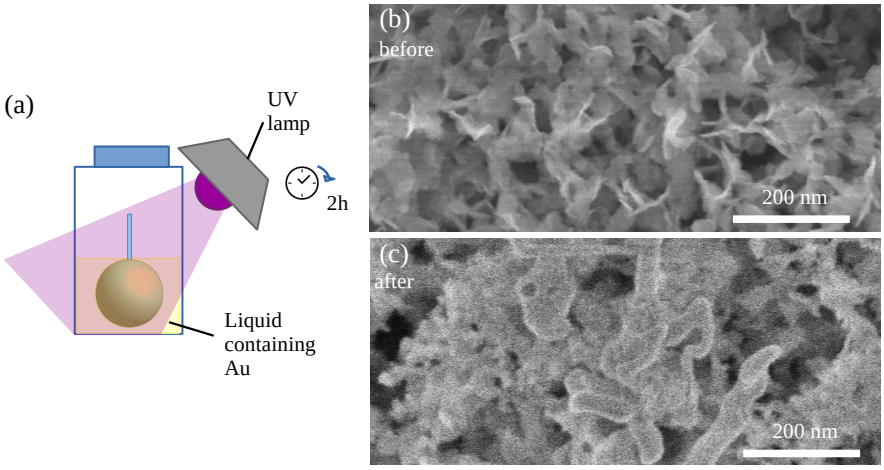

Figure 3.11: ZnO structures with Au coated on WGM resonator:(a)ZnO coated WGM resonator was dipped in suspension with Au and irradiated with UV light; SEM images of ZnO coating (b) before and (c) after treatment.

ZINC ACETATE To have ZnO coat the whole surface of the WGMR, the solution for drop coating was changed to Zinc acetate ($Zn(OAc)_2$) in methanol. Different concentrations (1-4 mg/ml) and drop volumes (20-30 µL) were used to deposit thin layers of ZnO on the WGMR surface. The solvent evaporated in about 20 minutes. It was followed by annealing at 350°C for 1 hour.

In many cases, the ZnO coating on the WGMRs could be seen in the microscope. Visible surface structures corresponded with those observed during WGM coupling. Optimal concentration was 2 mg/mL (see Fig. 3.12 a) and optimal drop size 20 µL applied as one drop or as two 10 µL drops (see Fig. 3.12 b).

These WGMR/ZnO structures were used to add proteins for the toxin sensor.

3.3.6 *Proteins*

To fabricate a toxin sensor the surface of ZnO coated WGM resonator (WGMR/ZnO) was further modified. The step by step coating scheme for toxin sensor based on antigen/antibody reaction is shown in Fig. 3.13 where the WGMR/ZnO is coated with antigens protein (BLV) to obtain WGMR/ZnO/BLV and then protein from cows (BSA) for the sensor structure WGMR/ZnO/BLV/BSA. It was used to test anti-

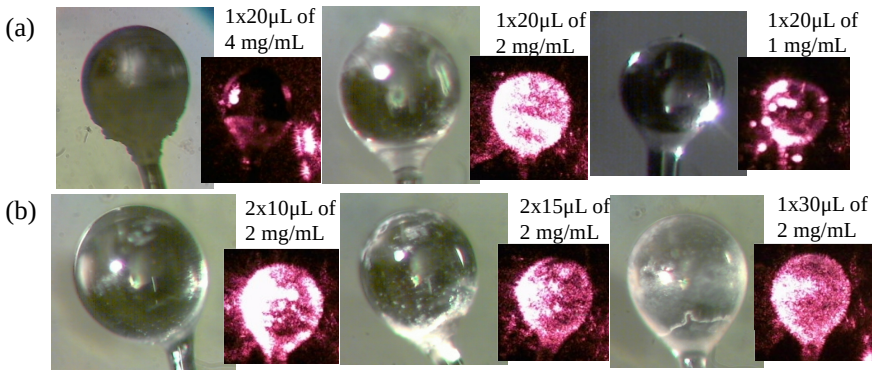

Figure 3.12: The WGM resonators coated with ZnO: for various Zn acetate (a) concentrations and (b) deposition drop volumes in microscope and during coupling.

gen/antibody reactions in a BLV-positive probe. The Positive probe contained specific antibodies against the BLV proteins.

BLV Bovine leukemia virus or BLV is a protein that causes an infection in cattle resulting in disease. BLV antibody and antigen were used in the bioanalytical system. BLV antigen was diluted to the concentration of 0.5 mg/L with the physiological solution of NaCl (0.85%).

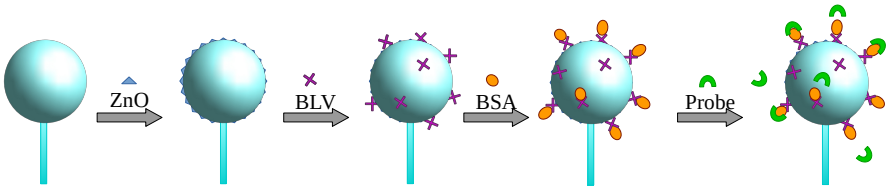

Figure 3.13: The functionalization scheme of the WGM resonator for a toxin sensor.

BSA Bovine serum albumin or BSA is a small, stable, moderately non-reactive protein derived from cows. A 0.5 mg/mL concentration of BSA was used in order to prevent non-specific adsorption of proteins.

First, the same drop-coating method as used for ZnO coatings was attempted. A Teflon tub with space for all 3 drops (1 - ZnO, 2 - BLV, 3 - BSA) was prepared (see Fig. 3.14 a). However, the solutions containing BLV and BSA were very slow to evaporate.

Next, a dip-coating method was implemented (see Fig. 3.14 b and c). The resonator was attached to a glass microscope slide to elevate it and avoid directly touching the base of the Petri dish. A drop containing 20 µL of BLV solution was deposited on the resonator. For the

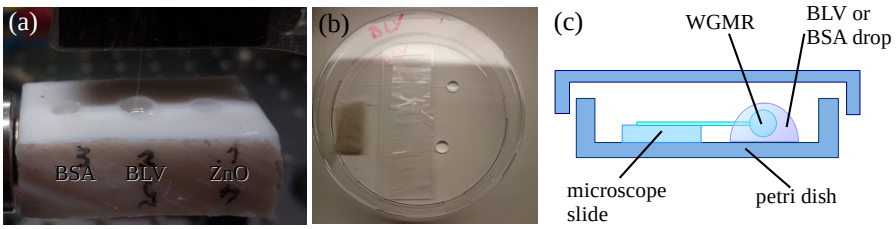

Figure 3.14: Coating the WGMR/ZnO surface with BLV and BSA: (a) drop coating method, (b) and (c) dip coating method.

drop to maintain a hemispherical shape the dish needed to be clean and dry. Multiple resonators could be coated at the same time but a suitable distance between them was important for the drops did not touch. The WGMR/ZnO were left in the solution for 20 minutes. Afterwards, they were removed from the petri dish and any unattached BLV molecules were rinsed using a drop of PBS.

The same-dip coating method was used for BSA, only a different petri dish was used for each type of molecule. The WGMR/ZnO/BLV was left in a 20 µL drop of BSA for 20 minutes and any unattached proteins rinsed off with a drop of PBS afterwards. The obtained WGMR/ZnO/BLV/BSA was dried in air at room temperature.

3.4 COUPLING LIGHT INSIDE WGMR

To couple light inside a WGMR, several approaches can be used. A common technique to couple light into the resonator is prism coupling. Experimental studies have shown that prism coupling has approximately 80% efficiency [51, 65]. The system with prism coupling is robust and the surface can be easily cleaned if necessary. For example, working with liquid suspension samples, nanoparticles can adhere to the surface and decrease the coupling efficiency. However, it is a bulky component and requires collimation optics, as the laser beam travels through the air. More details about prism coupling can be found in section 2.3.2.

In this section, two different setups are described. The main element of all the setups was a coupling prism and collimation optics. The first setup had a glass prism and was mainly used for WGM resonator characterization. The second setup had a GGG prism combined with temperature stabilization and was used for measurements in liquids. Both setups were interrogated using a 780 nm laser.

3.4.1 *Setup with Glass Prism for WGM Resonator Characterization*

In this section, a simple Q factor measurement setup and the scan method are presented. All WGM resonators can be characterized by

their resonant frequency f_0 and their quality factor Q. The measurement system was set up to characterize the optical properties of microsphere resonators fabricated by melting a single-mode fiber using a H_2 flame. The system consisted of a 780 nm ECDL laser (spectral linewidth < 1 MHz), a couple of mirrors, a focusing lens (F = 1 cm), a coupling prism, and a photo-detector connected to an oscilloscope (see Fig. 3.15 a and b). To control the coupling process an additional camera is used to observe the microresonator and the surface of the coupling prism where the total internal reflection of laser light occurs. Also, X-Y-Z micrometer screws are needed to adjust the microresonator position. For the scan method, the laser was finely swept at a low frequency around resonance, and simultaneously the transmission amplitude was recorded. Experimentally, in the time domain, a dip in the transmission of the laser was observed. The transmission dips in the transmission spectra corresponded to a series of WGM resonances at different wavelengths. Resonators with a lower Q factor glowed brighter and had wider dips than resonators with a higher Q factor. The measurement of the full-width at half-maximum of a resonant mode led to the Q factor of the resonator.

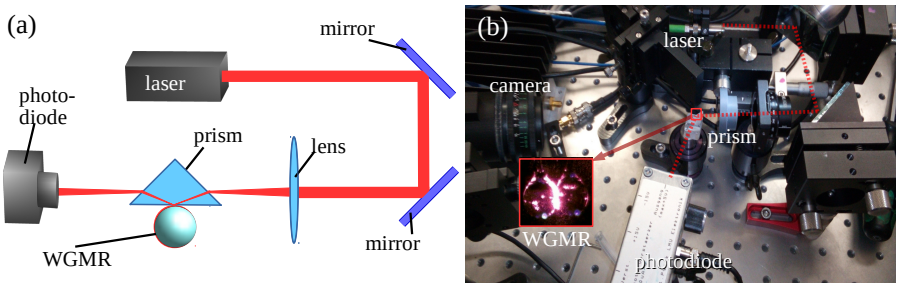

Figure 3.15: The measurement system setup with a glass prism: (a) the basic block-scheme and (b) an actual photo where red dotted line shows the infrared 780 nm laser path and the inset shows the WGMR as seen by the camera.

.

The relatively slow frequency scan of the resonant frequency resulted in the shift due to thermal effects or other perturbations during the measurement [70]. It was difficult to be sure that the observed resonant curve was completely free from this problem.

Additionally, a reference signal was needed to convert the time domain seen on the screen into the frequency domain. To do that a reference optical fiber was used. The fiber ends acted as a Fabry Perot resonator and results in fringes. The frequency between the two modes could be calculated:

$$\Delta f_{ref} = \frac{c}{2nL}, \tag{3.2}$$

where c is the speed of light, n is the refraction index of the fiber core and L is the length of the fiber. Hence the distance between two

modes for 2 m long silica optical fiber is approximately 50 MHz. A more precise value was found to be (48.77 ± 0.39) MHz when using an additional reference. Using the reference fringes the width of resonance could also be calculated in MHz. Q factor was then obtained.

FINDING RESONANCE FULL WIDTH AT HALF MAXIMUM Since the Q factor can be obtained by dividing the frequency with the full width at half maximum, one must first find it. A couple of approaches can be used. The most simple method is to find the height of a resonance peak, then determine the halfway point and measure the width. This approach is good to estimate the Q factor of the resonator quickly but is inaccurate. A more accurate method is an approximation of the resonance peak using Lorentzian function (see Fig. 3.16 a):

$$Y = y_0 - A\frac{\frac{1}{2}\Gamma_{FWHM}}{(x-x_0)^2 + (\frac{1}{2}\Gamma_{FWHM})^2}, \tag{3.3}$$

where Γ_{FWHM} is the width parameter, x_0 is the peak position offset in x direction, y_0 is the peak position offset in y direction and A is the function stretch parameter (for more details see Section B.1). This approach uses all the data points recorded which form the resonance intensity dip. However, this method is less effective, if the dip consists of multiple resonances or is asymmetric.

For asymmetric peaks, a different approximation function is required. Fano resonance is a type of resonant scattering phenomenon that leads to an asymmetric line shape. Fano resonance can be described with the following function (see Fig. 3.16 b) [71]:

$$Y = y_0 - A\frac{(\frac{q}{2}\Gamma_{FWHM} + x - x_0)^2}{(x-x_0)^2 + (\frac{1}{2}\Gamma_{FWHM})^2}, \tag{3.4}$$

where q is the Fano parameter, which determines the spectral shape. The Fano resonance line-shape is due to interference between two scattering amplitudes, when a discrete quantum state interferes with a continuum band of states [71]. If an external perturbation does not couple to the continuum of states, $q \to \pm\infty$ and the Fano lineshape becomes a symmetric Lorentzian function.

CRITICAL COUPLING The distance between the WGMR and the surface of the prism is crucial. During experiments between a glass coupling prism and WGM silica microsphere resonator, strong van der Waals forces were observed. The resonators clang to the surface of the prism and made it difficult to control the gap between the two. However, this gap became crucial to obtain critical coupling conditions for resonators with very high Q factors. Problems became really noticeable for resonators with Q factors higher than 10^7. As seen in Fig. 3.17 the resonances became very broad and calculations were off for about an order of magnitude.

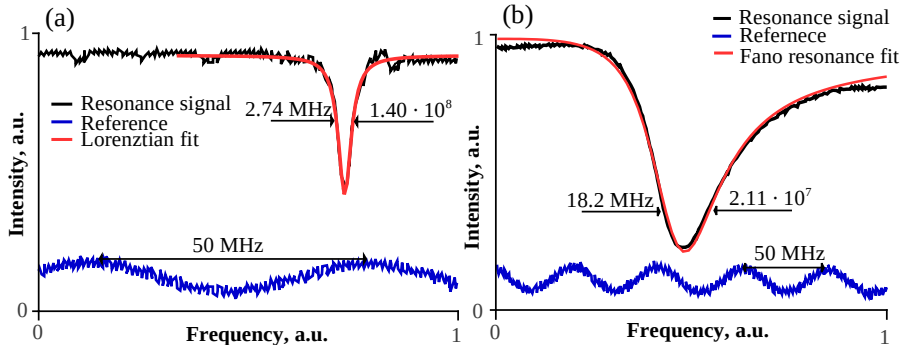

Figure 3.16: Approximation of resonance peaks using (a) Lorentzian function (Eq. 3.3) for a symmetric dip and (b) Fano resonance function (Eq. 3.4) for asymmetric dip.

.

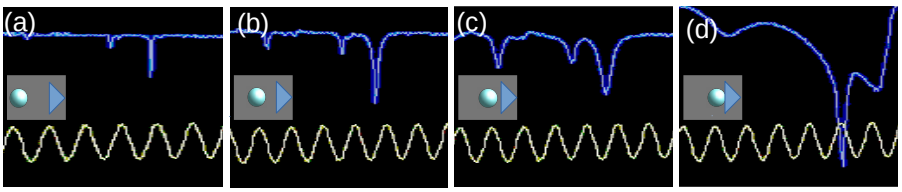

Figure 3.17: Microsphere resonator coupling conditions: (a) under-coupling when the gap is too wide and signal is very weak, (b) critical coupling conditions optimal for measurements and Q factor $6 \cdot 10^7$, (c) over-coupling when the gap is too small and the resonances become broader, (d) over-coupling, when resonator touches the prism due to van der Waals force attraction and the resonances, are very broad and Q factor inaccurate $9 \cdot 10^6$.

To measure the Q factor as accurately as possible an optimal resonance position was found. The WGMR was moved away from the prism and slowly moved back closer. Rarely, the optimal gap could be found by simply increasing the distance and moving the resonator further from the prism. The fiber stem is flexible and the resonator simply "popped away" from the surface suddenly. If the attempt of finding the optimal gap was unsuccessful and the resonator attached to the surface of the prism due to the van der Waals forces, the distance was again increased and then slowly decreased. The process was repeated until success. Sometimes the critical coupling could be achieved for a moment and shortly after the over-coupling or under-coupling followed depending on either the distance decreasing due to van der Waals forces or increasing due to fiber stem flexibility forces.

3.4.2 *Setup with GGG Prism for Measurements in Liquids*

To obtain the WGM resonances in a liquid environment, a small Teflon tub (it is hydrophobic and does not wet water nor water-containing substances) was used to hold the liquid and due to the surface tension, the liquid level was higher than the rim of the tub. Water has a refractive index of 1.33, therefore a prism with a higher refractive index than glass was selected to ease the coupling process. A Gadolinium Gallium Garnet (GGG) prism has a refractive index of 1.95. The basic setup scheme was the same as described in the previous section (see Fig. 3.18 a). Pipes were used for adding and draining the liquid from the tub.

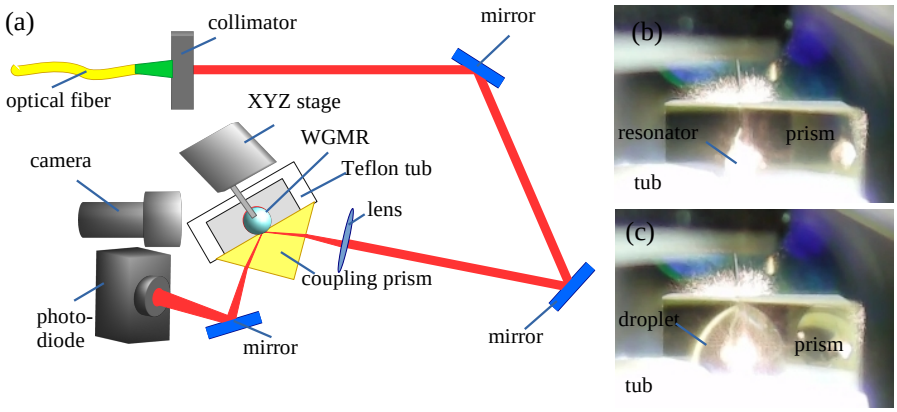

Figure 3.18: The measurement system setup with GGG prism for measurements in liquids. In (a) a simplified block scheme of the setup; (b) and (c) are the camera shots without and with the liquid drop respectively.

To see the resonator with a camera, it was positioned above the rim of the tub (see Fig. 3.18 b) and the liquid formed a droplet above the rim and engulfed the resonator (see Fig. 3.18 c). Using a photodetector and an oscilloscope resonance signal was observed. The higher loss in water shows itself as a decrease in Q factor, therefore, in liquid, the resonances were broader than in air.

The resonance shifts due to temperature changes. First, it was investigated if the resonance shift is linear as the theory suggests. For silica glass thermo-optical α coefficient and the expansion coefficient β contribute to the shift of resonance frequency:

$$\frac{df}{f} = -(\alpha + \beta)\, dT, \tag{3.5}$$

where df is the frequency shift, dT is the temperature shift. The $-$ sign indicates that the resonance frequency decreases as the temperature increases. The experimental setup was upgraded. A Peltier element was used for temperature control (see Fig. 3.19 a, b). The prism and

tub was mounted on the Peltier (Melcor 2×2 cm) with the temperature sensor (AD590), temperature controller (Thorlabs TTC001 digital or Thorlabs TED200C analog) was used to set the temperature.

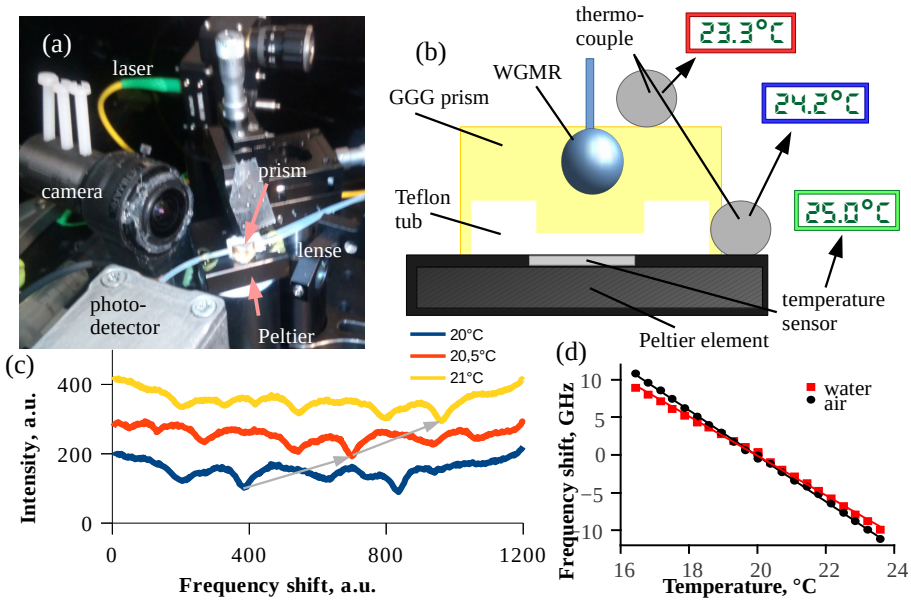

Figure 3.19: The upgraded setup with Peltier element for temperature scanning. In (a) an actual photo of the system; (b) temperature gradient present (c) the resonance spectrum slowly shifts to the right when heated; (d) the WGM resonance shifted about 3000 MHz for 1°C.

The resonator was first heated from 20°C to 25°C with a step of 0.5°C, then cooled from 25°C to 15°C and lastly heated from 15°C to 20°C and resonance spectra recorded for each step. The resonances slowly shifted to the right when heated (see Fig. 3.19 c) and to the left when cooled. This means that the frequency decreases when shifting to the right and increases when shifting to the left. Overall the shifting direction depends on which side of the scanning laser slope was visible in the screen of the oscilloscope. Comparing two resonances for different temperatures the shift was found. The temperature scanning was linear with the frequency shift of (3030 ± 20) MHz per 1°C in the air (see Fig. 3.19 d). In the water droplet, it took significantly longer to reach the target temperature due to the large heat capacity of water and the droplet kept evaporating. The frequency shift of resonance was (2621 ± 24) MHz per 1°C in water. Since the experiment took a long time the laser drifted as a shift of reference signal happened. This was avoided by using an additional Rb saturation spectroscopy signal as a reference.

RB SATURATION SPECTROSCOPY AS REFERENCE Saturation spectroscopy is a high resolution spectroscopy free of Doppler broaden-

ing of lines (see Appx. B.1 for more details). A monochromatic and tunable laser beam is absorbed in the Rb vapor in the 780 nm region. If the transmitted light is monitored as a function of frequency, a Doppler broadened absorption spectrum will be observed. If the laser beam is split into two beams where one is a strong and second a weak one, coming from opposite directions the Doppler-free absorption can be observed because only excited atoms with no velocity component in either direction can interact, the others don't match in frequency because of the opposite Doppler shift. The sharp absorption lines have nearly the natural linewidth and Lorentzian profile. Additionally, frequencies in the middle between two levels will also be visible in the saturation spectra and are known as the cross-over frequencies.

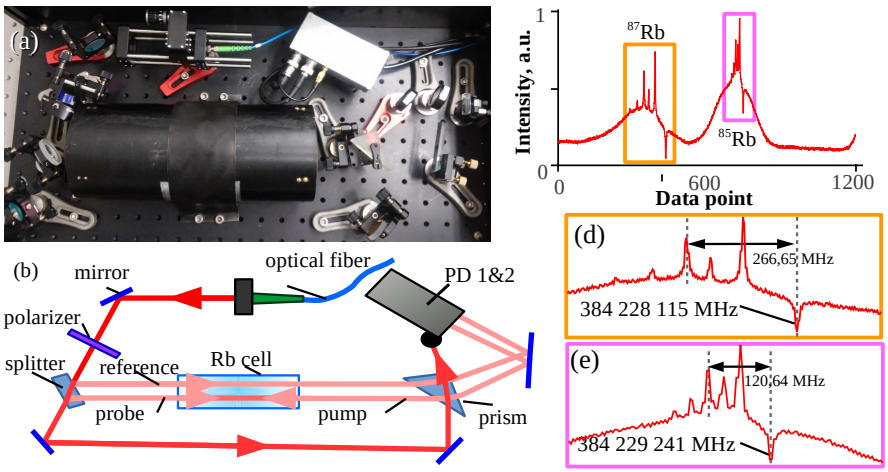

Figure 3.20: Rb saturation spectroscopy setup: (a) an actual photo of the optical components, (b) drawn block scheme and (c) measured spectra of (d) ^{87}Rb and (e) ^{85}Rb D2 line (see Appx. B.2.3 for detailed information about Rb hyperfine splitting).

The setup used for Rb saturation spectroscopy reference signal can be seen in Fig. 3.20 a, b and the obtained signal in Fig. 3.20 c. ^{87}RbD2 (Fig. 3.20 d) and ^{85}RbD2 (Fig. 3.20 e) lines can be seen. The hyperfine structure consists of 3 Rb lines (see Appx. B.2 for more details) and 3 cross-over peaks for each isotope D2 line. However, observing the Rb spectra and reference signal obtained from fringes it is clear that the laser frequency scanning was not linear in this range. Using the known hyperfine structure of the Rb isotopes it was specified that the period of the reference fringes was 48.77 MHz. Both references gave vital information about the laser and were used in the measurements.

The absolute frequency could be found by using a single Rb saturation line. For practical reasons, 87Rb D2 inverse line was chosen for alignment. The oscilloscope can display 1200 data points for each channel. Each data point is given a consecutive number so that the

number aligned with the chosen Rb saturation line was corrected to be 0 (see Fig. 3.21 a). Using the consecutive numbers and fringes with the period of 48.77 MHz the relationship between the two was found and 4th order polynomial $f = Ax^4 + Bx^3 + Cx^2 + Dx$ approximation was used (see Fig. 3.21 b inset). 0 point has frequency 0 MHz and the absolute value of the chosen Rb line 384228115,2095 MHz [72] has to be added to the polynomial (see Fig. 3.21 b).

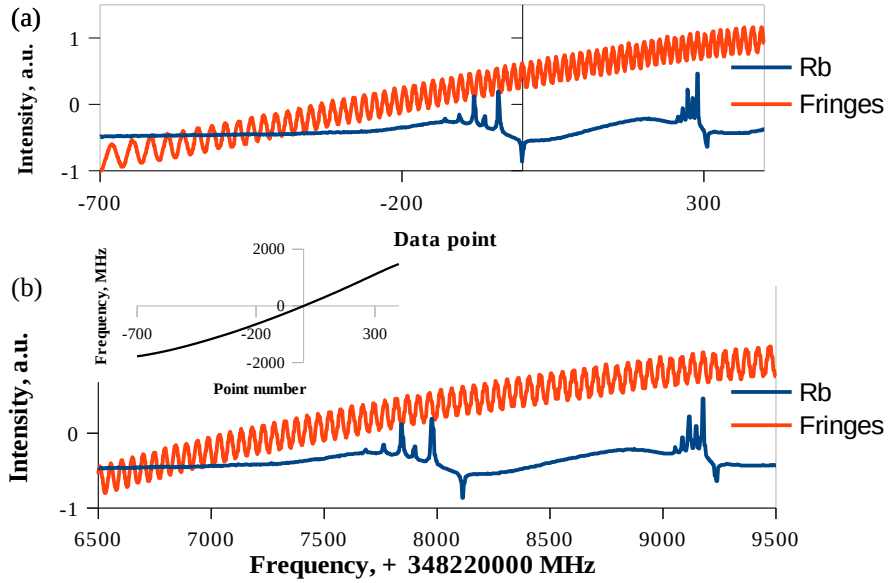

Figure 3.21: Calibrating the frequency scale by using fringes and Rb lines: (a) recorded Rb saturation spectroscopy lines and interferometric fringes with period 48.77MHz for calibration where the position of one Rb line is chosen as data point 0, (b) Rb and fringes after calibration, the inset shows the calibration curve.

3.5 TESTING WGM RESONATOR SENSORS

WGMRs were characterized by finding the Q factor to appraise the quality of the coatings. 780 nm ECDL laser was coupled inside the resonator using a glass prism and the transmission spectra were recorded. To test the sensor-like response of the functionalized WGMRs 780 nm ECDL laser was coupled inside the resonator using a GGG prism and a small Teflon tub to hold the liquid was used. Both the prism and the tub were mounted on a Peltier element with a temperature sensor.

3.5.1 *Characterizing the Coated Resonators*

The WGMR microspheres both bare and coated with Au NPs, GOx, ZnO, etc. were characterized by finding the Q factor, which describes the ability to store energy inside the microcavity. 780 nm ECDL laser

was coupled inside the resonator using prism coupling and the setup described in Section 3.4.1.

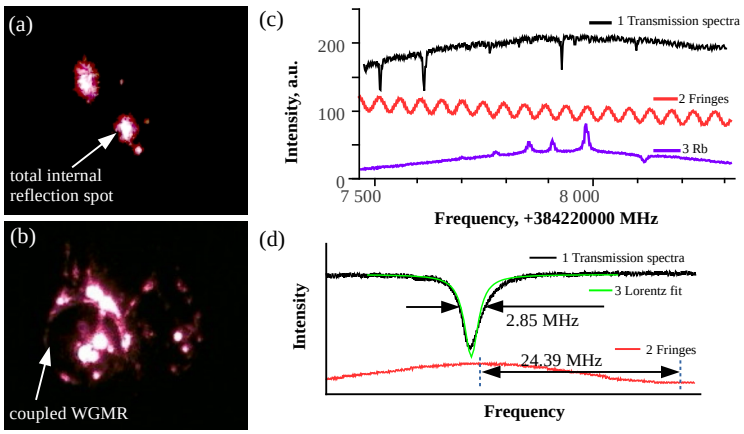

Figure 3.22: Coupling WGMR for characterization: (a) the total internal reflection spot on the surface of the prism could be seen in camera (second visible bright spot is the beam entering the prism); (b) the WGMR had to be aligned with the total internal reflection spot; (c) recorded transmission spectra and reference signals; (d) the FWHM was found by approximating the WGM resonance peak with Lorentz function for Q factor.

The coupling was achieved as the laser beam underwent total internal reflection inside the prism (see Fig. 3.22 a) and created an evanescent field. The WGMR was aligned with the total internal reflection spot on the surface of the prism (see Fig. 3.22 b), which was visible in the camera. The resonator was positioned using the X-Y-Z translation stage. The transmission spectrum of the signal was recorded using an oscilloscope (see Fig. 3.22 c). Two reference signals were used for calibration. The fringes were used to calibrate the frequency and Rb peaks to determine the absolute frequency. The measured FWHM of the WGM resonance was used to calculate the Q factor (see Fig. 3.22 d). It was used to appraise the fabricated resonators and any coating coated on the surface. For coated resonators, they were first characterized as bare-WGMRs. For clean high Q resonators, the surface was dark as no shining was detected. After coating the resonances were broader and the Q factor lower. The coating could be seen in the camera as it scattered light. For some coated resonators, for example, coated with ZnO, GOx, no resonances in the air were detected. In many cases, liquid helped with the ability to see WGM resonances for the characterization. These samples had to be characterized using the setup described in detail in Section 3.4.2 while submerged in a drop of PBS.

3.5.2 *Testing Sensor Response*

To test the sensor response of the coated WGMR samples an experimental setup described in Section 3.4.2 was used. 780 nm ECDL laser was coupled inside the resonator using GGG prism coupling which has a higher index of refraction than glass prism. The coupling prism and a small Teflon tub to hold the liquid was mounted on a Peltier element. WGMRs are very sensitive to temperature changes, therefore, temperature stabilization was crucial. Temperature stabilization was set a couple of degrees below room temperature to slow down the evaporation of liquid drop.

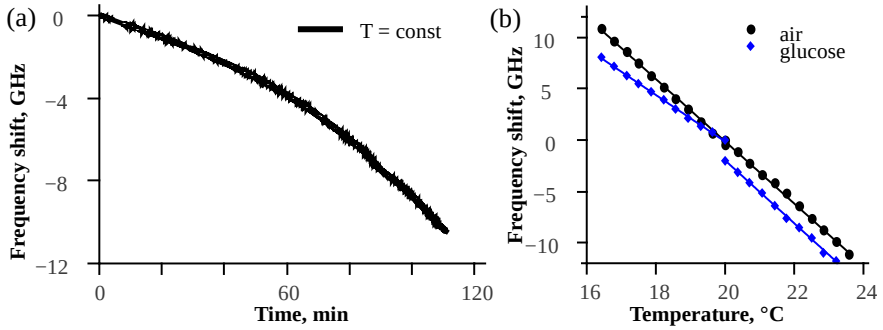

Figure 3.23: Glucose drop evaporation influences the frequency shift as the index of refraction changes: WGM resonance shift of a microsphere resonator inside a 5% glucose droplet (a) at constant temperature as the water evaporates in time and (b) changing the temperature from 20°C to 25°C and from 20°C to 15°C.

When performing testing inside liquid drop evaporation was an important effect (see Eq. 3.1). The evaporating water from the droplet changed the concentration of the surrounding medium. This shifted the WGM resonance position significantly as more liquid evaporated in time (see Fig. 3.23 (a)) when the temperature was stabilized. WGM resonance shift from temperature effects and evaporation stacked on top of each other. The evaporation impacted the temperature scanning by slowing down the WGM shift when heating the sample when the resonance shift from both effects was in opposite directions and speeding up when cooling (see Fig. 3.23 (d)).

WGM resonance signals were first found in the air by aligning the resonator with the total internal reflection spot on the surface of the prism visible in the camera with the resonator. Next, a drop of PBS (40 – 75 µL) was deposited on the resonator. Then the same volume of test probe was added. The WGM resonances for coated WGM resonators were observed in time. The data of Rb line position and a resonance peak were recorded every second using LabVIEW software. The measurements lasted for 10-15 minutes because the drop evaporation was a long process and sensor response a fast process. The

WGM resonance shifted in time. A rapid exponential resonance shift occurred for the first couple of minutes due to the temperature difference of the liquid and stabilization temperatures. The exponential signal could be mathematically subtracted from the data. The signals were fitted using a function:

$$d\omega = \omega_0 + A \cdot \exp(-t/\tau) + B \cdot t, \tag{3.6}$$

which consisted of an exponential part $\omega_0 + A \cdot \exp(-t/\tau)$ for frequency shift $d\omega$ from temperature in time t and a linear part $B \cdot t$ for evaporation and sensor response $B = B_{sens} + B_{evap}$.

A new set of measurements together with control measurements were recorded. The control measurements were important to eliminate the possibility of the WGM resonance shift due to other effects besides the sensor response.

3.6 WGM RESONATOR CHARACTERIZATION

The WGMR microspheres both bare and coated were characterized by finding the Q factor. For characterization, the WGM transmission spectra were recorded together with calibration signals.

3.6.1 *Bare WGM Resonators*

Microsphere WGMRs fabricated from the optical fiber had the Q factor of $10^6 - 10^8$. One resonator can have many Q factors as different mode groups have slightly varied coupling conditions. Only the best found Q factor was used for characterization because it was closer to intrinsic Q of the WGMR. Few bare WGMR samples with Q factors lower than 10^6 were discarded. The Q factor of 60 different microsphere samples from batches fabricated on different days can be seen in Fig. 3.24a. It shows that approximately a third of the samples had a Q factor 10^6 and a quarter of the samples had a Q factor 10^8. The measured Q factor of some samples may be higher due to the effect of over-coupling.

As the fabrication method was upgraded with more automated steps the ratio of the resonators with Q factor 10^8 was improved. About half of microspheres fabricated on the same day had very high Q factors (see Fig. 3.24b).

3.6.2 *Glucose Sensor*

Au NPs increase the sensitivity of the sensor. GOx makes the sensor selective and sensitive to the glucose in a liquid drop, therefore, it is considered a glucose sensor.

A WGM microsphere resonator coated with Au NPs and GOx was first characterized right after fabrication as a bare-WGMR. The diam-

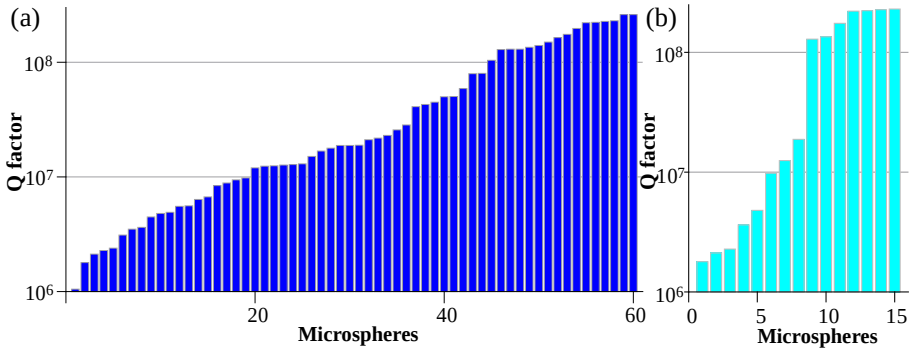

Figure 3.24: The Q factor of fabricated microsphere resonators: (a) 60 samples from different batches fabricated on different days while evolving the fabrication method with only a quarter having the Q factor 10^8 (arranged in ascending order) and (b) 15 samples from the same batch with half of the resonators with Q factor 10^8 after improving the fabrication process and reducing the number of manual steps.

eter was detected using a microscope (see Fig. 3.26 a) and the Q factor of $1.4 \cdot 10^8$ was found using the test system described in section 3.4.1 from the recorded transmission spectrum (see Fig. 3.26 b curve 1). The resonator surface could be seen in the camera (see Fig. 3.26 c). As expected for bare-WGMR the visible surface is dark and scatters very little light.

After dip coating the bare-WGMR in the solution containing Au NPs, the characterization was repeated. The individual nanoparticles could be seen while the light was coupled inside the resonator (see Fig. 3.26 d). The Q factor was lower than before the modification - only $2 \cdot 10^6$. (see Fig. 3.26 b curve 2).

The changes of WGMR and WGMR/Au-NPs optical response as it was dipped in Au solution multiple times are shown in Fig. 3.25. Forming of WGMR/Au-NPs resulted in the decrease of the Q factor (see Fig. 3.25 a). The intensity of excited WGM resonances dropped proportionally to the concentration of Au NPs, deposited on the WGMR surface (see Fig. 3.25 b).

When the GOx was coated on the WGMR/Au-NPs the resonator scattered light from the whole surface as seen in the camera during coupling (see Fig. 3.26 e), however, no resonances were detected in the air (see Fig. 3.26 b curve 3). Therefore, the test system described in section 3.4.2 was used for characterization. The measurements inside a liquid drop of the buffer solution were successful. The observed WGM resonances had the $Q = 6 \cdot 10^5$ (see Fig. 3.26 b curve 4). WGMR/Au-NPs/GOx structure was suitable for further measurements as sensor testing was performed in liquid environment only.

Adding each layer on WGMR surface reduced the Q factor. WGMRs with a higher Q factor were more sensitive. However, for sensor test-

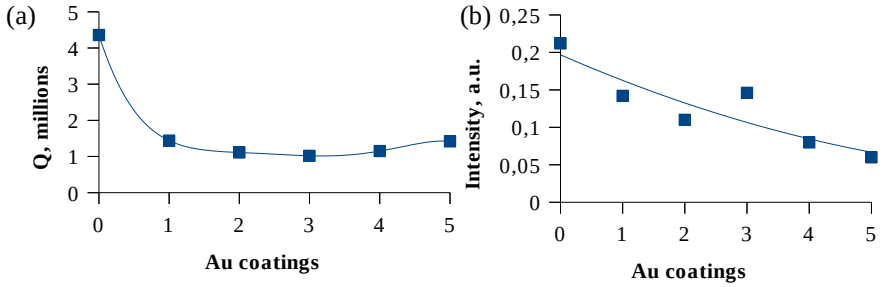

Figure 3.25: The changes of WGMR and WGMR/Au-NPs optical response dependent on the Au NP concentration: (a) dip-coating the same WGMR with Au NPs multiple times the Q factor noticeably dropped after the first coat and (b) the intensity of the resonances decreases rapidly.

ing, it was determined that the intensity of the WGM resonance was more important than how broad they were.

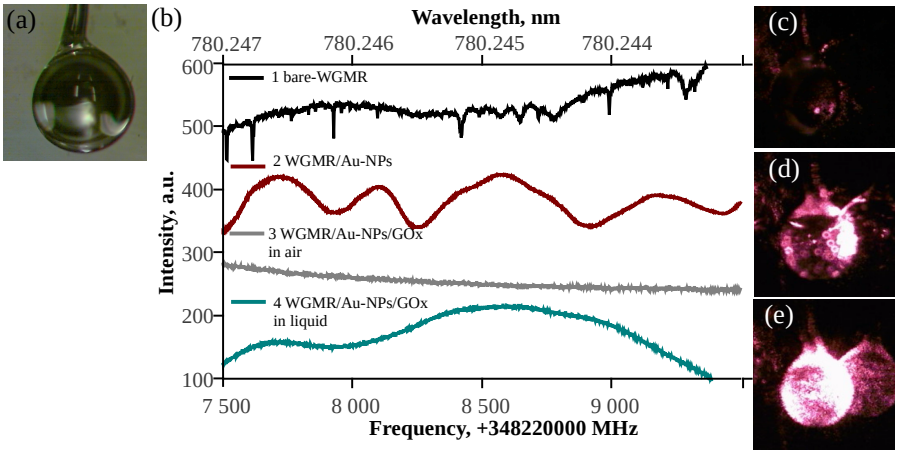

Figure 3.26: Glucose sensor characterization: (a) the diameter of the resonator was 634 μm; using the WGM resonance spectra (b curve 1) the Q factor of bare-WGMR was found and (c) surface of the resonator recorded during coupling; after coating the resonator with Au NPs (d) individual nanoparticles could be seen on the WGMR/Au-NPs and the resonance were broader (b curve 2); when the GOx was coated on the surface (e) it scattered light from the whole surface and WGMR/Au-NPs/GOx no resonances were detected for WGMR/Au-NPs/GOx in the air (b curve 3), the resonances were detected in a liquid drop of PBS (b curve 4).

3.6.3 *Toxin Sensor*

An important layer for the toxin sensor was the ZnO. It helped other proteins to adhere to the surface. An antigen BLV participated in the antigen/antibody reaction needed for detection. The BSA protein layer was used to prevent non-specific adsorption of proteins. Both of the layers ZnO and proteins needed to be characterized to avoid wasting time and coating samples with too weak WGM resonances.

3.6.3.1 *ZnO*

ZnO coated resonators were characterized using the same test system as described in section 3.4.1 and finding the Q factors.

ZNO NANORODS No WGM resonances were observed for ZnO nanorod coatings, therefore characterization with WGM resonances was not possible.

ZNO NANOLAYER WGMRs with ZnO nanolayer thicknesses of 5, 10, 20, 50, and 100 nm were characterized by exciting the WGM resonances and calculating the Q factors. For each sample, 2-4 WGM resonances were fitted by the Lorentz function and used to calculate the Q factor. In total 25 different samples were investigated and the average Q factor for each thickness was found.

Bare-WGMRs had quality factors of about $6 \cdot 10^6$. After deposition of the ZnO nanolayers over WGMRs resulted in the decrease of Q factor (see Fig. 3.27 a). The thickness of the ZnO layer played a significant role in the Q factor value. When coupling the light inside the WGMR the surface was visible in the camera (see Fig. 3.27 b). The WGMR/ZnO surface scatted light like a bright bulb. It was found that the Q factor improved in the WGMR/ZnO system for the thickness of 5-20 nm of the ZnO ALD layer. If the coating was too thin or too rough, it acted more as a surface defect and increased the surface scattering, and as a consequence lowering the Q factor. The Q factor reached the maximal value for 10-20 nm of ZnO. Further increase of the ZnO coating thickness led to a decrease of the Q factor value. For 50 and 100 nm thickness, the Q factor drop when compared with bare-WGMR was significant.

For comparison simulations were obtained using COMSOL Multiphysics software for different ZnO thicknesses. In the model, the silica glass microresonator had a diameter of 10 μm with refractive index n_{SiO_2} = 1.4585. The resonator was coated with varying thickness of the ZnO layer with refractive index n_{ZnO} = 2.0034. The area around the resonator had a refractive index n_{air} = 1 representing the air. The main simulations were performed for the distribution of the z-component of the electric field circulating inside the resonator. The same fundamental mode for different thicknesses of the ZnO layer

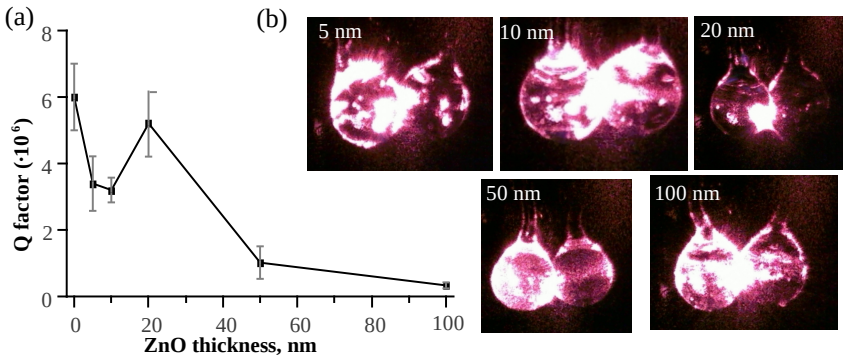

Figure 3.27: The WGMRs coated with ZnO ALD layer: (a) the Q factor dependence on the ZnO ALD layer thickness, the optimal layer thickness about 20 nm; (b) the surface of the WGMRs during coupling for different layer thicknesses.

was used to examine the cross-section of the electrical field's intensity. A strong fundamental WGM resonance was observed. It can be seen that with the increase of the layer thickness the peak of the resonance mode moved towards SiO_2 - ZnO boundary (see Fig. 3.28 a). For the thicker layers (d > 50 nm), the WGM resonance peak was located inside the ZnO coating. Contrary to the experimental results, the Q factor for thicker layers with higher increased because the light in the resonator was better confined by the higher refractive index of ZnO.

To make a more realistic simulation the upper surface of the ZnO layer was distorted. A randomized function was used to make a rough ZnO boundary with air which increased the losses due to surface scattering observed in experiments. In simulations, less than 40% of the light was transmitted. For the 100 nm layer, the depth of surface roughness was 30 nm. The electric field intensity decreased by 30% in the case of the rough surface for the electric field intensity cross-section (see Fig. 3.28 b).

Two competing phenomena were observed in ALD ZnO nanolayers, deposited on WGM resonators: increase of refractive index due to improvement of ZnO crystallinity [73] and enhanced light attenuation with ZnO nanolayer thickness increase. As a result, a maximum Q factor was observed at ZnO thickness of 20 nm. The experimental results correlated with simulations pointing to the increase of Q factor due to higher light trapping into thicker coatings and Q-factor suppression by light scattering due to surface roughness.

The WGMRs coated with ZnO using the ALD method were good. The whole surface was covered in a ZnO layer and the thickness could be controlled. However, special equipment is necessary to use the method, furthermore, it was time-consuming. A cheaper and faster

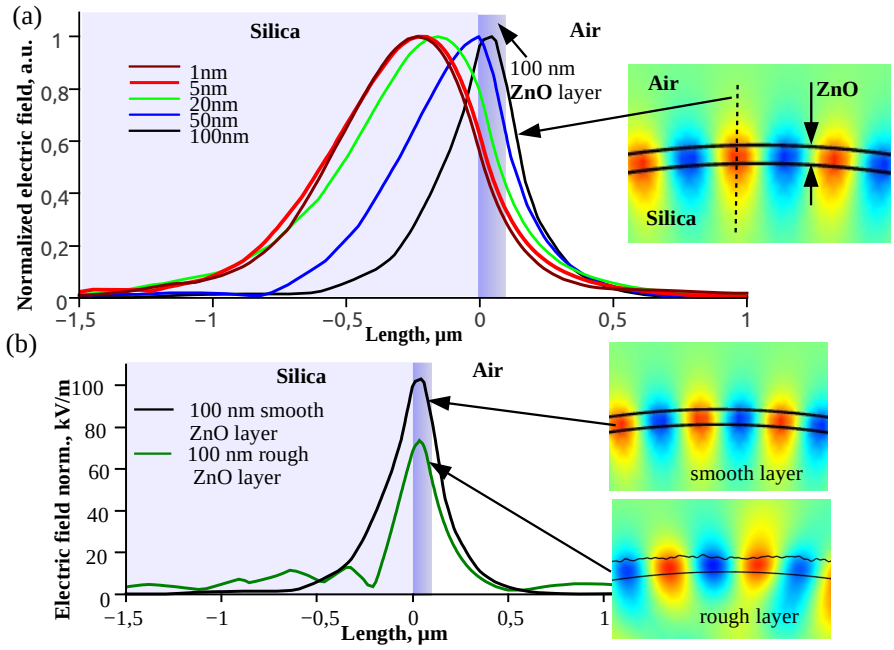

Figure 3.28: The simulation of ZnO coated WGM resonators: (a) intensity cross section in SiO_2/ZnO/air boundary for different thicknesses of ZnO coating; (b) electric field intensity cross-section in SiO_2/ZnO/air, coated with 100 nm layer of ZnO for a smooth and a rough boundary.

method was necessary to make many samples in bulk for the biotesting stage of the toxin sensor.

ZNO NANOCRYSTALS The Q factors of WGMRs coated with ZnO using the drop-coating method were typically $10^5 - 10^6$ (see Fig. 3.29 a) - lower than with the ALD method. Additionally, only about 50% of drop-coated WGMR samples were good enough to excite and record WGM resonances. Some resonators had WGM resonances only in liquid environment (see Fig. 3.29 b). Best samples of WGMR/ZnO with strong resonances in the air were selected for further functionalization with Au particles and proteins.

3.6.3.2 *Gold Particles*

The main issue of toxin sensor development was the addition of other layers on top of the WGMR/ZnO structure to obtain WGMR/ZnO/Au. A few Au coated resonators had visible WGM resonances, however, only in the liquid drop setting. The Q factor of the WGMR/ZnO/Au structure was 10^5 (see Fig. 3.30 a). The low success rate led to the discarding of the Au layer from the toxin sensor structure altogether.

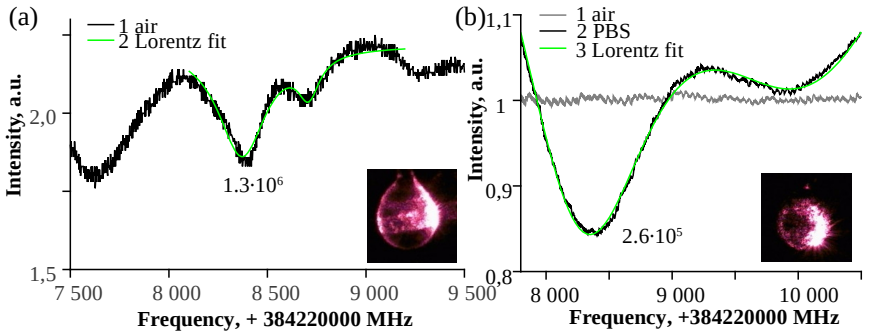

Figure 3.29: The characterization of WGMRs coated with ZnO using drop method: (a) WGMR/ZnO sample with strong resonances in air and $Q = 1.3 \cdot 10^6$; (b) WGMR/ZnO with weak resonances only in liquid drop of PBS $Q = 2.6 \cdot 10^5$.

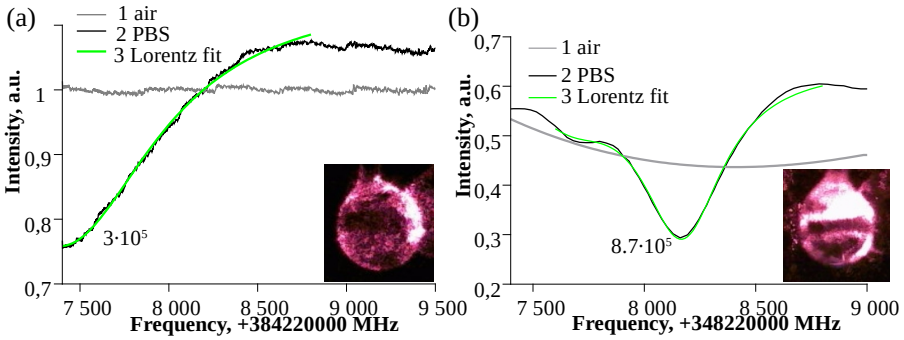

Figure 3.30: The characterization further functionalized ZnO WGM resonators: resonances observed only in liquid environment for (a) WGMR/ZnO/Au structure and (b) WGMR/ZnO/BLV/BSA structure.

3.6.3.3 *Proteins*

The WGMRs coated with ZnO were used as the surface for the proteins antigen BLV and BSA to attach. A similar problem as with WGMR/ZnO/Au was observed with samples WGMR/ZnO/BLV/BSA for toxin detection. The Q factor of the toxin sensor WGMR/ZnO/BLV/BSA structure was 10^5 (see Fig. 3.30 b). The resonances were observed only in the liquid drop of PBS. Samples with the strongest WGM resonances were tested for sensor response by adding the probe with antibodies for BLV to the liquid.

3.7 WGMR SENSORS

All sensor responses of WGMR samples were tested in a liquid environment. The WGM resonance position in time was recorded and further processed. The effects of temperature and evaporation of liq-

uid drop were vital for the interpretation of the results. Different control measurements were performed to understand the role of each functionalization layer coated on the surface of the WGMR sensor.

3.7.1 *Glucose Sensor*

To test for the sensor response the WGMRs had to be temperature stabilized. It was necessary to eliminate the resonance shift due to the change of room temperature as the WGM resonance shifted for more than 2000 MHz per 1°C. To minimize the evaporation the stabilization temperature was chosen below the room temperature. The drops of 75 µL of buffer solution and 75 µL of known glucose concentration solution were at room temperature. As a result, all signals had an exponential component from the thermal effect which had to be mathematically subtracted. This could be avoided by matching the temperature of the liquid to the stabilization temperature before adding it to the Teflon tub and the WGMR sample.

The WGM resonance shifted due to the glucose – GOx reaction and also depended on the concentration of the glucose sample. If the intensity of the WGM resonance signal was low and multiple WGM resonances were detected, the recorded signal was noisier.

The resonance shift observed in the case of WGMR/Au-NPs/GOx resonator after the incubation in glucose-containing solution is related to several main processes:

- the temperature difference of the solution drop and the stabilization temperature,
- the evaporation of water from the solution drop,
- glucose – GOx chemical reaction,
- charge transfer during GOx-catalyzed reaction from glucose towards Au-NPs.

Multiple control measurements were performed to test the glucose sensor samples.

3.7.1.1 *Sensitivity Enhancement Using Au NPs*

The Au NPs extended the evanescent field around the WGM resonator with localized surface plasmon resonances and, thus, increased the sensitivity. Comparing the WGMR/Au-NPs/GOx based resonator with WGMR/GOx the WGM resonance shift was recorded (see Fig. 3.31 a and b). The exponential temperature component was mathematically subtracted for data analysis (see Fig. 3.31 a and b inset). For control samples, the shift was larger when Au-NPs were coated on the WGMR compared to samples without Au-NPs when the measurements were performed in the same glucose concentration. Both

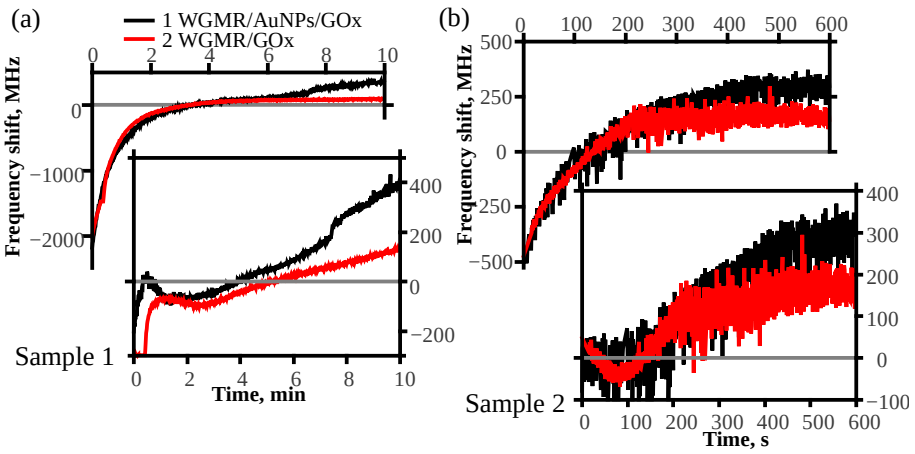

Figure 3.31: The comparison of the WGMR/Au-NPs/GOx based resonator sensor with the WGMR/GOx: (a) sample 1 and (b) sample 2 were tested in different concentration of glucose and both showed similar results - when Au-NPs were also coated (curve 1) the WGM resonances shifted more and the sensitivity of the sensor increased.

samples shown in Fig. 3.31 were tested in different glucose concentrations. For sample 1 the WGM resonance shift was about 200 MHz for WGMR/GOx and 400 MHz for WGMR/Au-NPs/GOx. For sample 2 the WGM resonance shift was about 150 MHz for WGMR/GOx and 300 MHz for WGMR/Au-NPs/GOx. The samples with Au NPs were about two times more sensitive.

3.7.1.2 *Glucose - GOx Reaction*

The WGM resonance did not shift when no GOx was coated on the sample surface. The WGMR/Au-NPs/GOx based resonator was compared with WGMR/Au-NPs based resonator (see Fig. 3.32 a and b). The exponential temperature component was mathematically subtracted for data analysis (see Fig. 3.32 a and b inset). The test confirmed that without GOx both WGMR/Au-NPs samples 1 and 2 were insensitive towards the glucose in the drop. Sample 1 and 2 were tested in different glucose concentrations.

Another important control measurement was done to investigate the glucose - GOx reaction. It was performed by using WGMR/Au-NPs/GOx sample and testing in liquid drop without glucose. The measurement was performed in two 75 µm drops of PBS. The observed response comparison can be seen in Fig. 3.33 a.

The reverse direction of the exponential part was due to the PBS which was removed from the fridge and used before reaching room temperature to perform the measurement. The WGMR/Au-NPs/GOx WGM resonances did not shift when the glucose was not present.

This confirmed the sensor response WGM shift was initiated by the glucose - GOx reaction.

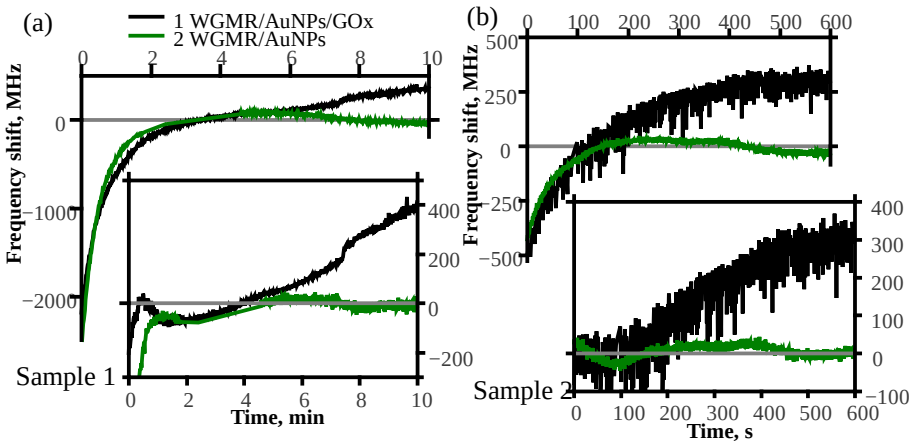

Figure 3.32: The comparison of the WGMR/Au-NPs/GOx based resonator sensor with the WGMR/Au-NP: (a) sample 1 and (b) sample 2 were tested in different concentration of glucose and both showed similar results - when GOx was coated on the WGM resonator (curve 1) the WGM resonance shifted while testing inside a glucose drop but without GOx (curve 2) no shift was observed.

3.7.1.3 *Glucose Concentration*

The response of WGMR/Au-NPs/GOx-based sensor for several glucose concentrations is presented in Fig. 3.33 b. The shift velocity of the WGM resonance shift of WGMRs increases when the glucose concentration increases. The dynamic range for the concentration region of the glucose sensor is limited by the relatively low Michaelis constant of GOx, which is in the range of 1 - 2 mM [74]. This limitation illustrates that WGM-shift based analytical signal of the WGMR/Au-NPs/GOx based sensor is clearly determined by GOx action.

3.7.2 *Toxin Sensor*

To test the toxin sensor the testing sensor for liquids was used. The WGMR/ZnO/BLV/BSA was attached to the X-Y-Z translation stage and laser light was coupled inside to observe the WGM resonances in the air. A 50 µL drop of PBS was added and the coupling position adjusted to see resonances if necessary. The 50 µL drop of Probe containing the 'BLV-positive' cattle serum containing antibodies against the BLV proteins (see Fig.3.34 a). The probe had a known concentration (1:10, 1:100) of antibodies diluted with the physiological solution of NaCl. WGM resonance shift was recorded in time. As the anti-

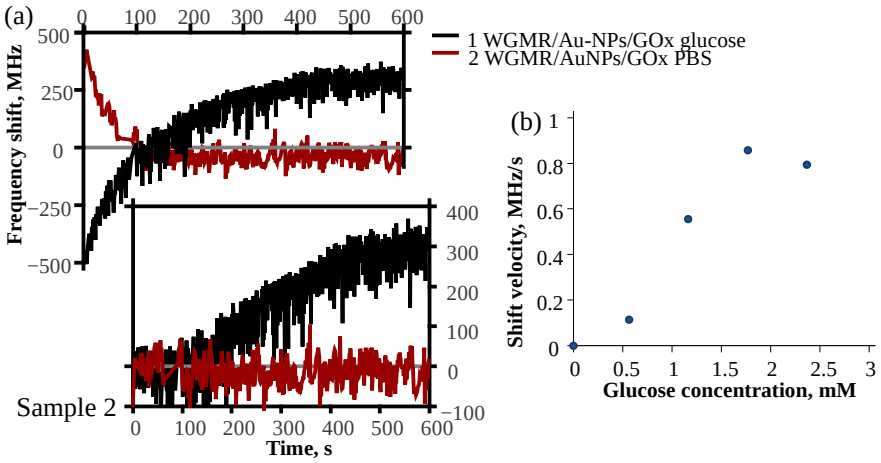

Figure 3.33: The response of WGMR/Au-NPs/GOx-based sensor for several glucose concentrations: (a) the comparison of the WGMR/Au-NPs/GOx based sensor response in glucose drop ($c > 0$ curve 1) and PBS drop ($c = 0$ curve 2), no WGM resonance shift was observed when testing without glucose; (b) the WGM shift velocity for different glucose concentrations.

gens attached to the antibodies the WGM resonances shifted. From the recorded resonance signal the temperature effects were mathematically subtracted. The resulting sensor response for 1:10 and 1:100 'BLV-positive' can be seen in Fig.3.34 b.

A "break" can be seen in the resonance shift speed. For the first 300 - 400 s, the WGM resonance shifted faster. It was assumed that the sensor response was detected in this section of resonance shift. However, additional control measurements need to be performed for verification with other probe concentrations and BLV-negative probes. As the antigen/antibody reaction concluded, the WGM resonance shift speed changed and liquid evaporation dominated. For the probe 1:10 with higher antibody concentration the shift the liquid evaporation was much slower than for probe 1:100.

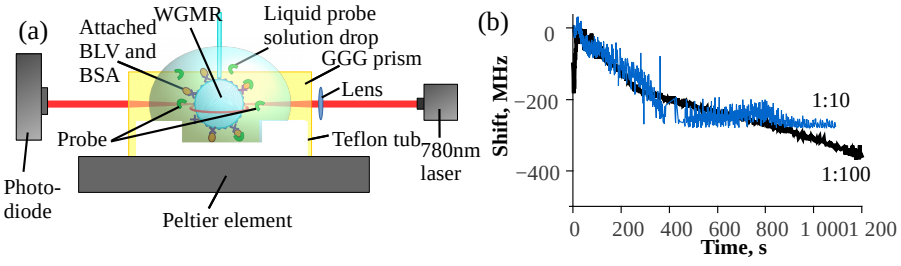

Figure 3.34: The testing of the toxin sensor WGMR/ZnO/BLV/BSA: (a) the scheme of the testing in a liquid probe drop containing BLV antibodies; (b) the WGM resonance shift in time for two different probe concentrations (1:10 and 1:100) shows sensor response.

One test was performed with WGMR/BLV/BSA sample, lacking the ZnO layer. It had no "break" in the WGM resonance shift speed leading to the belief that the proteins did not effectively attach to the bare-WGMR surface. Additional control tests are still necessary with different structure variations to determine the effects and the necessity of each functionalizing material.

Even though sensor response was observed, extensive testing was not performed. A crucial drawback in the fabrication and testing of the toxin sensor was the relatively low success rate of usable WGM-R/ZnO samples. Only about 50% were good enough for further functionalization. Taking into account that even more samples were unusable after adding BLV and BSA layers the overall fabrication method had to be improved first.

4

WHISPERING GALLERY MODE RESONATORS FOR FREQUENCY COMBS

4.1 OPTICAL FREQUENCY COMB

Fourier transform can be written as:

$$F\{g(t)\} = G(f) = \int_{-\infty}^{\infty} g(t)e^{-i2\pi ft} \quad (4.2)$$

The optical frequency comb spectrum consists of equidistant spectral lines. This type of spectrum is associated with ultrashort pulses emitted at regular intervals [31]. Using the Fourier transform of the signal $g(t)$ in the time domain where the signal amplitude is seen over the time to the main events $G(f)$ in the frequency domain are acquired by counting how many times each event occurred during the observation (see Fig. 4.1).

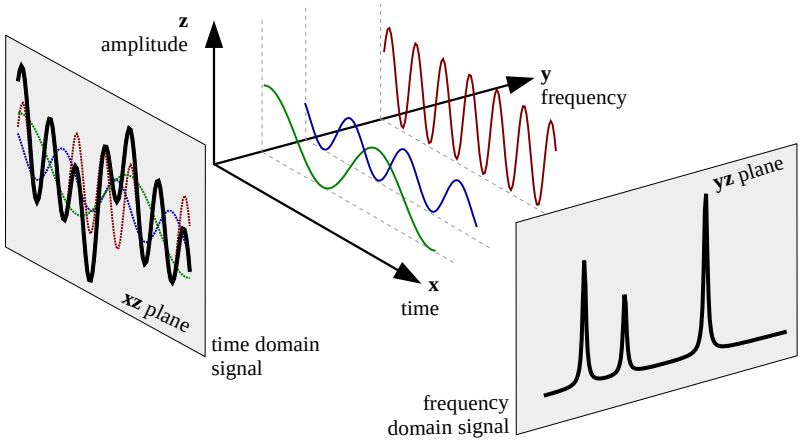

Figure 4.1: Representation in 3D space the projections of 2D time domain and frequency domain: if in the 3D space the amplitude is on the x-axis, on the y-axis the frequency and on the Z-axis the amplitude, then in the 2D space xz is the time domain and yz is the frequency domain.

4.1.1 *Frequency Comb Generation*

From the Heisenberg Principle of Uncertainty $\Delta x \Delta p \geqslant \frac{\hbar}{2}$, which indicates that particle location and momentum cannot be accurately measured at the same time, since we are irreversibly acting on the particle during measurement, and this interaction changes its other related parameters. Given the dual nature of light, Heisenberg's uncertainty can also be written in the form $\Delta E \Delta t \geqslant \frac{\hbar}{2}$. The shorter the

laser impulse, the more inaccurate we can determine its energy and frequency.

In the case of a uniform series of wave pulses separated by a fixed time interval T (see Fig.4.2 (a)), the spectrum can easily be obtained by means of the Fourier series, resulting in a comb-like structure with regularly spaced frequency teeth (see Fig.4.2 (b)). The spacing of the comb teeth, or repetition rate, is inversely proportional to the time between pulses [75]:

$$f_{rep} = \frac{1}{T}. \tag{4.3}$$

Successive pulses interfere with one another and constructive interference occurs only at frequencies where n_{rep} is an integer. Offset frequency can be between 0 and f_{ref}. Frequency comb offset is related to the phase shift between successive laser pulses. This phase shift in a pulse sequence occurs because the phase and group velocities are different [75]:

$$f_o = \left(\frac{\Delta\phi_o}{2\pi}\right) f_{rep}. \tag{4.4}$$

The phase velocity shows how the wave phase propagates in space, that is, the velocity at which all the frequency component moves. Group velocity is the rate at which a wave packet or wave amplitude modulation propagates through space.

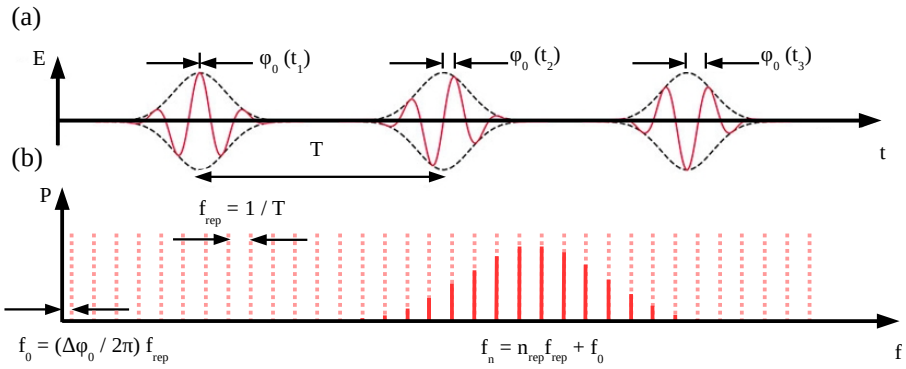

Figure 4.2: Frequency comb (a) generated using uniform series of ultrashort pulses (b) resulting in a comb-like structure with regularly spaced frequency teeth.

Octave-wide combs technology allows self referencing by finding the offset frequency. The frequency of the n-th line, where n_{rep} is the integer tooth number, can be calculated as $f_n = n_{rep} f_{rep} + f_0$ and for the 2n-th line as $f_2 n = 2n_{rep} f_{rep} + f_0$. If the n-th line is passed through a crystal that doubles the frequency, then $2f_n = 2(n_{rep} f_{rep} + f_0)$. All that remains is to measure the difference between the doubled frequency and the comb line of the 2n-th frequency [31, 75]:

$$2(n_{rep}f_{rep} + f_0) - (2n_{rep}f_{rep} + f_0) = f_0. \tag{4.5}$$

BEAT NOTE Unknown frequency can be found measuring a beat note - the difference in frequency between the unknown laser frequency and the comb frequencies. To observe the beat note (f_b), the following conditions must be met [76]:

- light field vectors must overlap;
- polarization states must not be orthogonal;
- difference in optical frequency must be within the range of sensitivity of the detectors;
- laser wavelengths must be within the sensitivity range of the detector.

The laser frequency can be calculated:

$$f_{laser} = n_{rep}f_{rep} \pm f_o \pm f_b. \tag{4.6}$$

The corresponding "+" or "-" sign depends on the experimental conditions and can be determined by changing the repetition rate - distances between the frequency comb teeth -, the offset frequency - sliding all the frequency comb teeth simultaneously - and observing how the beat note frequency changes (see Fig. 4.3 a - d).

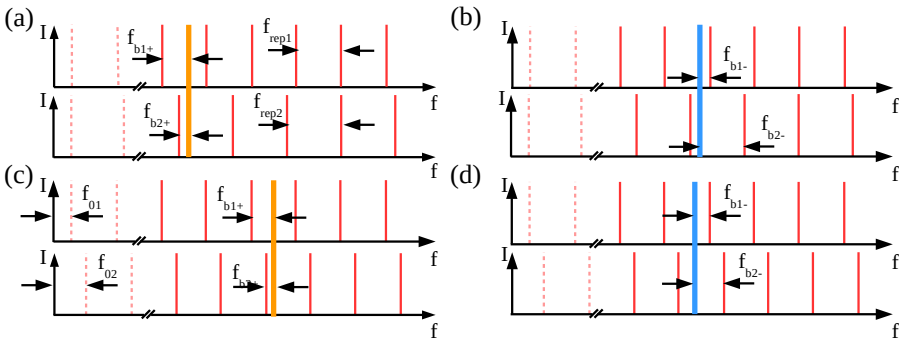

Figure 4.3: To determine the sign of the beat note the repetition frequency is changed: (a) if $f_b > 0$, when f_{rep} is increased the $f_b > 0$ decreased; (b) if $f_b < 0$, when f_{rep} is increased the $f_b > 0$ also increases. Next, to determine offset frequency sign, the reference frequency is kept constant and offset changed: c) for positive f_0 and $f_b > 0$, if f_0 is increased, f_b decreases; d) for positive f_0 and $f_b < 0$, if f_0 is increased, f_b increases.

The number n_{rep} can be calculated from the known repetition rate and the wave meter reading of the unknown wavelength:

$$n_{rep} = \frac{c}{\lambda_{laser} \cdot f_{rep}}. \tag{4.7}$$

4.1.2 *WComb*

Optical frequency combs have been demonstrated using WGMRs. Different WGMR geometries and materials have been used to generate the WCombs. The first report of the Kerr-nonlinearity induced optical four-wave mixing parametric oscillation was published by T. Kippenberg et al. [77] in a toroidal silica microcavity in 2004. The Q factor of the resonator was 10^8, the diameter 67µm, and the pump laser wavelength 1565 nm. The same year the effect was also observed in CaF_2 microdisks by A. Savchenkov et al. [78] using a 1.32µm laser. Cubic nonlinearities for CaF_2 are smaller than fused SiO_2 but due to the Q-factor being an order of magnitude higher it is sufficient to observe side-band generation. In silica microspheres, the side-band generation was observed by I. Agha et al. [79]. The Q factor of the microspheres was 10^7, the diameter 150µm, and the laser wavelength 1543 nm.

First broadband parametric frequency combs were reported by P. Del'Haye et al. [80] in a 75µm diameter monolithic toroid microcavity when pumped at 1550 nm. In a 5 mm diameter CaF_2, the first broadband comb was reported by I. Grudinin et al. [81] when pumped at 1560 nm. The broadband comb was also reported in an integrated Si_3N_4 microring with a Q factor 10^5, 58µm diameter when pumped at 1550 and 1560 nm by Levy et al [82].

In silica microspheres, frequency comb generation is reported by several groups.

N. Risen et al. [35] inspected several materials for optical frequency comb generation in microspheres. The zero-dispersion wavelength was a function of the diameter of the sphere for all materials discussed. For silica microspheres to generate the comb using 1550 nm the sphere size was around 150 µm.

K. E. Webb et al. [83] were using a 250 µm microsphere with $Q = 3.7 \cdot 10^7$.The microsphere was pumped with 1550 nm and 80 mW laser to generate the comb.

S. Zhu et al. [84] were using a 248 µm microsphere with $Q = 2.1 \cdot 10^8$ and pump $\lambda = 1548.45$ nm and a 139µm microsphere with $Q = 3.5 \cdot 10^8$ and pump $\lambda = 1553.7$ nm. The pump power is increased from 0.527 mW to 1.52 mW and from 0.191 mW to 0.656 mW respectively.

A.V. Andrianov and E.A. Anashkina [42] were using a 166 µm microsphere with $Q = 2 \cdot 10^7$ and pumped with $\lambda = 1555$ and 16 mW to generate a comb with 400 GHz FSR that matches every fourth channel used for telecommunications.

4.1.3 *Generating WComb*

A frequency comb can be generated using four-wave mixing in whispering gallery resonators. The advantage of this approach is in extremely high efficiency of four-wave mixing in high Q WGMRs, and the small size of the resonator allows for a low-power pump and is compact. A delicate double balance has to be achieved. First, the power gain in the WGMR cavity has to compete with various losses. The amplification is achieved through the nonlinear process of degenerate and non-degenerate four-wave mixing. Second, the normal dispersion in the WGMR material has to be combated by the Kerr effect to aid the soltion generation. It is easier to achieve the comb generation in the anomalous dispersion case than in the normal dispersion case. A parameter that can be controlled in the experiments is the pump laser frequency which can be either red detuned or blue detuned.

4.1.3.1 *Dispersion*

Dispersion is the dependence of the the refractive index on the frequency, as in a transparent optical medium the propagating light interacts with electrons of the medium [85]. It is an important phenomenon for microresonator frequency comb generation. The dispersion can be defined as normal dispersion and anomalous dispersion. It impacts the propagation of pulses as the frequency components of the pulse bandwidth following from the quantum mechanical uncertainty in the energy E and finite impulse. In the case of normal dispersion, the components of higher frequency propagate slower thus broadening the pulse (see Fig. 4.4 a). In the case of anomalous dispersion, the pulse is also broadened or chirped in the opposite manner (see Fig. 4.4 b).

KERR EFFECT The Kerr effect is a change in the refractive index of a material in response to an applied electric field. The optical Kerr effect occurs when an intense light propagates in the medium. This is a 3rd order nonlinear effect and the electrical field is generated due to light itself in the medium, which modifies the propagation properties of the light. The change in the refractive index can be positive or negative.

SOLITON Between the normal and anomalous dispersion is a zero-dispersion wavelength. In this region the propagation of soliton - a pulse that retains its shape as it propagates at a constant velocity in the medium (see Fig. 4.4 c) - is possible. Normal dispersion which broadens the pulse can be compensated with the Kerr effect induced anomalous dispersion which also broadens the pulse propagating in the material but the wavelength speed distribution is the opposite,

thus obtaining zero-dispersion suitable for soliton propagation (see Fig. 4.4 d).

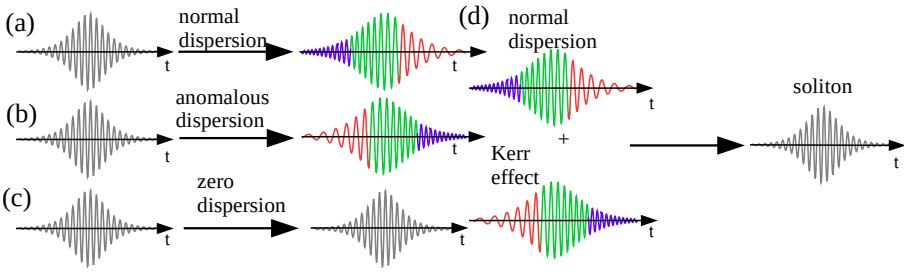

Figure 4.4: The propagation of a Gaussian pulse in an optical media where the dispersion is (a) normal - the signal broadens as shorter wavelengths propagate slower, (b) anomalous - the signal broadens as longer wavelengths propagate slower and (c) zero dispersion - the signal propagates maintaining the shape as all wavelengths propagate at the same speed; (d) normal (or anomalous) dispersion can be compensated with Kerr effect for soliton generation.

For microresonators, the total dispersion can be divided into material dispersion defined by the material the resonator is fabricated from and the geometrical dispersion - the parameters of the resonator geometry which define the optical path of the resonance [54].

MATERIAL DISPERSION The dispersion D can be calculated as the second order derivative of the refractive index n dependence from the wavelength λ:

$$D = -\frac{\lambda d^2 n}{c d\lambda^2} \tag{4.8}$$

The refractive index is given by the Sellmeier equations:

$$n^2 = 1 + \sum_{i=1}^{3} \frac{A_i \lambda^2}{\lambda^2 - B_i^2} \tag{4.9}$$

where A_i and B_i are the Sellmeier coefficients [54]. Using the Sellmeier coefficients for silica and combining the Eq. 4.9 and 4.8 the material dispersion of SiO_2 was calculated (see Fig. 4.5 a and Appx. C.1):

$$\begin{aligned} D &= -\frac{\lambda}{c}\frac{d^2}{d\lambda^2}\left(\sqrt{1 + \sum_{i=1}^{3} \frac{A_i \lambda^2}{\lambda^2 - B_i^2}}\right) = \\ &= -\frac{\lambda}{c}\sum_{i=1}^{3}\left(\frac{A_i}{(\lambda^2 - B_i^2)n} - \frac{5A_i\lambda^2}{(\lambda^2 - B_i^2)^2 n} + \frac{4A_i\lambda^4}{(\lambda^2 - B_i^2)^3 n} + \right. \\ &\qquad \left. + \frac{A_i^2 B_i^2 \lambda^2}{(\lambda^2 - B_i^2)^3 n^3} - \frac{A_i^2 B_i^2 \lambda^4}{(\lambda^2 - B_i^2)^4 n^3}\right). \end{aligned} \tag{4.10}$$

GEOMETRICAL DISPERSION The optical path of the WGM resonance is closely tied with the geometry of the resonator. Due to geometrical dispersion using various parameters, for example, resonator size, the total dispersion of the WGM microresonator can be modified. Microsphere resonators only have a single parameter - the resonator diameter - which can be modified to affect the dispersion. The zero-dispersion wavelength increased if the diameter decreased [35] (see Fig. 4.5 b). For other WGM resonator geometries, the number of parameters increases. Other spheroid WGM geometries, like the microtoroid, depend on both the diameter and the curvature diameter [54], while disk resonators are defined by resonator diameter, thickness, and the disk angle [54].

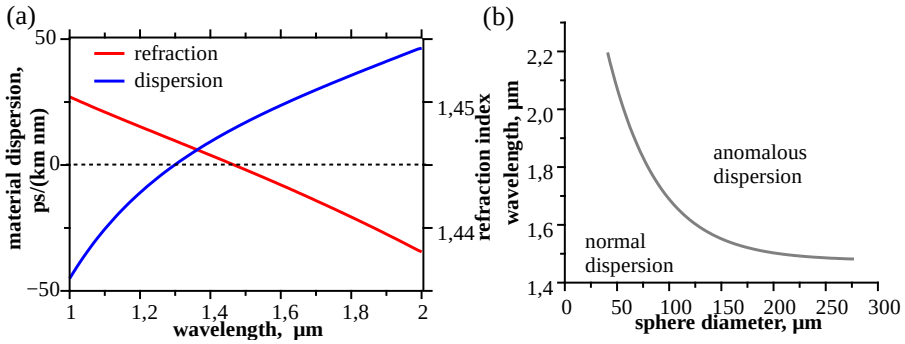

Figure 4.5: Total dispersion of silica: (a) refractive index (see Eq. 4.9) and material dispersion (see Eq. 4.10) dependence on wavelength and (b) zero dispersion dependence on microsphere diameter [35] due to geometrical dispersion.

4.1.3.2 *FWM*

Four-wave mixing is a nonlinear effect from a third-order optical nonlinearity. It can occur if at least two different frequency components propagate together in a nonlinear medium and as a result two new waves are generated (see Fig. 4.6 a). The two pump lasers with frequencies f_{p1} and f_{p2} generate frequency $f_s = f_{p2} + (f_{p2} - f_{p1}) = 2{\cdot}f_{p2} - f_{p1}$ named signal and $f_i = f_{p1} - (f_{p2} - f_{p1}) = 2{\cdot}f_{p1} - f_{p2}$ named idler [86]. The frequency f_s or f_i can be amplified. The frequency difference between pump and ideler or signal $f_{p1} - f_s = f_i - f_{p2} = \Delta f$ is the same.

If the two pump frequencies coincide $f_{p1} = f_{p2} = f_p$ it is known as a degenerate FWM and $2 \cdot f_p = f_s + f_i$ (see Fig. 4.6 b). A single pump laser can provide amplification for the signal. Two photons are taken away from the pump and put into the signal and one is put into an idler resulting in two frequency components equidistant from the pump signal.

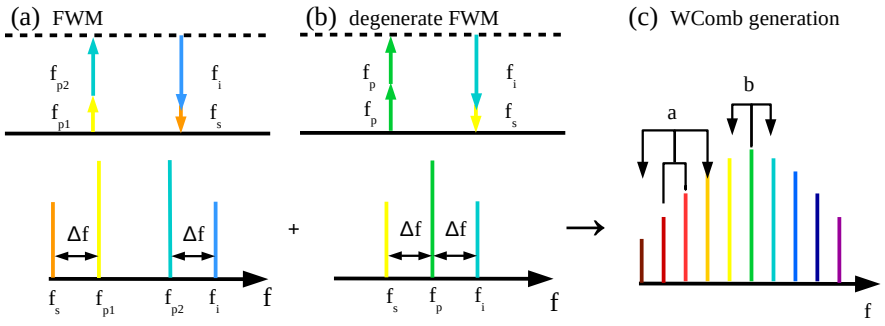

Figure 4.6: FWM in case of (a) two pump frequencies and (b) one pump frequency and (c) how both can contribute to WComb generation.

The parametric amplification by both degenerate and non-degenerate FWM is used to generate frequency comb in WGMR (see Fig. 4.6 c). First, degenerate FWM results in an equidistant signal and idler lines which can then extend spectrally in cascade through both regular and degenerate FWM generate new equidistant lines. The repetition rate equals FSR or a multiple of FSR. The FSR depends on the radius of the microresonator (see Eq. 2.17).

4.1.3.3 *Detuning*

An external pump laser provides a control device to achieve the double balance of Kerr effect and dispersion for solitons and FWM parametric gain and loss for WComb generation. The laser pump power and pump frequency detuning are readily available parameters for controlling the Kerr comb [77] generation. The pump detuning with respect to the cavity resonance frequency $\Delta = f_{pump} - f_{cavity}$ can be positive for a laser with a frequency greater than the WGM resonance frequency and is called blue-detuned or negative and therefore smaller and is called red-detuned.

Blue-detuned excitation is thermally stable at room temperature (becomes unstable in cryogenic temperatures). The resonator and laser form a feedback loop that stabilizes the laser cavity detuning. Red-detuned excitation is thermally unstable (the opposite is true than for blue-detuning) and it is required for soliton formation. The signature of soliton generation in transmission spectrum is discrete steps during pump detuning scanning [33].

The evolution of the power inside the WGMR cavity as a function of pump laser detuning is described by Herr et al. [32] and Kippenberg et al. [33]. The modulation instability evolution could be seen as the signal and idler were generated with some instability, when breather soliton was generated the amplitude of power was unstable, as multiple solitons existed in the cavity a step-like power jumps were observed during detuning. Last, the single Kerr soliton comb

state was achieved the last step before the comb generation ceased, as the laser was detuned away from the WGM resonance.

Additional effects can also shift resonant wavelength. When the power reaches the threshold the Kerr effect causes a rapid redshift of the resonance wavelength (see Fig. 4.7 a). The thermal effects induce significant changes in the cavity resonant wavelength. Immediately after the Kerr effect, the cavity is heated due to the absorption of light as the heat flows into the cavity is a function of the pump power, coupling efficiency, optical absorption and the deviation of the pump wavelength [87].

The thermo-optic effect occurs with the local temperature variation while the thermal expansion effect depends on the global temperature change [88]. The redshift of the resonance will occur after the temperature rises for materials with the positive thermo-optic coefficient (see Fig. 4.7 a). Therefore, the detuning needs to compensate for the shift introduced by both the nonlinear effects and the thermal effect for materials with positive thermo-optic effect to meet the Kerr comb generation conditions [89]. The adjustment of the laser scan speed was critical for the system to achieve the thermal equilibrium necessary for the generation of the soliton state [88]. The soliton state can be achieved in SiO_2 microcavities but the process is difficult. The combs obtained in the thesis were in Turing rolls and modulation instability mode. Solitons could not be obtained. Zhu et. al. [84] observed the Kerr comb teeth did redshift as the power of light introduced to the stem of the silica microsphere heated the resonator.

For materials with negative thermo-optic effect the resonance is blue-shifted (see Fig. 4.7 b). The blue shift plays the same role as the laser scanning. Therefore, in CaF_2 microcavity the soliton state can be obtained automatically without a laser scan [88]. Scanning towards a longer wavelength is required when the thermal expansion effect is dominant over the thermo-optic effect.

The laser pump power is a second parameter that can be controlled. In the experiments by Karpov et al. [34] the generation of WCombs was observed at both relatively low pump powers where soliton crystal states (PSC) - a set of solitons distributed evenly on the resonator circumference - were achieved and at high pump powers where only multiple-soliton states with a structured spectrum and irregular soliton arrangements formed. The advantage of lower pump powers and PSC states is that the comb power is distributed in a few comb lines [34].

4.1.4 *Applications of WComb in Communications*

Optical frequency combs have many applications in optical clocks, spectroscopy and communications [36–40]. WCombs are being ex-

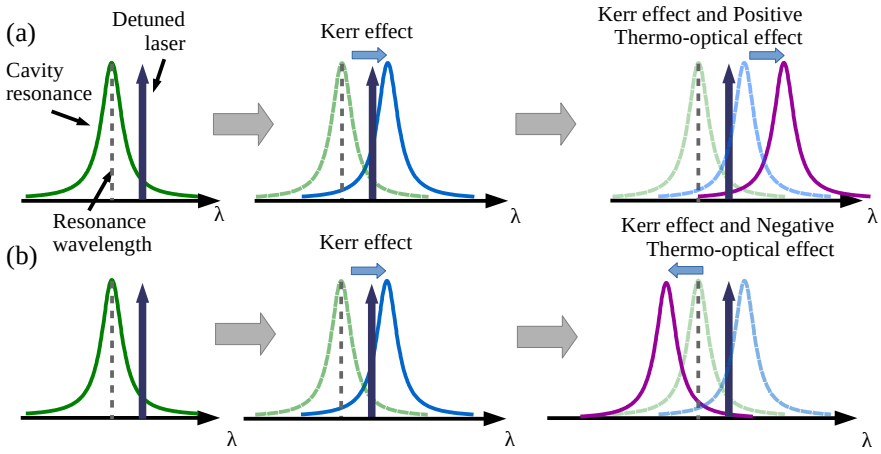

Figure 4.7: The shift of WGM cavity resonance (a) red shift due to the Kerr effect alone, and the Kerr effect and a positive thermo-optic effect [89], for example, in silica, (b) red shift due to the Kerr effect and blue shift of the cavity resonance caused by a negative thermo-optic effect [88], for example, in CaF_2.

plored for tradeoffs such as stability versus power consumption, cost, and size to provide miniature frequency comb systems.

WDM DATA TRANSMISSION A wavelength-division multiplexing (WDM) system uses a multiplexer to combine multiple optical wavelength signals together for the data to be sent simultaneously over one single optical fiber.

For the WDM system, the wavelength of each optical signal ranges from 1470 nm to 1610 nm, divided into 8 bands. For dense WDM data transmission 1530 nm - 1565 nm (C-band) region and 1570 nm - 1610 nm (L-band) regions are used [90]. Common WDM channel intervals are 200 GHz, 100 GHz, 50 GHz, and 25 GHz [90]. To construct WDM systems currently, relatively expensive laser arrays are used, each channel corresponds to a separate laser.

WCombs have potential as a WDM source. A single pump laser is required to generate optical frequency comb lines inside a WGM resonator, which are equidistant.

4.2 COUPLING LIGHT INSIDE WGMR

The best known way to couple light inside WGMRs is by using tapered optical fiber. The tapered coupling can have 98% coupling efficiency [51]. Tapered fiber is a single-mode optical fiber that is stretched and therefore significantly thinned in the middle. It is an easy to align coupling system. Also, the whole system can be made so light travels only in optical fibers. However, it requires delicately drawn tapered fibers, which are very brittle and require careful handling. Also, it

is almost impossible to clean the tapered fiber, so it is not suitable when working with liquid suspensions. More details about tapered fiber coupling can be found in subsection 2.3.3.

4.2.1 *Setup with a GGG Prism for WComb Generation*

In this section, a setup similar to in Section 3.4.1 is described. The main component of the setup is the coupling prism. A lens is used to focus the beam on the surface of the prism where the total internal reflection occurs (see inset in Fig. 4.8 (a)). To couple light inside the resonator, a X-Y-Z translation stage with the built-in Piezo (Thorlabs NanoMax-TS) was used to achieve critical coupling and align the WGMR with the total internal reflection spot. For alignment purposes, first, a red laser (650 nm) was used, which was visible in the camera. It was switched with a pumping 1550 nm laser with a narrow linewidth of 50 kHz (Thorlabs SFL1550s) to excite the WGM resonances. The setup can be seen in Fig. 4.8 (a) and (b). A switchable gain amplified photo-detector (Photodiode Thorlabs PDA20CS2, λ= 800 – 1700 nm) connected with a digital storage oscilloscope was used to record the received transmission signal. A detected WGM resonance is shown in Fig. 4.8 (c). For the frequency scale calibration, an electro-optical modulation signal was used with 100 MHz sidebands, as seen in Fig. 4.8 (d). This allowed finding the FWHM of the resonance. The Q factor of the resonance was calculated as $2.6 \cdot 10^6$.

To achieve critical coupling the X-Y-Z translation stage was controlled by Piezo. This allows one to control the gap between the prism and resonator. In Fig. 4.9 a the gap was slowly decreased. First, weak under-coupled resonances appeared in the transmission spectra. As the gap was reduced the intensity of the signal dropped gradually but the WGM resonance dip depth increased (see Fig. 4.9 b). When the resonator touched the prism over coupling occurred and the dip depth decreased. The Q factor of the resonance increased as the gap also increased (see Fig. 4.9 c). When the gap was less than 0.05 µm, the vibrations from the air could be seen in the transmission spectrum. These vibrations came from the microsphere resonator which was attached using the fiber stem. The vibrations corresponded to self-oscillation frequency as the microsphere acted as a pendulum.

To be able to see the spectrum using OSA (Advantest Q8384 resolution 0.01 nm) and observe the generation of WComb, the setup was slightly modified to couple the light from free space inside an optical fiber (see Fig. 4.10). By using a 50/50 slitter, the signal was observed both using a photo-diode to see the WGM resonances and OSA to record comb spectra. To generate the WComb the laser had to be scanned very fast to prevent any thermal effects from the high laser power. The scan frequency was set to about 5 kHz. No successful WComb was generated using the setup. It was observed that the opti-

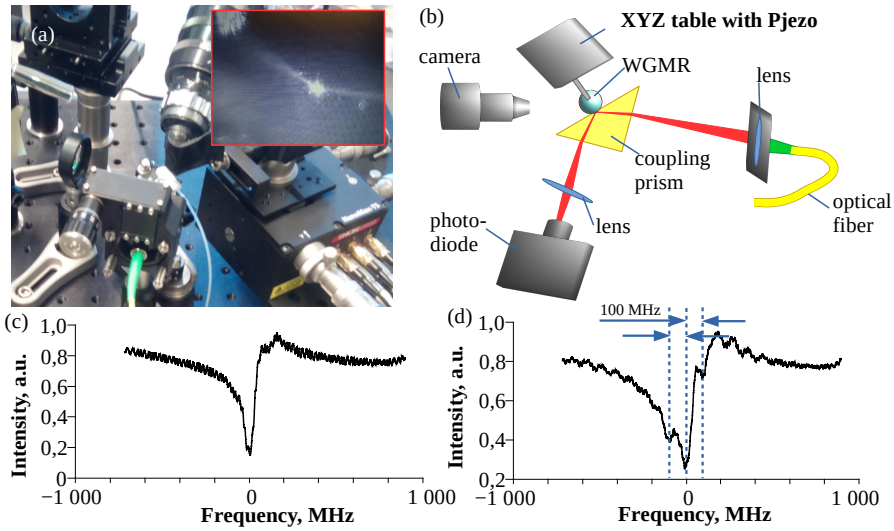

Figure 4.8: Setup using prism coupling to couple 1550 nm laser light inside WGMR: (a) photo of setup and the inset of the total internal reflection spot on prism and (b) scheme of the setup with prism and XYZ position table with sphere to control the gap between the resonator and prism and (c) WGM resonance and (d) WGM resonance with 100 MHz frequency modulation side bands for frequency calibration.

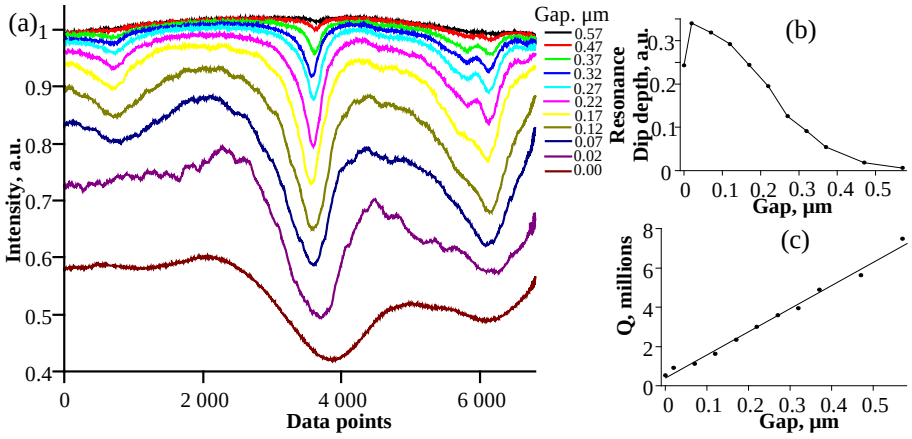

Figure 4.9: Coupling conditions are dependent on the gap between prism and resonator: (a) transmission spectra for the WGM resonances as the gap is slowly reduced; (b) resonance dip depth changes and (c) Q factor.

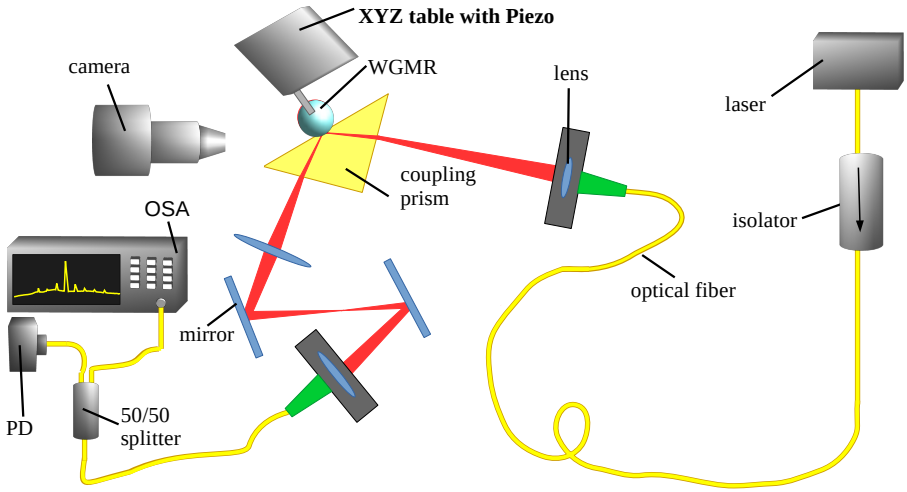

Figure 4.10: Free space beam coupling using a prism WComb detection: fiber couples were used to couple light inside the optical fiber for connection with two detectors - photodiode and OSA.

mal gap distance between prism and resonator was hard to maintain manually. Further setup optimization was necessary.

4.2.2 *Setup Based on a Tapered Fiber*

The main component of the setup is the tapered fiber. First, a tapered fiber must be fabricated with high transmission after the tapering. Second, the fabricated WGMR must have a high Q factor and the nonlinear effects should be visible when scanning the laser and detecting the transmission signal with photo-diode.

4.2.2.1 *Tapered Fiber Pulling*

Tapered fiber is fabricated from a 125 µm standard ITU-T G.652 single-mode telecommunication fiber. First, the fiber was cut in half and the plastic jacket and coating, which protects the fiber, were removed from both sides. The fiber was next cleaned using ethanol and a lint-free wipe. When it was clean a "screeching" sound could be heard when wiping. The fiber ends were cut using a fiber cutter and fused together with a commercial arc fusion splicer (Sumitomo Fusion Splicer - T 71C). Alternatively, if a new fiber patch was used no cutting or splicing was necessary. It was stripped of jacket and coating only in the region of 1 - 2 cm where it will be near the flame. Hydrogen flame was chosen as a heat source as it produces only water and heat as it burns. Also, the burning temperature of hydrogen flame is lower than hydrogen-oxygen flame and it is sufficient to melt and soften the fiber slowly. Temperature of 1400° was measured with thermocouple. Slow heating is more desirable as the time period for certain steps is more

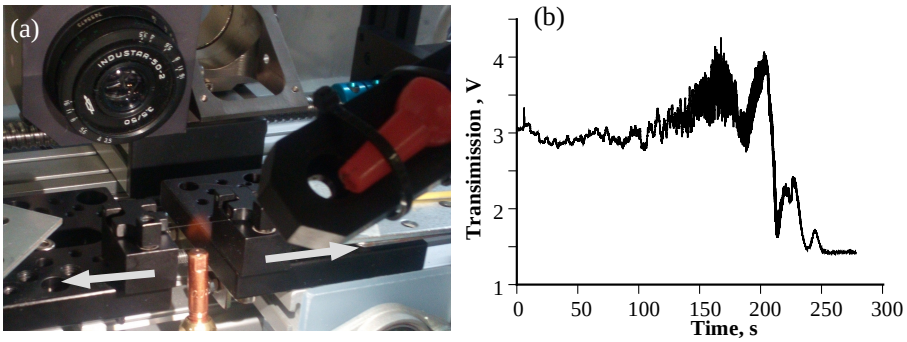

Figure 4.11: Fabrication of the tapered fiber: (a) the set up with hydrogen flame as the fiber is clamped between two holders and pulled using motors; (b) the transmission signal through the fiber is monitored during taper pulling to control when the core melts with the cladding and the fiber becomes single mode again.

flexible. The cleaned fiber was placed horizontally and held by two fiber holders, which were positioned about 2 cm from each other. Two step motors were used to pull the fiber from both ends and stretch it. The pulling speed was about 80 μm/s. When the fiber was stretched in both directions the tapered middle was more uniform in diameter. If it was stretched in only one direction, the taper from one side was more rapid than the other side which was slowly stretched (see Fig. 4.11 a).

The fiber was stretched for 15-20 mm. During tapering the transmission spectrum of the fiber was monitored (see Fig. 4.11 b). This allowed beholding when the fiber coating and core melted and the single-mode fiber became multi-mode. This was represented with the wave-like form in the transmission signal intensity. As the fiber was stretched more it eventually became single-mode again and the transmission intensity was constant. The final diameter of the taper was 1.5 μm measured by a microscope.

4.2.2.2 *Simple Tapered Fiber Setup for WComb Generation*

The tapered fiber coupled with a WGM resonator microsphere can be seen in Fig. 4.12 a and the setup can be seen in Fig. 4.12 b.

The pump laser λ = 1550 nm and linewidth of 50 kHz laser, Thorlabs SFL1550s) was amplified with an erbium-doped fiber amplifier (EDFA, Keopsys). The laser frequency was scanned by changing the current with a triangle signal using a frequency generator. The EDFA output power level was fixed between 10-23 dBm (varied in the case of the used SiO_2 microsphere). The isolator on the EDFA output is used to prevent back-scattered light. The polarization state was adjusted using the polarization controller (PC) before coupling the amplified optical signal into the microsphere through a tapered fiber. An

optical power splitter (PS, splitting ratio 50/50) was used to monitor the transmission signal using a high resolution optical spectral analyzer (OSA, Advantest Q8384 resolution 0.01 nm) and InGaAs switchable gain amplified photo-detector (Photodiode Thorlabs PDA20CS2, λ = 800 – 1700 nm) connected with a digital storage oscilloscope was used to record the received transmission signal. A webcam, which has been modified by adding an F = 30 mm photo camera objective lens for magnification was used to capture and control the touch-point of the resonator with the tapered fiber for best coupling conditions where WComb generation was observed. The 3-axis X-Y-Z micropositioner stage with the built-in Piezo controller (Thorlabs NanoMax-TS) was used to achieve coupling (see Fig. 4.5.a inset). The laser frequency was scanned very fast to prevent any thermal effects in the resonator from the changing laser power. The scan speed of the laser frequency was chosen 5-10 kHz and 500 MHz range.

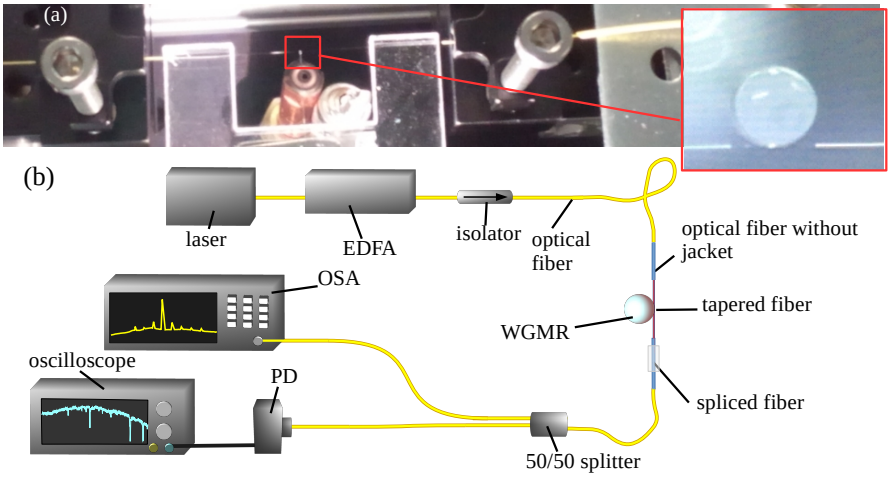

Figure 4.12: Setup based on tapered fiber: (a) tapered fiber coupling and (b) scheme of the setup.

The fabricated tapered fiber was used to couple the laser light inside the microsphere resonator. WGM resonances were observed (see Fig. 4.13 a). The line width of the resonances depended on the wavelength scan direction as described in subsection 4.1.3.3. The WGM resonance seen on the left is blue-detuned (see Fig. 4.13 b) and thermally stable. The recorded resonance is visually narrow. As the scan changed direction WGM resonance became red-detuned (see Fig. 4.13 c) and thermally unstable. The unstable resonances are visually broadened. Red-detuning is required for soliton formation and WComb generation.

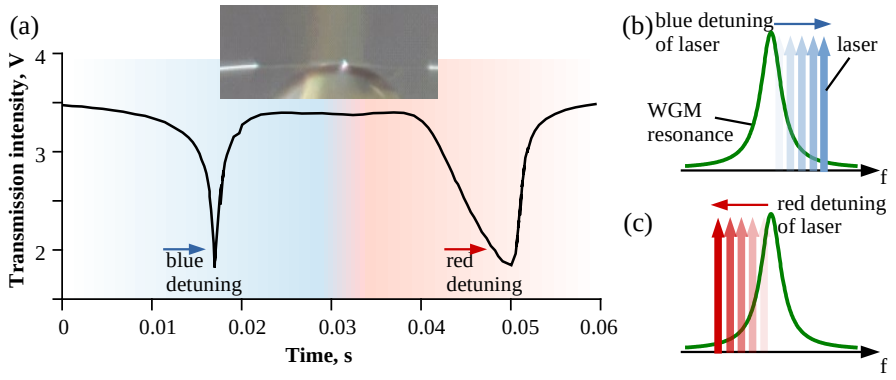

Figure 4.13: WGM resonance excitation: WGM transmission spectra where the dips are WGM resonances, the wavelength scan changes direction in the middle and the resonances broaden due to thermal instability; the inset shows the tapered fiber and silica microsphere touching.

4.2.2.3 *Advanced Tapered Fiber Setup for WComb Generation*

To identify the WGM resonances which generated the WComb, the setup was slightly modified by adding several elements. The polarization state was adjusted using the polarization controller (PC) before coupling the amplified optical signal into the microsphere through a tapered fiber. To reduce the thermal effect for a more precise Q factor estimation an optical variable attenuator (VAO, EXFO FVA-3150) was used to reduce the power pumped inside the microsphere when necessary. An additional PS was used to connect a second photo-detector (λ = 800 – 1700 nm) with an optical bandpass filter (OBPF, Santec OTF-350) to detect which WGM resonances generated the WComb. The optical bandwidth of the bandpass filter at -3 dB level was 10 nm, and its the central wavelength was tuned 5nm away from the pumping laser. It passes all wavelengths above the pumping laser wavelength. Only when the WComb was generated in the WGMR, a signal was detected with the second photo-detector.

To get rid of the laser scanning a pumping continuous wave (CW) tunable laser (Agilent 81989A) was used which could be scanned in steps (0.001 nm). This laser could be tuned in a wider range 1465-1575 nm. The optical fiber connected to the laser was lightly tapped to trigger the generation of the comb lines [83].

CALIBRATING THE FREQUENCY To calibrate the frequency scale two separate calibration methods were combined. A fiber with flat ends was used to obtain interference fringes with an unknown period. The length of the fiber was about 3 m and the fringes were expected to have a period of about 33 MHz. The WGM resonance signal and fringes were recorded by using a 99/1 splitter (see Fig.

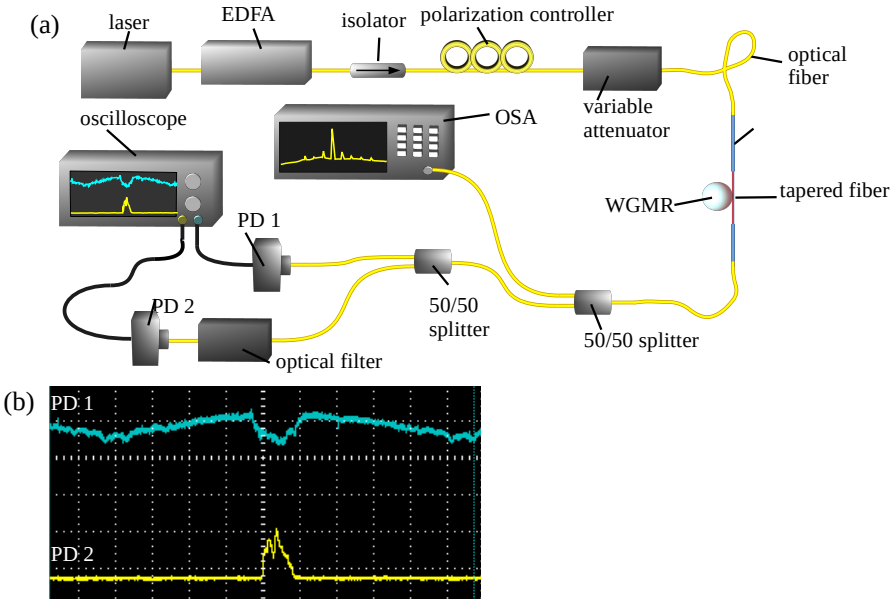

Figure 4.14: Modified setup based on tapered fiber: (a) scheme of the setup expanded with an optical filter and a second photo-diode; (b) observed signal of both photo-diodes using an oscilloscope to identify WGM resonances which generate WComb.

4.15 a curve 1 and 2). To calibrate the fringes electro-optical modulation of the resonance signal was used. The WGM resonance signal was recorded with 50, 70, and 100 MHz modulation sidebands (see Fig.4.15 a curve 3, 4, and 5 respectively).The fringe period calculated (35.2 ± 1.1) MHz. The fringe maxima were found (see Fig. Fig.4.15 b) and used for recorded data point calibration. The calibration function is shown in Fig. 4.15 c. The fringe calibration method was preferred because the modulation signal was very weak as only 15% of the light was transmitted trough the electro-optical modulator. Additionally, information about the laser mode jumping during the scan could also be obtained.

4.3 WCOMB GENERATION

4.3.1 *WComb Generation using Laser Scan*

First WComb was obtained using a resonator made from Light Guide Optics International Ltd. optical fiber with the sphere diameter of 270 µm (see Fig. 4.16 inset) and Q factor of $2 \cdot 10^7$. The transmission efficiency of the tapered fiber was 96%. The 1550 nm laser was amplified with an EDFA, and the EDFA output power was fixed to +20 dBm (100 mW). 50/50 optical power splitter was used to monitor the transmission signal sent to the OSA and the photodiode connected with an oscilloscope. The laser frequency was scanned very fast to prevent

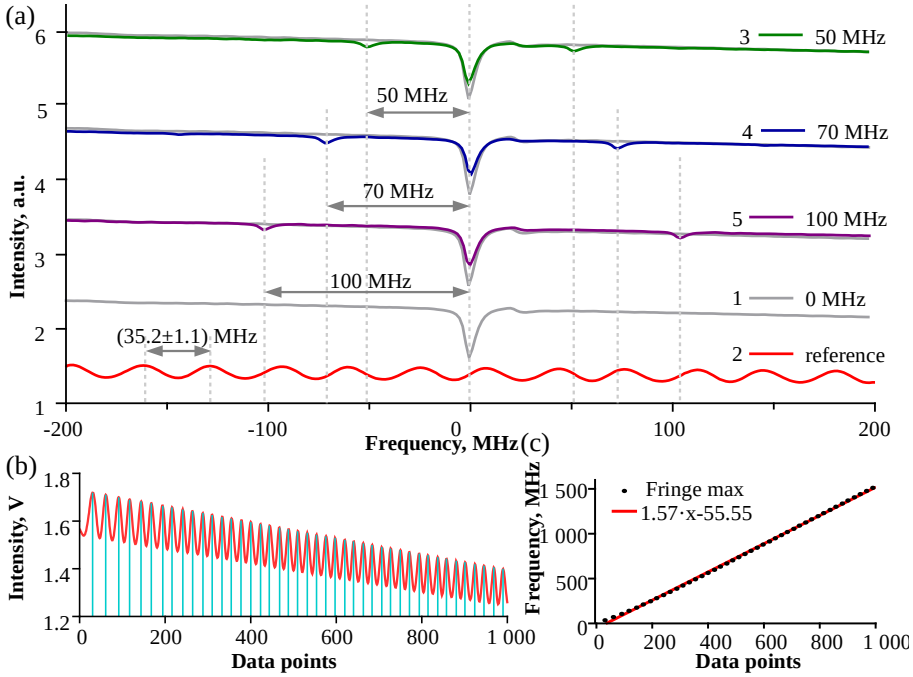

Figure 4.15: Calibration of frequency scale: (a) using electro-optical modulation to calibrate the fringe period (35.2 ± 1.1) MHz; (b) fringe maximums were found to acquire the (c) calibration function for maxima data points frequency in MHz.

any thermal effects. The scan speed was set to about 5 kHz. A comb-like structure with comb spacing 2.31 nm or 288 GHz was observed (see Fig. 4.16). However, the structure was unstable. The laser scanning speed was not changed.

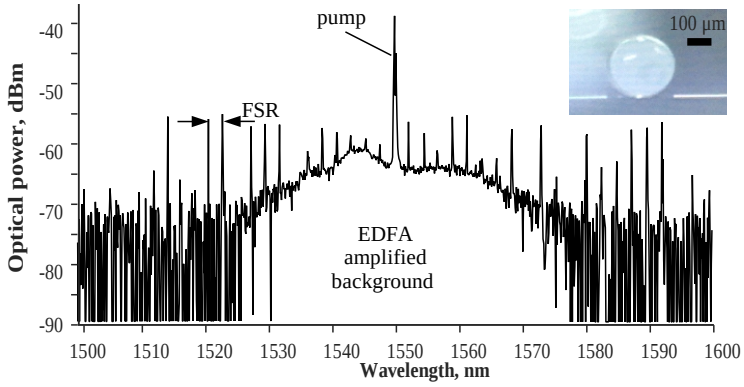

Figure 4.16: First results for microsphere WComb when pumped with scanning 1550 nm laser: the registered comb data and the inset shows the microsphere resonator.

The second WComb was generated using the WGMR, which was also made from Light Guide Optics International Ltd. optical fiber,

d=120 µm (see Fig. 4.17 a) and Q factor of $1.2 \cdot 10^7$ (see Fig. 4.17 b). This was the smallest resonator used. EDFA output power was fixed to +23 dBm. The laser frequency was scanned with 10+ kHz frequency. A comb-like structure with comb spacing 4.31 nm or 538 GHz was observed (see Fig. 4.17 c). Using the Eq. 2.17, the resonator radius was calculated as (61 ± 1) µm. The generated WComb was very sensitive to light polarization. The WComb was relatively stable and, without changing the settings, did not drift or disappear.

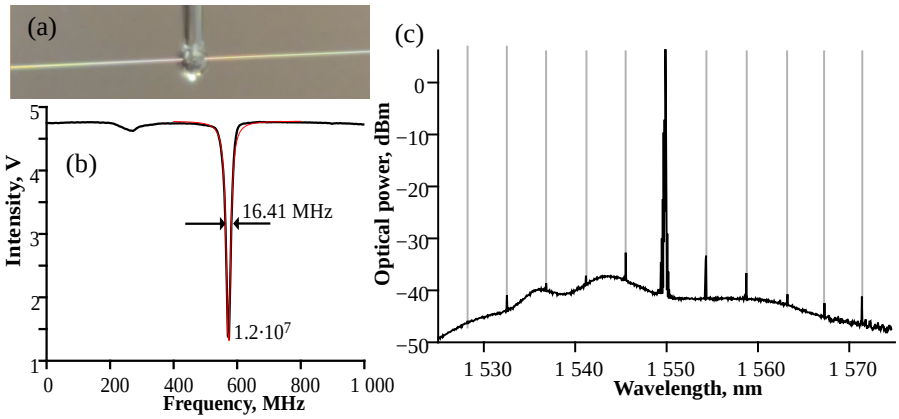

Figure 4.17: WComb generation: (a) 120 µm WGMR resonator fabricated from "Light Guide Optics International Ltd." optical fiber coupled with 1550 nm laser using a tapered fiber; (b) the Q factor of the resonator was $1.2 \cdot 10^7$; (c) the generated WComb had multiple stable comb lines.

Changing the light polarization affected the optical power of the comb lines.

Lowering the power or scan frequency led to the suspension of comb generation below a threshold value.

Changing the position of the WGMR in contact with tapered fiber or changing the laser frequency using the temperature affected how many comb lines were excited and the optical power distribution of the lines.

The WGMR microsphere fabricated from SMF28 optical fiber with a diameter of d=170 µm (Fig. 4.18 a) and Q = $4.6 \cdot 10^7$ (Fig. 4.18 b) was used to generate WComb. The lowest pump power for a successful WComb generation with only a few lines was +10 dBm (without EDFA). WComb with comb spacing 3.14 nm or 392 GHz was observed (see Fig. 4.18 c). The resonator radius calculated from FSR was (84 ± 1) µm which correspond with measurements obtained using the microscope. The laser scanning speed could be slowed down, however, the scan could not be turned off completely successfully. A different tunable laser was used further.

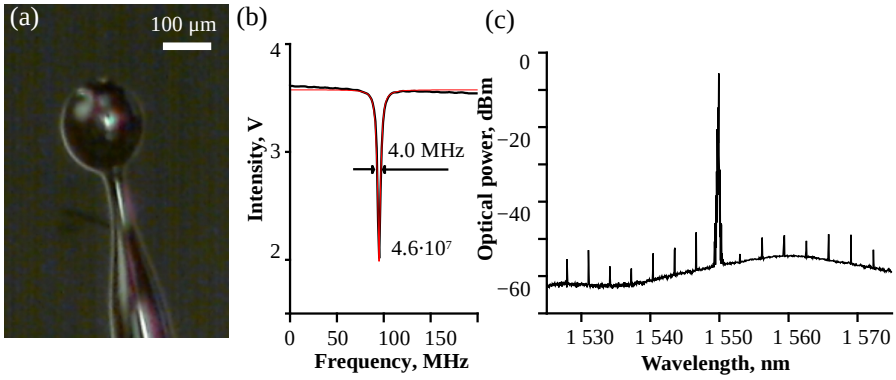

Figure 4.18: WComb generation: (a) 170 µm WGMR resonator; (b) the Q factor of the resonator was $4.6 \cdot 10^7$; (c) the generated WComb had multiple stable comb lines.

4.3.2 *WComb Generation Using Tunable Laser*

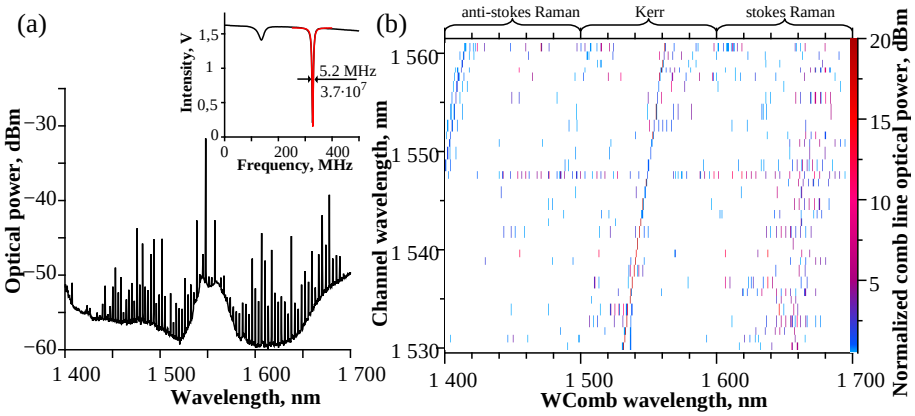

Figure 4.19: WComb excitation using C-band channels inside a 166 µm WGMR resonator: (a) the generated WComb had multiple stable comb lines, inset shows the Q factor of the resonator $3.7 \cdot 10^7$; (b) Kerr and Raman WComb excited with 32 different C-band channel pump wavelengths (1530.33 -1560.61 nm).

To solve the problem of turning off laser scanning a different tunable laser (Agilent 81989A 1465-1575 nm) was used which could change the frequency in steps in the whole telecom C-band range. To trigger the generation of the comb lines instead of scanning like before the kick method was used [83]. To generate the kick, the optical fiber connected to the laser was lightly tapped. The tapping modulated the power of the pump laser for a short time. The power drop causes the resonator to rapidly cool and the resonances to blue shift. After the kick, it is again thermally locked [83]. The frequency comb was excited inside 166 µm silica microsphere WGMRs with a Q factor

of $5.2 \cdot 10^7$ (Fig. 4.19 a inset). Using a 1547.72 nm laser light a broadband comb was obtained spanning from 1400 – 1700 nm (see Fig. 4.19 a) by combining the Kerr comb with stokes and anti-stokes Raman comb with FSR of (3.17 ± 0.08) nm. 32 different C-band channel frequencies were subsequently pumped inside the WGM microsphere and the comb signal was recorded (see Fig. 4.19 b). It was relatively easy to excite stokes Raman comb lines (28 out of 32 channels) while anti-stokes Raman comb lines were rare. For 12 different channels, Kerr comb lines were excited. It was easier to excite Kerr comb lines for longer wavelength channels working in the anomalous dispersion regime. For the Kerr OFC generation, the excitation laser above 1547 nm was better as more intense comb lines were generated.

4.3.3 *Distance Between Comb Lines*

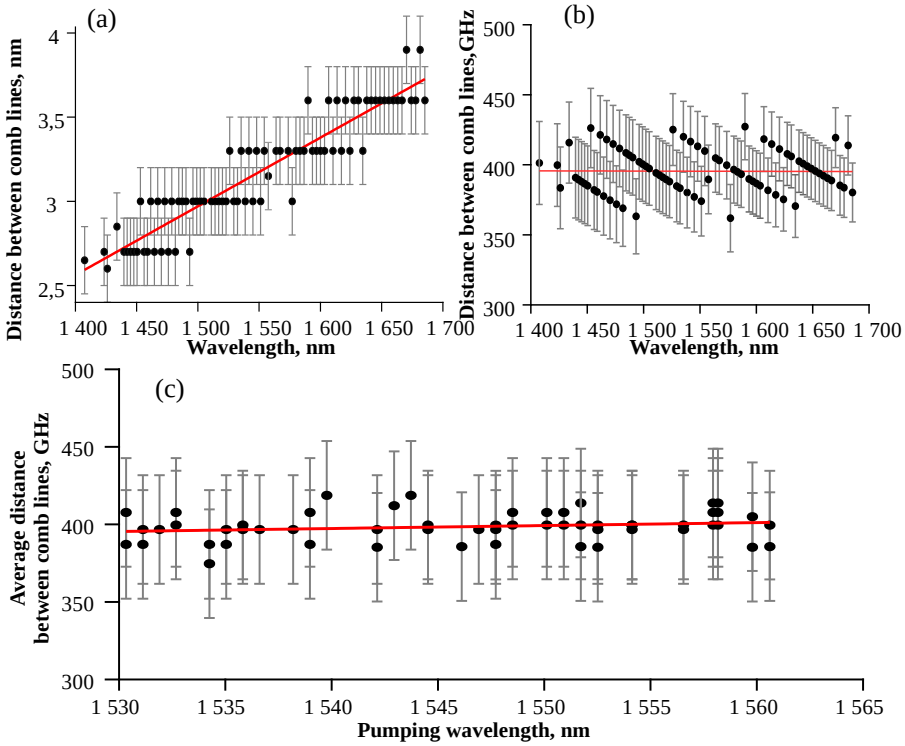

Figure 4.20: The distance between frequency comb lines: (a) for broadband comb the distance between lines was not equidistant in nm (b) and constant in GHz - (397 ± 10) GHz; (c) for combs generated at different C-band channel pumping wavelengths, linear slope of (0.19 ± 0.13) GHz per nm was observed.

When the comb lines are equidistant then the system operates at zero dispersion range [35]. This effect can limit the generation of broader frequency combs. Looking at the distance between the comb lines of registered spectra with a pumping wavelength of 1548 nm a

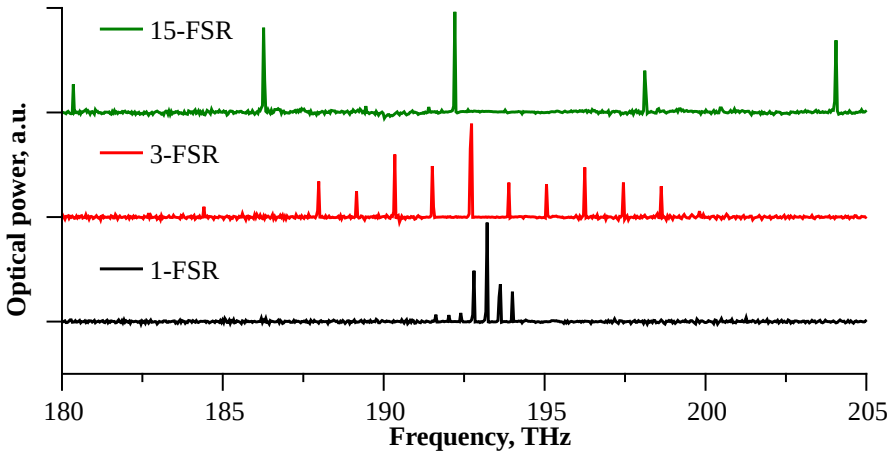

Figure 4.21: Multi FSR WComb generated in 166 μm WGMR: 1-FSR (400 GHz) black curve, 3-FSR (1200 GHz) red curve and 15-FSR (600 GHz) green curve.

slight mismatch from the equidistant grid can be seen - as the wavelength increases so does the spacing between comb lines (see Fig. 4.20 a). However, after converting the x-axis units from nm to GHz it becomes obvious that the distance between the comb lines is constant and the slope of the linear function is -0.0016 GHz per nm (see Fig. 4.20 b). The distance between lines was (397 ± 10) GHz. With OSA resolution could not determine such small changes in repetition rate.

When changing the pumping laser wavelength it was observed that the spacing between the comb lines slowly increased (see Fig. 4.20 c). The linear slope is (0.19 ± 0.13) GHz per nm.

It was possible to observe multiple FSR WCombs where every second, third or n-th comb line was generated. In Fig. 4.21 WComb is generated in the same 166 μm silica microsphere WGMR using different pumping laser frequencies. 1-FSR comb line gap of 400 GHz was generated at 1552.5 nm, 3-FSR of 1200 GHz was generated at 1556.6 nm, and 15-FSR of 6000 GHz was generated at 1560.6 nm. Multiple

Table 4.1: WGMR size and WComb FSR comparison.

d, μm measured	R, μm	λ_{FSR}, nm measured	f_{FSR}, GHz measured	f_{FSR}, GHz calculated
270 ± 10	135	2.31 ± 0.12	288 ± 15	246 ± 9
120 ± 5	60	4.31 ± 0.10	538 ± 12	553 ± 23
166 ± 5	83	3.17 ± 0.08	397 ± 10	400 ± 12
170 ± 5	85	3.14 ± 0.04	392 ± 5	390 ± 11

n-FSR means that inside the resonator are circulating n pulses spaced along the circumference.

In Table 4.1 measured distance between lines and calculated FSR is compared. Calculated and measured FSR match within error limits very well for 120, 166, and 170 μm microsphere resonators. For 270 μm microsphere measured FSR was larger suggesting the measured diameter might have been inaccurate and the microsphere was smaller or the mode generating the WComb could be a radial mode located deeper inside.

4.3.4 *Power Circulating Inside Microspheres*

Microresonators with high Q factor can build up a significant internal circulating power P_{circ} with low pump powers P_{in}.The P_{circ} in the silica microsphere WGMR is related to the P_{in} as [91]:

$$P_{circ} = P_{in} \frac{\lambda Q_{intr}}{\pi^2 n R} \frac{K}{(K+1)^2} \tag{4.11}$$

where λ is the resonance wavelength, n is the refractive index, R the microsphere radius, K the coupling parameter (see Eq. 2.15) and Q_{intr} is the intrinsic Q factor. By combining Eq. 2.14, 2.15 and 2.16 Q_{intr} can be evaluated as:

$$Q_{intr} = (1+K)\, Q = \left(1 + \frac{1 \mp \sqrt{T}}{1 \pm \sqrt{T}}\right) Q, \tag{4.12}$$

where Q is the measured total quality factor, T is transmission at resonance frequency and signs correspond to over-coupling or under-coupling case respectively.

To find the optical intensity circulating inside I_{circ} the WGMR the effective area of the mode area A_{eff} was found first using simulations. As parameters resonator radius, refractive index and resonance

Table 4.2: Power and optical intensity circulating inside the WGMR built up from 0.1 W input laser power.

R, μm	Q $\cdot 10^7$	T	K	Q_{intr} $\cdot 10^7$	P_{circ} W	A_{eff}, μm^2	I_{circ}, GW/cm^2
135	2.0	0.17	1.69	5.4	1016	36.15	2.8
60	1.2	0.26	2.05	3.7	1468	18.45	8.0
85	4.6	0.54	3.89	22.0	4671	24.62	19.0
83	3.7	0.14	1.61	9.7	3000	24.14	12.4

frequency at 1550 nm for fundamental mode were used. For the fundamental mode the effective area is highly localized. The circulating intensity was found [91]:

$$I_{circ} = \frac{P_{circ}}{A_{eff}}. \tag{4.13}$$

The P_{circ} and I_{circ} results are compiled in Table 4.2 (see Appx. C.2). Resonators with higher Q_{intr} had higher power and intensity circulating inside. This can also be distinguished in the generated WComb spectra as more intense comb lines were generated inside 170 and 166 µm microsphere resonators.

4.3.5 *Stability of the Comb lines*

For high-quality data transmission in WDM fiber optic communication systems, the signal-to-noise (the WComb line to EDFA broad band emission spectrum) ratio must be at least 20 dB. The line has to be intense enough to be filtered to satisfy the necessary optical power budget of the transmission system [92]. The optical power stability was examined as it could interfere with data transmission. Any short-term stability would be detected during the data transmission, therefore only long-term instability was investigated further. The WComb spectrum of the 166 µm microsphere was recorded every 10 minutes for several hours.

4.3.5.1 *Stability of 800 GHz WComb Lines*

Kerr WComb pumped at 1551.67 nm had only 5 comb lines with the line spacing of 2-FSR (800 GHz) between them. The excited comb lines were intense and appeared to be stable in time (see Fig. 4.22 a). The optical power of the (-1) and (+1) carriers wast at least 30 dB above the noise level. The optical power of the pumping laser was stable (see Fig. 4.22 b curve of the optical carrier (0)). The optical power of the generated comb lines over time are shown in Fig. 4.22 b (see curve of optical carriers (-3) - (-1) and (+1) - (+2)). For the first 4 hours, all of the WComb lines were relatively stable. For the last 4 hours, however, the comb line optical power was increasingly fluctuating. The optical power of each Kerr WComb line changed independently. To verify the visual interpretation of data stability the data set was split into three 4 hour intervals - 0-4 h where the signal appeared stable, 5-9 h where some instability was observed, and 10-14 h where the signal was unstable - and fast Fourier transform (FFT) was used. FFT contains information about the fluctuation frequency content of the signal. The FFT amplitude of the pumping laser carrier (0) for all three intervals was similar (see Fig. 4.22 c). The FFT amplitude of the optical carrier (+1) confirmed that more optical power

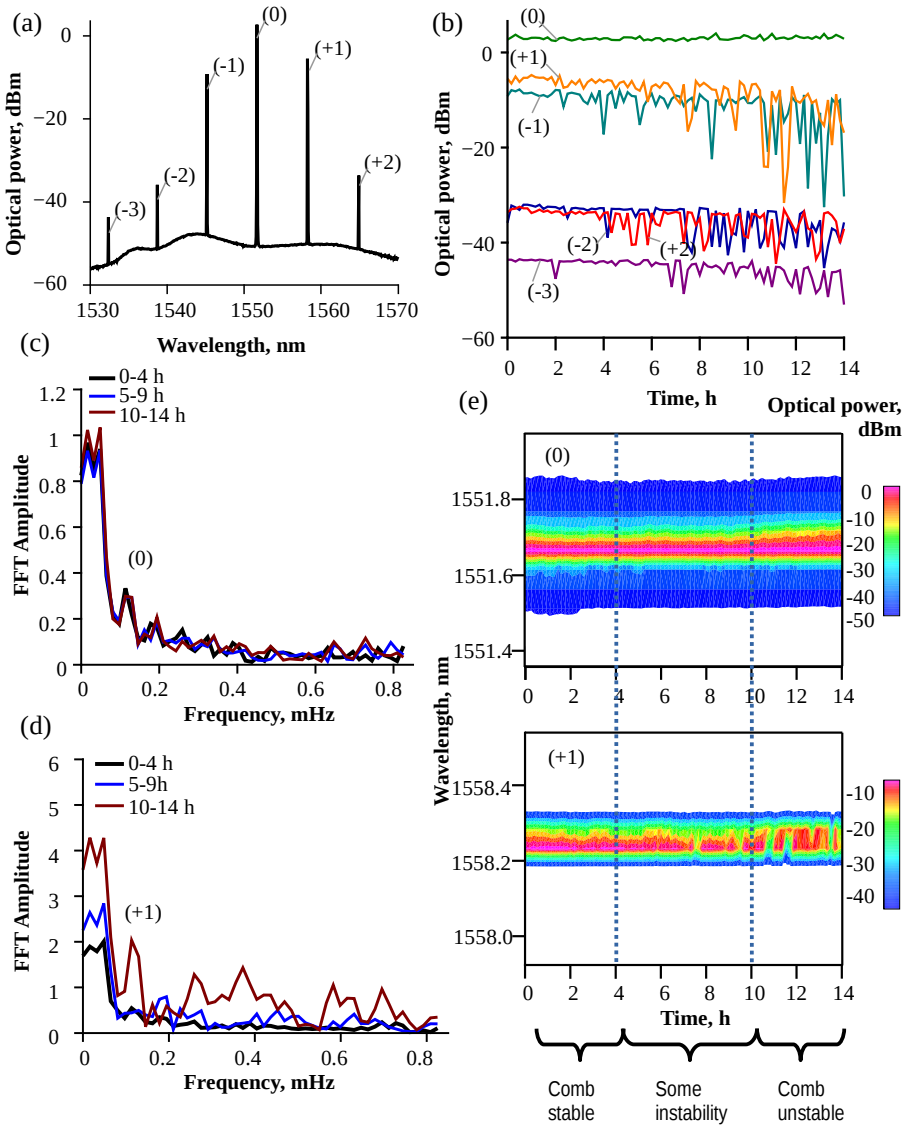

Figure 4.22: The stability of 800 GHz WComb comb lines: (a) stable Kerr WComb excited with 1551.67 nm pump laser and 2-FSR or 800 GHz gap between the lines; (b) the optical power change of all generated WComb lines over 14 hour time period; FFT of the comb optical power for 3 equal length time intervals for (c) (0) and (d) (+1) carrier for signal oscillation comparison; (e) WComb optical power maps for the pumping laser carrier (0) and comb line carrier (+1).

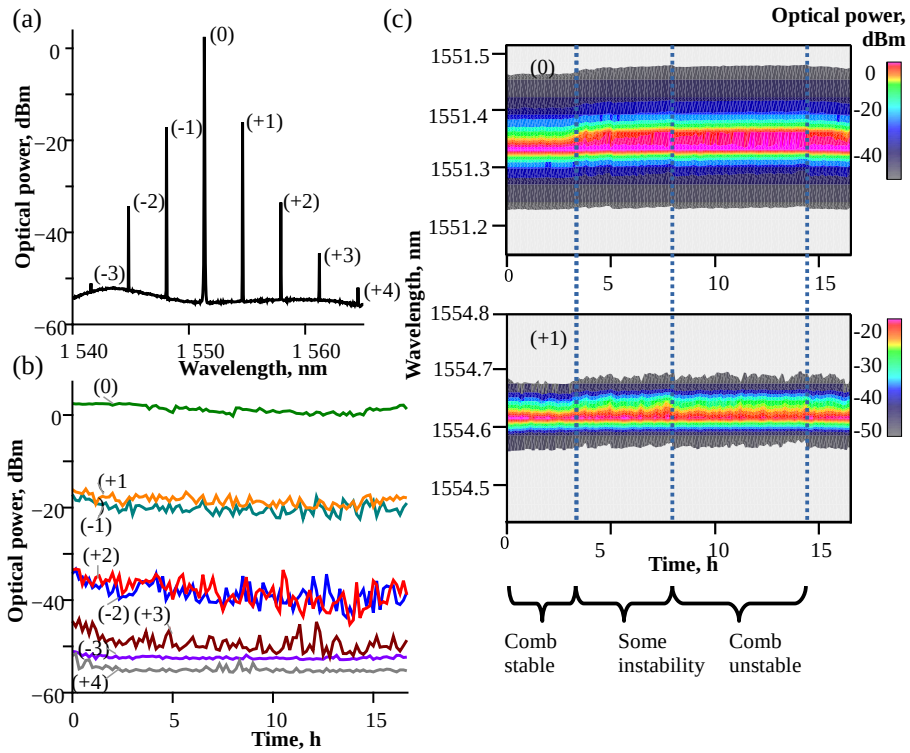

Figure 4.23: The stability of 400 GHz WComb comb lines: (a) stable Kerr WComb excited with 1551.35 nm pump laser and 1-FSR or 400 GHz gap between the lines; (b) the optical power change of all generated WComb lines over 16.5 hour time period; (c) WComb optical power maps for the pumping laser carrier (0) and comb line carrier (+1).

oscillation frequencies were present for the 10-14 h interval (see Fig. 4.22 d). Comparing the FFT amplitude of both the pump and the generated comb line for the first interval 0-4 h signal oscillations were comparable.

For the stability the environment of the WGMR and tapered fiber coupling was relevant. It was inside a protective setup to slow down the degradation of the Q factor. The box protected from both the ambient moisture and dust slows down the degradation of the SiO_2 microsphere. An important parameter that could impact the stability was the temperature. The drift of 1-2°C degrees during the measurement time affected the comb generation. The temperature changes can impact multiple factors. First, the position of the sphere in contact with the tapered fiber could change. Second, the WGM resonance frequency may shift by the change of the external environment temperature. Last but not least, the polarization of the light traveling through optical fibers may change. The instability observed from 4 to 10 hours could be explained by the slight change of coupling conditions which triggered some instability. The coupling conditions of

the microsphere and tapper fiber may change also due to mechanical vibrations. To reduce vibrations, passive stabilization system - an optical table with vibration isolation supports. Observing the optical power distribution in time for the profile of the pumping laser the signal broadened after 10 hours (see Fig. 4.22 e carrier (0)). We believe the broadening happens due to the polarization changes of the pumping carrier. The same broadening could be observed for the WComb line (see Fig. 4.22 e carrier (+1)). The timing of the pump broadening corresponds with the deterioration of the stability.

4.3.5.2 *Stability of 400 GHz WComb Lines*

Kerr comb excited at 1551.35 nm had only 9 comb lines with the line spacing of single FSR (400 GHz) between them. The excited comb lines were intense and stable (see Fig. 4.23 a). The optical power of the (-1) and (+1) carriers wast at least 30 dB above the noise level. The optical power of the pumping laser and the generated comb lines over time are shown in Fig. 4.23 b. Overall the stability was similar to 800 GHz WComb.

Observing the optical power distribution in time for the profile of the pumping laser the signal broadened after 4 hours (see Fig. 4.23 c carrier (0)). The same broadening could be observed for the WComb line (see Fig. 4.23 c carrier (+1)). Around the 15-hour mark, the WGM resonator and taper coupling positioning, as well as the pump polarization was readjusted. It improved both the optical power of the WComb lines and the stability.

5 DISCUSSION

5.1 SUMMARY

In the thesis "Whispering gallery mode silica microsphere resonator applications for biosensing and optical frequency combs" WGMR silica microspheres fabricated from standard optical fiber are presented for glucose sensor and bovine leukemia virus toxin sensor applications as biosensors, as well as WComb generation evaluation of circulating power in resonators and their long-term stability studies for possible applications in data transfer.

To fabricate a WGMR/Au-NPs/GOx glucose sensor, WGMR was coated with Au NPs, which enhanced the sensitivity, and glucose oxidase, which provided the selectivity. The sensor response was observed in a liquid drop containing glucose solution. We verified the sensitivity of Au NPs and glucose - GOx reaction by performing several control measurements. A single measurement of the WGM resonances shift due to glucose - GOx reaction took 10 - 15 minutes. The liquid drop evaporated in time, thus changing the concentration of glucose and inducing additional WGM resonance shift. This shift is in the opposite direction than the glucose - GOx reaction induced shift. The rate of the WGM resonance shift varied over time depending on the glucose concentration in the liquid drop. The concentrations used were chosen similar as are found in human blood and perspiration to confirm the adequacy of the WGMR/Au-NPs/GOx glucose sensor for applications in medicine. Our presented data illustrate that WGMR/Au-NPs/GOx glucose sensors are potentially suitable for the determination of glucose concentration in water-based samples. The proposed approach could be optimized for on-chip resonators and integrated with microfluidics resulting in a small and compact device, which potentially will suffer less undesirable effects due to the temperature stabilization necessity.

To develop a toxin sensor WGMR was first coated with a ZnO layer needed to provide the surface for protein to attach. We determined that the best method for coating ZnO on WGMRs was ALD method. A cheaper and faster method for ZnO deposition on the surface and mass-producing samples for testing was the drop coating. The drop method has potential, however, the low success rate hindered further functionalization of WGMR/ZnO and toxin sensor testing. WGMR/ZnO/BLV/ BSA structure was tested and indications of sensor response were observed, extensive control measurements were not performed.

For generating WComb silica microspheres were coupled with a 1550 nm laser using a tapered fiber. Comb-like structures were observed. The distance between comb lines coincided with the FSR of the WGMR (see Table 4.1). It was possible to also observe multiple FSR WCombs. 166 μm microsphere generated 800 GHz and 400 GHz WComb. Optical carriers (-1) and (+1) of the 400 GHz WComb had sufficient signal-to noise ratio to be used for WDM data transmission demonstration. Calculations to show the power buildup showed that the input laser power was built up at least 10^5 times (see Table: 4.2) and intensities GW/cm^2 were obtained, which were necessary for WComb generation. The investigation of long-term WComb stability indicated that temperature stabilization might be vital for telecom data transfer applications using WComb lines as data carriers as both the coupling conditions and pump polarization impacted the long-term stability.

5.2 CONCLUSIONS

According to the aim and objectives of the dissertation, the following main results have been obtained.

5.2.1 *WGM Resonator Sensors*

The role of WGMR surface functionalization is to introduce new material or sensing properties. The designed glucose sensor model had two functionalization layers.

1. For the WGMR biosensor model, the surface functionalization layer which provides selectivity is important. GOx was chosen as the selective layer for glucose sensing because it oxidizes glucose. Control measurements confirmed the WGM resonance shifting only when both GOx layer was applied and glucose in the drop of test fluid was present.

2. As an additional functionalization layer, Au NPs were introduced to the WGMR surface to help extend the evanescent field through the LSPR and increase the sensitivity of the WGMR. It proved beneficial because control measurements confirmed the increase in sensitivity for samples with both Au NPs and GOx compared to samples only with GOx.

The designed toxin sensor model had more functionalizing layers. Antigen/antibody BLV reaction was chosen for the selectivity. To help the proteins adhere to the surface ZnO layer was chosen. From tested ZnO structures, the best quality was ALD nanolayer with 10 - 20 nm thickness. ZnO nanorod structure was too rough to observe WGM resonances while only 50% of samples achieved with drop-coating with ZnO nanocrystal structure were good.

5.2.2 *WComb*

It was possible to generate WCombs using silica WGMR microspheres. The radius of the sphere determined the distance between comb lines. 166 μm microsphere generated WComb with 800 GHz or 400 GHz FSR. Moreover, two of the generated 400 GHz WComb lines (carriers (-1) and (+1)) satisfied the required >20 dBm signal-to-noise ratio. This allowed to use the generated WComb for WDM data transmission testing [7]. To adapt FSR for the WDM grid of 100 or 50 GHz larger microspheres should be tested, however, the power circulating inside the sphere not only depends on the Q factor but decreases with increasing radius. For silica microspheres, the Q factor is limited to 10^8, which means larger spheres have to be pumped with a higher power laser (200 mW - 1W).

The long-term stability of WComb generation in microsphere resonators is affected by temperature stability. Temperature can change both the coupling conditions and laser polarization.

5.2.3 *Thesis Statements*

1. In WGMR/Au-NPs/GOx structure Au NPs help to extend the evanescent field through the LSPR and increase the sensitivity of the WGMR glucose sensor.
2. In WGMR/ZnO/BLV/BSA structure ZnO nanolayer surface is best for coating on WGMR, and it has an optimal thickness of 10 - 20 nm and a Q factor of about $5 \cdot 10^6$.
3. The size of the microsphere determines the distance between the generated WComb lines, which allows to adapt it to the application for WDM ITU-T G.694.1 grid data transmission. A suitable microsphere diameter to match the distance between WComb lines was 166 μm, which generated 400 GHz (1-FSR) and 800 GHz (2-FSR) WComb.
4. WComb long-term stability is affected by temperature, which can change both the coupling conditions and laser polarization.

5.3 RECOMMENDATIONS FOR FUTURE RESEARCH

In the thesis, the glucose-GOx reaction as the cause of the WGM resonance shift is explored in detail. Selectivity test was validated using buffer solution. GOx has been extensively tested as a selective layer for various glucose biosensors[93]. Nevertheless, the selectivity of GOx towards glucose should be investigated in more detail in both simple, for example, fructose solution drop, and more complex liquids (blood, saliva). Further testing of the toxin sensor has to be

done to validate the drawn conclusions about the observed sensor response. The function and necessity of each sensor layer has to be investigated.

Observed sensor response for both the glucose and toxin sensor should be overall applicable for other WGMR geometries. Chosen functionalizing layers for either sensor could be incorporated with on-chip WGMR and microfluidics. It may also be applicable to prevent several complications introduced by liquid drop evaporation.

WGMR microsphere has only one controllable parameter - resonator radius - which limits possible manipulations of WComb FSR and geometric dispersion. Using other WGMR geometries like microrods, microtoroids or photonic belt WGMRs open the possibility to choose the distance between comb lines suitable for WDM data transmissions and zero-dispersion wavelength needed for WComb generation more independently. Additionally, an active stabilization system for WComb generation can be developed to improve long-term stability.

ACKNOWLEDGEMENTS

I would like to thank the supervisor of the dissertation **asoc. prof. Janis Alnis** for supervising the work from the work idea, which has changed several times over time, until the writing of the dissertation. Thank you for the various practical tips in the design and improvement of test equipment. I would also like to express my deep gratitude to **asoc. prof. Roman Viter**, who took on an equal role as a supervisor when working on WGMR biosensor research.

Thanks also to **prof. habil. Dr. Arunas Ramanavicius** on consultations in interpreting glucose sensor measurement results. Prof. Ramanavicius monitors and publishes dozens of scientific publications every year, so I gained a valuable experience and various worthy tips when writing our joint publication.

I would like to thank my colleagues Karlis Grundsteins and Arvids Sedulis for making microspheres, and Kristians Draguns for the mathematical simulations performed. Thanks to Aigars Atvars for project preparation. Thanks also to Toms Salgals for insight into the use of WComb in telecommunications.

I thank the partners from Riga Technical University who provided the equipment needed to generate WComb. I thank the partners from the Institute of Applied Physics of the Russian Academy of Sciences and the NanoBioMedical Center of Adam Mickiewicz University.

The research results of the dissertation have been used for the implementation of scientific research projects:

- ERDF No. 1.1.1.1/16/A/259;
- ERDF No. 1.1.1.1/18/A/155;
- LZP No. Lzp-2018/1-0510.

NATIONAL DEVELOPMENT PLAN 2020 | EUROPEAN UNION European Regional Development Fund

INVESTING IN YOUR FUTURE

FLPP FUNDAMENTAL AND APPLIED RESEARCH PROJECTS

BIBLIOGRAPHY

[1] I. Brice, K. Grundsteins, A. Atvars, J. Alnis, and R. Viter. "Whispering gallery mode resonators coated with Au nanoparticles." In: *Nanoengineering: Fabrication, Properties, Optics, Thin Films, and Devices XVI*. Ed. by A.J. Attias and B. Panchapakesan. Proceedings of SPIE, 2019, p. 65. DOI: 10.1117/12.2528677.

[2] I. Brice, K. Grundsteins, A. Atvars, J. Alnis, R. Viter, and A. Ramanavicius. "Whispering gallery mode resonator and glucose oxidase based glucose biosensor." In: *Sensors and Actuators B: Chemical* 318 (2020), p. 128004. DOI: 10.1016/j.snb.2020.128004.

[3] I. Brice, R. Viter, K. Draguns, K. Grundsteins, A. Atvars, J. Alnis, E. Coy, and I. Iatsunskyi. "Whispering gallery mode resonators covered by a ZnO nanolayer." In: *Optik* 219 (2020), p. 165296. DOI: 10.1016/j.ijleo.2020.165296.

[4] I. Brice, K. Grundsteins, A. Sedulis, T. Salgals, S. Spolitis, V. Bobrovs, and J. Alnis. "Frequency comb generation in whispering gallery mode silica microsphere resonators." In: *Laser Resonators, Microresonators, and Beam Control XXIII*. Ed. by A.M. Armani, A.V. Kudryashov, A.H. Paxton, V.S. Ilchenko, and J.V. Sheldakova. Vol. 11672. Proceedings of SPIE, 2021, p. 1167213. DOI: 10.1117/12.2577148.

[5] J. Alnis, I. Brice, A. Pirktina, A. Ubele, K. Grundsteins, A. Atvars, and R. Viter. "Development of optical WGM resonators for biosensors." In: *Biophotonics—Riga 2017*. Ed. by J. Spigulis. Vol. 10592. Proceedings of SPIE, 2017, p. 19. DOI: 10.1117/12.2297551.

[6] J. Braunfelds, R. Murnieks, T. Salgals, I. Brice, T. Sharashidze, I. Lyashuk, A. Ostrovskis, S. Spolitis, J. Alnis, J. Porins, and V.S Bobrovs. "Frequency comb generation in WGM microsphere based generators for telecommunication applications." In: *Quantum Electronics* 50 (2020), pp. 1043–1049. DOI: 10.1070/QEL17409.

[7] T. Salgals, J. Alnis, R. Murnieks, I. Brice, J. Porins, A.V. Andrianov, E.A. Anashkina, S. Spolitis, and V. Bobrovs. "Demonstration of a fiber optical communication system employing a silica microsphere-based OFC source." In: *Optics Express* 29 (2021), p. 10903. DOI: 10.1364/OE.419546.

[8] K. Draguns, I. Brice, A. Atvars, and J. Alnis. "Computer modelling of WGM microresonators with a zinc oxide nanolayer using COMSOL multiphysics software." In: *Laser Resonators, Microresonators, and Beam Control XXIII*. Ed. by A.M. Armani, A.V.

Kudryashov, A.H. Paxton, V.S. Ilchenko, and J.V. Sheldakova. Vol. 11672. Proceedings of SPIE, 2021, p. 1167216. DOI: 10.1117/12.2578210.

[9] R. Berkis, J. Alnis, A. Atvars, I. Brice, K. Draguns, and K. Grundsteins. "Quality Factor Measurements for PMMA WGM Microsphere Resonators Using Fixed Wavelength Laser and Temperature Changes." In: *2019 IEEE 9th International Conference Nanomaterials: Applications & Properties (NAP)*. IEEE, 2019, 01P05–1–01P05–4. DOI: 10.1109/NAP47236.2019.219072.

[10] R. Berkis, J. Alnis, I. Brice, A. Atvars, K. Draguns, K. Grundšteins, and P.K. Reinis. "Mode family analysis for PMMA WGM micro resonators using spot intensity changes." In: *Laser Resonators, Microresonators, and Beam Control XXIII*. Ed. by A.M. Armani, A.V. Kudryashov, A.H. Paxton, V.S. Ilchenko, and J.V. Sheldakova. Vol. 11672. Proceedings of SPIE, 2021, p. 1167217. DOI: 10.1117/12.2577025.

[11] P.K. Reinis, L. Milgrave, K. Draguns, I. Brice, J. Alnis, and A. Atvars. "High-Sensitivity Whispering Gallery Mode Humidity Sensor Based on Glycerol Microdroplet Volumetric Expansion." In: *Sensors* 21 (2021), p. 1746. DOI: 10.3390/s21051746.

[12] E.A. Anashkina, V. Bobrovs, T. Salgals, I. Brice, J. Alnis, and A.V. Andrianov. "Kerr Optical Frequency Combs With Multi-FSR Mode Spacing in Silica Microspheres." In: *IEEE Photonics Technology Letters* 33 (2021), pp. 453–456. DOI: 10.1109/LPT.2021.3068373.

[13] K.J. Vahala. "Optical microcavities." In: *Nature* 424 (2003), pp. 839–846. DOI: 10.1038/nature01939.

[14] S. Soria, S. Berneschi, M. Brenci, F. Cosi, G. Nunzi Conti, S. Pelli, and G.C. Righini. "Optical Microspherical Resonators for Biomedical Sensing." In: *Sensors* 11 (2011), pp. 785–805. DOI: 10.3390/s110100785.

[15] G.C. Righini, Y. Dumeige, P. Feron, M. Ferrari, G. Nunzi Conti, D. Ristic, and S. Soria. "Whispering Gallery Mode microresonators: Fundamentals and applications." In: *Rivista del Nuovo Cimento* 34 (2011), pp. 435–488. DOI: 10.1393/ncr/i2011-10067-2.

[16] M. Gomilšek. *Whispering gallery modes*. Tech. rep. University of Ljubljana, 2011, p. 15.

[17] S. Yang, Y. Wang, and H. Sun. "Advances and Prospects for Whispering Gallery Mode Microcavities." In: *Advanced Optical Materials* 3 (2015), pp. 1136–1162. DOI: 10.1002/adom.201500232.

[18] D.V. Strekalov, C. Marquardt, A.B. Matsko, H.G.L. Schwefel, and G. Leuchs. "Nonlinear and quantum optics with whispering gallery resonators." In: *Journal of Optics* 18 (2016), p. 123002. DOI: 10.1088/2040-8978/18/12/123002.

[19] A.B. Matsko, A.A. Savchenkov, D. Strekalov, V.S. Ilchenko, and L. Maleki. "Review of Applications of Whispering-Gallery Mode Resonators in Photonics and Nonlinear Optics." In: *IPN Progress Report* 42 (2005), pp. 1–51.

[20] Q. Ma, T. Rossmann, and Z. Guo. "Temperature sensitivity of silica micro-resonators." In: *Journal of Physics D: Applied Physics* 41 (2008), p. 245111. DOI: 10.1088/0022-3727/41/24/245111.

[21] A. Rahman. "Temperature sensor based on dielectric optical microresonator." In: *Optical Fiber Technology* 17 (2011), pp. 536–540. DOI: 10.1016/j.yofte.2011.06.014.

[22] J.M. Ward, N. Dhasmana, and S. Nic Chormaic. "Hollow core, whispering gallery resonator sensors." In: *The European Physical Journal Special Topics* 223 (2014), pp. 1917–1935. DOI: 10.1140/epjst/e2014-02236-5.

[23] P. Bianucci. "Optical microbottle resonators for sensing." In: *Sensors (Switzerland)* 16 (2016). DOI: 10.3390/s16111841.

[24] G. Righini and S. Soria. "Biosensing by WGM Microspherical Resonators." In: *Sensors* 16 (2016), p. 905. DOI: 10.3390/s16060905.

[25] A. Petermann, T. Hildebrandt, U. Morgner, B. Roth, and M. Meinhardt-Wollweber. "Polymer Based Whispering Gallery Mode Humidity Sensor." In: *Sensors* 18 (2018), p. 2383. DOI: 10.3390/s18072383.

[26] M.R. Foreman, J.D. Swaim, and F. Vollmer. "Whispering gallery mode sensors." In: *Advances in Optics and Photonics* 7 (2015), p. 168. DOI: 10.1364/AOP.7.000168.

[27] A. Bozzola, S. Perotto, and F. De Angelis. "Hybrid plasmonic–photonic whispering gallery mode resonators for sensing: a critical review." In: *The Analyst* 142 (2017), pp. 883–898. DOI: 10.1039/C6AN02693A.

[28] A. Tereshchenko, M. Bechelany, R. Viter, V. Khranovskyy, V. Smyntyna, N. Starodub, and R. Yakimova. "Optical biosensors based on ZnO nanostructures: advantages and perspectives. A review." In: *Sensors and Actuators B: Chemical* 229 (2016), pp. 664–677. DOI: 10.1016/j.snb.2016.01.099.

[29] M. Wang, J.T. Lin, Y.X. Xu, Z.W. Fang, L.L. Qiao, Z.M. Liu, W. Fang, and Y. Cheng. "Fabrication of high-Q microresonators in dielectric materials using a femtosecond laser: Principle and applications." In: *Optics Communications* 395 (2017), pp. 249–260. DOI: 10.1016/j.optcom.2016.05.025.

[30] A. Chiasera, Y. Dumeige, P. Féron, M. Ferrari, Y. Jestin, G. Nunzi Conti, S. Pelli, S. Soria, and G.C. Righini. "Spherical whispering-gallery-mode microresonators." In: *Laser & Photonics Reviews* 4 (2010), pp. 457–482. DOI: 10.1002/lpor.200910016.

[31] T.W. Hänsch. "Nobel Lecture: Passion for precision." In: *Reviews of Modern Physics* 78 (2006), pp. 1297–1309. DOI: 10.1103/RevModPhys.78.1297.

[32] T. Herr, V. Brasch, J.D. Jost, C.Y. Wang, N.M. Kondratiev, M.L. Gorodetsky, and T.J. Kippenberg. "Temporal solitons in optical microresonators." In: *Nature Photonics* 8 (2014), pp. 145–152. DOI: 10.1038/nphoton.2013.343.

[33] T.J. Kippenberg, A.L. Gaeta, M. Lipson, and M.L. Gorodetsky. "Dissipative Kerr solitons in optical microresonators." In: *Science* 361 (2018), eaan8083. DOI: 10.1126/science.aan8083.

[34] M. Karpov, M.H.P. Pfeiffer, H. Guo, W. Weng, J. Liu, and T.J. Kippenberg. "Dynamics of soliton crystals in optical microresonators." In: *Nature Physics* 15 (2019), pp. 1071–1077. DOI: 10.1038/s41567-019-0635-0.

[35] N. Riesen, S. Afshar Vahid, A. François, and T.M. Monro. "Material candidates for optical frequency comb generation in microspheres." In: *Optics Express* 23 (2015), p. 14784. DOI: 10.1364/OE.23.014784.

[36] A. Pasquazi, M. Peccianti, L. Razzari, D.J. Moss, S. Coen, M. Erkintalo, Y.K. Chembo, T. Hansson, S. Wabnitz, P. Del'Haye, X. Xue, A.M. Weiner, and R. Morandotti. "Micro-combs: A novel generation of optical sources." In: *Physics Reports* 729 (2018), pp. 1–81. DOI: 10.1016/j.physrep.2017.08.004.

[37] J. Ye, H. Schnatz, and L.W. Hollberg. "Optical Frequency Combs: From Frequency Metrology to Optical Phase Control." In: *IEEE Journal on Selected Topics in Quantum Electronics* 9 (2003), pp. 1041–1058. DOI: 10.1109/JSTQE.2003.819109.

[38] T. Fortier and E. Baumann. "20 Years of Developments in Optical Frequency Comb Technology and Applications." In: *Communications Physics* 2 (2019), pp. 1–16. DOI: 10.1038/s42005-019-0249-y. arXiv: 1909.05384.

[39] K. Niizeki, D. Yoshida, K. Ito, I. Nakamura, N. Takei, K. Okamura, M.Y. Zheng, X.P. Xie, and T. Horikiri. "Two-photon comb with wavelength conversion and 20-km distribution for quantum communication." In: *Communications Physics* 3 (2020), pp. 1–7. DOI: 10.1038/s42005-020-00406-1.

[40] R. Gotti, T. Puppe, Y. Mayzlin, J. Robinson-Tait, S. Wójtewicz, D. Gatti, B. Alsaif, M. Lamperti, P. Laporta, F. Rohde, R. Wilk, P. Leisching, W.G. Kaenders, and M. Marangoni. "Comb-locked frequency-swept synthesizer for high precision broadband spectroscopy." In: *Scientific Reports* 10 (2020), pp. 1–10. DOI: 10.1038/s41598-020-59398-1.

[41] J. Pfeifle, C. Weimann, F. Bach, J. Riemensberger, K. Hartinger, D. Hillerkuss, M. Jordan, R. Holtzwarth, T.J. Kippenberg, J. Leuthold, W. Freude, and C. Koos. "Microresonator-Based Optical Frequency Combs for High-Bitrate WDM Data Transmission." In: *Optical Fiber Communication Conference*. Washington, D.C.: OSA, 2012, OW1C.4. DOI: 10.1364/OFC.2012.OW1C.4.

[42] E.A. Anashkina, M.P. Marisova, A.V. Andrianov, R.A. Akhmedzhanov, R. Murnieks, M.D. Tokman, L. Skladova, I.V. Oladyshkin, T. Salgals, I. Lyashuk, A. Sorokin, S. Spolitis, G. Leuchs, and V. Bobrovs. "Microsphere-Based Optical Frequency Comb Generator for 200 GHz Spaced WDM Data Transmission System." In: *Photonics* 7 (2020), p. 72. DOI: 10.3390/photonics7030072.

[43] A.E. Siegman. *Lasers*. University Science Books,U.S., 1986, p. 1283.

[44] R. Paschotta. *Gain Media*. Visited on 30.10.2020. URL: https://www.rp-photonics.com/gain_media.html.

[45] M. Bertolotti. *The History of Laser*. IOP Publishing Ltd., 1999, p. 316.

[46] W.T. Silfvast. *Laser Fundamentals*. Cambridge University Press, 2012, p. 674.

[47] G. Schunk, J.U. Fürst, M. Förtsch, D.V. Strekalov, U. Vogl, F. Sedlmeir, H.G.L. Schwefel, G. Leuchs, and C. Marquardt. "Identifying modes of large whispering-gallery mode resonators from the spectrum and emission pattern." In: *Optics Express* 22 (2014), p. 30795. DOI: 10.1364/OE.22.030795.

[48] M.Y. Ye, M.X. Shen, and X.M. Lin. "Transmission spectra of sausage-like microresonators." In: *Optics Express* 23 (2015), p. 25846. DOI: 10.1364/OE.23.025846.

[49] J. Tang, J. Liu, C.. Shang, C. Xie, H. Guo, K. Qian, C. Xue, and J. Liu. "Fabrication and spectral characterizations of high Q asymmetric resonant cavities." In: *Optics Communications* 355 (2015), pp. 269–273. DOI: 10.1016/j.optcom.2015.06.077.

[50] H. Lee, M.G. Suh, T. Chen, J. Li, S.A. Diddams, and K.J. Vahala. "Spiral resonators for on-chip laser frequency stabilization." In: *Nature Communications* 4 (2013), p. 2468. DOI: 10.1038/ncomms3468.

[51] W. Pongruengkiat and S. Pechprasarn. "Whispering-Gallery Mode Resonators for Detecting Cancer." In: *Sensors* 17 (2017), p. 2095. DOI: 10.3390/s17092095.

[52] S.B. Papp, P Del'Haye, and S.A. Diddams. "Mechanical Control of a Microrod-Resonator Optical Frequency Comb." In: *Physical Review X* 3 (2013), p. 031003. DOI: 10.1103/PhysRevX.3.031003. arXiv: 1205.4272.

[53] I.S. Grudinin, V.S. Ilchenko, and L. Maleki. "Ultrahigh optical Q factors of crystalline resonators in the linear regime." In: *Physical Review A* 74 (2006), p. 063806. DOI: 10.1103/PhysRevA.74.063806.

[54] S. Fujii and T. Tanabe. "Dispersion engineering and measurement of whispering gallery mode microresonator for Kerr frequency comb generation." In: *Nanophotonics* 9 (2020), pp. 1087–1104. DOI: 10.1515/nanoph-2019-0497.

[55] A. Barucci, S. Berneschi, A. Giannetti, F. Baldini, A. Cosci, S. Pelli, D. Farnesi, G. Righini, S. Soria, and G. Nunzi Conti. "Optical Microbubble Resonators with High Refractive Index Inner Coating for Bio-Sensing Applications: An Analytical Approach." In: *Sensors* 16 (2016), p. 1992. DOI: 10.3390/s16121992.

[56] L. Shang, A. Wen, B. Li, and T. Wang. "Coupled spiral-shaped microring resonator-based unidirectional add–drop filters with gapless coupling." In: *Journal of Optics* 13 (2011), p. 015503. DOI: 10.1088/2040-8978/13/1/015503.

[57] M.L. Gorodetsky, A.A. Savchenkov, and V.S. Ilchenko. "Ultimate Q of optical microsphere resonators." In: *Optics Letters* 21 (1996), p. 453. DOI: 10.1364/OL.21.000453.

[58] T. Toyoda and M. Yabe. "The temperature dependence of the refractive indices of fused silica and crystal quartz." In: *Journal of Physics D: Applied Physics* 16 (1983), pp. L97–L100. DOI: 10.1088/0022-3727/16/5/002.

[59] M. Tabib-Azar, P.S. Pathak, G. Ponchak, and S. LeClair. "Nondestructive superresolution imaging of defects and nonuniformities in metals, semiconductors, dielectrics, composites, and plants using evanescent microwaves." In: *Review of Scientific Instruments* 70 (1999), pp. 2783–2792. DOI: 10.1063/1.1149795.

[60] S.M. Spillane, T.J. Kippenberg, O.J. Painter, and K.J. Vahala. "Ideality in a Fiber-Taper-Coupled Microresonator System for Application to Cavity Quantum Electrodynamics." In: *Physical Review Letters* 91 (2003), p. 043902. DOI: 10.1103/PhysRevLett.91.043902.

[61] B.E. Little, J.P. Laine, D.R. Lim, H.A. Haus, L.C. Kimerling, and S.T. Chu. "Pedestal antiresonant reflecting waveguides for robust coupling to microsphere resonators and for microphotonic circuits." In: *Optics Letters* 25 (2000), p. 73. DOI: 10.1364/OL.25.000073.

[62] F.de Fornel. *Evanescent Waves: From Newtonian Optics to Atomic Optics*. Springer, 2001.

[63] R. Paschotta. *Total Internal Reflection*. Visited on 28.06.2017. URL: https://www.rp-photonics.com/total_internal_reflection.html.

[64] V.S. Olkhovsky and E. Recami. "Recent developments in the time analysis of tunneling processes." In: *Physics Reports* 214 (1992), pp. 339–356. DOI: 10.1016/0370-1573(92)90015-R.

[65] A.A. Savchenkov, H. Mahalingam, V.S. Ilchenko, S. Takahashi, A.B. Matsko, W.H. Steier, and L. Maleki. "Polymer Waveguide Couplers for Fluorite Microresonators." In: *IEEE Photonics Technology Letters* 29 (2017), pp. 667–670. DOI: 10.1109/LPT.2017.2675279.

[66] O. Leminger and R. Zengerle. "Determination of the variable core-to-surface spacing of single-mode fiber-coupler blocks." In: *Optics Letters* 12 (1987), p. 211. DOI: 10.1364/OL.12.000211.

[67] B.D. Hauer, P.H. Kim, C. Doolin, A.J.R. MacDonald, H. Ramp, and J.P. Davis. "On-chip cavity optomechanical coupling." In: *EPJ Techniques and Instrumentation* 1 (2014), p. 4. DOI: 10.1140/epjti4. arXiv: 1401.5482.

[68] G. Adamovsky and M.V. Ötügen. "Morphology-Dependent Resonances and Their Applications to Sensing in Aerospace Environments." In: *Journal of Aerospace Computing, Information, and Communication* 5 (2008), pp. 409–424. DOI: 10.2514/1.35775.

[69] T. Weigel, C. Esen, G. Schweiger, and A. Ostendorf. "Whispering gallery mode pressure sensing." In: *Proceedings of SPIE - The International Society for Optical Engineering*. Ed. by F. Berghmans, A.G. Mignani, and P. De Moor. Vol. 8439. 2012, 84390T. DOI: 10.1117/12.921759.

[70] O. Llopis, P.H. Merrer, A. Bouchier, K. Saleh, and G. Cibiel. "High-Q optical resonators: characterization and application to stabilization of lasers and high spectral purity microwave oscillators." In: *Proceedings of SPIE Photonics West*. Ed. by A.V. Kudryashov, A.H. Paxton, and V.S. Ilchenko. 2010, 75791B. DOI: 10.1117/12.847164.

[71] M.F. Limonov, M.V. Rybin, A.N. Poddubny, and Y.S. Kivshar. "Fano resonances in photonics." In: *Nature Photonics* 11 (2017), pp. 543–554. DOI: 10.1038/nphoton.2017.142.

[72] D.A. Steck. *Rubidium 87 D Line Data*. Tech. rep. available online (revision 2.1.1, 30 April 2009). 2009. URL: http://steck.us/alkalidata.

[73] A.A. Chaaya, R. Viter, I. Baleviciute, M. Bechelany, A. Ramanavicius, Z. Gertnere, D. Erts, V. Smyntyna, and P. Miele. "Tuning Optical Properties of Al 2 O 3 /ZnO Nanolaminates Synthesized by Atomic Layer Deposition." In: *The Journal of Physical Chemistry C* 118 (2014), pp. 3811–3819. DOI: 10.1021/jp411970w.

[74] N. German, A. Kausaite-Minkstimiene, A. Ramanavicius, T. Semashko, R. Mikhailova, and A. Ramanaviciene. "The use of different glucose oxidases for the development of an amperometric reagentless glucose biosensor based on gold nanoparticles covered by polypyrrole." In: *Electrochimica Acta* 169 (2015), pp. 326–333. DOI: 10.1016/j.electacta.2015.04.072.

[75] J.L. Hall and T.W. Hänsch. "History Of Optical Comb Development." In: *Femtosecond Optical Frequency Comb: Principle, Operation and Applications*. Kluwer Academic Publishers / Springer Norwell, MA, 2004.

[76] R. Paschotta. *Beat Note*. Visited on 15.03.2014. URL: http://www.rp-photonics.com/beat_note.html15.03.2014.

[77] T.J. Kippenberg, S.M. Spillane, and K.J. Vahala. "Kerr-Nonlinearity Optical Parametric Oscillation in an Ultrahigh-Q Toroid Microcavity." In: *Physical Review Letters* 93 (2004), p. 083904. DOI: 10.1103/PhysRevLett.93.083904.

[78] A.A. Savchenkov, A.B. Matsko, D. Strekalov, M. Mohageg, V.S. Ilchenko, and L. Maleki. "Low Threshold Optical Oscillations in a Whispering Gallery Mode CaF2 Resonator." In: *Physical Review Letters* 93 (2004), p. 243905. DOI: 10.1103/PhysRevLett.93.243905.

[79] I.H. Agha, Y. Okawachi, M.A. Foster, J.E. Sharping, and A.L. Gaeta. "Four-wave-mixing parametric oscillations in dispersion-compensated high-Q silica microspheres." In: *Physical Review A* 76 (2007), p. 043837. DOI: 10.1103/PhysRevA.76.043837.

[80] P. Del'Haye, A. Schliesser, O. Arcizet, T. Wilken, R. Holzwarth, and T.J. Kippenberg. "Optical frequency comb generation from a monolithic microresonator." In: *Nature* 450 (2007), pp. 1214–1217. DOI: 10.1038/nature06401.

[81] I.S. Grudinin, N. Yu, and L. Maleki. "Generation of optical frequency combs with a CaF_2 resonator." In: *Optics Letters* 34 (2009), p. 878. DOI: 10.1364/OL.34.000878.

[82] J.S. Levy, A. Gondarenko, M.A. Foster, A.C. Turner-Foster, A.L. Gaeta, and M. Lipson. "CMOS-compatible multiple-wavelength oscillator for on-chip optical interconnects." In: *Nature Photonics* 4 (2010), pp. 37–40. DOI: 10.1038/nphoton.2009.259.

[83] K.E. Webb, M. Erkintalo, S. Coen, and S.G. Murdoch. "Experimental observation of coherent cavity soliton frequency combs in silica microspheres." In: *Optics Letters* 41 (2016), p. 4613. DOI: 10.1364/OL.41.004613. arXiv: 1608.03370.

[84] S. Zhu, L. Shi, L. Ren, Y. Zhao, B. Jiang, B. Xiao, and X. Zhang. "Controllable Kerr and Raman-Kerr frequency combs in functionalized microsphere resonators." In: *Nanophotonics* 8 (2019), pp. 2321–2329. DOI: 10.1515/nanoph-2019-0342.

[85] R. Paschotta. *Chromatic Dispersion*. Visited on 4.11.2020. URL: https://www.rp-photonics.com/chromatic_dispersion.html.

[86] R. Paschotta. *Four-wave Mixing*. Visited on 24.05.2021. URL: https://www.rp-photonics.com/four_wave_mixing.html.

[87] T. Carmon, L. Yang, and K.J. Vahala. "Dynamical thermal behavior and thermal self-stability of microcavities." In: *Optics Express* 12 (2004), p. 4742. DOI: 10.1364/OPEX.12.004742.

[88] T. Kobatake, T. Kato, H. Itobe, Y. Nakagawa, and T. Tanabe. "Thermal Effects on Kerr Comb Generation in a CaF 2 Whispering-Gallery Mode Microcavity." In: *IEEE Photonics Journal* 8 (2016), pp. 1–9. DOI: 10.1109/JPHOT.2016.2538965.

[89] A. Pasquazi, M. Peccianti, L. Razzari, D.J. Moss, S. Coen, M. Erkintalo, Y.K. Chembo, T. Hansson, S. Wabnitz, P. Del'Haye, X. Xue, A.M. Weiner, and R. Morandotti. "Micro-combs: A novel generation of optical sources." In: *Physics Reports* 729 (2018), pp. 1–81. DOI: 10.1016/j.physrep.2017.08.004.

[90] Xiaozaojun. *Understand WDM in one minute*. Visited on 17.02.2021. URL: https://www.programmersought.com/article/39614155370/.

[91] A. Kovach, D. Chen, J. He, H. Choi, A.H. Dogan, M. Ghasemkhani, H. Taheri, and A.M. Armani. "Emerging material systems for integrated optical Kerr frequency combs." In: *Advances in Optics and Photonics* 12 (2020), p. 135. DOI: 10.1364/AOP.376924.

[92] A. Udalcovs, T. Salgals, L. Zhang, X. Pang, A. Djupsjöbacka, S. Spolitis, V. Bobrovs, S. Popov, and O. Ozolins. "Optical Power Budget of 25+ Gbps IM/DD PON with Digital Signal Post-Equalization." In: *Applied Sciences* 10 (2020), p. 6106. DOI: 10.3390/app10176106.

[93] V.B. Juska and M.E. Pemble. "A Critical Review of Electrochemical Glucose Sensing: Evolution of Biosensor Platforms Based on Advanced Nanosystems." In: *Sensors* 20.21 (2020), p. 6013. DOI: 10.3390/s20216013. URL: https://www.mdpi.com/1424-8220/20/21/6013.

[94] J.M. Hollas. *Modern Spectroscopy*. Wiley, 2004, p. 482.

[95] R. Nave. *Hydrogen Fine Structure*. Visited on 25.10.2016. URL: http://hyperphysics.phy-astr.gsu.edu/hbase/quantum/hydfin.html.

[96] S. Gray. *Hyperfine Splitting*. Visited on 12.01.2017. URL: http://chem.libretexts.org/Core/Physical_and_Theoretical_Chemistry/Spectroscopy/Magnetic_Resonance_Spectroscopies/Electron_Paramagnetic_Resonance/Hyperfine_Splitting.

Part II

APPENDIX

A

PUBLICATIONS

[P1] I. Brice, K. Grundsteins, A. Atvars, J. Alnis, and R. Viter. "Whispering gallery mode resonators coated with Au nanoparticles." In: *Nanoengineering: Fabrication, Properties, Optics, Thin Films, and Devices XVI*. Ed. by A.J. Attias and B. Panchapakesan. Proceedings of SPIE, 2019, p. 65. DOI: 10.1117/12.2528677

[P2] I. Brice, K. Grundsteins, A. Atvars, J. Alnis, R. Viter, and A. Ramanavicius. "Whispering gallery mode resonator and glucose oxidase based glucose biosensor." In: *Sensors and Actuators B: Chemical* 318 (2020), p. 128004. DOI: 10.1016/j.snb.2020.128004

[P3] I. Brice, R. Viter, K. Draguns, K. Grundsteins, A. Atvars, J. Alnis, E. Coy, and I. Iatsunskyi. "Whispering gallery mode resonators covered by a ZnO nanolayer." In: *Optik* 219 (2020), p. 165296. DOI: 10.1016/j.ijleo.2020.165296

[P4] I. Brice, K. Grundsteins, A. Sedulis, T. Salgals, S. Spolitis, V. Bobrovs, and J. Alnis. "Frequency comb generation in whispering gallery mode silica microsphere resonators." In: *Laser Resonators, Microresonators, and Beam Control XXIII*. Ed. by A.M. Armani, A.V. Kudryashov, A.H. Paxton, V.S. Ilchenko, and J.V. Sheldakova. Vol. 11672. Proceedings of SPIE, 2021, p. 1167213. DOI: 10.1117/12.2577148

Whispering gallery mode resonators coated with Au nanoparticles

Inga Brice, Karlis Grundsteins, Aigars Atvars, Janis Alnis, and Roman Viter

Institute of Atomic Physics and Spectroscopy, University of Latvia,
Jelgavas Street 3, Riga, Latvia

ABSTRACT

Whispering gallery mode resonators (WGMRs) are very interesting for sensing because a resonance shift could be caused by any perturbation of the surrounding environment. Additionally such a resonator is coated with nanomaterials to tailor and enhance the sensitivity for a specific purpose. WGMR were fabricated using standard telecommunication fiber and a hydrogen flame, characterized using the scan method to obtain the quality factors and then coated with gold nanoparticles (Au NPs) using dip coating method and characterized again for comparison. Au NPs were chosen because their positive impact on microresonator sensitivity has been mentioned before and the surface can later be functionalized. The deposited layer was investigated and new properties no over-coupling due to Van der Waals forces and suppression of higher order modes were observed after coating the resonator. To observe the localized surface plasmon resonance a glucose sensor test was performed using the WGMRs coated with Au NPs and glucose oxidase. Comparing the results with control measurements, the resonance shifted more for samples with Au NPs.

Keywords: WGMR, surface functionalizaion, Q factor, Au NPs, Van der Waals forces, glucose sensor

1. INTRODUCTION

Whispering gallery mode resonators (WGMRs) are optical microsensors. Among different types of photonic sensor devices the WGMRs are known with their ultra high quality (Q) factors. One of the important properties of WGMR is the sensitivity to changes in the surrounding medium. Any perturbation to the optical path of the coupled light inside the WGMR results in the shift of the resonance spectrum.[1] This makes them interesting for sensing applications. The sensitivity of WGMRs is directly related to its Q factor. The Q factor indicates the amount of energy stored within the system divided by the energy loss. Therefore, inside a WGMR with higher Q factor the loss of energy is slower and the resonances can circulate longer. As result, the light can interact with the surrounding media and nanoparticles (NPs) attached to the surface of the WGMR multiple times.

Silica microsphere WGMRs with a very high Q factor of 10^7 - 10^8 can be easily fabricated directly on the tip of a standard telecom fiber by melting in hydrogen flame.[2] The surface of the resonator can be coated by nanomaterials layer. It is important to form a homogeneous and thin coating in the range 10 - 100 nm to provide effective light coupling[1,3] However, coating silica microspheres with any type NPs through deposition on the surface will lead to the degradation of the Q factor due to the increased losses from the absorption in the coating and scattering from the surface roughness. Nevertheless, the NPs may bring other important surface properties and improve the usefulness of the WGMR.

For example, the WGM resonators can be combined with localized surface Plasmon resonance (LSPR) nanostructures to enhance the sensitivity of WGM sensors by extending the evanescent field with large tails out of the metal particles.[4] The LSPR in gold nanoparticles (Au NPs) has been the subject of intense research efforts.[5] The Au NPs have the ability to amplify the electromagnetic field at nanometric distance from the metal surface while being highly chemically and photo-stable.

In this paper we report on dip-coating deposition of Au NPs on top of WGMR (WGMR-Au) from water solution. Coated resonators showed weaker van der Waals forces between the WGMR and a glass coupling prism. WGMR-Au resonators were modified with glucose oxidize (GOx) and tested to glucose (GLC). Q factor and kinetic parameters of the developed sensor probes were analyzed. Sensitivity and response time of the WGMR-Au-GOx structures to GLC were estimated. Possible mechanisms of interaction were discussed.

Inga Brice: E-mail: inga.brice@lu.lv

Nanoengineering: Fabrication, Properties, Optics, Thin Films, and Devices XVI,
edited by Balaji Panchapakesan, André-Jean Attias, Proc. of SPIE Vol. 11089,
110891T · © 2019 SPIE · CCC code: 0277-786X/19/$21 · doi: 10.1117/12.2528677

2. MATERIALS AND METHODS

2.1 Materials

GOx and GLC were purchased from Sigma Aldrich. Colloidal suspension Au NPs (average size 13 nm) in water was prepared as described in 6.

2.2 Fabrication of WGMR

WGMRs were fabricated from a standard Corning SMF28 Optical Telecommunication fiber. A Hydrogen flame torch was used as a heating source to reduce chance of soot, toxic or unwanted fumes from residing on the surface of the WGMR. The fiber was cut and stripped and soaked in acetone to remove any remains of the protective fiber jacket and cleaned with ethanol to remove possible dust particles from the surface of optical fiber. The striped and cleaned telecom fiber was attached to a step motor and slowly moved towards the flame. It melted and due to surface tension a microsphere grew on the tip of the fiber stem. To better observe the fabrication process a camera (Eakins Microscope Camera) was used. A blue LED light can be used for contrast to better see the transparent fiber and the growing sphere. The final result was WGMR spheres with a diameter of 0.3 mm - 0.7mm. The drawbacks of this method are the ability to fabricate only 1 sphere at a time and a low repeatability to obtain spheres with the same diameter. Also the stripped and cleaned fiber should be exposed to the ambient air for the shortest time possible before melting to reduce the amount of moisture silica adsorbs because excess moisture will lead to the drop of Q factor.

2.3 Measurement of WGMR response

The resonators were characterized using the scan method. A basic scheme of the measurement system is shown in Fig. 1A. The measurement system was set up using a scan-wavelength 780 nm ECDL laser (spectral line <1MHz) to excite the resonances, a couple mirrors, focusing lens (F = 1 cm) and coupling prism to provide a light coupling into the WGMR. A photo-detector (Photodiode HL7851G) connected with an oscilloscope (RIGOL DS1074 4 channel) was used to record the transmittance signal. The transmission dips correspond to a series of WGM resonances (see Fig. 1C blue line). Additionally, two reference signals are used (see Fig. 1C green and orange lines). First reference is the ^{85}Rb and ^{87}Rb D2 lines obtained using saturation spectroscopy. Second reference is interferometer fringes from optical fiber, which has flat ends. First reference was used to calculate the interferometer period of 48.78 MHz for the second reference and to follow the laser frequency drift in time. The second reference was used to monitor the laser scan mode and calibrate frequency of the transmitted spectra signals. The resonators were characterized by calculated Q factors. The Q factor of a WGMR describes the ability to store energy inside the microcavity and indicates the fraction of light lost during each cycle around the cavity. Mathematically it can be described as:

$$Q = \frac{\omega}{\Delta\omega} = \omega\tau, \tag{1}$$

where ω is the frequency of the resonance mode and $\Delta\omega$ is the full width at half maximum (FWHM) and τ is the lifetime of light in the resonator. Several losses limit the maximum value of the optical Q factor of the resonator: surface scattering, material losses, influence of the coupler, and the radiative loss.[7] The $\Delta\omega$ is obtained by fitting the resonance dip using a Lorentz function (see Fig. 1D) and Eq. 1. The calculated Q factors of the fabricated silica microspheres was up to 10^8.

The Q factor of the resonator is formed by two main types of losses:

$$\frac{1}{Q} = \frac{1}{Q_0} + \frac{1}{Q_e}, \tag{2}$$

where Q_0 are internal coupling losses and Q_e external coupling losses. Q_e can be adjusted by changing the gap between the coupling prism or tapered fiber and the resonator, thus changing the overlap between the evanescent fields of the resonator and coupling element.[8] If the resonator is too far from the surface of the prism, where the evanescent wave is located, then the field is too faint to efficiently couple the light in to the resonator. Then

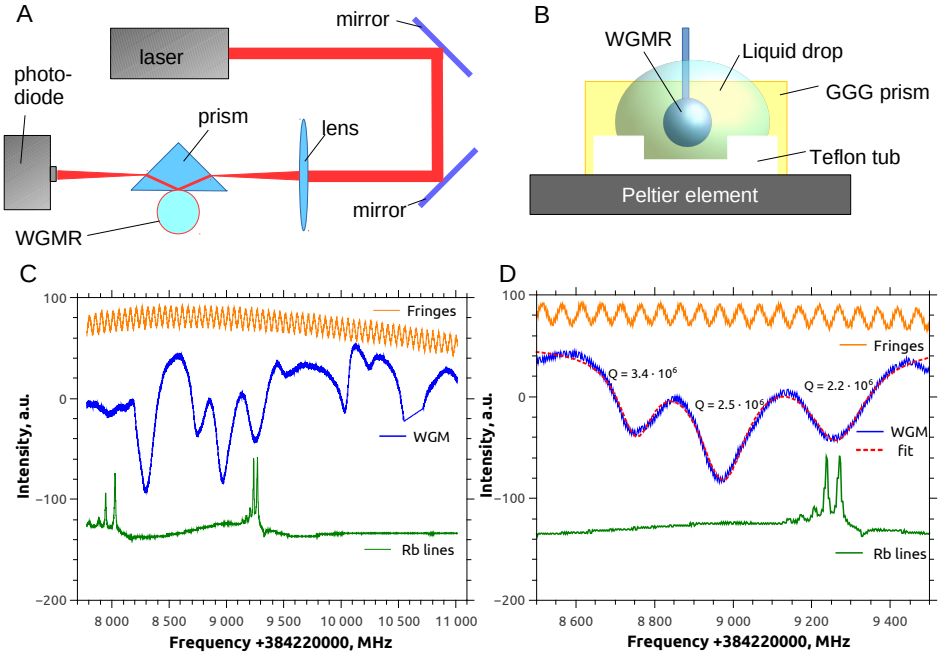

Figure 1. The experimental measurement system and results. (A) Basic scheme from the top view to characterize the WGMR in the air using a glass prism to couple light; (B) a scheme from the side view for measurements in liquids where a GGG prism is used instead mounted on a Peltier element for temperature stabilization, and a small teflon tub to hold liquid droplet are used; (C) acquired data consisting of WGM resonance spectra and references Rb lines and interferometer fringes; (D) data fitted with a Lorentz function and calculated Q factors for several resonances.

$Q_e > Q_0$ and is known as the under coupling. If the resonator is too close to the surface, the resonances broaden. This happens when $Q_e < Q_0$ and is known as over coupling. Critical coupling is the point where a certain gap is achieved between coupler and microresonator so that $Q_e = Q_0$ and the entire coupled power is lost inside the resonator. Between a glass coupling prism and silica WGMR strong van der Waals forces have been observed. The WGMR clings to the surface of the prism and makes it difficult to control the gap between the two. Rarely can critical coupling be done by simply increasing the distance because the fiber stem is flexible and the WGMR simply "pops away" from the surface suddenly. It has to be slowly moved towards the prism. If the attempt is unsuccessful and van der Waals forces have attached the resonator to the surface of the prism, the distance is again increased and then slowly decreased, the process repeated until success. The gap is crucial to obtain critical coupling conditions for resonators with very high Q factors ($5 \cdot 10^7$ or higher) else over-coupling severely broadens the WGM resonances leading to inaccurate Q factor calculations and loss of sensitivity occurs.

2.4 Au deposition, GOx modification and GLC testing

The characterized WGM silica microspheres were coated with Au by dip coating the resonator in solution containing the Au NPs to enhance the sensitivity of the resonator. The Au NP size is 10 - 13 nm. Afterwards the WGMR coated with Au NPs (WGMR-Au) was characterized using the measurement system and the structure of the coating studied using SEM images. To determine if Au NPs enhance the sensitivity of the resonator a GLC sensor response was observed by using a slightly modified measurement test system (see Fig. 1B). The glass prism was substituted with a GGG prism and a small Teflon tub for containing the liquid. Both were mounted on a Peltier element (Melcor 2x2 cm) with a temperature sensor (AD590). It was used to minimize sensitivity of

the WGMR to the temperature by stabilizing the temperature a couple degrees below room temperature. To test whether LSPR resonances in Au NPs enhance the sensitivity of WGMR a GLC sensor response was performed. WGMR-Au was dip coated in GOx - an enzyme widely used to determine the presence of GLC in liquids. Using the modified test system a WGM resonances are first found in air. Then a drop of buffer solution (75 μl) is added on the resonator. The resonance position shifts slightly and should be adjusted. Next a small amount of GLC solution with a known concentration (c = 1.8 mM) is added to the buffer drop (75 μl). If the temperature of the GLC solution is different tan the temperature used to stabilize the system it may take a minute or two for the system to temperature stabilize. The data of a Rb line position and a resonance peak is recorded in time using LabWIEW. For comparison several control measurements are also performed. The same test is performed using WGMR coated in GOx without coating them with Au NPs first, WGMR-Au without coating them with GOx and WGMR without any coatings.

3. RESULTS AND DISCUSSION

When characterizing the WGMR with the measurement test system between a glass coupling prism and silica WGMR van der Waals forces have been observed. The resonators stick to the surface of the prism and makes it difficult to control the gap between the two. However, this gap becomes crucial to obtain critical coupling conditions for resonators with very high Q factors. As seen in Fig. 2A the resonances become very broad when the resonator touched the prism and calculations are off for about an order of magnitude. WGMR-Au have demonstrated weaker van der Waals forces and no resonance line broadening even when the WGMR-Au touches the prism and higher order modes are suppressed (see Fig. 2B).

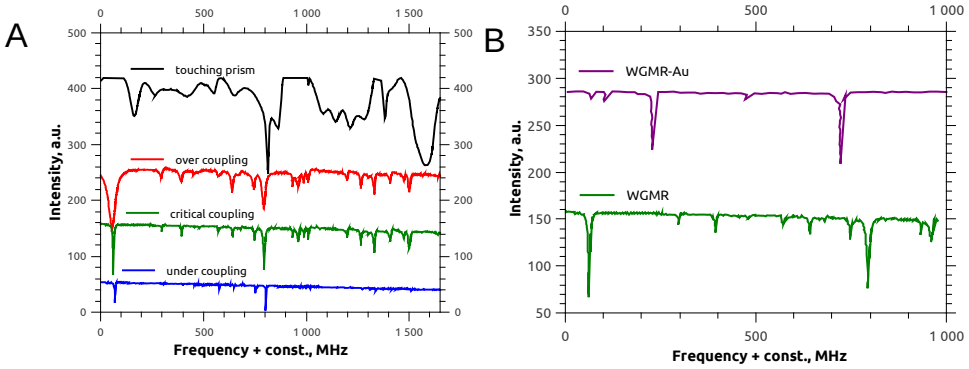

Figure 2. WGMR with Q factor $6 \cdot 10^7$ (A) coupling conditions before coating with Au NPs: blue line under-coupling when the gap is too big and signal is very weak, green line critical coupling conditions optimal for measurements and , red line over-coupling when the gap is too small and the resonances become broader, black line over-coupling when resonator touches the prism due to van der Waals force attraction and the Q factor drops to $9 \cdot 10^6$; (B) Comparing WGMR before coating with critical coupling conditions and WGMR-Au touching the prism during coupling (Q factor $5.4 \cdot 10^7$) resonance signal.

It was found that the Au NPs was randomly attached to the WGMR surface forming clusters of 200 nm in diameter. The changes in WGMR and WGMR-Au optical response were shown in Fig. 3A-E. Forming of WGMR-Au resulted in decrease of the Q factor. The intensity of excited modes dropped proportionally to concentration of Au NPs, deposited on the surface (see Fig. 3E). The observed results related to light scattering on Au nanoclusters on the WGMR surface.

The results of GLC sensor tests can be seen in Fig. 4A.The signal are similar in the first couple of minutes for all measurements and the position of the resonance increases exponentially. WGMRs are very sensitive to temperature changes:

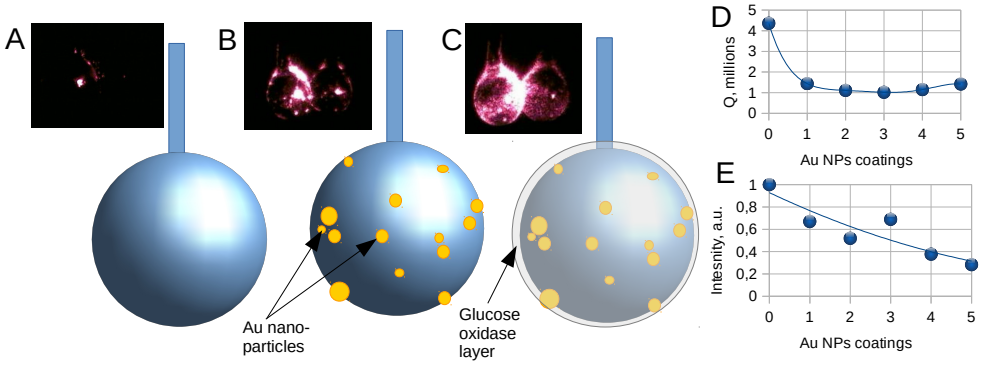

Figure 3. WGMR a basic scheme of surface and as seen in camera when coupling using measurement system (A) before coating the surface does not scatter the light as no particles are attached to the surface; (B) after coating the Au NPs attach to some places on the surface and scatter light intensively; (C) after coating with the GOx a layer coats the whole surface and it scatters the light; (D) coating the same WGMR with Au NPs multiple times the Q factor noticeably drops after the firs coat and (E) the intensity of the resonances decreases rapidly.

$$\frac{d\omega}{\omega} = -\left(\frac{1}{n}\frac{\partial n}{\partial T} + \frac{1}{r}\frac{\partial r}{\partial T}\right) dT, \tag{3}$$

where $d\omega$ is the frequency shift and ω is the frequency of the resonance, n is the refraction index and r is the radius of the WGMR and dT is the temperature shift. The exponential signal occurs due to a temperature difference between the liquid sample at room temperature and the WGMR temperature stabilized a couple degrees lower. It could be excluded by cooling the sample liquid to the same temperate as the resonator.

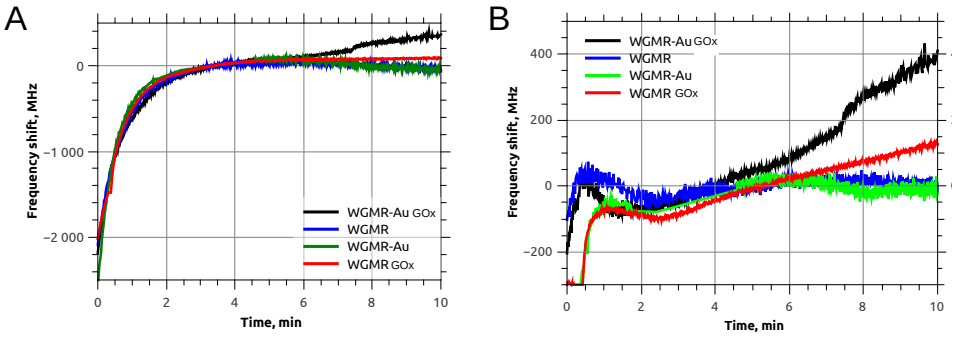

Figure 4. GLC sensor test responses for three control samples (unmodified WGMR, WGMR-Au and WGMR GOx sample) and a WGMR-Au-Gox sample (A) before and (B) after removing evaporation and temperature effects from the data. Samples without the GOx were not sensitive to GLC, but resonance of WGMR GOx shifted $\sim$ 200 MHz and the resonance of WGMR-Au-GOx sample shifted $\sim$ 400 MHz in about 7 minute period after the temperature stabilization.

The two control measurement curves of WGMR and WGMR-Au without any GOx are not sensitive to GLC. Both curves are very similar. However, after reaching temperature stability the resonance frequency starts decreasing. This happens as the drop containing GLC evaporates, and the concentration increases. This effect is diminished by the relatively big liquid drop volume and the stabilization temperature, however, the relatively longer measurement time still allows to detect it. The other two samples should be sensitive to GLC in the

liquid drop. When the WGMR are coated with GOx the effects of evaporation are still present but are surpassed by the response to GLC. For WGMR-Au the effect is stronger due to LSPR resonance effect. The evaporation effect was removed from the data by approximating the control curves without the sensor response with a linear slope and substantiating it from data. Similarly temperature exponent then is approximated and subtracted from curves. The data without the evaporation end temperature can be seen in Fig. 4B. The first two minutes of data are complicated and have residue from the temperature stabilization cycle and other unknown fast effects may be present. Control measurements without GOx do not shift in time and the GLC sensor response can be only seen for samples coated with GOx. WGMR-Au is more sensitive and the resonance shifts two times more than without Au NPs.

The observed WGMR shifts in WGMR-Au-GOx structures after GLC incubation are related to three main processes: evaporation of water from dropped solution, charge transfer due to GLC-GOx interaction and refractive index changes due to GLC-GOx complex formation. Water evaporation is a long term process. It is reflected in the kinetic curves at times more than 10 minutes. Charge transfer should change electron concentration in Au NP and stimulate high changes in Au refractive index. As it was not observed, we suppose the third mechanism of interaction, related to the change of refractive index on the surface of WGMR.

Control measurements of bare WGMR and non modified WGMR-Au showed the influence of evaporation and non-specific interaction between GLC and the resonator surface. After subtracting of the base signal, the specific signal of WGMR-Au-GOx - GLC interaction was achieved. Average response time was of 1-2 minutes. The developed sensor platform will be available for detection of glucose in the range of necessary for medical applications in glucose monitoring.

ACKNOWLEDGMENTS

We thank for financial support **ERDF project No. 1.1.1.1/16/A/259**: Development of novel WGM microresonators for optical frequency standards and biosensors, and their characterization with a femtosecond optical frequency comb.

REFERENCES

[1] Foreman, M., Swaim, J., and Vollmer, F., "Whispering gallery mode sensors," *Advances in Optics and Photonics* **7**(2), 168–240 (2015).

[2] Brice, I., Pirktina, A., Ubele, A., Grundsteins, K., A, A., Viter, R., and Alnis, J., "Development of optical wgm resonators for biosensors," in [*Biophotonics-Riga 2017*], *Proceedings of SPIE* **10592** (2017).

[3] Righini, G. and Soria, S., "Biosensing by wgm microspherical resonators," *Sensors (Basel)* **16**(6) (2016).

[4] Bozzola, A., Perotto, S., and Angelis, F., "Hybrid plasmonicphotonic whispering gallery mode resonators for sensing: a critical review.," *Analyst* **14**(6), 883–898 (2012).

[5] Amendola, V., Pilot, R., Frasconi, M., Marago, Q., and Iati, M., "Surface plasmon resonance in gold nanoparticles: a review.," *Journal of Physics: Condensed Matter* **29**(20) (2017).

[6] Ramanaviciene, A., Voronovic, J., Popov, A., Drevinskas, R., Kausaite-Minkstimiene, A., and Ramanavicius, A., "Investigation of biocatalytic enlargement of gold nanoparticles using dynamic light scattering and atomic force microscopy," *Colloids and Surfaces A: Physicochemical and Engineering Aspects* **510**, 183–189 (2016).

[7] Grudinin, I., Ilchenko, V., and Maleki, L., "Ultrahigh optical q factors of crystalline resonators in the linear regime," *Physical Review A - Atomic, Molecular and Optical Physics* **74**(6) (2006).

[8] Ma, Q., "Fabrication, characterization and sensor applications of optical whispering gallery mode coupling system.," (2010).

Sensors & Actuators: B. Chemical 318 (2020) 128004

Contents lists available at ScienceDirect

Sensors and Actuators B: Chemical

journal homepage: www.elsevier.com/locate/snb

Whispering gallery mode resonator and glucose oxidase based glucose biosensor

Inga Brice[a], Karlis Grundsteins[a], Aigars Atvars[a], Janis Alnis[a], Roman Viter[a,b,*], Arunas Ramanavicius[c,**]

[a] Institute of Atomic Physics and Spectroscopy, University of Latvia, Jelgavas Street 3, Riga, LV-1004, Latvia
[b] Center for Collective Use of Scientific Equipment, Sumy State University, 31, Sanatornaya st., 40018 Sumy, Ukraine
[c] Department of Physical Chemistry, Institute of Chemistry, Faculty of Chemistry and Geosciences, Vilnius University, Naugarduko 24, LT-03225 Vilnius, Lithuania

ARTICLE INFO

Keywords:
Whispering gallery mode (WGM) resonators
Glucose oxidase based optical biosensors
Gold nanoparticles (Au-NPs)
Localized surface plasmon resonance (LSPR)
Optical fiber based biosensors
Enzymatic biosensors

ABSTRACT

In this research whispering gallery mode resonators (WGMRs) were applied in new concept of glucose sensor based on the shift of WGM resonance frequency induced by enzymatic oxidation of glucose by glucose oxidase (GOx), which was immobilized on WGM-resonator surface. During the enzymatic reaction catalyzed by GOx electrons from glucose via GOx are transferred towards co-immobilized gold nanoparticles (Au-NPs). WGM-resonators were fabricated from standard telecommunication optical-fiber melted in a hydrogen flame. Whispering gallery mode resonance based optical signals generated by these WGM-resonators were evaluated. These WGM-resonators, which were characterized by sufficient quality factors, were modified with Au-NPs using dip coating method in order to form hybrid WGM-resonator (WGMRs/Au-NPs) structure. Then WGMRs/Au-NPs structure was investigated using SEM and, after these investigations, the sensitivity of WGMRs/Au-NPs-based resonators towards glucose has been assessed by the evaluation whispering gallery mode resonance based optical signals. Then the next modification step of WGMRs/Au-NPs resonators by enzyme – GOx – has been performed in order to design WGMRs/Au-NPs/GOx-based resonator structure, which showed increased sensitivity towards glucose in comparison to that of WGMRs/GOx-based resonators, which were not modified by Au-NPs. WGMRs/Au-NPs/GOx-based glucose sensor was tested at several glucose concentrations in the range up to 2.4 mM and it was determined that WGM-resonance frequency shift rate significantly increases at higher glucose concentrations. Therefore, WGM-resonance frequency shift rate was determined as characteristic of analytical signal suitable for the determination of glucose concentrations by sensors based on both WGMRs/GOx and WGMR/Au-NPs/GOx resonators.

1. Introduction

Whispering gallery mode (WGM) resonators (WGMRs) are expected to be suitable transducers in the development of optical micro-sensors, because among different types of photonic devices, the WGM-resonators are characterized by their ultra-high quality (Q) factors. One of the important properties of WGM-resonators is the sensitivity to some changes in the surrounding medium. Any perturbation in the optical path of the coupled light inside the WGM-resonator results into the shift of the resonance frequencies of WGM spectra [1–4]. WGM-resonators, which are based on silica microspheres, can be easily fabricated directly on the tip of a standard telecom optical-fiber by melting it in hydrogen flame and mostly such WGM-resonators are characterized by a very high Q factor of 10^7 - 10^8 [5,6]. In order to increase the selectivity of WGM-resonators the surface of the resonator can be modified by particular materials [1,4,7,8]. It was demonstrated that effective light coupling can be achieved if homogeneous and thin coating layer in the range of 10–100 nm, which is below the evanescent field penetration depth, is formed [8,9]. However, coating of silica microspheres with the most types of nanoparticles (NPs) through NPs deposition on the surface is leading to the degradation of the Q factor due to the increased signal losses due to optical absorption of the coating and scattering of light from the rough surface modified by NPs [6,10,11]. But despite of some above mentioned disadvantages, the NPs may provide useful

* Corresponding author at: Institute of Atomic Physics and Spectroscopy, University of Latvia, Jelgavas Street 3, Riga, LV-1004, Latvia; Center for Collective Use of Scientific Equipment, Sumy State University, 31, Sanatornaya st., 40018 Sumy, Ukraine
** Corresponding author at: Department of Physical Chemistry, Institute of Chemistry, Faculty of Chemistry and Geosciences, Vilnius University, Naugarduko 24, LT-03225 Vilnius, Lithuania
E-mail addresses: roman.viter@lu.lv (R. Viter), Arunas.ramanavicius@chf.vu.lt (A. Ramanavicius).

https://doi.org/10.1016/j.snb.2020.128004
Received 25 November 2019; Received in revised form 1 March 2020; Accepted 14 March 2020
Available online 06 May 2020
0925-4005/

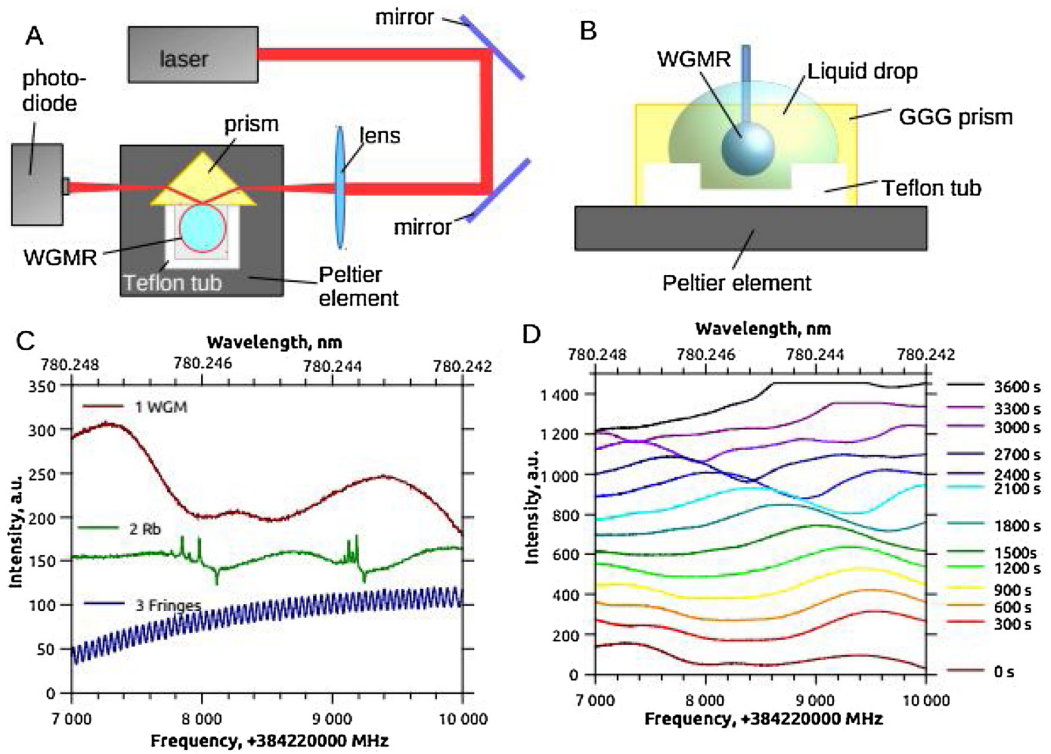

Fig. 1. Representation of experimental measurement system and registered WGM-based optical signals. A – measurement scheme, which was applied to characterize the WGM-resonators based GGG prism, lens and mirrors; B – side view of WGM-resonator mounting, which is based on a small Teflon tube to hold liquid droplet formed on a Peltier element for temperature stabilization; C – data acquired during WGM measurement: WGM-resonance spectra (curve 1), references Rb lines (curve 2) and interferometer fringes (curve 3); D – variation of analytical signals based on WGM-resonance frequency shift registered with WGMR/Au-NPs/GOx-based resonator in 1.2 mM of glucose containing solution drop in time.

physico-chemical properties, which improve the efficiency of WGMRs modified by nanoparticles [8,12–14]. Due to above mentioned effects, the WGMRs can be combined with localized surface plasmon resonance (LSPR) generating nanostructures in order to enhance the sensitivity of WGMRs-based sensors by extending the evanescent field with large tails out of the metal particles [15–17]. Therefore, gold nanoparticles (Au-NPs), which exhibit LSPR, have been the subject of intense research efforts [12,18]. In addition, Au-NPs have the ability to amplify the electromagnetic field at nanometric distance from the metal surface while being highly chemically and photo-stable.

In this paper we have evaluated the applicability of differently modified WGM-resonators for sensing of glucose. We have designed and tested several different modifications of WGM-resonators: (i) modified by Au-NPs (WGMR/Au-NPs), (ii) modified by glucose oxidase (WGMR/GOx) and (iii) modified by Au-NPs and glucose oxidase (WGMR/Au-NPs/GOx). *Q* factor and kinetic parameters of sensors based on these resonators were analyzed. Sensitivity and response time of all above mentioned WGMR-based structures towards glucose has been estimated and possible mechanisms of development of WGM-based analytical signals have been discussed.

2. Materials and methods

2.1. Materials

Enzyme – glucose oxidase (GOx) – and their substrate – glucose – were purchased from Sigma Aldrich. Glucose solutions containing 1.2–4.8 mM of glucose was used for biosensor testing. Glucose oxidase was deposited on WGMRs from 10 mg/mL solution in PBS, pH 7.4. Colloidal suspension of Au-NPs (average diameter – 13 nm) dispersed in water (concentration of suspension – 3,75 nM) was prepared as it is described in previous research [19].

2.2. Fabrication of WGMRs

WGMRs were fabricated from a standard Corning SMF28 Optical Telecommunication fiber. The fiber was cut, stripped and soaked in acetone to remove any remains of the protective fiber jacket and cleaned with ethanol to remove all impurities from the surface of optical fiber [5]. The striped and cleaned telecom fiber was attached to a step motor and slowly moved towards the flame. A hydrogen flame torch was used as a heating source to reduce formation of soot, toxic or unwanted fumes from residing on the surface of the WGMRs. The silica melted and due to surface tension a microsphere grew on the tip of the fiber stem. Video microscope camera, Eakins (China) was used to observe the fabrication process. A blue LED light has been used to get better contrast during the imaging of transparent optical fiber and the growing sphere. The diameter of the resonator was determined by optical microscopy as 634 μm (Fig. S2A).

2.3. Modification of WGMRs by Au-NPs and GOx

To enhance the sensitivity the WGM-resonators were modified with Au-NPs by dip-coating procedure. During this procedure the resonator was dipped into water based colloidal solution of Au-NPs, which were of 13 nm diameter, for 15 – 20 s. The structure of the coating was imaged by scanning electron microscope (SEM) S4800 from Hitachi High-Technologies (Tokyo, Japan). The sensitivity of WGMRs towards

glucose was evaluated at several glucose concentrations in the range from 0 up to 4.8 mM. A set of different WGM-resonators (namely WGMR/Au-NPs, WGMR/GOx and WGMR/Au-NPs/GOx) was fabricated using below described surface modification procedures. WGMR/Au-NPs/GOx-based resonator structure was designed by dip-coating based modification of WGM-resonator by Au-NPs followed by dip-coating of WGMR/Au-NPs in water based solution containing 10 mg/mL of glucose oxidase (GOx) – an enzyme, which is oxidizing glucose and is often used in the design of various glucose sensors that are mostly based on the determination of electrochemical [20] or optical [21] signals. Similarly were prepared WGMR/GOx-based resonator structures: bare WGM-resonators were dip-coated by GOx in 10 mg/mL of glucose oxidase (GOx) containing solution.

2.4. Measurement of WGM-resonance based analytical signal

WGM-resonators (WGMR/GOx or WGMR/Au-NPs/GOx) were mounted into optical system (Fig. 1A) to determine WGM-resonances of resonators covered by a liquid drop containing known glucose concentration. The resonance frequencies of both WGMR/GOx or WGMR/Au-NPs/GOx resonators are shifting due to GOx-catalyzed oxidation of glucose. To determine WGM-resonance frequency shifts that are triggered by GOx-catalyzed oxidation of glucose several different WGM-resonators (namely WGMR/Au-NPs, WGMR/GOx, WGMR/Au-NPs/GOx and bare-WGMR) were investigated by the deposition of a glucose containing solution on the surface of these WGM-resonators. WGM-resonance frequency shift rate was determined as analytical signal suitable for the determination of glucose concentrations by above mentioned WGM-resonators. The WGM-resonator structures, which are the most sensitive towards glucose are shifting WGM resonance frequencies much faster in comparison to others.

The WGM-resonance spectra of differently modified WGM-resonators were recorded using the laser frequency scan method. A basic scheme of the measurement system is represented in Fig. 1A and B. The measurement system was based on sweep of optical wavelengths in the range from 780.23 up to 780.25 nm. For this 780 nm ECDL laser with spectral line < 1 MHz was applied to excite the WGM-resonances, in addition a couple mirrors, focusing lens (F = 1 cm) and coupling prism (GGG) were used to provide a light coupling into the WGM-resonator (Fig. 1A), and a small Teflon tub was applied to hold the liquid on WGM-resonator surface (Fig. 1B). Both the prism and the tub were mounted on a Peltier element Melcor 2 × 2 cm from Melcor Corporation (Lawrence Township, USA) with a temperature sensor AD590 from Analog Devices (Norwood, USA). A photo-detector based on Photodiode THORLABS PDA-36A from THORLABS (Newton, United States) connected with a 4 channel oscilloscope RIGOL DS1074 from RIGOL Technologies (Beijing, China) was used to register the transmittance spectra. The transmission dips correspond to a series of WGM-resonances (Fig. 1C curve 1" WGM"). Additionally, two reference signals were used (Fig. 1C curve 2" Rb" and curve 3" Fringes"): first reference is the ^{85}Rb and ^{87}Rb 5s-5p D_2 lines registered using saturation spectroscopy; second reference is interferometer fringes from optical fiber, which has flat ends. First reference was used to calculate the interferometer period of 48.78 MHz for the second reference and to follow the laser frequency drift in time. The second reference was used to monitor the laser scan mode and to calibrate frequency of the transmitted spectra signals. More details about the calibration of optical system are presented in 'Supplementary Material' figure S1: The laser was adjusted in a mode to measure both ^{87}Rb D2 and ^{85}Rb D2 lines in the scanning region. The hyper fine structure consists of 3 Rb lines with known frequencies and 3 cross over peaks for each isotope D_2 line; First reference was used to calculate (Fig. S1A3) the interferometer period of 48.78 MHz for the second reference, to follow the laser frequency drift due to change of ambient room conditions by choosing one of the Rb lines as 'data point 0', and to indicate the absolute frequency; The second reference was used to monitor the laser scan mode; Observing the reference signal obtained from fringes it is clear that the laser frequency scanning is nonlinear and, therefore, additional calibration of the laser scan frequency using the fringes was performed (Fig. S1B); Transmission spectra signals were then obtained in frequency scale and the corresponding wavelength scale was added (Fig. S1C).

The WGM-resonators were characterized by calculating the quality factor (*Q* factor). The *Q* factor is a characteristic of a WGM-resonator describes the ability to store light energy inside the 'micro-cavity', which is the main part of WGM resonator. Mathematically it can be described as:

$$Q = \frac{\omega}{\Delta\omega} = \omega\tau \quad (1)$$

where ω is the frequency of the mode and $\Delta\omega$ is the full width at a half maximum (FWHM) and τ is averaged lifetime of light scattering within the resonator. Losses of optical intensity of the beam are limiting the maximal value of the optical *Q* factor of the resonator: surface scattering, material losses, influence of the coupler, and the radiative loss [22]. The $\Delta\omega$ is determined by fitting the WGMRs resonance signal using a Lorentz function, which is used to calculate the *Q* factor [5]. If resonators are covered by liquid materials observed WGM resonances became broader than that registered in air. In air a bare-WGMR was characterized by $Q = 1.4{\cdot}10^6$, when it was covered by PBS, pH 7.4, was characterized by $Q = 0.7{\cdot}10^6$.

To determine the influence of Au-NPs on the enhancement of the sensitivity of WGM-resonators towards glucose the responses of several different sensing structures (bare-WGMR, WGMR/GOx, WGMR/Au-NPs and WGMR/Au-NPs/GOx) were evaluated. WGM resonance based signals for each resonator were first determined in air using the test system, which are presented in Fig. 1. More details about the WGM resonances and *Q* factors of different structures are presented in 'Supplementary Material' figure S2: WGM-resonance spectra (Fig. S2B curve 1) was evaluated and the Q factor was determined as 1.4×10^8; The resonator image was determined by optical camera during the coupling (i) before any modifications (Fig. S2C); after the coating of WGM-resonator with Au-NPs (WGMR/Au-NPs structure) individual nanoparticles can be seen while the light is being coupled inside the WGMR/Au-NPs (Fig. S2D) and the area of resonance frequencies become broader (Fig. S2B curve 2) and Q factor become lower than that before the modification – 2×10^6. When the GOx is deposited on the surface of WGMR/Au-NPs structure the scattered light from the whole surface could be observed by the camera during coupling (Fig. S2E), however, for WGMR/Au-NPs/GOx no resonances were detected in the air (Fig. S2B curve 3); In contrary, when a drop of PBS was distributed over WGMR/Au-NPs/GOx-based resonator then several resonance frequencies (Fig. S2B curve 4) were determined and Q factor become lower than that before any previous modification – $Q = 6 \times 10^5$.

During WGM-measurements in liquid aliquots a drop (75 μL) of buffer solution was carefully distributed on WGM-resonator as it is illustrated in Fig. 1B. Then the WGM-resonator was attached to the x-y-z translation stage by the fiber stem on which it was formed on. Then the most optimal coupling position of WGM-resonance frequencies shifted slightly due to the change of coupling conditions in liquid environment and, therefore, the coupling was adjusted by aligning the laser and the resonator. The addition of the drop was performed very gently in order to prevent the touching and or damaging of the resonator. In such was a 75 μL of 1.2–4.8 mM glucose solution with a known glucose concentration was gently deposited on WGM-resonator. The temperature of all solutions including glucose solution was stabilized to a room temperature before all experiments. The WGM-resonances for evaluated WGM-resonators were observed at different time periods (Fig. 1D). The data of a Rb line position and a resonance peak were registered using LabWIEW software. Several control measurements were also performed in order to determine the influence of each material used for the modification of WGM-resonators. The same test was performed for all types of WGM-resonators based on: bare-WGMR, WGMR/Au-NPs,

WGMR/GOx and WGMR/Au-Nps/GOx structures.

3. Results and discussion

If the optical fiber was moved towards the hydrogen flame slowly, a small, round sphere resonator was formed with the core and cladding melted together. When the fiber was moved rapidly, a much bigger spheres were formed, which were more elliptical and the core spirals inside the cladding were formed from the core and cladding was not melted together. The final result of fabrication was a formation of WGM-resonator spheres with a diameter of 0.3 mm – 0.7 mm. The drawback of this method is the ability to fabricate only 1 sphere at a time. Also, we have determined that, the stripped and cleaned fiber should be exposed to the ambient air for possibly shortest time before melting in order to reduce the amount of impurities, which may attach to the surface of WGM-resonator, what in such case will lead to the decrease of *Q* factor. This issue is critical, because the sensitivity of WGM-resonators is directly related to *Q* factor of the resonator. The *Q* factor represents the energy stored within WGM-resonator divided by the energy, which is lost during single cycle of light beam within WGM-resonator. Therefore, inside a WGM-resonator with higher *Q* factor the loss of energy is slower and the light circulates within the resonator for a longer time. As a result, the light can interact with media, which is surrounding WGM-resonator.

Au-NPs were chosen for the modification of WGM-resonator because their ability to reflect visible light and in this way to increase the sensitivity of WGM-resonators. From SEM images, which are presented in Fig. 2A, it was determined that the size of Au-NPs, which were adsorbed to Si substrate, is in the range of 10 – 13 nm. However, the Au-NPs were randomly adsorbed on the surface of WGM-resonator, which are forming clusters that were of 200 nm in diameter. Also the rate in which a flat and curved surface is coated by NPs is different [23] and, therefore, surface density of deposited NP cannot be directly compared. The differences of bare-WGM-resonator, WGMR/Au-NPs and WGMR/Au-NPs/GOx optical response are shown in Fig. 2C–E. Before the modification of WGM-resonator with AuNPs the light is just slightly scattered by some features formed on the surface of WGM-resonator. Therefore, the bare-WGMR surface is rather dark (Fig. 2C). After the modification of the surface with Au-NPs significant light-scattering was observed on many spots of the WGMR/Au-NPs-surface (Fig. 2D), this effect is related to light scattering by clusters consisting of Au-NPs, which were formed on the surface of WGMR/Au-NPs. The surface of WGMR/Au-NPs/GOx is seen in Fig. 2E and in such way the whole surface is coated with GOx and it scatters light.

The WGM-resonators, which were characterized by sufficient quality factors, were coated with gold nanoparticles (Au-NPs) using dip coating method in order to get advanced WGM resonator structure (WGMRs/Au-NPs). Fig. 2A and B illustrates that some Au-NPs are agglomerating together and are forming larger clusters.

WGMR/Au-NPs-based resonators were modified with glucose oxidizing enzyme – GOx, and in this way WGMR/Au-NPs/GOx-based resonators were formed, which were tested in the presence of different glucose concentrations. Several control measurements were performed to avoid misinterpretation of analytical signal, which is based on the shift of WGM resonance induced by glucose oxidation by GOx. During this evaluation the analytical signal variation, which was induced by the change of the temperature and slow evaporation of solvent from solution drop deposited on WGM-resonator, were assessed.

As it is seen from Fig. 1D, the velocity of WGM resonance frequency shift increases when WGM resonance spectra is recorded longer than 1500s. This effect is related to solvent (water) evaporation from the layer which is formed over the WGM-resonator. It should be noted that sensor response towards glucose and water evaporation are shifting WGM-based analytical signal into opposite directions. Some evaporation of water takes over all glucose determination process. Therefore, some attempts to reduce the evaporation of the glucose-containing drop were applied. It was performed by the increase of the liquid volume and decreasing the temperature of the drop and cooling all system below room temperature down to 20 °C. The results of other control measurements and glucose sensor tests is presented in Fig. 3A–C. A control measurement was performed by WGMR/Au-NPs/GOx-based resonator at the same conditions but in this case WGMR/Au-NPs/GOx-based resonator was covered with pure water layer without any glucose. As it is seen from Fig. 3C in such case no WGM resonance frequency shift based response was observed. It confirms that a GOx catalyzed reaction is responsible for the generation of WGM resonance frequency shift based analytical signal of WGMR/Au-NPs/GOx resonator. The analytical signals of all control measurements are similar during the first couple of minutes and the WGM resonance frequency shift velocity increases exponentially. It should be noted, that WGM-resonators are sensitive to temperature changes:

$$\frac{d\omega}{\omega} = -\left(\frac{1}{n}\frac{\partial n}{\partial T} + \frac{1}{r}\frac{\partial r}{\partial T}\right)dT \quad (2)$$

where dω is the frequency shift and ω is the frequency of the resonance, n is the refraction index and r is the radius of the WGM-resonator and dT is the temperature shift. The exponential shift of analytical signal occurs due to a temperature differences between the liquid sample, which is at room temperature, and the WGM-resonator, which in our experiment was stabilized by a bit lower than the room temperature to

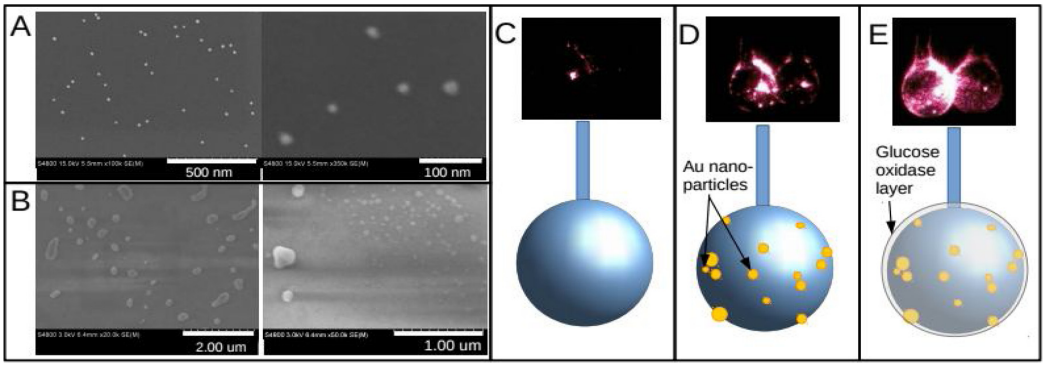

Fig. 2. A – SEM image of Au-NPs deposited on Si substrate, this figure reveals that the size of particles is in the range of 10-13 nm, and B – SEM image of Au-NPs deposited on the surface of WGMR/Au-NPs-based resonator. C – Illustration of WGM-resonator before surface modification (bare-WGMR) in which no light scattering is observed; D – Illustration of WGM-resonator after the modification by Au-NPs (WGMR/Au-NPs), where significant light scattering is observed; E – Illustration of WGMR/Au-NPs resonator after the coating with the GOx (WGMR/Au-NPs/GOx), here even more significant light scattering is observed. Pictures presented in insets C,D,E represent WGMR/Au-NPs pictures, which were taken by optical camera.

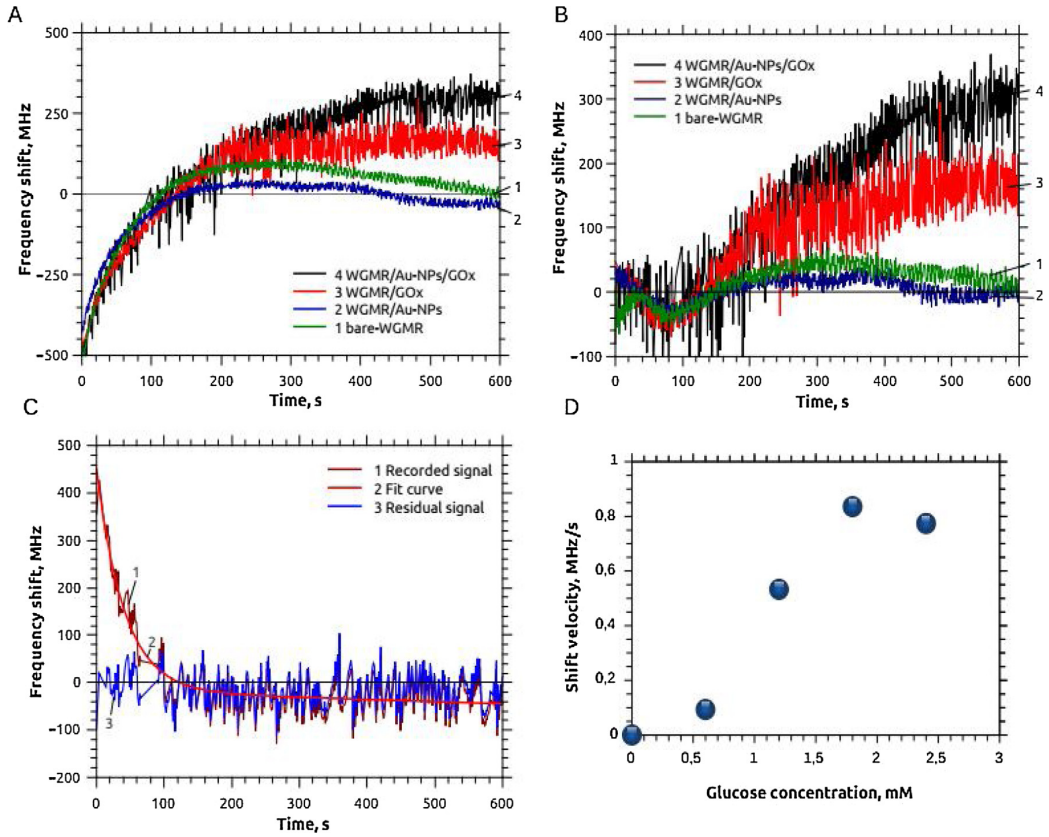

Fig. 3. Responses of glucose sensors based on differently modified WGM-resonators: bare-WGMR (curve 1), WGMR/Au-NPs- (curve 2), WGMR/GOx- (curve 3) and WGMR/Au-NPs/GOx-based resonator (curve 4). A – before and B – after the elimination of evaporation and temperature induced effects from initial data. Both (bare-WGMR and WGMR/Au-NPs) resonators without the GOx were not sensitive to the glucose, while the resonance of WGMR/GOx-based resonator shifted about 180 MHz and the resonance of WGMR/Au-NPs/GOx-based resonator shifted by about 300 MHz. C – WGMR/Au-NPs/GOx tested without glucose. GOx was not sensitive to liquid if no glucose was present. D – The response of WGMR/Au-NPs/GOx-based resonator towards various glucose concentrations.

reduce the evaporation rate of the water layer, which is surrounding the resonator. It should be noted that such WGM-resonance frequency shift based on resonator temperature changes can be easily reduced and/or completely excluded by cooling down the liquid sample to the same temperate as the resonator.

Control measurements performed by sensing systems based on bare-WGMR and WGMR/Au-NPs resonators enabled to investigate the influence of solvent (water) evaporation and the influence of glucose to the formation of analytical signal (Fig. 3A curves 3 and 4). Both measurements are very similar and they illustrate that both (bare-WGMR and WGMR/Au-NPs) structures are insensitive towards glucose. However, after the stabilization of temperature at 20 °C after 200 s WGM resonance frequency starts to decrease (Fig. 3A curves 3 and 4). This effect is observed when the solution drop containing glucose evaporates, and the concentration of glucose increases. Water evaporation is a long term process, which is well reflected in the kinetic curves when the duration of experiment exceeds 10 min (see Fig. 1D). This effect is reduced by the stabilization of temperature below the room temperature at 20 °C. However, if the measurement is performed for relatively long time, then solvent evaporation based effect can be still observed.

The other two sensors based on WGMR/GOx- and WGMR/Au-NPs/GOx-based resonators were sensitive towards the presence of glucose in solution drop (Fig. 3A curves 1 and 2). When both WGMR/GOx- and WGMR/Au-NPs/GOx-based resonators were tested, then the effect of evaporation was still at some extent observed, but it is surpassed by the response towards glucose. For WGMR/Au-NPs/GOx-based resonator this effect is stronger due to additional LSPR resonance effect, which is induced by the presence of Au-NPs. The analytical signals at different glucose concentrations were fitted using a function:

$$d\omega = \omega_0 + A{\cdot}exp(-t/\tau) + B{\cdot}t \quad (3)$$

which consist of an exponential part $\omega_0 + A{\cdot}exp(-t/\tau)$ for temperature, as the resonance shift $d\omega$ depends on temperature change dT (see Eq. 2) and the temperature changes exponentially in time t, with coefficients ω_0, A and τ and a linear part $B{\cdot}t$ for evaporation and sensor response with coefficient $B = B_{(evap.)} + B_{(resp.)}$, respectively.

To separate the influence of evaporation $B_{(evap.)}$ from analyte (glucose) induced sensor response $B_{(resp.)}$ the measurements were performed with WGMR/Au-NPs- and WGMR/Au-NPs/GOx-based -resonators and are presented in Table 1. After the subtracting of the recorded signal, which is represented in Fig. 3A, the specific analytical signal of WGMR/Au-NPs/GOx-based resonator induced by GOx catalyzed reaction was extracted as it is represented in Fig. 3B. Average sensor response time was within 60–120 seconds. Analytical signal increased with the increase of glucose concentrations. Charge transfer from glucose *via* GOx towards AuNPs, which also was observed in our previous researches [24–26], is changing charge (free electron concentration) in Au-NP and therefore it stimulates significant changes in Au refractive index. It should be noted that our experiments demonstrate that the difference of refractive index on interphase between solution and WGM-resonator in the presence/absence of glucose was not very significant and therefore it induced only minor variations of

Table 1
The coefficient $B_{(evap.)}$ for WGMR/Au-NPs-based resonator was determined taking into account only the evaporation based WGM resonance frequency shift, coefficient B for WGMR/Au-NP/GOx-based resonator was determined assuming both (i) the evaporation induced WGM resonance frequency shift and (ii) WGM resonance frequency shift induced by GOx-based enzymatic glucose oxidation. Taking into account values of both coefficients (B and $B_{(evap.)}$) $B_{(resp.)}$ was determined for different glucose concentrations as $B_{(resp.)} = B\text{-}B_{(evap.)}$.

C, mM	0.0	0.6	0.9	1.2	2.4
$B_{(evap.)}$, MHz/s	−0.045	0.022	−0.343	−0.289	−0.480
B, MHz/s	−0.044	0.115	0.190	0.547	0.294
$B_{(resp)}$, MHz/s	0.001	0.093	0.533	0.835	0.774

analytical signal.

Calculated analytical signals are shown in Fig. 3B. During the first two minutes registered data are complicated and have some residual effects from the temperature stabilization and some fast surface stabilization effects, which occur after the deposition of the solution drop on sensor surface. Control measurements with bare-WGMR- and WGMR/Au-NPs-based systems do not provide any substantial analytical signal (Fig. 3B, curves 2 and 1), which is observed in the case of WGMR/GOx- and WGMR/Au-NPs/GOx-based resonators (Fig. 3B, curves 3 and 4). In the case of WGMR/Au-NPs/GOx-based resonator the resonance shift was two times higher than that in the case of WGMR/GOx-based resonator (Fig. 3B curves 4 and 3).

The resonance shift observed in the case of WGMR/Au-NPs/GOx-based resonator after the incubation in glucose containing solution is related to several main processes: (i) the evaporation of water from solution drop, (ii) charge (electron) transfer during GOx-catalyzed reaction from glucose towards Au-NPs (in this case from two glucose molecules 4 electrons are transferred towards one GOx molecule, which is a dimer and contains two active sites containing incorporated FAD-based moieties, and in the case of WGMR/Au-NPs/GOx these electrons can be transferred from GOx to Au-NPs as it was demonstrated in some other our researches [24–26], (iii) possible change of refractive index during glucose/-GOx complex formation and (iv) conversion of glucose into glucono lactone, which both are slightly different by values of refraction indexes.

The response of WGMR/Au-NPs/GOx-based sensor for several glucose concentrations is presented in Fig. 3D. The velocity of the WGM resonance shift of WGM-resonators increases when the glucose concentration increases. Fig. 3D illustrate that the dynamic range of such sensor is limited by relatively low Michaelis constant (K_M) of GOx, which is in the range of 1–2 mM [19]. This limitation of dynamic range illustrates that in such way immobilized (adsorbed) GOx is acting in kinetically controlled mode and it one more time illustrates that WGM resonance frequency shift based analytical signal of WGMR/Au-NPs/GOx-based sensor is clearly determined by GOx action.

4. Conclusions and future developments

This research demonstrate that WGM-resonators can be coated with materials, which are increasing sensitivity towards selected analyte, to tailor and to enhance the sensitivity of WGMRs-based sensor. Here presented data illustrate that WGMR/Au-NPs/GOx resonator based sensors are potentially suitable for the determination glucose concentration in water-based samples. We hope that after some optimizations WGMR/Au-NPs/GOx resonator based sensor platform will be suitable for the determination of glucose.

In our future researches we are planning to integrate WGM-resonators within microfluidic chip. The adaptation of WGM-resonator within particular microfluidic system may resolve some in this research mentioned problems related to solvent evaporation and variation of temperature between WGM-resonator and liquid-based aliquot. Our further investigations in this field will be related to the application of whispering gallery mode resonators in the design of some other kinds of biosensors e.g. immunosensors, etc.

CRediT authorship contribution statement

Inga Brice: Data curation, Formal analysis, Investigation, Methodology, Validation, Visualization, Writing - original draft. **Karlis Grundsteins:** Methodology, Formal analysis. **Aigars Atvars:** Methodology, Formal analysis. **Janis Alnis:** Methodology, Formal analysis. **Roman Viter:** Conceptualization, Methodology, Experiment, Visualization, Writing - review & editing, Formal analysis, Writing - original draft, Funding acquisition, Supervision. **Arunas Ramanavicius:** Conceptualization, Methodology, Visualization, Writing - review & editing, Formal analysis, Supervision.

Declaration of Competing Interest

None.

Acknowledgments

Financial support for IB, KG, AA, RV, AR and JA by ERDF project No. 1.1.1.1/16/A/259 ‘Development of novel WGM microresonators for optical frequency standards and biosensors, and their characterization with a femtosecond optical frequency comb’ and for RV and AR by the European Union’s Horizon 2020 MSCA-RISE-2017 project CanBioSe under grant agreement No: 778157.

Appendix A. Supplementary data

Supplementary material related to this article can be found, in the online version, at doi:https://doi.org/10.1016/j.snb.2020.128004.

References

[1] M.R. Foreman, J.D. Swaim, F. Vollmer, Whispering gallery mode sensors, Adv. Opt. Photonics 7 (2015) 632, https://doi.org/10.1364/AOP.7.000632.
[2] N. Miri, M. Mohammadzaheri, Optical sensing using microspheres with different size and material, IEEE Sens. J. 14 (2014) 3593–3598, https://doi.org/10.1109/JSEN.2014.2329191.
[3] G. Guan, S. Arnold, M.V. Otugen, Temperature measurements using a microoptical sensor based on whispering gallery modes, AIAA J. 44 (2006) 2385–2389, https://doi.org/10.2514/1.20910.
[4] A. Petermann, T. Hildebrandt, U. Morgner, B. Roth, M. Meinhardt-Wollweber, Polymer based whispering gallery mode humidity sensor, Sensors 18 (2018) 2383, https://doi.org/10.3390/s18072383.
[5] J. Alnis, I. Brice, A. Pirktina, A. Ubele, K. Grundsteins, A. Atvars, R. Viter, Development of optical WGM resonators for biosensors, in: J. Spigulis (Ed.), Biophotonics—Riga 2017, SPIE, 2017, , https://doi.org/10.1117/12.2297551 p. 19.
[6] I. Brice, K. Grundsteins, A. Atvars, J. Alnis, R. Viter, Whispering gallery mode resonators coated with Au nanoparticles, in: A.-J. Attias, B. Panchapakesan (Eds.), Nanoeng. Fabr. Prop. Opt. Thin Film. Devices XVI, SPIE, 2019, , https://doi.org/10.1117/12.2528677 p. 65.
[7] S. Soria, S. Berneschi, M. Brenci, F. Cosi, G. Nunzi Conti, S. Pelli, G.C. Righini, Optical microspherical resonators for biomedical sensing, Sensors 11 (2011) 785–805, https://doi.org/10.3390/s110100785.
[8] G. Righini, S. Soria, Biosensing by WGM microspherical resonators, Sensors 16 (2016) 905, https://doi.org/10.3390/s16060905.
[9] A. Barucci, S. Berneschi, A. Giannetti, F. Baldini, A. Cosci, S. Pelli, D. Farnesi, G. Righini, S. Soria, G. Nunzi Conti, Optical microbubble resonators with High refractive index inner coating for bio-sensing applications: an analytical approach, Sensors 16 (2016) 1992, https://doi.org/10.3390/s16121992.
[10] Y. Yin, Y. Niu, L. Dai, M. Ding, Polarization characteristics of gold-coated microdisk resonators, AIP Adv. 7 (2017) 095008, , https://doi.org/10.1063/1.4986982.
[11] I. Kandas, B. Zhang, C. Daengngam, I. Ashry, C.-Y. Jao, B. Peng, S.K. Ozdemir, H.D. Robinson, J.R. Heflin, L. Yang, Y. Xu, High quality factor silica microspheres functionalized with self-assembled nanomaterials, Opt. Express. 21 (2013) 20601, https://doi.org/10.1364/OE.21.020601.
[12] V. Amendola, R. Pilot, M. Frasconi, O.M. Maragò, M.A. Iatì, Surface plasmon resonance in gold nanoparticles: a review, J. Phys. Condens. Matter. 29 (2017) 203002, , https://doi.org/10.1088/1361-648X/aa60f3.
[13] A. Ramachandran, S. Wang, J. Clarke, S.J. Ja, D. Goad, L. Wald, E.M. Flood, E. Knobbe, J.V. Hryniewicz, S.T. Chu, D. Gill, W. Chen, O. King, B.E. Little, A universal biosensing platform based on optical micro-ring resonators, Biosens.

Bioelectron. 23 (2008) 939–944, https://doi.org/10.1016/j.bios.2007.09.007.
[14] R. Guider, D. Gandolfi, T. Chalyan, L. Pasquardini, A. Samusenko, G. Pucker, C. Pederzolli, L. Pavesi, Design and optimization of SiON ring resonator-based biosensors for aflatoxin M1 detection, Sensors 15 (2015) 17300–17312, https://doi.org/10.3390/s150717300.
[15] H. Nadgaran, M. Afkhami Garaei, Enhancement of a whispering gallery mode microtoroid resonator by plasmonic triangular gold nanoprism for label-free biosensor applications, J. Appl. Phys. 118 (2015) 043101, , https://doi.org/10.1063/1.4927266.
[16] A. Bozzola, S. Perotto, F. De Angelis, Hybrid plasmonic–photonic whispering gallery mode resonators for sensing: a critical review, Analyst 142 (2017) 883–898, https://doi.org/10.1039/C6AN02693A.
[17] M.A. Garaei, M. Saliminasab, H. Nadgaran, R. Moradian, A hybrid plasmonic bimetallic nanoshell-microsphere sensor for cancer market protein detection, Plasmonics 12 (2017) 1953–1960, https://doi.org/10.1007/s11468-016-0467-z.
[18] J.-H. Lee, H.-Y. Cho, H. Choi, J.-Y. Lee, J.-W. Choi, Application of gold nanoparticle to plasmonic biosensors, Int. J. Mol. Sci. 19 (2018) 2021, https://doi.org/10.3390/ijms19072021.
[19] N. German, A. Kausaite-Minkstimiene, A. Ramanavicius, T. Semashko, R. Mikhailova, A. Ramanaviciene, The use of different glucose oxidases for the development of an amperometric reagentless glucose biosensor based on gold nanoparticles covered by polypyrrole, Electrochim. Acta. 169 (2015) 326–333, https://doi.org/10.1016/j.electacta.2015.04.072.
[20] A. Ramanavicius, N. German, A. Ramanaviciene, Evaluation of electron transfer in electrochemical system based on immobilized Gold nanoparticles and glucose oxidase, J. Electrochem. Soc. 164 (2017) G45–G49, https://doi.org/10.1149/2.0691704jes.
[21] R. Mikhailova, T. Semashko, O. Demeshko, A. Ramanaviciene, A. Ramanavicius, Effect of some redox mediators on FAD fluorescence of glucose oxidase from penicillium adametzii LF F-2044.1, Enzyme Microb. Technol. 72 (2015) 10–15, https://doi.org/10.1016/j.enzmictec.2015.01.009.
[22] I.S. Grudinin, V.S. Ilchenko, L. Maleki, Ultrahigh optical Q factors of crystalline resonators in the linear regime, Phys. Rev. A. 74 (2006) 063806, , https://doi.org/10.1103/PhysRevA.74.063806.
[23] J. Yi, C.-Y. Jao, I.L.N. Kandas, B. Liu, Y. Xu, H.D. Robinson, Irreversible adsorption of gold nanospheres on fiber optical tapers and microspheres, Appl. Phys. Lett. 100 (2012) 153107, , https://doi.org/10.1063/1.3701730.
[24] A. Ramanaviciene, G. Nastajute, V. Snitka, A. Kausaite, N. German, D. Barauskas-Memenas, A. Ramanavicius, Spectrophotometric evaluation of gold nanoparticles as red-ox mediator for glucose oxidase, Sens. Actuators B Chem. 137 (2009) 483–489, https://doi.org/10.1016/j.snb.2009.01.021.
[25] N. German, A. Ramanavicius, A. Ramanaviciene, Electrochemical deposition of gold nanoparticles on graphite rod for glucose biosensing, Sens. Actuators B Chem. 203 (2014) 25–34, https://doi.org/10.1016/j.snb.2014.06.021.
[26] N. German, A. Ramanavicius, A. Ramanaviciene, Amperometric glucose biosensor based on electrochemically deposited Gold nanoparticles covered by polypyrrole, Electroanalysis 29 (2017) 1267–1277, https://doi.org/10.1002/elan.201600680.

Mg. Phys. Inga Brice is a scientific assistant at Quantum Optics Laboratory, Institute of Atomic Physics and Spectroscopy, University of Latvia. She obtained Mg. in 2013 at University of Latvia by researching luminescence of Ce and Eu ions activated oxyfluoride glass and glass ceramics. Currently I. Brice is a PhD student in University of Latvia researching precision laser spectroscopy using femtosecond optical frequency comb and whispering gallery mode resonators.

Kārlis Grundšteins is a laboratory assistant at Quantum Optics Laboratory, Intstitute of Atomic Physics and Spectroscopy, University of Latvia. Current research interests of K. Grundšteins lie in biosensors, nanomaterials and MEMS based analytical devices. K. Grundšteins is active in preparation and implementation of various research projects.

Dr. Aigars Atvars is a leading researcher at Quantum Optics Laboratory, Institute of Atomic Physics and Spectroscopy, University of Latvia. He obtained his PhD in 2008 at University of Latvia by performing theoretical simulations on atom-light interaction processes in sodium atoms (Rb, Cs). Current research interests of A. Atvars lie in calculations and simulations of various optical processes, including light propagation in whispering gallery mode resonators. A. Atvars is active in preparation and implementation of various research projects.

Dr. Phys. Janis Alnis is leading a Laboratory of Quantum Optics at the Institute of Atomic Physics and Spectroscopy in Riga and is a member of Latvian Academy of Sciences. He received PhD in 2002 from the University of Latvia on gas spectroscopy using semiconductor diode lasers. As a postdoc he worked on hydrogen precision spectroscopy, femtosecond frequency combs and ultra-stable optical resonator design at the Institute of Quantum Optics in Garching, Germany.

Dr. Roman Viter got a MSc degree in physic at Odessa National I.I. Mechnikov University, Odessa, Ukraine in 2000. He got his PhD at Odessa National I.I. Mechnikov University, Odessa, Ukraine in 2011. Since 2014 he has obtained a position of Senior researcher at Institute of Atomic Physics and Spectroscopy, University of Latvia. He is a coordinator of Latvian and H2020 projects. He is a supervisor of MSc, PhD and postdoc projects. His main research is focused on development and characterization of photonic nanomaterials for applications in optical sensors and biosensors

Prof. Habil. Dr. Arunas Ramanavicius is a professor and head of Department of Physical Chemistry at faculty of Chemistry of Vilnius University. He is also leading the laboratory of NanoTechnology at Research Center of Physical Sciences and Technologies. Prof. Arunas Ramanavicius is a member of Lithuanian Academy of sciences. In 1998 he received PhD degree and in 2002 doctor habilitus degree from Vilnius University. Prof. A. Ramanavicius is serving as expert-evaluator in Horizon 2020 program coordinated by European Commission and he is technical advisor of many foundations located in European and non-European countries. He has research interests in various aspects of nanotechnology, bionanotechnology, nanomaterials, biosensorics, bioelectronics, biofuel cells and MEMS based analytical devices. He is/was a national coordinator of several nanotechnology-related COST actions.

Optik - International Journal for Light and Electron Optics 219 (2020) 165296

Contents lists available at ScienceDirect

Optik

journal homepage: www.elsevier.com/locate/ijleo

Whispering gallery mode resonators covered by a ZnO nanolayer

Inga Brice [a], Roman Viter [a,*], Kristians Draguns [a], Karlis Grundsteins [a], Aigars Atvars [a], Janis Alnis [a], Emerson Coy [b], Igor Iatsunskyi [b]

[a] Quantum Optics Laboratory, Institute of Atomic Physics and Spectroscopy, University of Latvia, 19 Raina Blvd., Riga, LV-1586, Latvia
[b] NanoBioMedical Centre, Adam Mickiewicz University, 3 Wszechnicy Piastowkiej Str., 61-614, Poznan, Poland

ARTICLE INFO

Keywords:
Whispering gallery mode resonators (WGMR)
ZnO layer
Optical properties
Surface scattering and radiation losses
Transmission spectra

ABSTRACT

The exceptional ability of whispering gallery mode resonators (WGMRs) to confine light within makes them interesting for sensing applications. The small size and high values of quality (Q) factors of the WGMR can be combined with a broad range of supporting optical elements. The surface of the resonator can be coated to enhance the desired attributes.

In this paper, the impact of the ZnO layer thickness on the Q-factor of the WGMR has been studied. WGMRs were fabricated on a tip of a standard telecom fiber melted with an oxyhydrogen flame. The surface of the WGMR was coated with ZnO nanolayers of different thickness (5–100 nm) by atomic layer deposition (ALD). The Q-factor of as-prepared WGMR was in the range of 10^7, whereas the Q-factor of ZnO-WGMR decreased 2–10 times. The optimal thickness of functional ZnO coating on WGMR was 10−60 nm. Mechanism of the ZnO layer thickness influence to Q-factor was based on two competing phenomena such as the change of refractive index and surface roughness due to ZnO growth. The effect of the ZnO as a protective coating against the Q-factor degradation was studied. The thicker ZnO layers prevented degradation of the Q-factor of the WGMR.

1. Introduction

ZnO is a well-known material for different optoelectronic applications, such as sensors, biosensors, and optical coatings [1–4]. A number of techniques have been developed for ZnO deposition, such as chemical bath deposition, pulsed laser deposition, etc. [5,6]. However, among these methods, Atomic layer deposition (ALD) is a powerful method for conformal deposition of ZnO with tailored structure and optical properties [3,7,8]. In our previous work, we showed that ZnO thickness is an important parameter, influencing crystallization, grain size, band gap and defect concentration [3,7,8]. It was shown that the refractive index of ZnO enhanced with the increase of the thickness due to amorphous-to-crystalline transition [3,7,8].

Whispering gallery mode resonators (WGMRs) are solid-state cavities that confine light in small geometrical volumes for long periods of time [9]. It is achieved by the total internal reflection of light within WGMR. The simplest way of production of WGMR is high temperature melting of an optical fiber by using a heating source, for example, a CO_2 laser or a gas flame [10]. The only disadvantage is the requirement of glass in the form of a rod or fiber and the fabrication of only one microsphere at a time. Due to the round shape, WGMR with low surface roughness and high-Quality factors (Q-factor) in the range of 10^6 to 10^9 is formed on the tip of the optical fiber by surface tension [10,11].

* Corresponding author.
E-mail address: roman.viter@lu.lv (R. Viter).

https://doi.org/10.1016/j.ijleo.2020.165296
Received 18 February 2020; Received in revised form 17 July 2020; Accepted 20 July 2020
Available online 24 July 2020

ZnO microstructures (spheres, rods, etc.) have been used as WGMRs for laser and sensor applications due to a high refractive index (important for light coupling), biocompatibility, and functionality of the surface [12–14]. However, the integration of ALD ZnO nanolayers and WGMRs is still missing the point. It is expected that ZnO nanolayers will limit the Q-factor of WGMRs, protect it from dust and moisture and decrease Van der Waals forces due to the screening of the surface charge of WGMR.

In this paper, we report on the deposition of ZnO ALD nanolayers with different thickness on WGMRs. The structure and optical properties of the layers have been investigated. Q-factor dependence on ZnO thickness was analyzed.

2. Methods and materials

Fused silica telecommunication optical fiber Corning SMF-28 with a diameter of 125 micrometers was used for the fabrication of WGMRs. Optical fibers were pre-treated before the melting in the following procedure:

- removal of the polymeric fiber coating by stripping and solving in acetone;
- ultrasonic treatment of the stripped fiber in ethanol for 5 min;
- drying in clean air flow to prevent the attachment of dust to the wet surface.

A home-made set up for WGMR fabrication by oxyhydrogen flame melting has been developed. The cleaned fiber was inserted into a V-groove fiber holder and fiber tip slowly moved by a motorized translation stage into the oxyhydrogen flame for melting. Due to the surface tension, the melting part of the fiber gradually started to form a spherical shaped tip. Within 10 s a ball has been formed. The fiber end was rotated to assure that the ball formed symmetrically corresponding to the stem of the fiber. As deposited resonators were stored inside a container to avoid degradation. The as-prepared resonator image obtained by an optical microscope showed a symmetric spherical shape with an estimated diameterof 450–600 μm (Fig. 1.A).

WGMR optical testing was performed using the following experimental scheme (Fig. 1.B). The measurement system was set up using a tuneable wavelength external cavity diode laser (Hitachi, HL7851 G, 780 nm, spectral linewidth <1 MHz) to characterize optical properties of microsphere resonators. The laser spot was aligned by using a pair of mirrors and focused with a lens (F = 1 cm). A glass coupling prism provided the light coupling into the WGMR. The coupling process was controlled using a web-camera, which has been modified by removing the IR filter and adding an F = 50 mm photo camera objective lens (Industar 50) for magnification. A photodetector (Thorlabs PDA36A) was connected to an oscilloscope (RIGOL DS1074 4 channel, scan rate 5 ms, sensitivity 1−10 mV) that was used for signal collection.

Successful coupling of the light into the WGMR was observed visually with the camera due to radiative losses and surface scattering. The transmittance spectra were analyzed by using the oscilloscope. It showed transmittance signal dips which correspond to WGM resonances (see Fig. 1.C curve 2). WGMRs with higher Q-factor had narrower resonances. An optical fiber with flat ends was used as a reference signal. The fiber ends acted as an interferometer with a 50 MHz period sinusoidal waveform (see Fig. 1.C curve 1). The frequency scale was recalibrated from arbitrary units to MHz [15]. Resonance was fitted by using a Lorentzian function (see Fig. 1.C curve 3) to calculate the full width half maximum (FWHM). The Q-factor was calculated according to the following equation [16]:

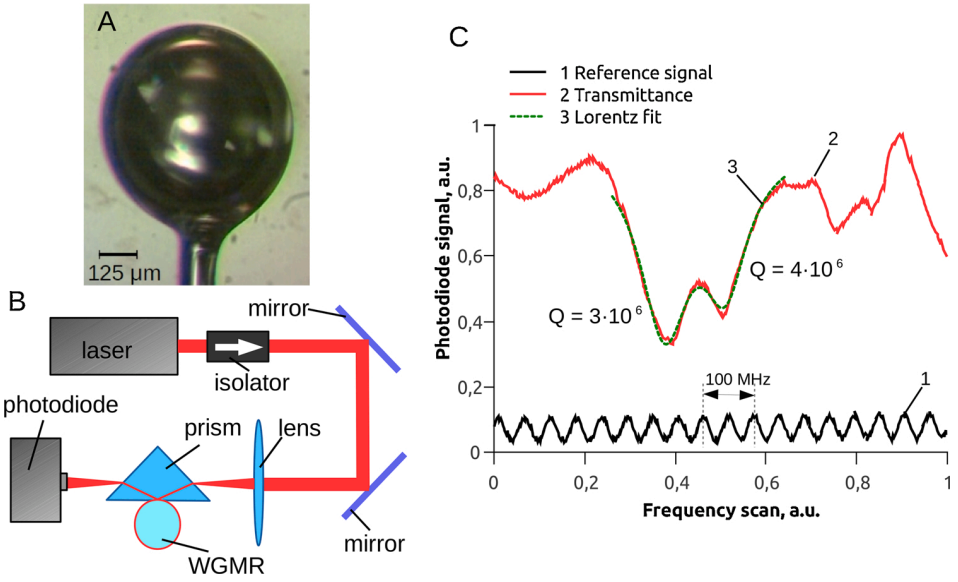

Fig. 1. (A) As-prepared WGMR, (B) WGMR testing system, and (C) resonance spectra of a WGMR coated with 20 nm ZnO ALD layer.

$$Q = \frac{\omega}{\Delta\omega} \tag{1}$$

where ω is the frequency of the light and $\Delta\omega$ is the full width at half maximum of the resonance.

Computer simulations were made by using COMSOL Multiphysics software wave optics module 2D mode. In the proposed model, the silica glass microresonator had a diameter of 10 μm with refractive index $n_{silica} = 1.4585$ and was coated with varying thickness of the ZnO layer with refractive index $n_{ZnO} = 2.0034$. The area around the resonator had a refractive index $n_{air} = 1$ representing the air. At distance $\lambda/12$ there was a 0.5 μm thick and 20 μm long rectangle with ports at either side which represented a tapered fiber. The selected light wavelength was λ =780 nm. The main simulations were performed for the distribution of the z-component of the electric field. This allowed obtaining azimuthal and radial modes in the resonator. Transmittance spectra were first obtained to find the fundamental mode resonance frequency. The same fundamental mode for different thicknesses of the ZnO layer was used to examine the cross-section of the electrical field's intensity. The distance of the resonance mode from the surface was analyzed. To estimate the effect of the surface roughness of the ZnO coating, the equation for the surface of the outer ZnO layer was generated by using random functions. This approach allowed to involve surface roughness and imperfections of the ZnO coating.

ZnO layers were deposited on the WGMR surface by the ALD method. WGMRs were cleaned by oxygen plasma for 30 min using the Reactive Ion Etching (RIE) machine (Microsystems). After plasma cleaning the WGMRs were placed in the ALD reactor (Picosun). The ZnO thin films were deposited onto the resonators using Diethylzinc (DEZ) and deionized (DI) water as ALD precursors. Nitrogen (N_2) flow was used as a carrier and a purging gas. The Zn precursor and water were evaporated at 20 °C. In this study, the standard cycle consisted of 0.4 s DEZ exposure, 4 s N_2 purge, 0.4 s exposure to DI water, and 4 s N_2 purge, which has been used. The total flow rate of the N_2 was 150 sccm. ZnO thin films were grown at a temperature of 200 °C. The growth rate was typically 2 Å/cycle for ZnO grown on a flat surface. The growth per cycle has been controlled by measuring the thickness of the film on Si-wafer reference substrates placed in the reactor. The thickness of ZnO coatings varied from 5 to 100 nm.

Structural properties of ALD ZnO-WGMR were studied by scanning electron microscopy (SEM) (JEOL, JSM-7001 F) with an Energy dispersive X-Ray (EDX) analyzer, Atomic Force Microscopy (AFM) (Icon Bruker) and Raman scattering (Renishaw micro-Raman spectrometer equipped with a confocal microscope (Leica) and laser ($\lambda_{exitation}$ = 514 nm).

3. Results and discussion

The simulation results are shown in Fig. 2. A strong whispering gallery mode (WGM) located inside the 100 nm thick ZnO layer was

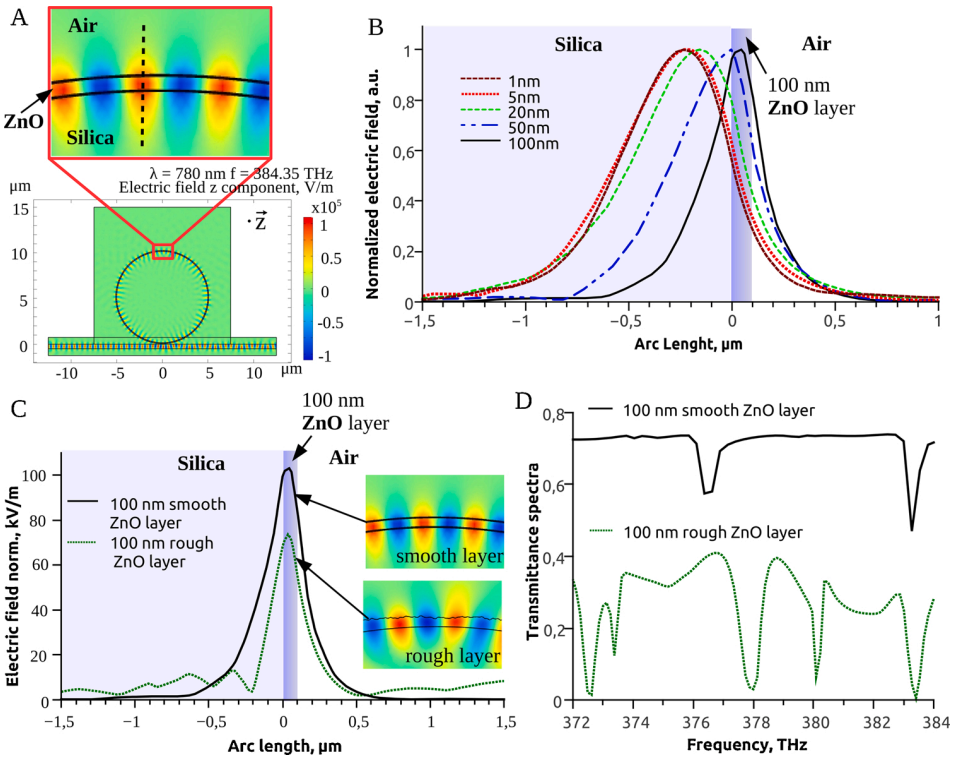

Fig. 2. The simulation data: (A) distribution of z-component of the electric-field into a 10 μm microresonator coated with 100 nm ALD ZnO layer; (B) intensity cross section in SiO_2/ZnO/air for different thicknesses of ZnO coating; (C) electric field intensity cross section in SiO_2/ZnO/air, coated with 100 nm of the smooth and rough layer of ZnO and (D) transmittance spectra for WGMR coated with 100 nm of ZnO.

observed due to the difference in refractive indexes of silica, ZnO, and air. It can be seen that with the increase of the layer thickness the peak of the resonance mode moves towards SiO_2 – ZnO boundary (see Fig. 2.B). For the thick layers (d > 50 nm), the WGM resonance peak moves inside the coating. The upper surface of the ZnO layer was distorted using a randomized function to take into account losses due to surface scattering. For the 100 nm layer, the depth of surface roughness was 30 nm. The electric field intensity decreased from 100 kV/m to 70 kV/m in the case of a rough surface for the electric field intensity cross section (Fig. 2.C). Less than 40 % of the light was transmitted to the detector and additional WGM resonance modes appeared as the surface thickness of the rough ZnO coating varied (see. Fig. 2.D).

It was found, that WGMR fabrication by H_2 flame melting results in the forming of structural defects on the surface of the resonator and the generation of a static surface charge. Due to electrostatic interaction between the resonator surface and coupling prism, attachment of the resonator to the prism occurred when the distance was smaller than 1 mm. It caused a rapid change of the collected optical signal. Strong electrostatic interaction between the resonator and the prism leads to sticking in contact and broadening of the resonances [16,17]. This restricts optical measurements in as-prepared WGMRs. The deposition of ZnO layers over WGMR solved the problem with light coupling. ALD deposited nanolayers screened the surface charge on WGMRs surface. As a result, the electrostatic interaction between WGMR and the prism was diminished.

Typical SEM images of the WGMR surface before and after 100 nm ZnO deposition are shown in Fig. 3.A and. B. The initial WGMRs had an almost smooth and mirror-like surface. After ALD, SEM images indicate that the ZnO layer conformally coated the WGMR. The rough surface and polycrystalline structure of produced the ZnO layer can be seen in Fig. 3.C.

ZnO surface is formed by elongated crystallites with an average size of about 20−30 nm in length. Basically, ALD ZnO layers are smooth and polycrystalline for the 100 nm thickness [8]. However, it was shown that the morphology and the crystalline phase for ZnO deposited on the rough and curved surface (e.g. cylinders, cones, etc.) had the highly polycrystalline surface [18–20]. EDX measurements were carried out to evaluate the chemical composition of ZnO-WGMR. EDX confirms that ZnO-WGMR contains Zn, O, C, and Si on its surface, which points to the successful deposition of ZnO on the WGMRs surface.

The optical resonance measurement is shown in Fig. 1C. The signal was compared with the reference signal obtained from the optical fiber with flat ends. The interference period of 50 MHz was used for frequency calibration. The resonance peaks were fitted by Lorentz function and Q-factor was estimated according to the Eq. (1). For each individual sample, 2–4 WGM resonances were used to calculate the Q factor.

The obtained Q-factors of ZnO-WGMR with different thicknesses are shown in Fig. 4.A. As-prepared WGMRs had quality factors of about $6{\cdot}10^6$, whereas deposition of ZnO nanolayers over WGMRs resulted in the decrease of Q-factor from $6{\cdot}10^6$ to 10^6.

The thickness of the ZnO layer played a significant role on the Q-factor value. It was found that the Q-factor improved in the ZnO-WGMR system for the thickness of 5−20 nm of the ZnO ALD layer. The Q-factor reached the maximal value for 20 nm of ZnO. Further increase of the ZnO coating thickness led to a decrease of the Q-factor value.

It is known that the Q-factor of WGMR depends on the refractive index of the coating and the thickness of the coating [21]. In case the coating is too thin or too rough, it acts as a surface defect and increases the surface scattering, and as a consequence lowers the Q-factor.

In our previous works, we have reported on optical properties of ultrathin ZnO nanolayers, formed by ALD. It was shown that the band gap and refractive index significantly depend on ZnO thickness [3,8]. It was shown, that thicker ALD deposited ZnO nanolayers had better crystallinity and lower defect concentration. Surface roughness increased with the thickness of the layer [3,8]. The refractive index of ZnO strongly depends on the crystallinity [3,8,22]. Improvement of crystallinity is accompanied by an increase of refractive index [3,8,22]. It was shown that the optimal thickness of the functional coating on WGMR is 10−60 nm [23]. Further increase of the coating thickness resulted in light attenuation [23].

Therefore, we assume that two competing phenomena were observed in ALD ZnO nanolayers, deposited on WGMRs: an increase of the refractive index due to improvement of ZnO crystallinity and enhanced light attenuation with ZnO nanolayer thickness increase. As a result, the maximum Q-factor was observed at ZnO thickness of 20 nm. Our experimental results correlated with simulation calculations pointing to the increase of Q-factor due to higher light trapping into thicker coatings and Q-factor suppression by light scattering due to surface roughness.

A decrease of the Q-factor in WGMRs is typically caused by dust or other contamination. ZnO coating on WGMR could provide a

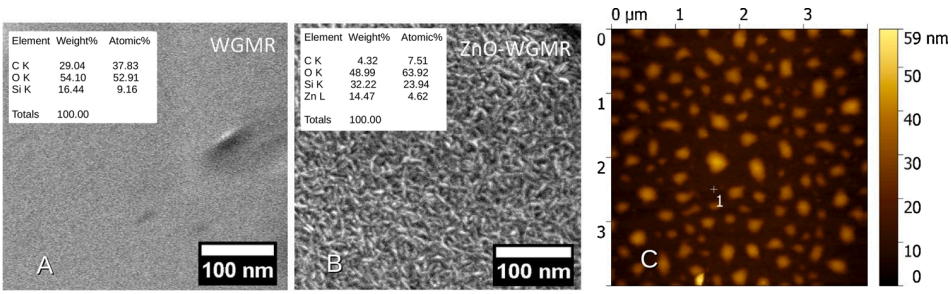

Fig. 3. SEM and EDX analysis of (A) as-prepared WGMR and (A) WGMR coated with 100 nm layer of ZnO; (C) AFM image of WGMR, coated with 100 nm layer of ZnO.

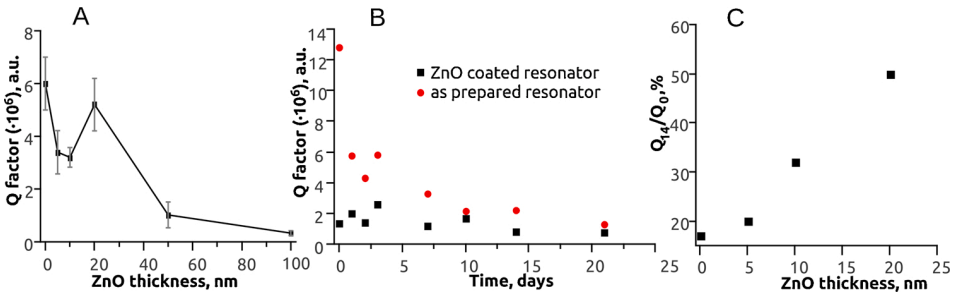

Fig. 4. (A) Q-factor dependence on ZnO ALD layer thickness in ZnO-WGMR structure; (B) degradation in time of Q-factor of as-prepared WGMR and ZnO-WGMR; (C) Q-factor degradation rate dependence on ZnO thickness at the end of the second week after coating.

protective coating against Q-factor degradation. Degradation of WGMRs was studied within 3 weeks. The measurements were performed twice per week. All the obtained data is collected in Fig. 4.B. One can see that due to high electrostatic interaction between the surface of the as-prepared WGMR and the surrounding environment, the decrease of Q-factor was significant during the first week. Saturation of the signal was observed by the end of the third week. As a result, the Q-factor dropped up to 15 times.

The Q-factor of WGMR modes depends on several factors [24]:

$$\frac{1}{Q} = \frac{1}{Q_{rad}} + \frac{1}{Q_{S.S.}} + \frac{1}{Q_{cont}} + \frac{1}{Q_{mat}} \tag{2}$$

where Q^{-1}_{rad}, $Q^{-1}_{S.S}$, Q^{-1}_{cont} and, Q^{-1}_{mat} are radiative losses, scattering losses on residual surface inhomogeneity, losses due to surface contaminants, and material losses, respectively.

Degradation of 10 nm ZnO-WGMR showed a drop of Q-factor up to 30 % at the end of the second week and 20 nm ZnO-WGMR - 50 %. Thickness dependence of the Q-factor degradation of ZnO-WGMR structures is shown in Fig. 4.C. The degradation percentage decreased with an increase of the thickness of the ZnO layer.

It is known that water and oxygen can be adsorbed by the ZnO surface forming charged surface states [3,8,22]. As a result, a depletion layer is formed on the surface region of ZnO.

It was shown, that adsorption of gases on the surface changes the refractive index of ZnO and it can be applied for optical gas sensing [25,26]. The refractive index changes of up to 0.005 were observed under 500 ppm of butane adsorption. Depending on the thickness, the depletion layer can spread to 10−20 nm of the ZnO layer, changing the refractive index of the ZnO. Therefore, changes of the refractive index due to surface adsorption are sufficient to lower the thicknesses of ZnO nanolayers.

In conclusion, we investigated conformal coatings of ZnO over whispering gallery mode resonators formed by Atomic layer deposition. The deposited nanolayers ‘screened’ surface charge of as-prepared WGMRs. The Q-factor of ZnO-WGMR was insignificantly lower than of as-prepared WGMRs. Light propagation in ZnO-WGMR with different thicknesses depends on the crystallinity and refractive index of the coating. Degradation of Q-factor due to ambient contamination was slower in ZnO-WGMR than in as-prepared WGMRs.

Declaration of Competing Interest

The authors declare that there is no competing interest that could have appeared so influence the work reported in this paper.

Acknowledgments

IB, RV, KD, KG, AA and JA would like to thank ERDF project No. 1.1.1.1/16/A/259 for funding this research.
II acknowledges the partial financial support from the NCN of Poland by the SONATA 11 project UMO-2016/21/D/ST3/00962.

References

[1] R. Viter, M. Savchuk, I. Iatsunskyi, Z. Pietralik, N. Starodub, N. Shpyrka, A. Ramanaviciene, A. Ramanavicius, Analytical, thermodynamical and kinetic characteristics of photoluminescence immunosensor for the determination of Ochratoxin A, Biosens. Bioelectron. 99 (2018) 237–243, https://doi.org/10.1016/j.bios.2017.07.056.
[2] A. Tereshchenko, M. Bechelany, R. Viter, V. Khranovskyy, V. Smyntyna, N. Starodub, R. Yakimova, Optical biosensors based on ZnO nanostructures: advantages and perspectives. A review, Sens. Actuators B: Chem. 229 (2016) 664–677, https://doi.org/10.1016/j.snb.2016.01.099.
[3] R. Viter, I. Baleviciute, A. Abou Chaaya, L. Mikoliunaite, Z. Balevicius, A. Ramanavicius, A. Zalesska, V. Vataman, V. Smyntyna, Z. Gertnere, D. Erts, P. Miele, M. Bechelany, Optical properties of ultrathin Al2O3/ZnO nanolaminates, Thin Solid Films 594 (2015) 96–100, https://doi.org/10.1016/j.tsf.2015.10.018.
[4] R. Viter, M. Savchuk, N. Starodub, Z. Balevicius, S. Tumenas, A. Ramanaviciene, D. Jevdokimovs, D. Erts, I. Iatsunskyi, A. Ramanavicius, Photoluminescence immunosensor based on bovine leukemia virus proteins immobilized on the ZnO nanorods, Sens. Actuators B: Chem. 285 (2019) 601–606, https://doi.org/10.1016/j.snb.2019.01.054.
[5] C. Verrier, E. Appert, O. Chaix-Pluchery, L. Rapenne, Q. Rafhay, A. Kaminski-Cachopo, V. Consonni, Tunable morphology and doping of ZnO nanowires by chemical bath deposition using aluminum nitrate, J. Phys. Chem. C 121 (2017) 3573–3583, https://doi.org/10.1021/acs.jpcc.6b11104.

[6] A. Krämer, S. Engel, N. Sangiorgi, A. Sanson, J.F. Bartolomé, S. Gräf, F.A. Müller, ZnO thin films on single carbon fibres fabricated by Pulsed Laser Deposition (PLD), Appl. Surf. Sci. 399 (2017) 282–287, https://doi.org/10.1016/j.apsusc.2016.12.046.
[7] R. Viter, Z. Balevicius, A. Abou Chaaya, I. Baleviciute, S. Tumenas, L. Mikoliunaite, A. Ramanavicius, Z. Gertnere, A. Zalesska, V. Vataman, V. Smyntyna, D. Erts, P. Miele, M. Bechelany, The influence of localized plasmons on the optical properties of Au/ZnO nanostructures, J. Mater. Chem. C 3 (2015) 6815–6821, https://doi.org/10.1039/C5TC00964B.
[8] A. Abou Chaaya, R. Viter, M. Bechelany, Z. Alute, D. Erts, A. Zalesskaya, K. Kovalevskis, V. Rouessac, V. Smyntyna, P. Miele, Evolution of microstructure and related optical properties of ZnO grown by atomic layer deposition, Beilstein J. Nanotechnol. 4 (2013) 690–698, https://doi.org/10.3762/bjnano.4.78.
[9] V.S. Ilchenko, A.A. Savchenkov, A.B. Matsko, L. Maleki, Generation of Kerr frequency combs in a sapphire whispering gallery mode microresonator, Opt. Eng. 53 (2014), 122607, https://doi.org/10.1117/1.OE.53.12.122607.
[10] L. Collot, V. Lefèvre-Seguin, M. Brune, J.M. Raimond, S. Haroche, Very high- q whispering-gallery mode resonances observed on fused silica microspheres, Europhys. Lett. (EPL) 23 (1993) 327–334, https://doi.org/10.1209/0295-5075/23/5/005.
[11] W. Pongruengkiat, P. Suejit, Whispering-gallery mode resonators for detecting cancer, Sensors 17 (2017) 25, https://doi.org/10.3390/s17092095.
[12] Y. Wang, G. Zhu, J. Mei, C. Tian, H. Liu, F. Wang, D. Zhao, Surface plasmon-enhanced two-photon excited whispering-gallery modes ultraviolet laser from Zno microwire, AIP Adv. 7 (2017), 115302, https://doi.org/10.1063/1.5008768.
[13] O. Lupan, V. Postica, J. Gröttrup, A.K. Mishra, N.H. de Leeuw, J.F.C. Carreira, J. Rodrigues, N. Ben Sedrine, M.R. Correia, T. Monteiro, V. Cretu, I. Tiginyanu, D. Smazna, Y.K. Mishra, R. Adelung, Hybridization of zinc oxide tetrapods for selective gas sensing applications, ACS Appl. Mater. Interfaces 9 (2017) 4084–4099, https://doi.org/10.1021/acsami.6b11337.
[14] Y. Xu, Y. Li, L. Shi, D. Li, H. Zhang, L. Jin, L. Xu, X. Ma, Y. Zou, J. Yin, Reverse-bias-driven whispering gallery mode lasing from individual ZnO microwire/p-Si heterojunction, Nanoscale 10 (2018) 5302–5308, https://doi.org/10.1039/C7NR06872G.
[15] I. Brice, K. Grundsteins, A. Atvars, J. Alnis, R. Viter, A. Ramanavicius, Whispering gallery mode resonator and glucose oxidase based glucose biosensor, Sens. Actuators B Chem. 318 (2020), 128004, https://doi.org/10.1016/j.snb.2020.128004.
[16] A. Chiasera, Y. Dumeige, P. Féron, M. Ferrari, Y. Jestin, G. Nunzi Conti, S. Pelli, S. Soria, G.C. Righini, Spherical whispering-gallery-mode microresonators, Laser Photon. Rev. 4 (2010) 457–482, https://doi.org/10.1002/lpor.200910016.
[17] I. Brice, K. Grundsteins, A. Atvars, J. Alnis, R. Viter, Whispering gallery mode resonators coated with Au nanoparticles, Proc. SPIE (2019) 230–235, https://doi.org/10.1117/12.2528677.
[18] R. Viter, A.A. Chaaya, I. Iatsunskyi, G. Nowaczyk, K. Kovalevskis, D. Erts, P. Miele, V. Smyntyna, M. Bechelany, Tuning of ZnO 1D nanostructures by atomic layer deposition and electrospinning for optical gas sensor applications, Nanotechnology 26 (2015), 105501, https://doi.org/10.1088/0957-4484/26/10/105501.
[19] I. Iatsunskyi, A. Vasylenko, R. Viter, M. Kempiński, G. Nowaczyk, S. Jurga, M. Bechelany, Tailoring of the electronic properties of ZnO-polyacrylonitrile nanofibers: Experiment and theory, Appl. Surf. Sci. 411 (2017) 494–501, https://doi.org/10.1016/j.apsusc.2017.03.111.
[20] I. Iatsunskyi, M. Baitimirova, E. Coy, L. Yate, R. Viter, A. Ramanavicius, S. Jurga, M. Bechelany, D. Erts, Influence of ZnO/graphene nanolaminate periodicity on their structural and mechanical properties, J. Mater. Sci. Technol. 34 (2018) 1487–1493, https://doi.org/10.1016/j.jmst.2018.03.022.
[21] D. Ristić, A. Chiappini, H. Gebavi, V. Derek, A. Lukowiak, R.R. Gonçalves, S. Pelli, G. Nunzi Conti, M. Ivanda, G.C. Righini, G. Cibiel, M. Ferrari, Spherical microresonators coated with a high refractive index coating for different applications. Progress in Electromagnetics Research Symposium, 2015.
[22] A.A. Chaaya, R. Viter, I. Baleviciute, M. Bechelany, A. Ramanavicius, Z. Gertnere, D. Erts, V. Smyntyna, P. Miele, Tuning optical properties of Al 2 O 3 /ZnO nanolaminates synthesized by atomic layer deposition, J. Phys. Chem. C 118 (2014) 3811–3819, https://doi.org/10.1021/jp411970w.
[23] G.C. Righini, S. Soria, Biosensing by WGM microspherical resonators, Sensors (Switzerland) 16 (2016) 1–25, https://doi.org/10.3390/s16060905.
[24] M.L. Gorodetsky, A.A. Savchenkov, V.S. Ilchenko, Ultimate Q of optical microsphere resonators, Opt. Lett. 21 (1996).
[25] T. Mazingue, L. Escoubas, L. Spalluto, F. Flory, G. Socol, C. Ristoscu, E. Axente, S. Grigorescu, I.N. Mihailescu, N.A. Vainos, Nanostructured ZnO coatings grown by pulsed laser deposition for optical gas sensing of butane, J. Appl. Phys. 98 (2005), 074312, https://doi.org/10.1063/1.2076442.
[26] A. Wei, L. Pan, W. Huang, Recent progress in the ZnO nanostructure-based sensors, Mater. Sci. Eng. B 176 (2011) 1409–1421, https://doi.org/10.1016/j.mseb.2011.09.005.

Frequency comb generation in whispering gallery mode silica microsphere resonators

Inga Brice[a], Karlis Grundsteins[a], Arvids Sedulis[a], Toms Salgals[b, c], Sandis Spolitis[b, c], Vjaceslavs Bobrovs[b], and Janis Alnis[a]

[a]Institute of Atomic Physics and Spectroscopy of the University of Latvia, 3 Jelgavas street, 1004 Riga, Latvia
[b]Institute of Telecommunications of the Riga Technical University, 12 Azenes street, 1048 Riga, Latvia
[c]AFFOC Solutions Ltd., 17 Andrejostas street, 1045 Riga, Latvia

ABSTRACT

Optical frequency combs (OFC) using different kinds of whispering-gallery-mode (WGM) microresonators have already shown different applications and especially their applications in fiber optical communication systems as replacements of laser-arrays. For this application the free spectral range (FSR) of 200 GHz or less is desirable. Besides the fabrication material for microspheres, the resonator radius can be modified to change the FSR.

In this paper use of silica microspheres for OFC represents an inexpensive alternative over the other microcombs: microring, microdisk, and microtoroid. We experimentally present a microsphere fabrication process from a different kind of silica (SiO_2) fibers by use of the hydrogen-oxygen melting technique. We experimentally review the OFC generation process the main microresonator parameters as FSR, Q-factor and evaluate the resulting WGM resonator generated OFC comb light source for further applications. An OFC was excited inside a 166 μm silica microsphere WGM resonators using a 1548 nm laser light. The obtained broadband OFC spanned from 1400–1700 nm with FSR of (397 $\pm$ 10) GHz.

Keywords: optical frequency comb (OFC), whispering gallery mode (WGM) resonator, silica (SiO_2) microsphere, tapered fiber coupling, Q factor, stability.

1. INTRODUCTION

Optical frequency combs (OFCs) have many applications in metrology, optical clocks, spectroscopy, communications.[1–4] The OFC spectrum can be composed of many thousands of equidistantly spaced narrow modes at known optical frequencies like an optical ruler.[5] The frequency combs cover a broad spectral interval that possibly allows the substitution of an expensive laser array solution for wavelength-division multiplexing (WDM) data transmission system.[6–8]

An OFC can be generated using third-order $\chi^{(3)}$ Kerr-nonlinearity induced four- wave mixing (FWM) generating the equidistant optical side-bands in the whispering gallery mode (WGM) microresonators.[9–11] The microresonators are an ideal platform for nonlinear interactions due to their ultrahigh quality (Q) factors, the efficiency of FWM, low-power pumping required, and compactness.[12,13]

Different WGM resonator geometries and materials have been used to generate the OFCs. The simplest way to fabricate the WGM resonator is to melt an optical fiber by using a high-temperature heating source, for example, a gas flame.[14] Silica (SiO_2) microspheres have a high Q factor of $10^7 - 10^8$. The Q factor of a WGM resonator describes the ability to store energy inside the microcavity. To enhance the light-matter interaction inside the resonator, it is necessary to increase the Q factor. It is limited by both the host material and the type of resonator. An important parameter for OFC generation in microresonators is dispersion. Both material dispersion and the geometrical dispersion contribute to the total dispersion. The geometrical dispersion can be modified by changing the geometrical parameters of the WGM resonators.[15] The resonator diameter influence for microspheres on the

Inga Brice: E-mail: inga.**brice**@lu.lv

Laser Resonators, Microresonators, and Beam Control XXIII, edited by Vladimir S. Ilchenko, Andrea M. Armani, Julia V. Sheldakova, Proc. of SPIE Vol. 11672, 1167213
 · doi: 10.1117/12.2577148

zero-dispersion wavelength is presented by Riesen et al.[12] First, FWM parametric oscillation was reported in SiO_2 microtoroid resonators,[16] calcium fluoride CaF_2 microdiscs[17] and SiO_2 microsphere resonators.[18] First broadband parametric OFCs were generated in SiO_2 microtoroid resonators,[19] CaF_2 microdisk resonators,[20] silicon nitride (Si_3N_4) microring resonators.[21] In microsphere resonators OFC generation has been demonstrated by several researcher groups.[7,22–24]

In this paper, we have prepared WGM microsphere resonators by melting a standard ITU-T G.652 single-mode telecommunication fiber several times by hydrogen-oxygen fame while the shape of the microresonator approached a spherical one. The resonators were characterized by coupling the light inside the spheres via tapered fiber and exciting WGM resonator OFC modes and finding the Q factor. The WGM resonator OFCs were generated inside the resonators using optical radiation from C-band region and the ability of generated OFC was explored and recorded optical spectra to determine the suitability of the system for applying the WGM WDM transmission.

2. MATERIALS AND METHODS OF DESIGNED SILICA WGM RESONATORS

2.1 Fabrication of the WGM Resonators

The WGM resonators were fabricated from Thorlabs, Inc. standard ITU-T G.652 single-mode telecommunication fiber, the core and cladding diameter d = 8.2 μm and D = 125 μm respectively, and from Light Guide Optics International Ltd. optical fiber, the core and cladding diameter d = 10 μm and D = 125 μm. The fiber was cut, the jacket stripped and the coating soaked in acetone before removal. Afterwards, the fiber was cleaned with ethanol to remove any dust particles and other contaminants from the surface. The striped and cleaned optical fiber was attached to a step motor which slowly moved it towards a hydrogen-oxygen flame. The SiO_2 melted and due to surface tension a microsphere grew on the tip of the fiber stem. To better observe the fabrication process microscope with a zoom and for contrast a blue LED light was used. The final result was a WGM resonator microsphere with a diameter of 300 μm - 700 μm. To fabricated smaller microspheres, the end of the fiber was tapered first before the melting. The disadvantage of this method is that only one WGMR microsphere could be fabricated at a time and each sphere was unique.

2.2 Characterization of silica WGM Resonators Spheres

The resonators were characterized by measurement of the Q factor. A basic scheme of the measurement system can be seen in Fig. 1a. The measurement system was set up using a pumping 1549.5 nm laser with a narrow linewidth of 50 kHz (Thorlabs SFL1550s) to excite the WGM resonator resonances. The laser frequency was scanned by changing the current with a triangle signal using a frequency generator. For coupling the light inside the WGM resonator a tapered fiber was prepared. The jacket and coating were stripped from a n ITU-T G.652 single-mode fiber (SMF) patch-cable with the core, cladding and jacket diameter of 9/125/900 μm. The fiber coating was removed only in the region of 1 - 2 cm where it was heated. If the process of taper fiber fabrication procedure, the previously ruptured SMF fiber was reused, broken fiber ends were cut using a fiber cleaver, cleaned and spliced together with commercial arc fusion splicer (Sumitomo Fusion Splicer - T 71C). A hydrogen flame was used to soften the SMF fiber and and 2 two-step motors were used to pull the fiber in both directions with a constant speed of 80 μm/s. The burning temperature of the hydrogen flame is lower than hydrogen-Oxygen flame. It melted and softened the fiber slowly, which was more desirable as the time period for tapered fiber fabrication steps was more flexible. A webcam, which has been modified by adding an F = 30 mm photo camera objective lens for magnification was used to capture and control the touch-point of the resonator with the tapered fiber for best coupling conditions where OFC carrier generation was observed. The 3-axis X, Y and Z micropositioner stage with the built-in Piezo controller (Thorlabs NanoMax-TS) was used to achieve critical coupling (see Fig. 1b). A switchable gain amplified photo-detector (Photodiode Thorlabs PDA20CS2, λ= 800 – 1700 nm) connected with a digital storage oscilloscope was used to record the received transmission signal. The transmission dips correspond to a series of WGM resonances (see Fig. 1c curve 1). Additionally, a reference signal was used to convert the time scale of the scan to the laser frequency scale. The interferometer fringes from a 3 m long optical fiber, which has flat ends, were used (see Fig. 1c curve 2). The interferometer period of (35.2 ± 1.1) MHz was calibrated using an electro-optical frequency modulator beforehand.

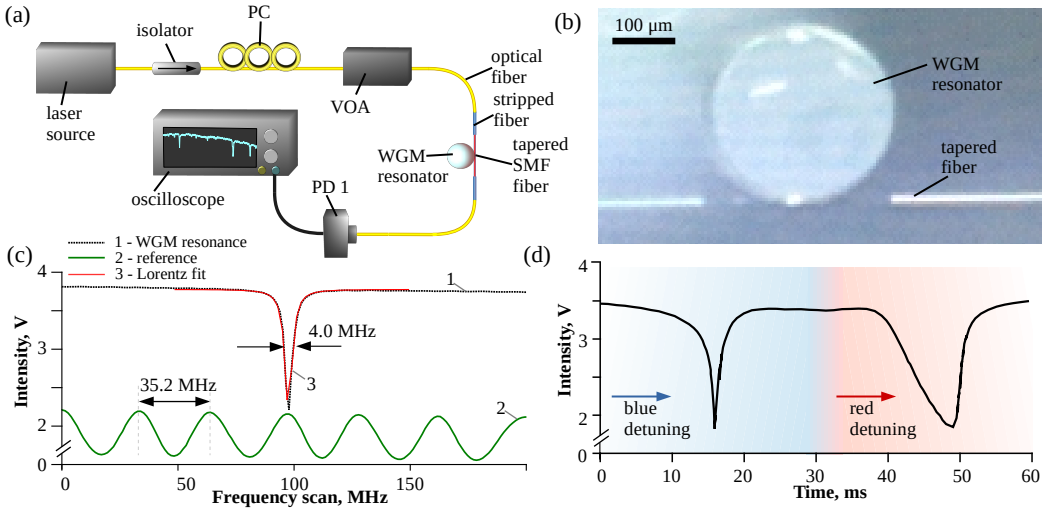

Figure 1. The characterization of silica WGM microsphere resonators: (a) the scheme of the experimental setup for characterization where (b) the WGM resonator was coupled with tapered SMF fiber and (c) the transmission spectra recorded together with the reference signal for the Q factor calculations; (d) depending on the scanning direction of the laser the WGM resonance dips were compresses for blue detuning or broadened for red detuning due to the nonlinear effects, variable attenuator (VOA) was used to reduce the power pumped inside the resonator and nonlinear effects.

The fabricated WGM resonators were characterized by using the Q factors. The Q factor mathematically can be described as:

$$Q = \frac{f}{\Delta f}, \tag{1}$$

where f is the frequency of the resonance mode and Δf is the full width at half maximum (FWHM). The Δf is obtained by fitting the resonance dip using a Lorentz function (see Fig. 1c curve 3) and Eq. 1. The calculated Q factors of the fabricated SiO_2 microspheres were $10^7 - 10^8$.

Several losses limit the maximum value of the optical Q factor of the WGM resonator[25] . **Material losses** are caused by the absorption in the material. Microspheres fabricated from SiO_2 adsorb the water from the moisture of the ambient air. This limits the Q factor of SiO_2 resonators and degrades the Q factor of improperly stored resonators over time.[26] **Surface scattering losses** are provoked by the surface roughness and tiny particles, for example, dust or nanoparticles.[27,28] It is one of the more important factors limiting the Q factor when functionalizing the WGM resonator surface with a coating. **Coupler losses** can be adjusted by controlling the distance between the resonator and the coupling element - coupling prism[7] or tapered fiber. **Radiative losses** happen due to imperfect total internal reflection from a curved surface. The radiative losses increase for smaller resonators.

In SiO_2 WGM microresonators it was possible to observe nonlinear effects while measuring the Q factor. The WGM resonance width depended on the direction of the laser scan (see Fig. 1d). In the blue-detuned scan over the resonance direction, the pumping was thermally stable and the WGM resonances were narrow. In the red-detuned direction the pumping was unstable and the resonances were broader. The thermal instability is required for soliton formation.[9,10] To reduce the thermal effect for a more precisely Q factor estimation an optical variable attenuator (EXFO FVA-3150) was used to reduce the power pumped inside the microsphere.

2.3 Experimental setup of OFC generation in silica WGM microsphere resonators

In the WGM resonators, the enhancement of the nonlinear effects (NOE) depends on the Q factor and mode volume. A high Q factor and small mode volume can compensate for a weak nonlinearity.[13] For example, the nonlinearity of CaF_2 is lower than SiO_2, but the Q factor of polished CaF_2 microdiscs can be a couple of orders of magnitude higher. It allowed the generation of OFC with a low power pump inside a CaF_2 microdiscs.[17,20] For OFC generation inside the WGM resonator cavity the amplification from the nonlinear process of FWM has to overcome the losses and the normal dispersion in the material has to be compensated by the Kerr effect for the soliton generation.[10] Both the degenerate and the non-degenerate FWM is used to generate OFC in WGM resonator. The degenerated FWM excites an equidistant signal and idler lines and through both regular and degenerate FWM new equidistant lines are generated. The repetition rate between the lines equals the full spectral range (FSR) or a multiple of FSR of the resonator.[20] The FSR can be calculated:

$$FSR = \frac{c}{2\pi Rn}, \tag{2}$$

where c is the speed of light, R is the radius of the WGM resonator and n is the refraction index of the material. For telecommunication applications, the repetition rate between the OFC lines has to be suitable for WDM applications following the ITU-T G.694.1 frequency grid.[29] This restricts the size of the SiO_2 microsphere resonators, for 200 GHz SiO_2 resonator diameter has to be 332 μm.[8]

It is easier to achieve the comb generation in anomalous dispersion case than in normal dispersion case,[13] as a major part of observed micro-combs has been generated in anomalous dispersion case (see Fig. 4b). Both the material and geometry dispersion of the WGM microresonator contribute to the total dispersion. It is possible with a careful design of the WGM microresonator geometry parameter to achieve zero or anomalous dispersion for resonators with normal material dispersion.[12,13,15] The telecom C-band wavelength used for data transmission also restricts the SiO_2 microsphere size.

A basic scheme of the WGM resonator OFC generation system can be seen in Fig. 2a. The pump laser $\lambda =$ 1550 nm and linewidth of 50 kHz nm laser was amplified with erbium-doped fiber amplifier (EDFA, Keopsys). The EDFA output power level was fixed between 10 - 23 dBm (varied in the case of used SiO_2 microsphere). The isolator on the EDFA output is used to prevent back-scattered light. The polarization state was adjusted

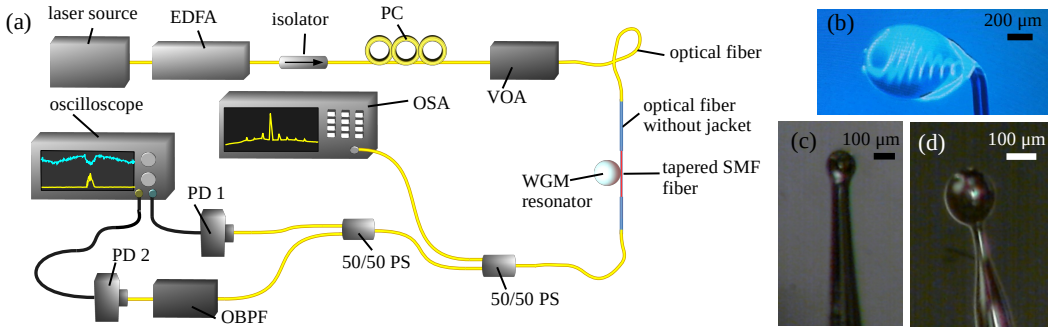

Figure 2. The Kerr OFC generation inside the silica WGM microsphere resonators: (a) the scheme of the setup for comb generation, the pumping laser source was amplified with EDFA, WGM resonator was coupled using a tapered SMF fiber, two 50/50 power splitters (PS) were used to detect the signal with OSA to record the OFC and two photo-detectors (PD) to detect the WGM resonances and an optical band pass filter (OBPF) before the PD2 identified which resonances generated the comb, polarization controller (PC) was used to optimize the OFC, which was very sensitive to the light polarization; (b) melting larger silica spheres using the hydrogen-oxygen flame the fiber core spiraled inside, the spiral was believed undesirable and interfered with Kerr OFC generation, (c) 120 μm large sphere fabricated with Light Guide Optics International optical fiber and (d) 170 μm large sphere fabricated from ITU-T G.652 SMF fiber.

using the polarization controller (PC) before coupling the amplified optical signal into the microsphere through a tapered fiber. First optical power splitter (PS, splitting ratio 50/50) was used to monitor the transmission signal using a high resolution optical spectral analyzer (OSA, Advantest Q8384 resolution 0.01 nm) and the second optical power splitter (splitting ratio 50/50) outputs were connected to two InGaAs switchable gain amplified photo-detectors (λ = 800 – 1700 nm). The first photo-detector was used to monitor the transmission signal and the second was used to identify the WGM resonances which generated the OFCs. Before the second photo-detector an optical band pass filter (Santec OTF-350) was used. The bandwidth was 10 nm at central frequency of 1550 nm (tuned 5nm away from the pumping laser) was used, which passes all generated comb wavelengths except the laser pump wavelength of 1550 nm. Only when the WGM resonator OFC signal carriers were generated the signal was detected through the filter. The laser frequency was scanned very fast to prevent any thermal effects from the changing laser power. The scan frequency was 2 - 10 kHz. Two microscopes with zoom cameras were used to monitor the position of the WGM resonator – top and side view. It was important to control the touch point of the resonator with the tapered fiber to excite the fundamental mode of the microsphere. Using the 3-axis X, Y and Z micropositioner stage with the built-in Piezo controller, it was possible to control the gap between the two elements and minimize the coupler losses and achieve critical coupling.

3. RESULTS

The size of the resonator microsphere could be controlled by varying the speed with which the fiber was moved towards the hydrogen-oxygen flame. By slowly moving the fiber towards the flame the resulting resonator was small approached a spherical shape, the core and cladding of the used SMF fiber melted together. If the fiber feed speed was increased, the resonators could be made with higher dimensions, they were more elliptical in shape. For higher dimensions, the core spiraled inside the sphere, which was made out of the cladding, both not fully melting together (see Fig. 2b). It was suspected that the spiraled core hindered the OFC generation. To fabricate smaller WGM resonators the SMF fiber end was first tapered and afterwards the sphere melted.

The WGM resonator microsphere fabricated from Light Guide Optics International optical fiber had a sphere diameter of 120 μm (Fig. 2c) and Q factor of $1.2 \cdot 10^7$. The Q factor was found using the Eq(1) (see Fig. 3a inset). To generate OFC the EDFA output optical power was fixed to 23 dBm and laser frequency scanned with 10 kHz frequency. An OFC like structure with comb spacing (4.31 $\pm$ 0.10) nm was observed (see Fig. 3a). Using the Eq. 2 and the measured FSR, the resonator radius was calculated as (61 $\pm$ 1) μm which corresponded with measurements obtained using high precision microscope with a camera (Fig. 2c).

The WGM resonator microsphere fabricated from ITU-T G.652 standard SMF telecom optical fiber had a sphere diameter of 170 μm (Fig. 2d) and Q factor of $4.6 \cdot 10^7$ (Fig. 3b inset). An OFC like structure with comb

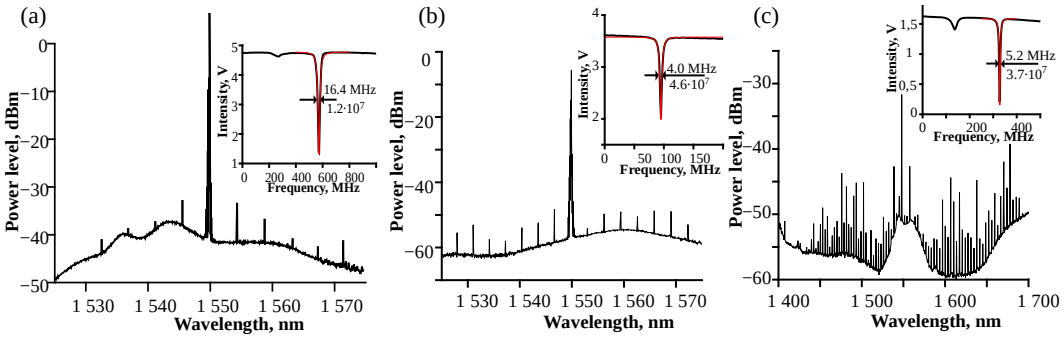

Figure 3. Recorded WGM resonator OFC spectra:(a) 120 μm resonator with 4.31 nm between the lines, the inset shows the characterization of the 16.4 MHz wide WGM resonance, (b) 170 μm resonator with 3,14 nm between the lines, the inset shows the characterization of the 4.0 MHz wide WGM resonance, (c) 166 μm resonator with 3.17 nm between the lines the OFC combines the Kerr comb with the Raman comb spanning for 1450 - 1700 nm, the inset shows the characterization of the 5.2 MHz wide WGM resonance.

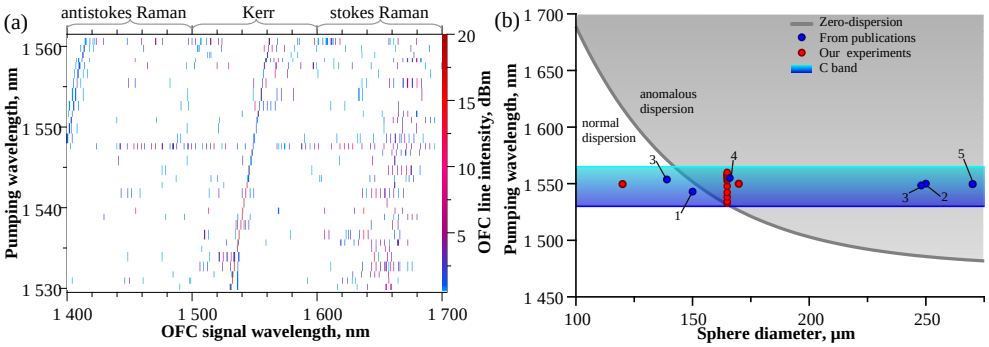

Figure 4. OFC pumping spectra of 166 μm diamater silica WGM microsphere resonators: (a) Kerr and Raman OFC excited with different C-band channel pump wavelengths (1530.33 -1560.61 nm); (b) the dispersion regime[12] and pumping wavelength for different sizes of microspheres both of our experiments and data from publications: 1,[18] 2,[22] 3,[23] 4,[24] 5.[7]

spacing (3.14 $\pm$ 0.04) nm was observed (see Fig. 3b). The resonator radius of the resonator was calculated as (84 $\pm$ 1) μm which correspond with measurements obtained using the microscope with a camera.

Changing the coupling conditions of the WGM resonator with the tapered fiber or changing pumping laser central frequency affected comb line generation and the intensity distribution of the lines. The generated WGM resonator OFC was very sensitive to the light polarization before coupling the optical signal into the microsphere through the tapered fiber. Changing the light polarization affected the intensity of the comb lines. Lowering the power leads to suspension of comb generation below a threshold value which is necessary for NOE. Lowering the laser scan frequency stopped the OFC generation due to thermal effects as the WGM resonator heated due to high optical power circulating inside. The laser detuning needed to compensate for the shift introduced by both the NOE and the thermal effect of the positive thermo-optic effect of SiO_2 to meet the soliton state and OFC generation conditions.[30,31]

To get rid of the scanning a pumping continuous wave (CW) tunable laser (Agilent 8163B) was used which could be scanned in steps (0.001 nm). Instead of scanning the optical fiber connected to the laser was lightly tapped to trigger the generation of the comb lines. OFC was excited inside a 166 μm SiO_2 microsphere WGM resonators with a Q factor of $3.7 \cdot 10^7$ (Fig. 3c inset). 32 different C-band channel frequencies (1530.33 -1560.61 nm) were pumped inside the WGM microsphere and the signal on OSA was recorded (see Fig. 4a). It was relatively easy to excite stokes Raman (region 1600 - 1700 nm) comb lines while antistokes Raman (region 1400 - 1500 nm) comb lines were rare. From 32 different channels only 12 Channels generated Kerr (region 1500 - 1600 nm) comb lines (see Fig. 4b). The most broadband OFC is generated when the pumping laser was slightly above the zero-dispersion wavelength.[32] Using a 1547.72 nm laser light a comb was obtained spanning from 1400 – 1700 nm (see Fig. 3c) by combining the Kerr com with stokes and anti-stokes Raman comb with FSR of (3.17 $\pm$ 0.08) nm or (397 $\pm$ 10) GHz. For the Kerr OFC generation, the pumping with laser above 1547.72 nm was more preferable as more intense Kerr comb lines were generated in the anomalous dispersion regime.

For WDM data transmission the OFC line should be at least 20 dBm above the EDFA broad spontaneous emmission spectrum to be intense enough to be filtered to satisfy the necessary optical power budget (OB) of the transmission system.[33] Kerr comb excited at 1551.67 nm had only 5 comb lines with the line spacing of 2 FSR (800 GHz) between them. The excited comb lines were intense and appeared to be stable in time (see Fig. 5a). The intensity stability was examined as it could interfere with data transmission. Any short term stability would be detected during the data transmission, therefore only long term stability was investigated further. The OFC spectrum was saved every 10 minutes for 14 hours. The intensity of the pumping laser was stable (see Fig. 5b curve of optical carrier (0)). The intensity of the generated comb lines over time are shown in Fig. 5b (see curve of optical carriers (-3) - (-1) and (+1) - (+2)). For the first 4 hours, all of the OFC lines were relatively stable. For the last 4 hours, however, the OFC line intensity was increasingly inconstant. The intensity of each Kerr comb line changed independently. The environment of the WGM resonator was important for the coupling

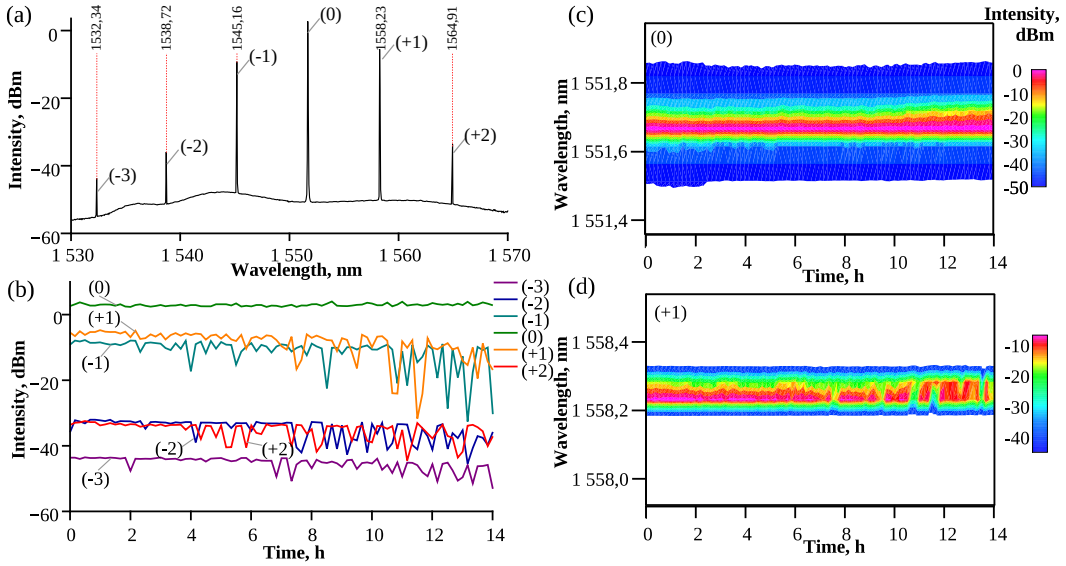

Figure 5. The stability of the WGM resonator OFC over a time period: (a) the stable Kerr comb excited with 1551.67 nm laser and 2 FSR gap between the lines, (b) the intensity change of OFC lines (curve for optical carriers (-3) - (2)) and OFC intensity maps (c) for the pumping laser (curve of optical carrier (0)) and (d) comb line (curve of optical carrier (+1)) over a time period.

conditions. It was inside a protective setup to slow down the degradation of the Q factor. The experimentally used humidity control and dust-prevention cover box protected from both the ambient moisture and dust slows down the degradation of SiO_2 microsphere.[26] Another important parameter that could impact the stability was the temperature. The changes in temperature can impact multiple factors. In such a case temperature drift of delta 1-2°C degrees at time period has affected the comb generation. First, the position of the sphere in contact with the tapered fiber could change. Second, the WGM mode frequency may shift by the change of the external environment temperature. Last but not least, the polarization of the light traveling through optical fibers may change. The instability observed from 4 to 10 hours could be explained by the slight change of coupling conditions which triggered some instability. The coupling conditions of the microsphere and tapper fiber may change also due to mechanical vibrations. Observing the intensity distribution in time for the profile of the pumping laser the signal broadened after 10 hours (see Fig. 5c). We believe the broadening happens due to the polarization changes. The same broadening could be observed for the OFC line (see Fig. 5d). The timing of this effect corresponds with the deterioration of the stability.

4. CONCLUSIONS

We have shown microsphere fabrication process from different kind of silica SiO_2 fibers by use of the hydrogen-oxygen melting technique. The size of the fabricated microsphere 166 μm correlated nicely with the 3.17 nm or 400 GHz FSR of the Kerr OFC as indicated by the mathematical calculations. With the dispersion calculation for pumping source wavelength, the silica microsphere WGMR resonators can be customized for the application in data transmission where the FSR matches the ITU-T spectral grid for WDM applications. Demonstrated results show that the WGM resonator generated OFC in silica microsphere has the potential to replace individual laser arrays as a multiple laser source for data communication solutions.

The designed SiO_2 microsphere resonators by slowly moving the fiber trough hydrogen-oxygen flame approached a spherical shape, while the core and cladding of ITU-T G.652 standard SMF fiber melted together. In case of higher dimensions resonators ($\approx$ 200 μm), they were more elliptical in shape, the core spiraled inside the

sphere made out of the cladding and not fully melting together, these microspheres hindered the OFC generation. Smaller WGMR microsphere resonators ($\leq$ 100 μm) must be first tapered and afterwards, the sphere melted. For higher diameter ($\geq$ 200 μm) microsphere resonators it is better to use SMF fibers with a core diameter close to the cladding diameter (110/125 μm) to prevent elliptical shape and core spiraled inside the sphere.

It was easier to excite the Raman OFC lines in the 1600 – 1700 nm region than Kerr OFC lines around 1550 nm. Kerr OFC generation was observed above 1545 nm for the 166 μm silica microsphere. The pumping wavelength used lies in the zero-dispersion or anomalous dispersion regime, which was necessary for the OFC generation.

The stability is an important parameter for telecom data transmission and the long term stability was explored for 14 hours. The temperature influence on the system was deemed crucial as it could affect multiple points, like the coupling position impacting WGM resonator OFC resonances and polarization of the input, which were determined to be integral for the OFC generation. Eliminating the causes of instability will improve both the stability and the suitability of the system for WDM data transmission and other applications as well.

ACKNOWLEDGMENTS

This research was funded by the European Regional Development Fund project **No. 1.1.1.1/18/A/155**: "Development of optical frequency comb generator based on a whispering gallery mode microresonator and its applications in telecommunications" and by the Riga Technical University's Doctoral Grant programme.

REFERENCES

[1] Ye, J., Schnatz, H., and Hollberg, L. W., "Optical Frequency Combs: From Frequency Metrology to Optical Phase Control," *IEEE Journal on Selected Topics in Quantum Electronics* **9**(4), 1041–1058 (2003).

[2] Fortier, T. and Baumann, E., "20 Years of Developments in Optical Frequency Comb Technology and Applications," *Communications Physics* **2**(1), 1–16 (2019).

[3] Niizeki, K., Yoshida, D., Ito, K., Nakamura, I., Takei, N., Okamura, K., Zheng, M. Y., Xie, X. P., and Horikiri, T., "Two-photon comb with wavelength conversion and 20-km distribution for quantum communication," *Communications Physics* **3**(1), 1–7 (2020).

[4] Gotti, R., Puppe, T., Mayzlin, Y., Robinson-Tait, J., Wójtewicz, S., Gatti, D., Alsaif, B., Lamperti, M., Laporta, P., Rohde, F., Wilk, R., Leisching, P., Kaenders, W. G., and Marangoni, M., "Comb-locked frequency-swept synthesizer for high precision broadband spectroscopy," *Scientific Reports* **10**(1), 1–10 (2020).

[5] Hänsch, T. W., "Nobel Lecture: Passion for precision," *Reviews of Modern Physics* **78**, 1297–1309 (nov 2006).

[6] Pfeifle, J., Weimann, C., Bach, F., Riemensberger, J., Hartinger, K., Hillerkuss, D., Jordan, M., Holtzwarth, R., Kippenberg, T., Leuthold, J., Freude, W., and Koos, C., "Microresonator-Based Optical Frequency Combs for High-Bitrate WDM Data Transmission," in [*Optical Fiber Communication Conference*], OW1C.4, OSA, Washington, D.C. (2012).

[7] Braunfelds, J., Murnieks, R., Salgals, T., Brice, I., Sharashidze, T., Lyashuk, I., Ostrovskis, A., Spolitis, S., Alnis, J., Porins, J., and Bobrovs, V., "Frequency comb generation in WGM microsphere based generators for telecommunication applications," *Quantum Electronics* **50**, 1043–1049 (nov 2020).

[8] Anashkina, E. A., Marisova, M. P., Andrianov, A. V., Akhmedzhanov, R. A., Murnieks, R., Tokman, M. D., Skladova, L., Oladyshkin, I. V., Salgals, T., Lyashuk, I., Sorokin, A., Spolitis, S., Leuchs, G., and Bobrovs, V., "Microsphere-based optical frequency comb generator for 200 GHz spaced WDM data transmission system," *Photonics* **7**(3) (2020).

[9] Herr, T., Brasch, V., Jost, J. D., Wang, C. Y., Kondratiev, N. M., Gorodetsky, M. L., and Kippenberg, T. J., "Temporal solitons in optical microresonators," *Nature Photonics* (December) (2013).

[10] Kippenberg, T. J., Gaeta, A. L., Lipson, M., and Gorodetsky, M. L., "Dissipative Kerr solitons in optical microresonators," *Science* **361**(6402) (2018).

[11] Karpov, M., Pfeiffer, M. H. P., Guo, H., Weng, W., Liu, J., and Kippenberg, T. J., "Dynamics of soliton crystals in optical microresonators," *Nature Physics* **15**, 1071–1077 (2019).

B

SPECTROSCOPY OF ATOMS

In 1666 Isaac Newton called the rainbow, which appeared as white light passed through a prism, a spectrum. This event is considered to be the first observation in spectroscopy - branch of physics that studies the structure of atoms and molecules using their spectra. Atoms of different elements have distinguished spectra, which allows to determine the chemical composition of a substance by studying its spectrum. Atomic spectra are simpler than molecular spectra because they have fewer degrees of freedom [94], namely only electron transitions and nuclear spins. In the molecular spectra of oscillation and rotation transitions appear.

B.1 SPECTRAL LINEWIDTH

The spectral line covers a small frequency range and not just one frequency, even if the instruments used to register the spectrum do not cause additional line broadening [94]. Monochromatic spectral lines and monochromatic sinusoidal oscillations are a mathematical model of approximation that does not materialize in nature. In classical mechanics, an atom can be described as a decaying oscillator, that is, an electron in an atom oscillates around an equilibrium state. The oscillations result in electromagnetic radiation, which carries some of the energy with it.

There are several reasons for the broadening of the spectral lines.

B.1.1 *Natural Width of the Spectral Line*

In classical mechanics, the equation for oscillations of the oscillator can be written as:

$$x(t) = \left\{ \begin{array}{c} 0, t < 0 \\ A e^{\frac{-kt}{2}} e^{i2\pi ft}, t \geqslant 0 \end{array} \right\}, \tag{B.1}$$

where A is the maximum amplitude, k is the first-order rate constant and $k = \frac{1}{\tau}$ is the lifetime of the population of the level, f is frequency, and t is time. This function shows fading oscillations. The amplitude of $x(t)$ gradually decreases and the radiated frequency is not monochromatic.

Quantum mechanics also shows the presence of the natural width of the spectral line. When an electron of a substance's atom is excited at a higher energy level, after a while this electron emits energy and

returns to a lower state. Looking at the number of N_n electrons in the excited state, its change over time can be described as:

$$-\frac{dN_n}{dt} = kN_n. \tag{B.2}$$

From Heisenberg's uncertainty $\Delta E\tau \geqslant \hbar$. In order to know exactly the energy and the frequency (see Eq. 2.1) emitted, the time must be infinite. However, the lifetime of the proposed condition is not. Therefore, the energy uncertainty interval ΔE and the frequency width Δf, respectively, arise. So the natural broadening of the spectral line depends on the lifetime:

$$\Delta f = \frac{1}{2\pi\tau}. \tag{B.3}$$

The spectral line, which has not expanded further due to other factors, has the Lorentz form (see Fig. B.1). This can be obtained by performing the Fourier transform of the function x(t):

$$F[x(t)] = \frac{1}{2\sqrt{2\pi}} \int_0^\infty A(f) e^{i2\pi ft} df. \tag{B.4}$$

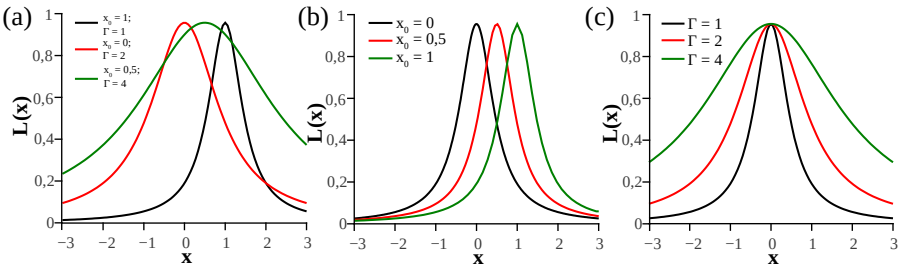

Figure B.1: Spectral lines have Lorentz form with (a) two parameters defining the shape: (b) x_0 moving the peak position and (c) Γ indicating the width of the line.

A function formula is obtained:

$$L(x) = \frac{1}{\pi} \frac{\frac{1}{2}\Gamma}{(x - x_0)^2 + (\frac{1}{2}\Gamma)^2} \tag{B.5}$$

where Γ is a parameter that indicates the full width at half maximum and the maximum of the function is at x_0 (see Fig. B.1 a-c).

Natural linewidth of a transition for Rb is abut 5-10 MHz.

B.1.2 *Doppler Broadening*

The Doppler effect is a change in the frequency of the oscillations when the source of the oscillations is in motion relative to the observer. If the source approaches, then its oscillation frequency increases, if it moves away, then it decreases accordingly. In addition,

the greater the speed of the source, the greater the effect. Dependence of wavelength change on speed description formula:

$$f^* = \left(1 + \frac{v_x}{c}\right) f \tag{B.6}$$

where f^* is the recorded frequency, v_x is the projection of the speed of the light source, c is the speed of light and f is the radiated frequency. We can conclude that the frequency of the spectral line depends on the direction and speed of the source and is caused by the thermal motion of the atoms. The energy distribution for the spectral line according to the Doppler extension is described by the Doppler contour or Gaussian profile (see Fig. B.2):

$$g(x) = \frac{1}{\sigma\sqrt{2\pi}} e^{-\frac{1}{2}\left(\frac{x-x_0}{\sigma}\right)^2}, \tag{B.7}$$

where σ is a parameter that indicates the standard deviation of the function and the maximum of the function is at x_0.

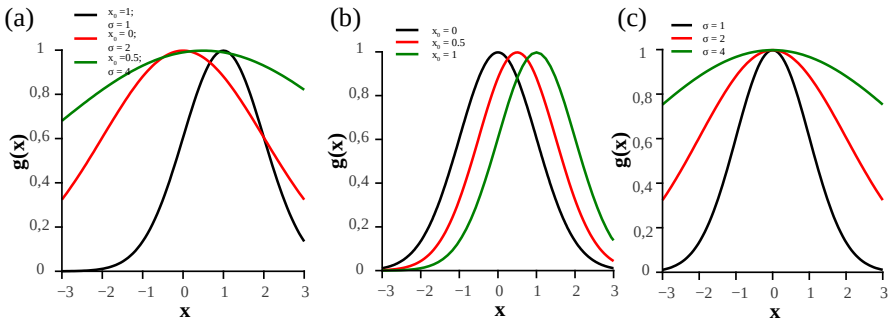

Figure B.2: Doppler broadening is defined by Gaussian form with (a) two parameters defining the shape: (b) x_0 moving the peak position and (c) σ indicating the width.

Doppler broadening σ depends on the temperature of observed gas:

$$\sigma = \sqrt{\frac{kT}{mc^2}} f, \tag{B.8}$$

where k is the Boltzmann constant, T is the temperature, m is the mass of the emitting particle.

B.2 ATOMIC STRUCTURE

An atom is made up of a positively charged nucleus surrounded by a negatively charged electron cloud. The physicist E. Rutherford proved that there is a positively charged nucleus in the center of the atom. The nucleus of an atom with an order of magnitude of 10^{-15}

m occupies a very small part of the size of an atom with the order of magnitude of 10^{-10} m. The entire atomic mass is concentrated in the nucleus. The planetary model of atoms, namely that electrons orbit the nucleus, was discovered by N. Bohr. In addition to the model, in 1914 Bohr put forward three important postulates:

1. an electron can move only in certain quantized orbits;
2. when moving through the orbits, the electron does not emit energy;
3. an electron emits energy only when it moves from an orbit farther from the nucleus to an orbit closer to the nucleus.

In 1929 De Broglie was awarded the Nobel Prize in Physics, after the wave-like behaviour of electrons was experimentally demonstrated in 1927.

In 1923 L. de Broglie hypothesized that an electron orbiting a nucleus is a moving particle, so it has wave properties according to the wave-particle duality. Today, the atomic model describes an electron orbital as an electron cloud. It is the part of space where an electron is located with a certain probability. If the probability distribution of an electron's location is plotted graphically, it forms a cloud that has diverse densities in different places.

B.2.1 *Energy Level Splitting*

The energy of an electron in an atom depends on the principal quantum number n. For atoms with one electron in the outer shell:

$$E_n = -13.6eV\frac{Z^2}{n^2}, \tag{B.9}$$

where E_n is the energy, Z is the nuclear charge, n is the principal quantum number. However, as the resolution of the instruments improved, instead of one level, two or even more levels with a small energy difference were observed. This is called the splitting of energy levels.

B.2.2 *Fine Structure*

One of the first proofs of the existence of atomic spin is the study of the hydrogen Hα line with a good resolution spectral apparatus. According to Bohr's theory, there is only one red line in the hydrogen spectrum, namely the Hα line, which arises when an electron changes from n = 3 energy level to n = 2 energy level. The wavelength of this line is 656.28 nm. However, two lines with a wavelength different by 0.016 nm [95] were observed in the experiments. This type of splitting of the spectral line is called a fine structure and occurs when the electron spin S and the electron's orbital momentum L interact.

Thus, in the H atom at the n = 3 energy level, the electron moves from the 3s sublevel to the n = 2 level. This level has two sub-levels

- 2s and 2p. The transition 3s-2s is forbidden because the angular momentum does not change. In turn, the transition 3s-2p is allowed. The 2p sublevel orbital quantum number l = 1 and spins s can assume values of ± 1/2. Thus, the total angular momentum j = l + s can take two values, respectively - j = 1/2 and j = 3/2 (see Fig. B.3 a).

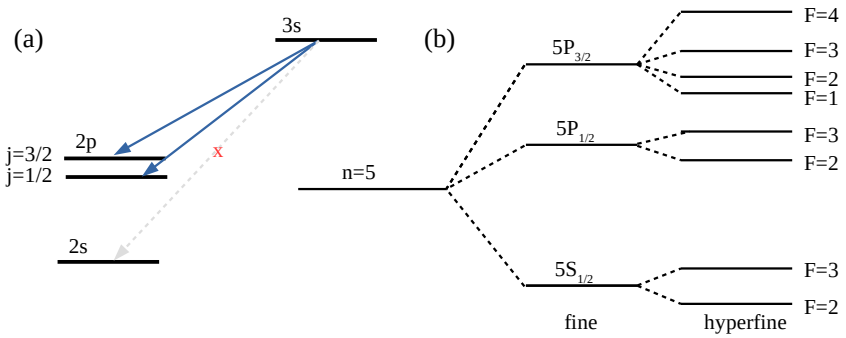

Figure B.3: Splitting of energy levels: (a) fine splitting of Hα 2p level; (b) hyperfine splitting of ^{85}Rb.

B.2.3 *Hyperfine Structure*

The hyperfine or superfine structure is about 1000 times finer than the fine structure. It occurs when the magnetic moment of a nucleus interacts with the electrons of an atom.

^{85}RB The hyperfine structure of ^{85}Rb for the $n = 5$ level. The sublevels 5s, 5p, 5d, etc. are possible. In the case of the fine structure, the 5p sublevel, similar to the 2p hydrogen sub-level, splits into $5P_{1/2}$ and $5P_{3/2}$ components with J = 1/2 and J = 3/2 due to the electron spin, respectively. ^{85}Rb has also an angular momentum of the nucleus I = 5/2. Now look at the total atomic angular momentum of rubidium F. $5S_{1/2}$ for sublevel J = 1/2, so it can split into two more levels F1 = I + J = 5/2 + 1/2 = 3 and F2 = I - J = 5/2 - 1/2 = 2. Similarly, the $5P_{1/2}$ sublevel can split into two more levels F1 = I + J = 5/2 + 1/2 = 3 and F2 = I - J = 5/2 - 1/2 = 2. In turn, the $5P_{3/2}$ sublevel can be split into four levels F1 = I + J = 5/2 + 3/2 = 4, F4 = I - J = 1 and F2 = 3 and F3 = 2 respectively (see Fig. B.3 b).

^{87}RB The hyperfine structure of ^{87}Rb is similar to ^{85}Rb. The angular momentum of the nucleus I = 3/2. The atomic angular momentum of rubidium F can split into two levels F1 = I + J = 3/2 + 1/2 = 2 and F2 = I - J = 3/2 - 1/2 = 1 for $5S_{1/2}$ and $5P_{1/2}$ sublevels and F1 = I + J = 3/2 + 3/2 = 3, F4 = I - J = 0 and F2 = 2 and F3 = 1, respectively for the $5P_{3/2}$ sublevel.

B.2.4 *Superhyperfine Structure*

Even finer energy level splitting - superhyperfine structure - occurs when an unpaired electron in the atom is subjected to the interaction of several groups of similar nuclei. It happens when the electron moves between several equivalent nuclei, but spends a different time interval near each nucleus [96]. As a result of this splitting, the levels of the hyperfine structure are split into finer levels. The splitting is small compared to the hyperfine structure, but it can be used to characterize the covalence of each molecule.

C

CALCULATION EXAMPLES

C.1 DISPERSION CALCULATIONS

In section 4.1.3.1 the dispersion of SiO_2 was found and plotted in Fig. 4.5 a. A fragment of the calculations is shown in Table C.1 where the complex equation is divided into smaller bite sized parts.

To find the refractive index for $\lambda = 1.00\ \mu m$, first, Sellmeier equation was solved:

$$\begin{aligned} n^2 &= 1 + \frac{A_1\lambda^2}{\lambda^2 - B_1^2} + \frac{A_2\lambda^2}{\lambda^2 - B_2^2} + \frac{A_3\lambda^2}{\lambda^2 - B_3^2} = \\ &= 1 + \frac{0.6961663 \cdot 1.00^2}{1.00^2 - 0.0684043^2} + \frac{0.4079426 \cdot 1.00^2}{1.00^2 - 0.1162414^2} + \frac{0.8974794 \cdot 1.00^2}{1.00 - 9.896161^2} = \\ &= 2.103711; \quad \text{(C.1)} \end{aligned}$$

$$n = \sqrt{n^2} = \sqrt{2.103711} = 1.4504. \quad \text{(C.2)}$$

Next, the Eq. 4.10 was divided into smaller parts:

$$\begin{aligned} \mathbf{1} &= \frac{A_1}{(\lambda^2 - B_1^2)n} + \frac{A_2}{(\lambda^2 - B_2^2)n} + \frac{A_3}{(\lambda^2 - B_3^2)n} = \\ &= \frac{0.6961663}{(1.00^2 - 0.0684043^2) \cdot 1.4504} + \frac{0.4079426}{(1.00^2 - 0.1162414^2) \cdot 1.4504} + \\ &\quad + \frac{0.8974794}{(1.00^2 - 9.896161^2) \cdot 1.4504} = 0.760961 \mu m^{-2}; \quad \text{(C.3)} \end{aligned}$$

$$\begin{aligned} \mathbf{2} &= -\frac{5A_1\lambda^2}{(\lambda^2 - B_1^2)^2 n} - \frac{5A_2\lambda^2}{(\lambda^2 - B_2^2)^2 n} - \frac{5A_3\lambda^2}{(\lambda^2 - B_3^2)^2 n} = \\ &= -\frac{5 \cdot 0.6961663 \cdot 1.00^2}{(1.00^2 - 0.0684043^2)^2 \cdot 1.4504} - \frac{5 \cdot 0.4079426 \cdot 1.00^2}{(1.00^2 - 0.1162414^2)^2 \cdot 1.4504} - \\ &\quad - \frac{5 \cdot 0.8974794 \cdot 1.00^2}{(1.00^2 - 9.896161^2)^2 \cdot 1.4504} = -3.867911 \mu m^{-2}; \quad \text{(C.4)} \end{aligned}$$

$$\begin{aligned} \mathbf{3} &= \frac{4A_1\lambda^4}{(\lambda^2 - B_1^2)^3 n} + \frac{4A_2\lambda^4}{(\lambda^2 - B_2^2)^3 n} + \frac{4A_3\lambda^4}{(\lambda^2 - B_3^2)^3 n} = \\ &= \frac{4 \cdot 0.6961663 \cdot 1.00^4}{(1.00^2 - 0.0684043^2)^3 \cdot 1.4504} + \frac{4 \cdot 0.4079426 \cdot 1.00^4}{1.00^2 - 0.1162414^2)^3 \cdot 1.4504} + \\ &\quad + \frac{4 \cdot 0.8974794 \cdot 1.00^4}{(1.00^2 - 9.896161^2)^3 \cdot 1.4504} = 3.119009 \mu m^{-2}; \quad \text{(C.5)} \end{aligned}$$

Table C.1: Table fragment for material dispersion calculations: Eq. 4.9 was used to find the refractive index, while dispersion was found using Eq. 4.10 (1-5 denote the countables in parentheses to reduce error possibility).

λ, μm	n^2	n	**1**, μm^{-2}	**2**, μm^{-2}	**3**, μm^{-2}	**4**, $\frac{10^{-3}}{\mu m^2}$	**5**, $\cdot 10^{-5}$, $\frac{10^{-5}}{\mu m^2}$	$\frac{d^2n}{d\lambda^2}$, $\frac{10^{-2}}{\mu m^2}$	D, $\frac{ps}{km \cdot nm}$
1.00	2.104	1.4504	0.76	-3.87	3.12	1.49	-2.12	1.35	-45.10
1.01	2.103	1.4503	0.75	-3.79	3.06	1.43	-1.98	1.27	-42.82
1.02	2.103	1.4502	0.73	-3.72	3.00	1.38	-1.86	1.19	-40.62
1.03	2.103	1.4500	0.72	-3.64	2.94	1.32	-1.75	1.12	-38.49
1.04	2.102	1.4499	0.70	-3.57	2.88	1.27	-1.64	1.05	-36.44
1.05	2.102	1.4498	0.69	-3.50	2.82	1.22	-1.54	0.984	-34.46
1.06	2.102	1.4497	0.68	-3.44	2.77	1.17	-1.45	0.921	-32.54
1.07	2.101	1.4496	0.66	-3.37	2.72	1.13	-1.36	0.860	-30.68
1.08	2.101	1.4494	0.65	-3.31	2.67	1.08	-1.28	8.02	-28.88
1.09	2.101	1.4493	0.64	-3.25	2.62	1.04	-1.21	0.747	-27.14
1.10	2.100	1.4492	0.63	-3.19	2.57	1.00	-1.14	0.694	-25.45

$$\mathbf{4} = \frac{A_1^2 B_1^2 \lambda^2}{(\lambda^2 - B_1^2)^3 n^3} + \frac{A_i 2^2 B_2^2 \lambda^2}{(\lambda^2 - B_2^2)^3 n^3} + \frac{A_3^2 B_3^2 \lambda^2}{(\lambda^2 - B_3^2)^3 n^3} =$$
$$= \frac{0.6961663^2 \cdot 0.0684043^2 \cdot 1.00^2}{(1.00^2 - 0.0684043^2)^3 \cdot 1.4504^3} +$$
$$+ \frac{0.4079426^2 \cdot 0.1162414^2 \cdot 1.00^2}{(1.00^2 - 0.1162414^2)^3 \cdot 1.4504^3} +$$
$$+ \frac{0.8974794^2 \cdot 9.896161^2 \cdot 1.00^2}{(1.00^2 - 9.896161^2)^3 \cdot 1.4504^3} = 0.001493 \mu m^{-2}; \quad \text{(C.6)}$$

$$\mathbf{5} = -\frac{A_1^2 B_1^2 \lambda^4}{(\lambda^2 - B_1^2)^4 n^3} - \frac{A_2^2 B_2^2 \lambda^4}{(\lambda^2 - B_2^2)^4 n^3} - \frac{A_3^2 B_3^2 \lambda^4}{(\lambda^2 - B_3^2)^4 n^3} =$$
$$= -\frac{0.6961663^2 \cdot 0.0684043^2 \cdot 1.00^4}{(1.00^2 - 0.0684043^2)^4 \cdot 1.4504^3} -$$
$$- \frac{0.4079426^2 \cdot 0.1162414^2 \cdot 1.00^4}{(1,00^2 - 0.1162414^2)^4 \cdot 1.4504^3}$$
$$- - \frac{0.8974794^2 \cdot 9.896161^2 \cdot 1.00^4}{(1,00^2 - 9.896161^2)^4 \cdot 1.4504^3} = -0.000021 \mu m^{-2}. \quad \text{(C.7)}$$

After adding up the individual parts, the second order derivative of refractive index was found followed by the dispersion:

$$\frac{d^2n}{d\lambda^2} = \mathbf{1} + \mathbf{2} + \mathbf{3} + \mathbf{4} + \mathbf{5} = 0.760961 - 3.867911 +$$
$$+ 3.119009 + 0,001493 - 0.000021 = 0.013530 \mu m^{-2}; \quad \text{(C.8)}$$

$$D = -\frac{\lambda}{c}\frac{d^2n}{d\lambda^2} = -\frac{1.00\cdot 10^{-6}}{3\cdot 10^8}\cdot 0.013530\cdot 10^{12} = -0.004510\frac{s}{m} = \\ = -45.10\frac{ps}{km\cdot nm}. \quad \text{(C.9)}$$

Obtained values for 1.00 - 2.00 μm were potted in Fig. 4.5 a for silica. Similarly other material material dispersion could be found by using right Sellmeier coefficients (see Fig. C.1).

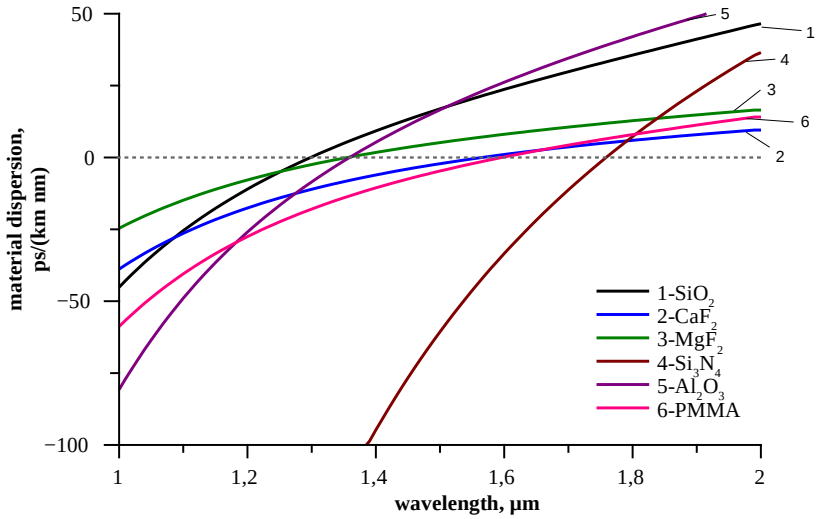

Figure C.1: Material dispersion of different materials found using Sellmeier coefficients.

C.2 CIRCULATING POWER CALCULATIONS

To find the built up power circulating inside the silica microsphere shown in Table 4.2, first, the the transmission and Q factor were found. Lets look at 170 μm resonator as an example. WGM resonance shown in Fig. 4.18 can be used to find both parameters. The transmission intensity detected using PD off resonance was 3.7 V while on resonance it dropped to 2.0 V. This allows to estimate the transmission on resonance as T = 0.54. Next, the resonance full width at half maximum $\Delta f_{FWHM} = 4.0$ MHz was found using the Lorentz function fit. This allowed to calculate the total Q factor:

$$Q = \frac{f}{\Delta f_{FWHM}} = \frac{193.4145\cdot 10^{12}}{4.0\cdot 10^6} = 4.6\cdot 10^7. \quad \text{(C.10)}$$

Then the coupling coefficient and intrinsic Q factor was calculated:

$$K = \frac{1+\sqrt{T}}{1-\sqrt{T}} = \frac{1+\sqrt{0.54}}{1-\sqrt{0.54}} = 3.78; \quad \text{(C.11)}$$

$$Q_{intr} = (1+K)Q = (1+3.78)\cdot 4.6\cdot 10^{7} = 2.20\cdot 10^{8}. \qquad \text{(C.12)}$$

Now all necessary parameters to find the circulating power are known:

$$P_{circ} = P_{in}\frac{\lambda Q_{intr}}{\pi^2 nR}\frac{K}{(K+1)^2} = 0.1\cdot\frac{1.550\cdot 10^{-6}\cdot 2.20\cdot 10^{8}}{3.14^2\cdot 1.44\cdot 83\cdot 10^{-6}}\cdot\frac{3.78}{(3.78+1)^2} = \\ = 4671W. \qquad \text{(C.13)}$$

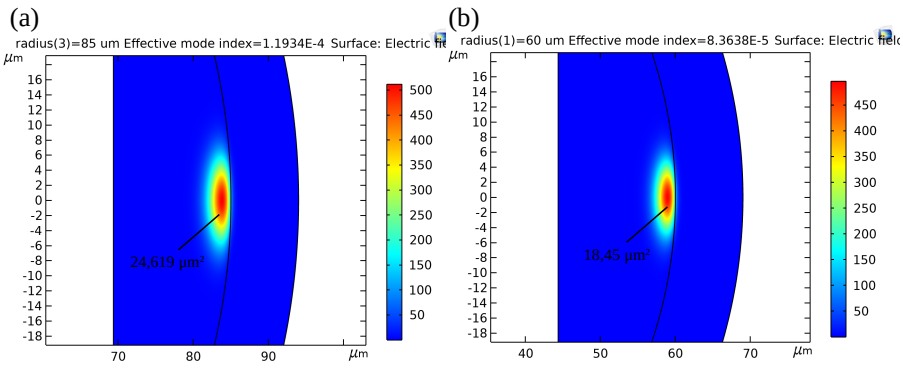

Figure C.2: Simulating fundamental mode excited inside WGMR with 1.55 μm: (a) for 170 μm sphere and (b) for 120 μm sphere.

To find the circulating intensity, simulations were performed, to determine the effective area of the mode (see Fig. C.2):

$$I_{circ} = \frac{P_{circ}}{A_{eff}} = \frac{4671}{24.619\cdot 10^{-12}} = 1.90\cdot 10^{14}\frac{W}{m^2} = 19.0\frac{GW}{cm^2}. \qquad \text{(C.14)}$$

COLOPHON

This document was typeset using the typographical look-and-feel `classicthesis` version 4.2 developed by André Miede. The style was inspired by Robert Bringhurst's seminal book on typography "*The Elements of Typographic Style*". `classicthesis` is available for both LaTeX and LyX:

https://bitbucket.org/amiede/classicthesis/

Final Version as of November 8, 2021